WAVES SERIES

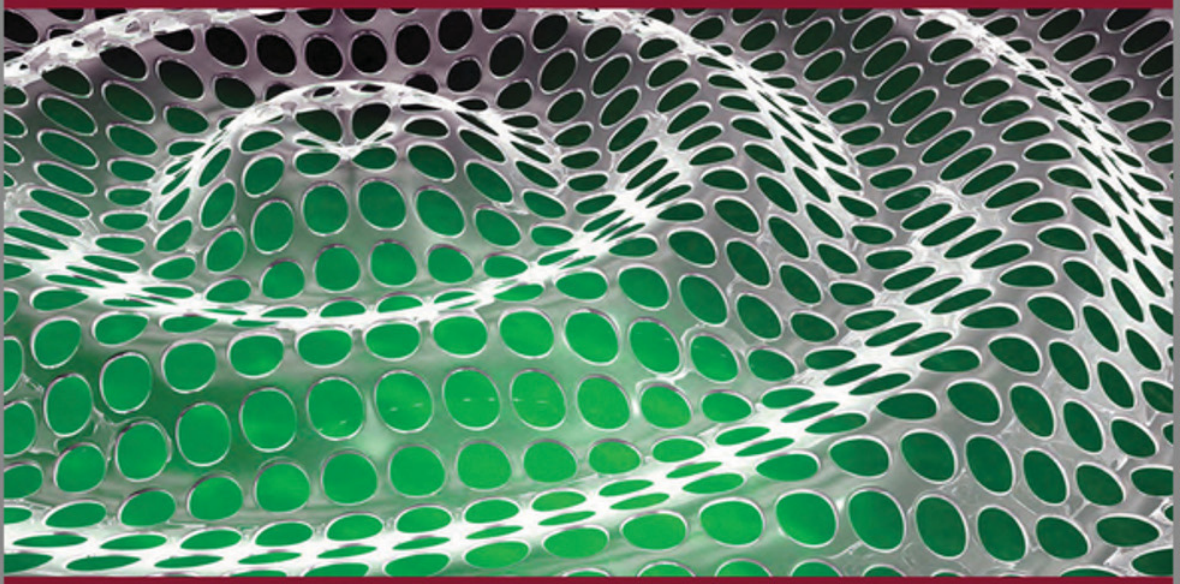

Metamaterials and Wave Control

Edited by
Éric Lheurette

ISTE
WILEY

Metamaterials and Wave Control

Metamaterials and Wave Control

Edited by
Éric Lheurette

Series Editor
Pierre-Noël Favennec

ISTE

WILEY

First published 2013 in Great Britain and the United States by ISTE Ltd and John Wiley & Sons, Inc.

ISTE Ltd
27-37 St George's Road
London SW19 4EU
UK

www.iste.co.uk

John Wiley & Sons, Inc.
111 River Street
Hoboken, NJ 07030
USA

www.wiley.com

Library of Congress Control Number: 2013947316

British Library Cataloguing-in-Publication Data
A CIP record for this book is available from the British Library
ISBN: 978-1-84821-518-4

Printed and bound in Great Britain by CPI Group (UK) Ltd., Croydon, Surrey CR0 4YY

Table of Contents

Introduction

Over the past 10 years, metamaterials have been the subject of a very extensive interest, as attested by numerous publications in both highly focused and wider public journals. On the one hand, the scientific attention finds its origin in the universal character of metamaterials. Indeed, this general concept can be applied to any physics domain involving the propagation of waves. On the other hand, metamaterials are relevant to everyday life and feed the imagination, especially with applications related to invisibility.

The project of this book was initiated during a thematic school organized by the network GDR ONDES 2451, supported by the French national organization CNRS (*Centre National de la Recherche Scientifique*) at Oléron from 29 May to 1 June 2012. The purpose of this event was to analyze the impact of the metamaterial approach in various fields of wave research and technologies. As a prospect, starting from an overview of the main research steps, we would like to propose metamaterials as a tool available to scientists and engineers working on the various domains related to the propagation of electromagnetic and acoustic waves. Before discussing the evolution of the metamaterial activity, let us define the metamaterial concept.

A metamaterial is an artificial structure whose dimensions are much smaller than the wavelength of interacting signals. If this condition is satisfied, the metamaterial can be considered as an average media. This media can then be modeled by effective constitutive parameters. For instance,

---

Chapter written by Éric LHEURETTE.

for the domain of electromagnetic waves, a metamaterial is characterized by its effective permittivity ε_{eff} and permeability μ_{eff}. This permittivity and permeability in turn describe the response of the metamaterial to electric excitation and magnetic fields, respectively. Following this principle, metamaterials appear like a new degree of freedom in the design of materials because their properties do not only rely on their basic compounds but also on the way these compounds are structured, namely the dimensions and the shape of the inclusions. Depending on these parameters, we can target unusual values of ε_{eff} and μ_{eff}, which give rise to outstanding physical properties like, for instance, the negative refraction if both ε_{eff} and μ_{eff} are negative. In the same manner, we can design the metamaterial structure in order to target very high or, on the contrary, near zero values of the permittivity and permeability.

One limit of this general concept lies in the definition of the metamaterial itself. Indeed, if the structure dimensions are required to be much smaller than the working wavelength, a given metamaterial loses its properties when the frequency is increased. This is due to the fact that the inclusions behave as scatterers when their dimensions are close to the incident signal wavelength. Therefore, the structured nature of a metamaterial is the first limitation of its working bandwidth.

The way to synthesize specific values of constitutive parameters is another source of frequency dispersion. Let us consider the case of electromagnetic material. These structures take their properties, especially artificial magnetism, from resonating inclusions. Because of this resonant behavior, the response of the artificial media to an electromagnetic excitation field strongly depends on frequency. Then, refractive index, for instance, can be negative over a very limited bandwidth.

This frequency dispersion comes along with anisotropy which is related to the arrangement of the structured media. Therefore, the response of a metamaterial to an incident wave depends on its incidence angle and polarization.

Because of these intrinsic dispersions, we can understand that metamaterials remain far behind the dream of an ideal media combining outstanding properties without any frequency, an incidence angle and polarization limitations. Nevertheless, as attested by the following bibliometric data, metamaterials have attracted an increasing interest for more than 10 years with an unquestionable impact on various domains of wave science and engineering.

Figure I.1 illustrates the general evolution of the metamaterial publications since the proposal of the concept at the beginning of the 21st Century. Let us recall that the term "metamaterial" was introduced in 2000 following two former articles by J.B. Pendry heralding the idea of a manufactured material with both negative permittivity and permeability. In the first article, Pendry [PEN 96] showed that the plasma frequency of a metallic medium, which marks the limit between its negative and positive permittivity regimes, can be tuned by means of an adequate structuration. Indeed, whereas the plasma frequency of a bulk metal equals several thousand terahertz, a metallic wire array under the approximation of a homogeneous medium is characterized by a lower plasma frequency, whose value depends on the main geometric dimensions of the array, namely the periodicity and filling factor. This allows for a tuning of the plasma frequency from the bulk metal value down to the lowest frequency range of the electromagnetic spectrum. This article led the way for negative permittivity engineering. In the second article, Pendry [PEN 99] proposed to use arrays of metallic inclusions, each behaving as a resonant current loop, in order to synthesize an effective permeability medium. One of the most exciting properties of such structures is the possibility to target negative values of the permeability close to the fundamental current loop resonance. This article, which marks the beginning of artificial magnetism, opened the way of permeability engineering.

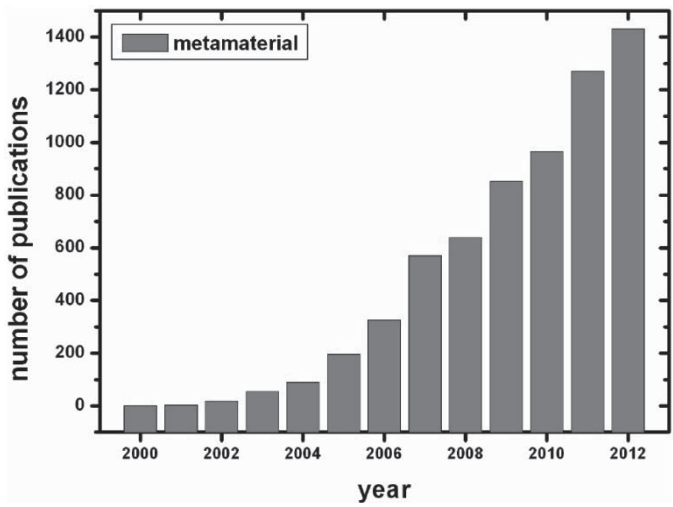

Figure I.1. *Evolution of the metamaterials related publications from 2000 to 2012, established from the SCOPUS database*

The natural result of these two major contributions is the definition of an artificial material combining negative effective permittivity and permeability over the same frequency band, allowing for the experimental demonstration of negative refraction predicted by V. Veselago back in 1968 [VES 68]. This demonstration was achieved by D.R. Smith *et al.* in 2001 [SHE 01]. These major theoretical and experimental contributions mark the beginning of metamaterial development, initially motivated by the new prospects of left-handed electromagnetism which were introduced as a mirror image of the right-handed electromagnetism describing the orientation of wave, electric field and magnetic field vectors in positive media, meaning a media where the constitutive parameters ε and μ are both positive. Left-handed electromagnetism means that if negative values of ε and μ are considered, the direction of the wave vector is reversed.

In order to further understand the exponential increase of metamaterial-related works observed over the last 10 years, we can analyze the global distribution of publications over several research and application fields. This distribution is depicted in Figure I.2. The selected fields are not exhaustive but they bring a structuring sight on metamaterial short history.

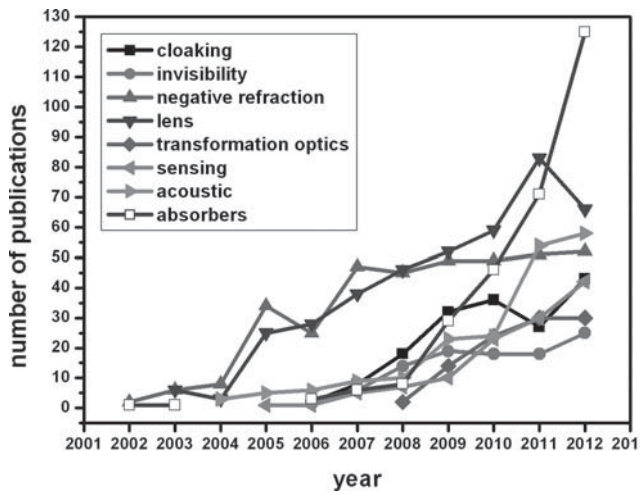

Figure I.2. *Distribution of the metamaterials related publications from 2000 to present, established from the SCOPUS database*

As a direct prospect of the former publications on left-handed electromagnetism, the first activities were mainly devoted to the synthesis of

a negative refractive index medium. This includes both fundamental contributions and efforts toward applications. The left-handed electromagnetism idea has a strong impact on several laws of wave physics. Among them, we can cite the reversal of the Snell–Descartes law, the reversal of the Doppler effect and the reversal of Cherenkov effect [VES 68]. A lot of early articles are related to negative refraction, firstly because negative refraction allows the focus of an electromagnetic signal by means of a flat lens which appears like a new degree of freedom. Following Smith's first demonstration [SHE 01], many other experimental works have been conducted mainly at microwave frequencies [HUA 04, CHE 05, LHE 08]. Furthermore, negative refraction studies were motivated by the dream of a perfect lens, i.e. a lens able to overcome the diffraction limit responsible for a maximum resolution of roughly half a wavelength. This new possibility was pointed out by Pendry in 2000 [PEN 00], who explained that a negative index media would be able to amplify evanescent waves, thus opening the way to unlimited resolution.

Fundamentally, this article has been the subject of many discussions. Despite these controversies, resolutions under the diffraction limit have been demonstrated, experimentally, from microwaves to optics [GRB 04, FAN 05, FAB 08].

However, we can note in Figure I.2 that the negative refraction and lens curves, initially superimposed and following a linear increase from 2002, are diverging from 2008. This behavior supports several interpretations. First, it should be noted that the synthesis of double negative media implies very important design and technological challenges, especially in optics. Moreover, if we target imaginary applications, the frequency dispersion and anisotropy, mentioned before, are two major issues. These required properties are much more restrictive in the case of the perfect lens proposed by Pendry which is based on an index value equal to −1. Moreover, if we consider the impedance matching condition, which is necessary to minimize the reflection at the edges of the focusing device, both the permittivity ε and permeability μ have to be equal to −1. These conditions suppose negligible imaginary parts. The difficulties of synthesizing a low loss, low dispersion double negative medium explain why researchers have progressively explored other ways to achieve focusing from an artificial material. Among them, the recovery of metamaterial lens activity finds its source in the gradient index approach. The idea of a progressive variation of n in order to confine electromagnetic energy emerged long before the metamaterial research field. As an example, this approach is commonly used in fiber optic technologies. Nevertheless, it

found an echo in the metamaterial community with the idea of synthesizing the gradient index by means of a variation in the dimensions of the metamaterial's elementary constituents. In this case, the focusing mechanism is based on the bending of the phase front due to local variations of the phase velocity [PAU 10]. This can be achieved either by means of negative or positive index values. For the latter case, the design constraints are considerably relaxed. Even if the requirement of perfect focus cannot be satisfied with positive index values, this solution appears valuable for many applications.

The perfect lens marks a very important step in the metamaterial research because it has opened new ways that could not be considered outside of this research field. For this reason, we can consider the perfect lens as the first dream in metamaterial's short history.

The idea of invisibility cloaking can be considered as the second dream of metamaterials with an increasing number of publications (see Figure I.2) since the pioneering article by Pendry [PEN 06] and, again, subsequent experimental demonstration by Smith *et al*. [SCH 06]. This idea is a step further in the control of an electromagnetic wave by means of metamaterials. It illustrates the possibility of bypassing an object without any reflection and without any signature in the transmitted wave front. This is a very important difference with respect to stealthing based on absorption and scattering. This new application is an example of the transformation optics research topic emerging from 2006 (see Figure I.2). This general concept benefits from propagation equations invariance with respect to the chosen coordinate system. For instance, Maxwell's equations, describing the propagation of an electromagnetic wave in a Cartesian space, can be applied to a curved space by means of adequate constitutive parameters. This approach illustrates the maturity of metamaterial structure design because it presupposes that metamaterials are able to synthesize a wide range of constitutive tensors following well-known design rules. Obviously, this assessment is a little bit optimistic and, for a given application, the most important challenge is to imagine coordinate transformations that can lead to realistic values of the constitutive tensors. Even if negative constitutive parameters are achievable, in many cases, it appears more convenient to work with positive values. Moreover, for ease of design, it also seems preferable to synthesize the transformed space by a single gradient, either permittivity or permeability, for the control of electromagnetic waves. As an example, the first experimental demonstration of invisibility cloaking involved a variation of the effective permeability between 0 and 1 [SCH 06]. Other efforts are

concentrated on a variation of the refractive index n, allowing the design of an invisibility cloak in optics, by using a photonic bandgap-related structure [ERG 10]. These tendencies are meaningful to the metamaterial activity evolution which can be seen as a convergence area between the difficulties to achieve a low-loss double negative media and the constant progress in terms of design and technology, allowing experimental realizations down to optical wavelengths.

Most of the published works so far are related to electromagnetic waves. However, the concept of metamaterial, as we defined it at the beginning of this introduction, can be applied to other domains of wave science. In particular, we can observe, in Figure I.2, a growing interest in acoustic metamaterials. As an illustration, we can cite the recent efforts toward the design of a cloak in order to protect buildings from seismic waves [BRU 13].

As explained before, the perfect lens and the invisibility cloak can be considered as two important steps in the metamaterial short history because they are a direct consequence of the new possibilities of the wave control brought by metamaterials. Apart from these new applications, metamaterials can also improve the performance of existing devices and systems. In particular, extensive work has been devoted to sensing since 2005 (see Figure I.2). The advantages of metamaterials for this activity domain are a great freedom in the design of structures, the use of high resonant patterns with an expected benefit on sensing detection and the capability to concentrate electromagnetic energy in order to optimize the interaction between the wave and the element to be detected. Following these general trends, several works have been published about multi-resonator surfaces which are able to fit complex spectral responses [BIN 08]. But the most innovative approach remains the concept of electromagnetic induced transparency, which benefits from the indirect excitation of a dark resonant state by means of coupling with a bright one [PAP 08, TAS 09]. The metamaterial approach also had a strong impact on microwave design and functions. Firstly, we can make the most of highly resonant artificial particles for the design of compact selective filters [GAR 06]. Secondly, the left-handed electromagnetism brings new possibilities for phase engineering [KUY 06, MAR 09]. Finally, as depicted in Figure I.3, most of the metamaterial key word articles concern the domain of antennas. Here, we have to separately consider the use of metamaterial structures [TIC 09] which involves arrays, including a large number of elementary particles from the use of single resonator devices, also termed “metamaterial inspired”

[ERE 08]. This last case is rather far away from the original idea of getting access to new properties from the synthesis of an artificial bulk material. The main benefit expected from the metamaterial approach for the antenna field is miniaturization. Again, controlling electromagnetic radiating energy from few resonating subwavelength particles is of prime interest. From a physical point of view, one of the most relevant properties is the concept of the zeroth-order resonator, which would be equivalent to a zero refractive index [SAN 03]. Indeed, at the zero-index frequency point, the wavelength tends to infinity which breaks the relationship between the physical length and resonance frequency, opening the way to very compact antenna designs.

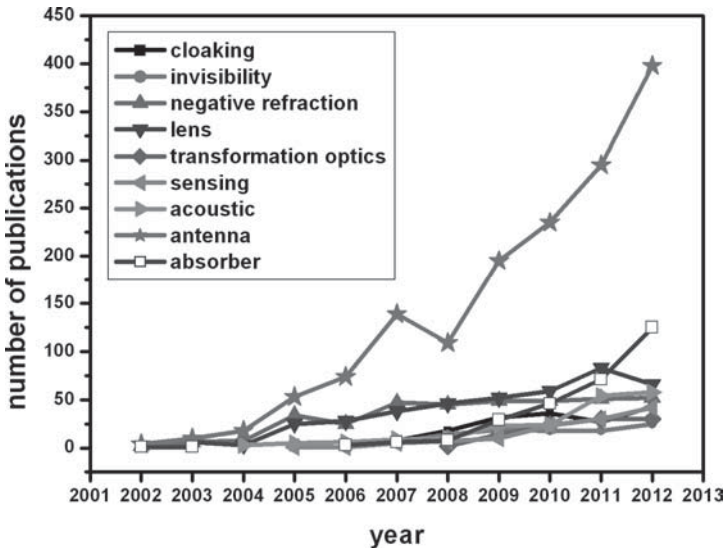

Figure I.3. *Distribution of the metamaterials related publications from 2000 to present showing the relative importance of antenna contribution, established from the SCOPUS database*

Finally, one of the most currently emerging fields is the application of metamaterial absorbers (see Figure I.2). Again, this development is indicative of the evolution of metamaterials. Indeed, the early years have been devoted to the demonstration of left-handed effects with a lot of effort focused on the reduction of losses. These efforts are currently continuing, notably around the idea of non-Foster metamaterials. However, we know that metamaterials, which often involve resonating inclusions, are intrinsically lossy. We can think about taking benefit from this drawback by optimizing the imaginary

parts of effective constitutive parameters for the design of absorbing layers. The main requested properties are the compactness, achievable with a metasurface design, angular and frequency independence which can be satisfied by multisize patterns. The specific benefit of an artificial material design is the fact that the absorbing properties are not restricted by the intrinsic losses of the constituent materials, which bring new degrees of freedom, from low frequencies to optical wavelengths, where the underlying metamaterial physics tends to merge with plasmonics.

Most of the topics discussed in this introduction will be covered in more detail in this book over eight chapters, written by experts in the related fields. As the demonstration and applications of electromagnetic metamaterial properties are strongly dependent on technology, this point will be discussed in the first chapter. To this aim, various typical frequency bands will be considered, from microwave to optics and several ways to tune the metamaterial structure frequency response will be presented. Special attention will be paid to the issue of losses, both with microwaves and optics. This key point will be the subject of Chapter 2. Considering the very abundant literature on microwave metamaterial devices, the microwave frequency band will be addressed in Chapters 3–5. The field of free-space applications, dominated by antennas, will also be looked at in Chapter 3. The specific concept of metalines, implying guided wave propagation, will be the subject of Chapter 4. As a prospect, the interest of the metamaterial concept for electromagnetic compatibility (ECM) will be developed in Chapter 5. Chapter 6 is dedicated to the applications of coordinate transformations for the synthesis of electromagnetic functions. Acoustic metamaterials will be introduced in Chapter 7 by means of an analogy with photonic artificial media. Finally, Chapter 8 will focus on the concept of electromagnetically induced transparency (EIT), and its applications to sensing.

I.1. Acknowledgments

I would like to thank all the participants of the GDR ONDES Oléron's thematic school, especially the lecturers Alain Bossavit, André de Lustrac, Sébastien Guenneau, Didier Lippens, Bruno Sauviac, Divitha Seetharamdoo and Philippe Tassin, also Ludovic Burgnies and Lionel Pichon for their involvement in its organization. Finally, I have to mention the unfailing support of Frédérique de Fornel, starting from the emerging ideas of Oléron's thematic school up to the finalization of this book.

I.2. Bibliography

[BIN 08] BINGHAM C.M., TAO H., LIU X., *et al.*, "Planar wallpaper group metamaterials for novel terahertz applications", *Optics Express*, vol. 16, no. 23, pp. 18565–18575, 2008.

[BRU 13] BRULÉ S., JAVELAU E., ENOCH S., *et al.*, "Seismic metamaterial: how to shake friends and influence waves," *arXiv.org > Physics > Geophysics*, available at http://arxiv.org/abs/1301.7642, 2013.

[CHE 05] CHEN H., RAN L., HUANGFU J., *et al.*, "Negative refraction of a combined double S-shaped metamaterial", *Applied Physics Letters*, vol. 86, no. 15, p. 151909, 2005.

[ERE 08] ERENTOK A., ZIOLKOWSKI R.W., "Metamaterial-inspired efficient electrically small antennas", *IEEE Transactions on Antennas and Propagation*, vol. 56, pp. 691–707, 2008.

[ERG 10] ERGIN T., STENGER N., BRENNER P., *et al.*, "Three-dimensional invisibility cloak at optical wavelengths", *Science*, vol. 328, no. 5976, pp. 337–339, 2010.

[FAB 08] FABRE N., LAOULAT L., CLUZEL B., *et al.*, "Optical near-field microscopy of light focusing through a photonic crystal flat lens", *Physical Review Letters*, vol. 101, no. 7, p. 073901, 2008.

[FAN 05] FANG N., LEE H., SUN C., *et al.*, "Sub-diffraction-limited optical imaging with a silver superlens", *Science*, vol. 308, no. 5721, pp. 534–537, 2005.

[GAR 06] GARCIA-GARCIA J., BONACHE J., GIL I., *et al.*, "Miniaturized microstrip and CPW filters using coupled metamaterial resonators", *IEEE Transactions on Microwave Theory and Techniques*, vol. 54, no. 6, pp. 2628–2635, 2006.

[GRB 04] GRBIC A., ELEFTHERIADES G.V., "Overcoming the diffraction limit with a planar left-handed transmission-line lens", *Physical Review Letters*, vol. 92, no. 11, p. 117403, 2004.

[HUA 04] HUANGFU J., RAN L., CHEN H., *et al.*, "Experimental confirmation of negative refractive index of a metamaterial composed of Omega-like metallic patterns", *Applied Physics Letters*, vol. 84, no. 9, pp. 1537–1539, 2004.

[KUY 06] KUYLENSTIERNA D., VOROBIEV A., "Composite right/left handed transmission line phase shifter using ferroelectric varactors", *IEEE Microwave and Wireless Components Letters*, vol. 16, no. 4, pp. 167–169, 2006.

[LHE 08] LHEURETTE É., HOUZET G., CARBONELL J., *et al.*, "Omega-type balanced composite negative refractive index materials", *IEEE Transactions on Antennas and Propagation*, vol. 56, no. 11, pp. 3462–3469, 2008.

[MAR 09] MARTEAU A., VÉLU G., HOUZET G., *et al.*, "Ferroelectric tunable balanced right- and left-handed transmission lines", *Applied Physics Letters*, vol. 94, no. 2, p. 023507, 2009.

[PAP 08] PAPASIMAKIS N., FEDOTOV V.A., ZHELUDEV N.I., *et al.*, "Metamaterial analog of electromagnetically induced transparency", *Physical Review Letters*, vol. 101, no. 25, p. 253903, 2008.

[PAU 10] PAUL O., REINHARD B., KROLLA B., *et al.*, "Gradient index metamaterial based on slot elements", *Applied Physics Letters*, vol. 96, no. 24, p. 241110, 2010.

[PEN 96] PENDRY J.B., HOLDEN A.J., STEWART W.J., *et al.*, "Extremely low frequency plasmons in metallic mesostructures", *Physical Review Letters*, vol. 76, no. 25, pp. 4773–4776, 1996.

[PEN 99] PENDRY J.B., HOLDEN A.J., ROBBINS D.J., *et al.*, "Magnetism from conductors and enhanced nonlinear phenomena", *IEEE Transactions on Microwave Theory and Techniques*, vol. 47, no. 11, pp. 2075–2084, 1999.

[PEN 00] PENDRY J.B., "Negative refraction makes a perfect lens", *Physical Review Letters*, vol. 85, no. 18, pp. 3966–3969, 2000.

[PEN 06] PENDRY J.B., SCHURIG D., SMITH D.R., "Controlling electromagnetic fields", *Science*, vol. 312, no. 5781, pp. 1780–1782, 2006.

[SAN 03] SANADA A., CALOZ C., ITOH T., "Novel zeroth-order resonance in composite right/left-handed transmission line resonators", *2003 Asia-Pacific Microwave Conference*, Seoul, Korea, 4–7 November 2003.

[SCH 06] SCHURIG D., MOCK J.J., JUSTICE B.J., *et al.*, "Metamaterial electromagnetic cloak at microwave frequencies", *Science*, vol. 314, no. 5801, pp. 977–980, 2006.

[SHE 01] SHELBY R.A., SMITH D.R., SCHULTZ S., "Experimental verification of a negative index of refraction", *Science*, vol. 292, pp. 77–79, 2001.

[TAS 09] TASSIN P., ZHANG L., KOSCHNY T., *et al*., "Low-loss metamaterials based on classical electromagnetically induced transparency", *Physical Review Letters*, vol. 102, p. 053901, 2009.

[TIC 09] TICHIT P.H., BUROKUR S.N., DE LUSTRAC A., "Ultradirective antenna via transformation optics", *Journal of Applied Physics*, vol. 105, no. 10, p. 104912, 2009.

[VES 68] VESELAGO V.G., "The electrodynamics of substances with simultaneously negative values of epsilon and mu", *Soviet Physics Uspekhi*, vol. 10, no. 4, pp. 509–514, 1968.

Chapter 1

Overview of Microwave and Optical Metamaterial Technologies

This chapter gives an exhaustive overview of the various metal and dielectric artificial material technologies that are currently developed in the microwave and optical regimes. Starting from the first proposals for negative index materials (NIMs), based on a split-ring resonator (SRR)/wire scheme, we show how this basic pattern has progressed to solving the problem of normal incidence with the so-called fishnet structure and to broadband with a transmission line approach. Full dielectric metamaterials whose operation relies on Mie resonance in the long wavelength regime or on band folding, close to the Bragg conditions, complete this analysis.

1.1. Introduction and background

Electromagnetic (EM) metamaterials are now attracting much interest owing to their singular properties notably with the achievement of *negative* effective parameters [CAI 09, SOL 09, RAM 08, MAR 08, ELE 05]. For illustration, Figure 1.1 shows the possibilities afforded by these engineered artificial materials by plotting the effective permeability (real part μ_r) versus effective permittivity (real part ε_r) diagram. With respect to *conventional* natural or structured materials with *positive* index value $n = (\varepsilon_r\mu_r)^{1/2}$, with extreme values (notably relative permittivity and permeability ε_r, $\mu_r > 100$

Chapter written by Didier LIPPENS.

through the use of ferroelectrics and ferromagnetics materials), metamaterials allow the fabrication of: (1) epsilon negative (ENG materials: $\varepsilon_r < 0$ and $\mu_r > 0$) or near-zero (NRZ) permittivity material (NRZ materials: $\varepsilon_r \sim 0$), (2) mu negative (MNG materials with $\mu_r < 0$ and $\varepsilon_r > 0$) and (3) double negative media (DNG with $\mu_r < 0$ and $\varepsilon_r < 0$).

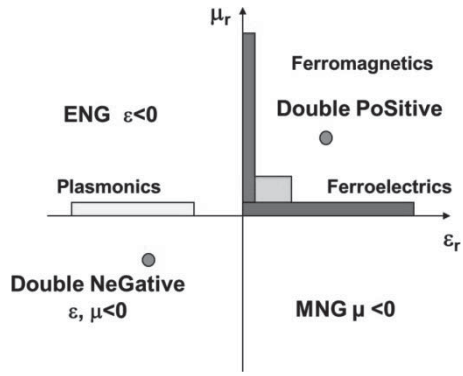

Figure 1.1. *Effective parameter space: ferroelectric and ferromagnetic natural materials enable the fabrication of extreme permittivity (ε_r between 100 and 1,000 for Barium Strontium Titanate material for instance). Metallic compounds involved in the fabrication of plasmonics devices such as gold or silver layers exhibit a naturally negative dielectric constant below their plasma frequency. As a result, they can be considered as ENG materials. Their structuring designs their dispersion characteristics via the plasma frequency engineering. MNG materials involve current loops*

From the viewpoint of EM wave propagation, metamaterials give the possibility of accurately controlling the following:

– The *phase* of the reflected waves in mirror-like devices (out-of-phase for a perfect electrical conductor (PEC) and in phase for a perfect magnetic conductor (PMC), also called artificial magnetic conductor (AMC)).

– The *backward* propagation for NIM (equivalent to DNG materials), which means that the group and phase velocities are antiparallel.

– The $\boldsymbol{k}$ vector magnitude including quasi-infinite wavelength for near-zero permittivity or balanced composite right–left-handed metamaterials (CRLH).

– The *negative* refraction angle (same half-space with respect to the impinging wave).

– The focusing of a point source placed in front of a NIM flat lens. Also *super-resolution* below the *Rayleigh diffraction limit* can be considered on the basis of the so-called amplification of evanescent waves.

In a first approximation (by neglecting the dispersion of constitutive materials), the EM characteristics scale to the size of the basic cell, whose relevant dimensions have to be much shorter than the operating wavelength to satisfy homogeneity conditions. From this scaling rule, it results that device operation over an *ultra-broad frequency band* (from radio frequency to visible optics) can be envisaged by downscaling all the relevant dimensions [RAM 08, SOL 09, CAI 09].

Basically, artificial media involve a structural transformation at the origin of the negative values of their effective constitutive parameters. This concept can be understood simply from the recognition that the response of a material to an impinging wave is *out-of-phase* with respect to the excitation, provided that the driving signal frequency is above the characteristic resonant frequency of the system. This basic principle is true (1) for cut-wire arrays, which exhibit a Lorentz-type permittivity dispersion (Figure 1.2), (2) for negative permeability plasmonic resonators and (3) for Mie resonance-based dielectric resonators.

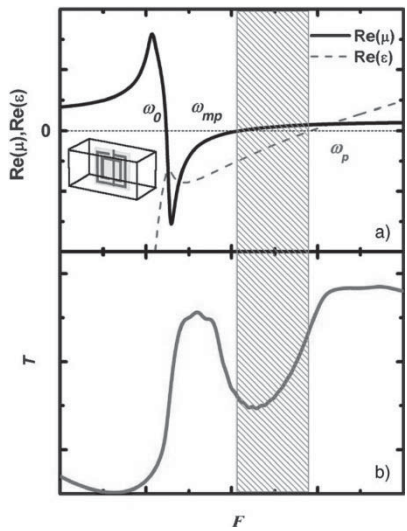

Figure 1.2. *Dispersion characteristics of constitutive parameters. MNG are fabricated from artificial structures mainly involving metallic current loops as in a miniaturized solenoid. DNG are achieved via the combination of ENG and MNG media. Propagation characteristics can be predicted on the basis of the dispersion of the effective (apparent) permittivity and permeability. Generally, μ_{eff} obeys a Lorentz-type (resonant) frequency variation while ε_{eff} follows a Drude-type (non-resonant) frequency dependence*

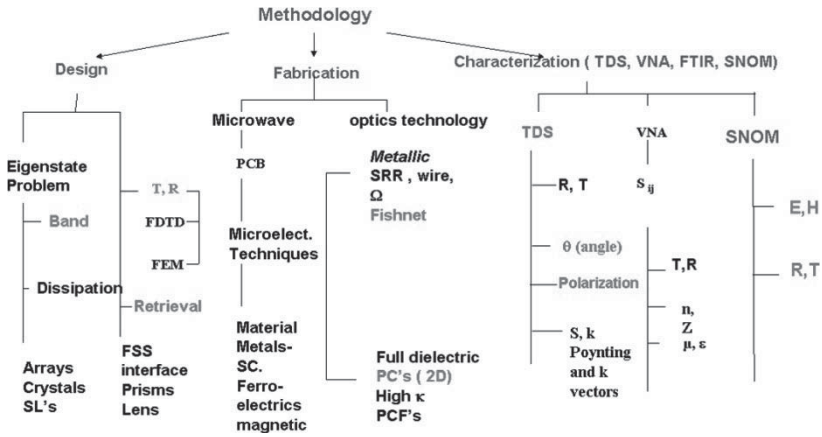

Figure 1.3. *Illustration of the methodology for the realization of artificial materials including the design, the fabrication and the experimental assessment. In grey character: the key issues addressed in this review*

A general study methodology is summarized in Figure 1.3. It consists of three stages permitting us to (1) first predict the geometrical specifications according to the data of the material constituents, (2) to synthesize the artificial structures and (3) to experimentally verify the targeted propagation characteristic resulting from the scattering of light with these artificial media. With respect to the design stage, the first step concerns solving the eigenstate master equations. With the target to achieve a highly dispersive EM characteristic, a large number of metamaterial structures are intrinsically resonant. Also, most of the microstructures used in metamaterial fabrication are periodic arrays. This periodicity condition is not strictly necessary since the basic response is due to the scattering of impinging waves on an isolated cell. However, it is worth mentioning that the coupling effects between basic cells, in densely packed arrays, play an increasing role, notably in the case of symmetry breaking that gives further degrees of freedom in the functionality of the devices. For instance, it was just shown that the *coupling* between an SRR (often considered as the canonical meta-atom) and its mirrored image by a PEC permits us to adjust the resonant frequency over a 10% fractional bandwidth. The counterpart of the highly dispersive nature of metamaterials is the *loss* issue and the second major stage in the device design is the estimate of the intrinsic and extrinsic loss contributions. The latter is of prime importance for the necessary impedance matching of a metamaterial to its environment. On this basis, the scattering parameter characteristics or,

equivalently, the complex transmission and reflection coefficients can be derived by using home-made or commercially available simulation codes.

With respect to the fabrication technologies, we have to distinguish between those enabling the fabrication of microwave devices and those that are employed for the fabrication of structures operating in the optical spectrum.

For the former, conventional printed circuit board (PCB) technology can be used for the host substrate and the metal patterns such as strips, pads, gaps, slots or apertures. These patterns generally form the basic cell of the metamaterial-inspired structure. However, in many cases, some originality can be drawn from the fact that structuring is realized on a micro- or nanometer scale with, thus, a very high aspect ratio between the wavelength and the relevant dimension of the basic cell.

In connection with the optics technology [LIU 08, JOA 08, KAN 11], two classes of device will be considered, namely plasmonic devices (in this case, metals are used as free-standing structures or deposited onto host dielectric substrates, including multilayered structures with dielectric spacing) or full dielectric micro- and nanostructures. The latter includes *photonic crystal*s, paying attention to their unusual dispersion characteristic rather than to their band gap. These dielectric structures are generally made up of semiconductors for their compatibility to integrated optics. Specially, this means the possibility of fabricating, for instance, hole and pillar arrays that exhibit negative refraction when operating in the second band of the dispersion diagram, or fabricating the so-called gradient index lens by varying the relevant dimensions of the basic cell locally.

At last with respect to the characterization stage, various techniques will be employed including first vector network analysis that is mainly dedicated to the analysis of microwave and millimeter wave metamaterials. The main advantage of this technique is the record of the magnitude and phase of the reflection (R) and transmission (T) characteristics that allow the *effective parameters* to be retrieved without any ambiguity [SMI 02]. Also, the mapping of the EM fields brings information of prime importance for the verification of wave bending via gradient index structures such as those involved in focusing and cloaking devices.

Turning now to the terahertz frequency range, in practice between 0.3 and 3 THz, the most powerful technique is the time domain spectroscopy (TDS) that also gives access to the magnitude and phase of R and T. These techniques can be used in a complementary manner by considering first the

frequency assessment of the dispersion of constitutive materials and then the characterization, at the device level, after microstructuring.

For the optics side, the experimental verification can be based on scanning near-field optical microscopy (*SNOM*) and Fourier transform infrared (*FTIR*). Basically, these techniques only provide magnitude information. However, an additional set-up can be used in order to get access to the phase data. A differential measurement, as is performed in TDS experiments, seems to be one of the most promising tracks toward this possibility of measuring simultaneously phase and magnitude.

At microwaves, the generic structure is made up of *SRRs* and *wire* arrays [PEN 96, PEN 99]. In this chapter, it will be shown that omega-type patterns are equivalent to a double negative medium (with a left-handed dispersion branch) in a relatively broad frequency range, which can be balanced with a right-handed dispersion branch. This EM artificial structure called CRLH metamaterial can be used for a beam steering wedge-type device such as the one discussed in the next section.

In a second part, we show how a full dielectric approach can replace the metal (plasmonic) approach by mainly targeting the isotropy of EM characteristics. This technology, known as a Mie resonance-type approach [MIE 08, LEW 47] will be exemplified via ferroelectric cube arrays. For both approaches (plasmonic and full dielectric), we show how tunable EM characteristics can be achieved by modifying the resonant frequency notably with the infiltration of liquid crystal (LC) whose orientation is controlled. In addition, it can be shown that backward waves, corresponding to a negative index, can be achieved by periodically loading a transmission line by series capacitances and shunt inductances. This *transmission line* approach will be briefly addressed in this chapter with the main emphasis on bulk structures. However, the transmission line approach is further developed by Bruno Sauviac in Chapter 2.

1.2. Omega-type arrays

Figure 1.4 illustrates the omega-type technology [HUA 04, LHE 07, SIM 03, ZHA 08a], with a schematic of the basic cell (a) along with the stacking scheme (b). The interconnected arms of the omega motifs constitute a *continuous* wire array (Drude-like dispersion) at the origin of the electrical activity. The C-shaped core is equivalent to the so-called SRR [PEN 99] that gives rise to a magnetic activity with a Lorentz-type dispersion characteristic.

Indeed, for a proper polarization of the magnetic field, i.e. normal to the metallic pattern (grazing incidence), the induced current in the metal loop yields a magnetic response (B) that is out-of-phase with respect to excitation field H. From the constitutive equation $B = \mu H$, it can be noted that the effective permeability is negative. From Figure 1.4, it can be seen that the basic cell consists of two omega patterns with a back-to-back configuration, aiming at cancelling the current induced by the electrical stimulus (through the gap) in the metal loop. It can be shown that such an arrangement is equivalent to broadside coupled SRRs [MAR 08].

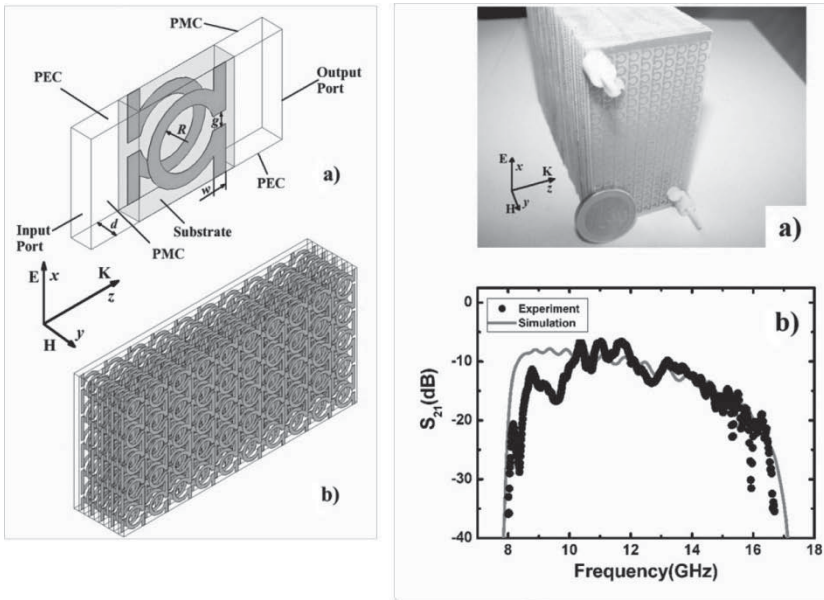

Figure 1.4. *Illustration of a balanced composite right–left-handed (CRLH) bulk metamaterial fabricated from omega-type motifs. Left panel a) basic cell and b) 3D configuration of the layered structure (the wire array corresponding to the omega arms is continuous for a Drude-like dispersion characteristic). Right panel a) image of a prototype operating in X- and Ku-bands and b) frequency dependence of the transmission coefficient S_{21}*

1.2.1. *Dispersion and angular properties*

In this chapter, the geometrical dimensions are chosen for an operation at centimeter wavelengths, with relevant dimensions (strip metal width (w), slot (g) and ring radius (R) typically one order of magnitude smaller than the

operating wavelength in order to satisfy the metamaterial regime (see section 1.1). In practice, this means dimensions on a millimeter scale.

Figure 1.4 shows the transmission characteristic (modulus of the scattering parameter S_{21}) of a slab-type prototype, fabricated by using PCB technology (image in inset). S_{21} was measured by means of a vector network analyzer (VNA) and the frequency response is compared with the results of full wave simulations. From this figure, it can be seen that the device exhibits a broadband transmission window between 8 and 16 GHz. This broadband is a result of a *balance CRLH* dispersion characteristic as aforementioned. This means that the transition between the left-handed (negative index) and the right-handed dispersion branches is seamless (no forbidden gap between them). At the turning frequency, the refractive index is zero with a non-vanishing group velocity ($v_g = \partial\omega/\partial k$). At this stage, it should be emphasized that this situation is totally different from a near-zero index via a zero permittivity value since *both* the effective permittivity and permeability are null at the same frequency. In terms of dispersion characteristic, this means that the electrical plasma frequency (ω_{pe}) equals the magnetic plasma frequency (ω_{pm}). The simulations carried out for assessing the transmission properties of a slab-type device were conducted by creating the periodicity via appropriate boundary conditions. The direct description of the whole structure under test can thus be simulated. However, it is clear that this *ab initio* approach is time consuming and very demanding in computational resources. As a result, it seems suitable to examine whether the metamaterial structure can be described via its effective parameters (ε_{reff} and μ_{reff}). There is a plethora of literature that addresses the equivalence between the EM response given by an effective medium approximation and the real geometrical configuration. We show hereafter that such an approximation is valid for the omega structures, provided that permittivity and permeability tensors are used for the constitutive equations (see Table 1.1).

Details for the retrieval of dispersion characteristics can be found in references [SMI 02, CRO 08b]. On the basis of this tensor approach, the direction of the refracted beam can be predicted numerically under a homogeneous medium approximation and compared with the exact solution taking all the details of the microstructure into account. This comparison is carried out for two representative frequencies corresponding to negative and zero values of the effective index represented by the field maps of Figure 1.5.

Frequency		10.9	12.8	15.0
n		–1.0052	–0.038	0.777
ε	ε_x	–3.49 + 0.13i	–0.17 + 0.04i	4.90 + 0.57i
	(tan ε_x)	(–0.036)	(–0.234)	(0.117)
	ε_y	4.07 + 0.08i	4.07 + 0.08i	4.07 + 0.08i
	(tan ε_y)	(0.02)	(0.02)	(0.02)
	ε_z	15.56 + 0.36i	16.66 + 0.38i	15.74 + 0.24i
	(tan ε_z)	(0.023)	(0.02)	(0.0153)
μ	μ_x	0.99 + 0.00034i	0.9858 + 0.0003i	0.9850 + 0.0003i
	(tan μ_x)	(0.0003)	(0.0003)	(0.0003)
	μ_y	–0.28 + 0.03i	0.0082 + 0.0002i	0.1232 + 0.005i
	(tan μ_y)	(–0.091)	(–0.022)	(0.04)
	μ_z	1.050 + 0.007i	1.055 + 0.002i	0.818 + 0.002i
	(tan μ_z)	(0.007)	(0.002)	(0.002)
θ_r (°) (Retrieval value)		–30.6°	–1.10°	23.2°
θ_r (°) Homogeneous prism		–28.6°	–2.6°	21.5°
θ_r (°) Microstructured prism		–25.6°	–0.4°	25.4°

Table 1.1. *Permittivity and permeability tensors for three relevant frequencies of an omega-type metamaterial operating at microwaves (negative, null, and positive index frequencies). Comparison is made in terms of the refracted angle for a wedge-type device by assuming anisotropic and isotropic values of the constitutive parameters and determined from full wave analysis (microstructured prism)*

From this figure, it can be noted that similar behavior is predicted for the homogeneous and the microstructure approaches in the near field via the mapping of the electric field magnitude and, in the far field, through the plot of the radiation patterns. By changing the operating frequency, negative, zero and positive refraction angles can be achieved continuously in the vicinity (near-field condition) of the tilted interface of this wedge-type device. As a result in the far field, the radiation pattern is steered around the normal to the wedge interface.

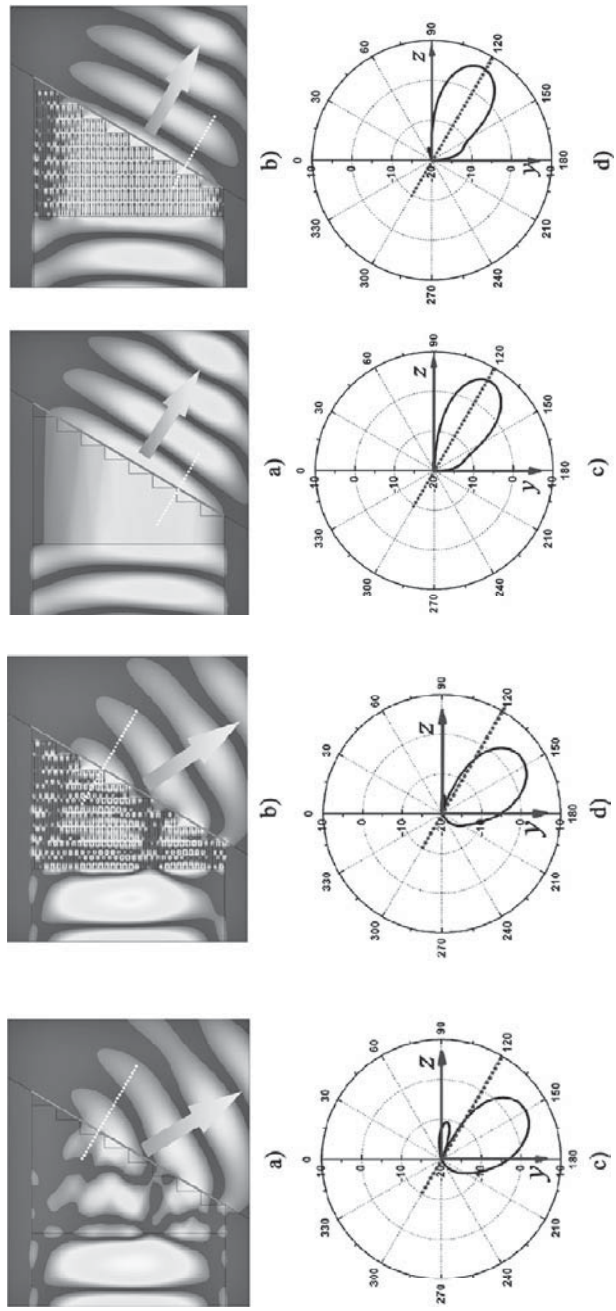

Figure 1.5. *Comparison between the near field response of a prism-like device made up of omega-type arrays and approximated by using the effective medium theory for f = 12.8 GHz (above side) and 10.9 GHz (below side)*

Experimental verification of the aforementioned beam steering can be demonstrated by using a scattering chamber such as the metal dual plate. For clarity, the top metal plate was removed in Figure 1.6(a) showing an image of the experimental set-up. The EM waves are radiated and detected via rectangular horn antennas connected to a VNA. In addition, absorbing materials slabs are positioned on the sides of the input path (between the input horn and the sample under test). In Figures 1.6(c) and (b), the angle dependence along with the image of a prism-like device are displayed, respectively. This structure has also been fabricated by means of stacked PCBs. According to the operation frequency *(f)*, it can be shown that the maximum of the detected signal peaks around $\theta = -22°$ for f =12 GHz, $\theta = 0°$ for 13.6 GHz and $\theta = +13°$ for f = 15 GHz.

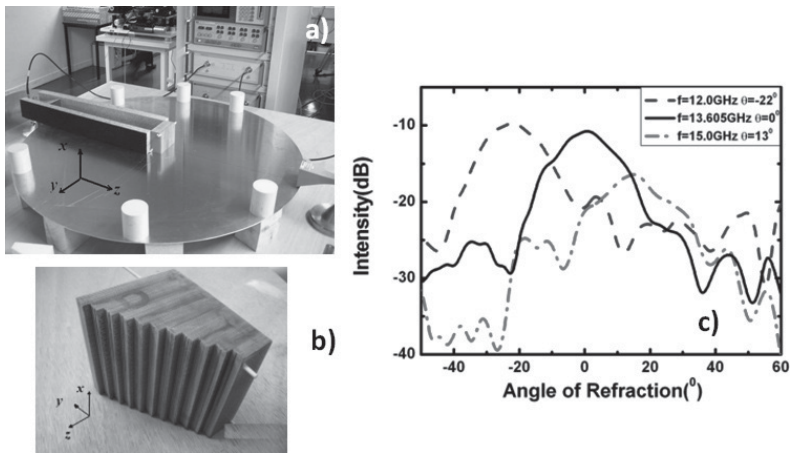

Figure 1.6. *a) Image of a scattering chamber using a parallel plate set-up (for clarity, the upper metal plate was removed), b) image of a wedge-type device and c) angle dependence of the refracted beam for three operating frequencies*

1.2.2. *Tunable omega-type structure*

The previous example shows the possibility of tuning the EM properties via a change of the operating frequency. However, in many practical applications, it is interesting to vary the operating point at a fixed frequency. This can be done by changing the dielectric properties of the constituent materials. In the following, such a change is exemplified via the use of LC technology [ZHA 08c, ZHA 08d].

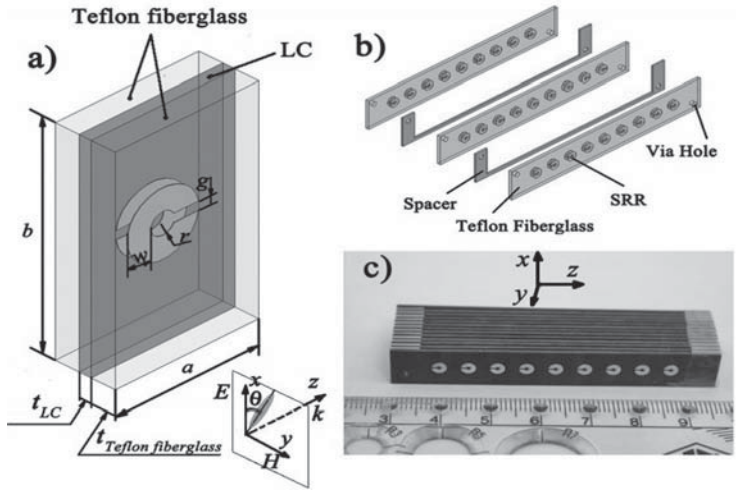

Figure 1.7. *Experimental demonstration of the tunability of single negative media (broadside coupled SRR-type motif). Tunability is achieved via liquid crystal (LC) infiltrated between the SRR-patterned array. Ellipsoidal-shaped nematics are reorientated by means of permanent magnets (not shown here)*

Indeed, it is well known that LCs such as nematic compounds are birefringent. This means that they exhibit different index values along the long and short axes of the ellipsoidal-shaped molecule (see inset of Figure 1.7 for illustration). The LC molecules can be oriented primarily, for instance via interface states, but also *reoriented* by means of external stimuli such as magnetic or electric fields. The underlying idea for tuning the properties of metamaterials is to reorientate LC films that are infiltrated within the two back-to-back C-shaped motifs of omega particles [ZHA 08a]. For the sake of clarity, a single negative medium, with negative value of the effective permeability while the effective permittivity is positive, is considered as an intermediate stage. The basic cell of the magnetic negative (MNG) medium is shown in Figure 1.7. The fact of using a back-to-back gap configuration is motivated by the search for a pure magnetic response as briefly explained earlier, by cancelling the electric field induced currents. Under the condition of a single negative medium, the index is purely imaginary. In terms of propagation properties, this corresponds to evanescent waves in the frequency band where μ_{reff} is negative. As a result, we expect a stop band rather than a passband transmission characteristic. For tunability purposes, according to the aforementioned basic principle, LCs are infiltrated between the two metal C-shaped motifs by means of spacer layers as illustrated in Figure 1.7. Their

reorientation (θ angle) as a function of the electric field polarization is controlled experimentally via permanent magnets. An image of a prototype is shown in Figure 1.7 [ZHA 09a].

In Figure 1.8, the frequency dependence of the transmission coefficient, measured through VNA and calculated by full wave analysis, is compared. Similar trends are obtained for calculated and measured data in agreement with the frequency shift predicted when θ is increased step by step between 0° and 90°.

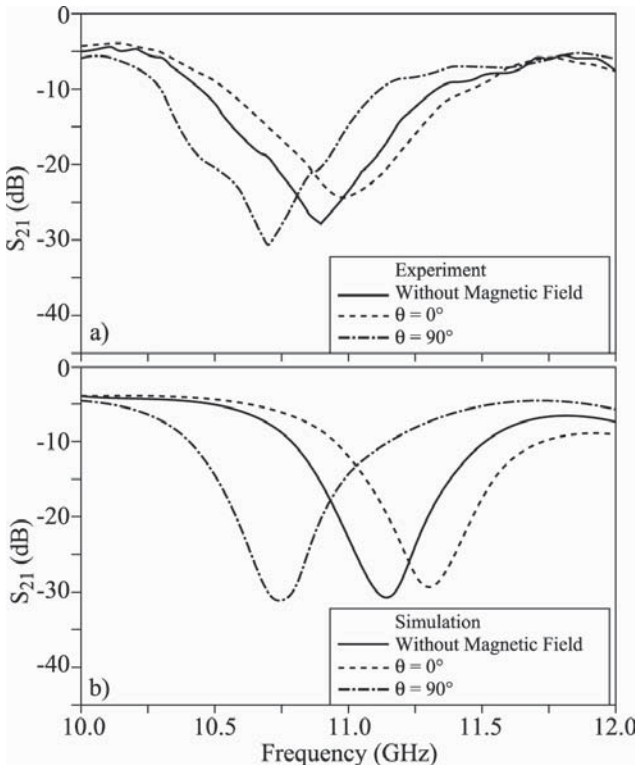

Figure 1.8. *Comparison between the frequency dependence of the S_{21} scattering parameter (experiment a) and simulation b)) for single negative permeability metamaterial. A stop band response is achieved with the possibility of tuning the anti-resonance dip by the reorientation of the infiltrated nematic molecules*

For a comprehensive study of the capabilities of the omega-type structures, we will now consider their operation at millimeter wavelengths.

1.2.3. *Omega-type pattern at millimeter wavelengths*

SRR/wire arrays [GOK 06, CRO 08a] and omega-type patterns [ZHA 08e] can also be used at higher frequencies at the cost of challenging technologies to satisfy the reduction in dimension. Therefore, instead of using PCB technology, monolithic integration has to be involved for stacking the various metal layers (Figure 1.9).

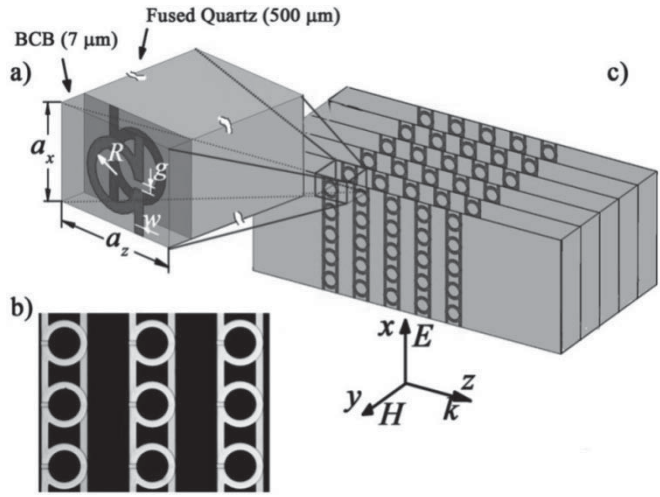

Figure 1.9. *Illustration of the monolithic stacking techniques for bulk metamaterial operation at millimeter wavelengths; a–c) schematic of the stacked arrangement of arrayed omega-type pattern with a close up view of the basic cell along with an image of the broadside coupled omega chains*

The FR4 dielectric substrates have been replaced by 7-µm-thick benzocyclobutene (BCB) layers deposited on fused silica substrates. As an example of the possibilities afforded by monolithic fabrication techniques, Figure 1.10 illustrates the transmission characteristic of an omega-type prototype aimed at operating at millimeter wavelengths.

Unlike the previous prototype operating at centimeter wavelengths, in the present case, there exists a band gap between the left- and right-handed dispersion branches. This can be noted in the frequency dependence of the magnitude S_{21} around 90 GHz. For identifying the left- and right-handed character of the passbands lying between 75 and 95 GHz and 100 and 110 GHz, respectively, we also plotted the phase of S_{21} for two prototypes of

different length, namely including 10 and 14 cells. We can note a positive phase difference for the former band while the difference becomes negative for the high-frequency band. This property is the signature of a cross-over within the gap. Also shown in the variation of the magnitude of S_{21} is the retrieved refractive index by a Fresnel inversion method [CRO 08b]. The value of the real part of n_{eff} is negative in the lower part of the W-band (50–75 GHz) corresponding to a backward wave and positive above 100 GHz. In the forbidden gap, the real part of n_{eff} is zero.

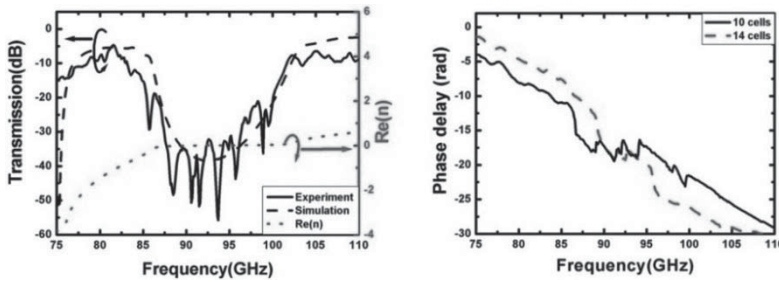

Figure 1.10. *Measured (solid line) and calculated (dashed line) transmission spectra, along with the retrieved effective index (dotted lines) versus frequency. Direct experimental evidence of the reversal of the k vector with respect to the Poynting vector, with a phase advance between 75 and 85 GHz and a phase delay between 85 and 110 GHz*

1.2.4. *SRRs at infrared*

The SRR technologies can also be extended to a higher frequency and notably in the infrared spectrum. The general concept, namely the phenomenon of a current loop, is scalable in frequency. As a result, negative values of the effective permeability can be expected up to the cutoff frequency of the material constituents, which corresponds to the plasma frequency for the metal layers. However, it is important to note that increasing the operating frequency up to visible optics is problematic due to the contribution of the kinetic inductance. This phenomenon will be detailed by Philippe Tassin in Chapter 8.

Not taking into account this physical effect, designing a SRR-based metamaterial for the infrared domain already faces several difficulties. The major difficulty arises from the requirement of an H-field excitation normal to the current loop plane. The other difficulty is the challenging fabrication technique of relatively large area samples, generally on the centimeter scale for proper illumination of the impinging wave, while the dimension of the

basic cell is reduced dramatically. As a result, it is generally thought to simplify the pattern of the basic cell by only keeping the key feature. The C-shaped structure satisfies this condition and most of the studies reported in the literature are based on such a simplified pattern [LIN 04, SOU 07]. For illustration [LIP 09], a scanning electron micrograph of a C-pattern array designed for operating at mid-infrared (typical wavelengths of 10 μm) is shown in Figure 1.11. The dimension is apparent in this figure and all the relevant dimensions, notably the periodicity, are less than 1 μm. The metamaterial criterion, i.e. the fact that all the dimensions are far shorter than the operating wavelength, is met by means of electron beam lithography. The device was characterized by FTIR spectroscopy while the frequency responses of the scattering parameters were calculated with the help of full wave codes. Figure 1.12(b) compares numerical results (upper panel) to the measured results for the two values of the electric field orientation along the gap-bearing arm (solid line) and for the E-field polarized normally to this direction (dotted lines). Calculation and experiment agree well with a pronounced dip on the transmission around 30 and 100 THz for an E-field polarization parallel to the gap-bearing arm and around 75 THz for the perpendicular polarization. From the retrieval procedure, using Fresnel inversion techniques, it can be shown that the electric response dominates the scattering of the impinging wave. Indeed, the experiment was conducted *under normal incidence* and hence with the magnetic field direction parallel and not perpendicular to the SRR plane. Strictly speaking, there is no pure magnetic activity in the present case because the magnetic moment is generated by a current loop induced by the EM force across the gap.

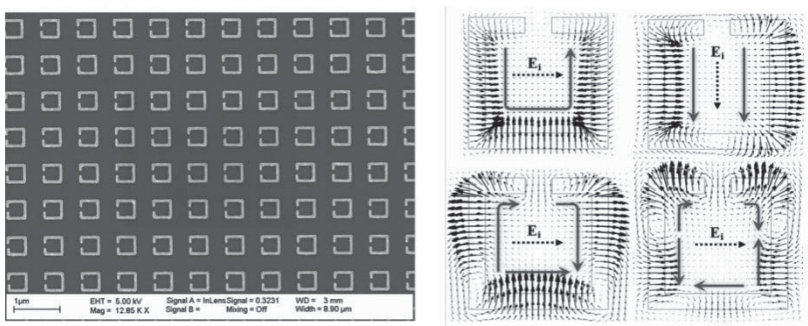

Figure 1.11. *Scanning electron microphotograph (SEM) of a split-ring resonator array for a mid-infrared operation and field mapping illustrating the various resonance modes for two polarization directions of the impinging EM field along and transverse to the gap-bearing arm*

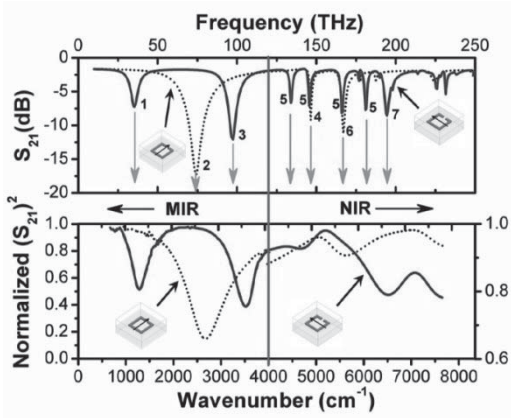

Figure 1.12. *Comparison of the transmission spectra calculated by finite element modeling (High Frequency Structure Simulator code (HFSS™)) and measured by means of FTIR experiments (respectively, solid line and dotted line)*

How to preserve a current loop induced by the incident magnetic field and not the electric field for observing a pure magnetic response will be addressed in the following with the introduction of the so-called *fishnet structure*. Before this, we will show how to broaden the left-handed dispersion branch using a *transmission line approach*. This will be performed by means of two representative prototypes operating at centimeter and millimeter wavelengths, respectively. This will permit us to illustrate the vector network analysis and the TDS characterization techniques.

1.3. Transmission lines with series capacitances and shunt inductances

The basic idea for achieving negative values of the effective index in a transmission line model was first proposed in the following references [OLI 02, CAL 04, CAL 06]. Unlike conventional transmission lines that are described by means of distributed series inductance L_{RH} and shunt capacitance C_{RH} (lossless case), RH standing for right handed, the circuit also consists of series capacitance C_{LH} and shunt Inductance L_{LH}. The result of a dual configuration on the propagation properties is a phase advance giving rise to backward propagation. This property was already reported in the literature several decades ago. The underlying idea is to combine both right- and left-handed features in order to achieve a *balanced CRLH* dispersion characteristic that was already pointed out in the analysis of the omega-type array in the previous section.

1.3.1. *Tuneable phase shifter for centimeter wavelengths*

As an illustration of the CRLH properties, we will present the key results of the study reported in [MAR 09] that makes use of a coplanar wave guide technology (see Figure 1.13).

The series capacitance C_{LH} is designed by means of an interdigited pattern. The shunt inductances are realized with stub-like motifs. In this section, a thin ferroelectric film is deposited onto the substrate prior to the metallization for tunability purposes [VEL 06]. The inductance metal strips are also used for biasing the electronically controlled capacitance through the variation of the permittivity of ferroelectrics films. However, bounded shunt wires ensure the electric continuity of the lateral ground planes.

The measured dispersion characteristics, which can be retrieved from the complex scattering parameters measurements performed in X and Ku bands, are shown Figure 1.13(b). It can be shown that the transition between the left-handed dispersion branch (negative value of k with a corresponding positive group velocity) and the right-handed dispersion branch is seamless and thus without any forbidden gap between the two transmission bands. From the inset of Figure 1.13, it can be shown that biasing the varactors allows shifting positively the corner frequency between left- and right-handed bands.

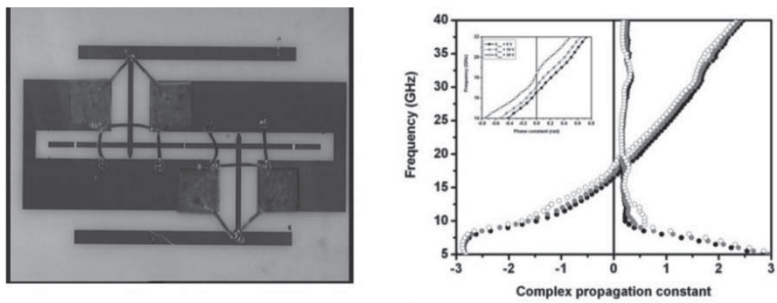

Figure 1.13. *Image of a prototype based on a CPW transmission line loaded with series capacitances and shunt inductances. Voltage controlled capacitances are integrated here by means of a ferroelectric (BST) thin film. Dispersion characteristics for various DC voltages controlling the ferroelectric film permittivity*

1.3.2. *Left-handed transmission lines at tetrahertz frequencies*

The transmission line approach is not restricted to the centimeter wavelengths. Here again, the extension toward higher frequencies is

challenging in terms of fabrication techniques and experimental assessment. Indeed, it is shown that most of the metamaterial effects are related to the control of the dispersion and hence of the phase of the propagating waves. This involves accurately controlling not only the magnitude of the transmitted wave, by avoiding as far as possible any loss contribution, but also the phase through the artificial structure. Although the scattering parameters measurement via VNA allows the determination of the complex elements (magnitude and phase) of the scattering matrix [S_{ij}], it is imperative to preserve this measurement of the phase at millimeter and sub-millimeter wavelengths. For commenting such an issue, the key results of reference [CRÉ 05] are reproduced here and discussed via the illustrations shown in Figure 1.14. The upper panel shows a scanning electron microphotograph of a dual strip transmission line loaded by series capacitances and shunt inductances. The series capacitances were realized by means of a metal overlay deposited onto a dielectric layer (Si_3N_4). The series inductances are designed by folded narrow strip patterns using electron beam lithography while plasma reactive etching was used for defining the capacitances locally.

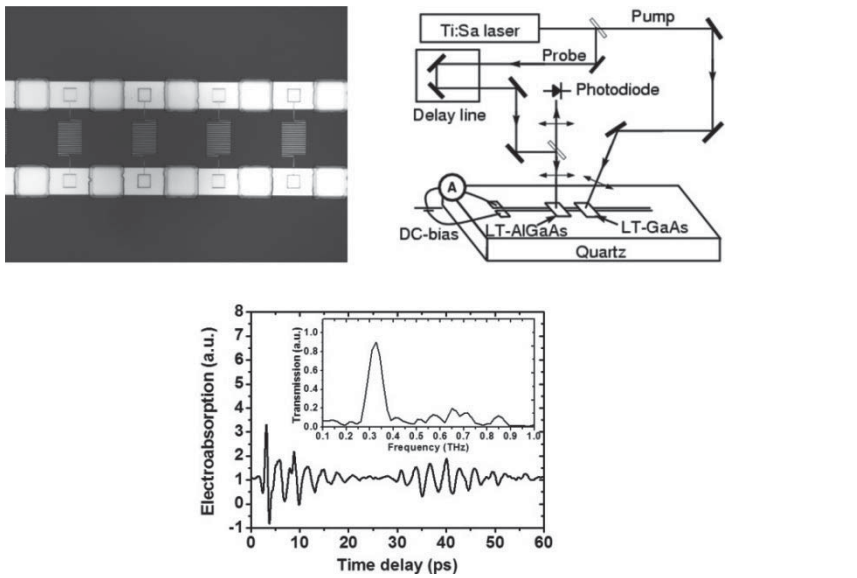

Figure 1.14. *Scanning electron microphotograph of a left-handed coplanar strip transmission line operating around 0.3 THz (far infrared spectral region) with parallel plate series capacitance and meander-like shunt inductances. Schematic of the pump-probe time domain spectroscopy (TDS) using low temperature (LT) grown GaAs-based semiconductor patches. Time and spectral response showing a transmission window at the millimeter/sub-millimeter wavelength transition. Propagation is backward*

The right panel of Figure 1.14 shows a schematic of the experimental set-up with a voltage pulse generated across the two strips of the transmission line by a femtosecond laser illumination. To preserve the phase information, a pump probe scheme was used. In short, the laser pulse supplied by a femtosecond Ti/Sa laser (typical pulse duration of about 100 fs) is split into two beams. The pump optical beam creates a voltage pulse owing to the shunt of the two transmission lines strip by photoionization. The probe beam allows the tracking of the transmitted signal via a photodiode that converts the electrical pulse into an optical one. The detection of the transmitted pulse in magnitude and phase is achieved through the phase coherency of the two laser beams. The TDS used in this chapter is a sampling technique that allows the recording of the transmitted wave versus time. Subsequent Fourier transform allows the reconstruction of the passband with subsequent analysis through Fresnel inversion. The bottom panel of Figure 1.14 shows the time and frequency response of a typical device designed for operation at the transition between the millimeter and the sub-millimeter wavelengths (300 GHz). Direct evidence of the left-handed character can be achieved by tracking in real time the phase advance of the transmitted wave in the left-handed dispersion branch. Another clue of the left-handed character can be obtained by comparing the phase shift between two lines with a different number of cells in a manner similar to the one described for omega structures operating around 100 GHz (see section 1.2.3).

To our knowledge, the aforementioned study is among the highest frequency experimental evidence of backward propagation. For an extension into the far infrared and targeting an operation at mid- and near infrared, it is imperative to select another configuration that is called fishnet. This is addressed in the following section.

1.4. Fishnet approach

Turning now to the so-called fishnet approach that was first introduced in optics, Figure 1.15 shows the key illustration of the study reported in [ZHA 11]. It is important to note that the basic cell, displayed in the left-hand panel, is primarily made up of a tri-layered structure that consists of a dielectric slab sandwiched between two metal films. Such a configuration is motivated by the search for inducing a current loop by the incident magnetic field and not the electrical one *under normal incidence*. Indeed by coupling two metal planes via the displacement current within the dielectric spacer, it can be shown that a current loop is formed provided that the conduction currents in the metal layers are antiparallel. However, wire arrays can be responsible for the creation of an electrical dipole as in conventional

wire/SRR arrays. As a result, for a proper determination of the dimensions, it is now possible to fabricate a double negative medium (negative index material) for excitation under normal incidence.

1.4.1. *Tunable fishnet for centimeter wavelengths*

In this section, the realization of a tunable fishnet metamaterial operating at centimeter wavelengths is illustrated on the basis of the work reported in [ZHA 11]. Figures 1.15(a) and (b) show schematic views of a tunable fishnet metamaterial structure, which is composed of three layers, i.e. a pair of fishnet topologies patterned on the surface of Teflon fiberglass slabs with void in between designed to be infiltrated with a nematic LC. The underlying idea for tuning the LH passband is to change the effective permittivity of substrate via LC molecular reorientation, by applying a DC voltage between the top and bottom metal layers. To achieve all angle LC reorientation between 0° and 90° and hence a large tuning range, a thin layer of polyimide (PI) was spanned on the surface of Teflon substrate and copper element to force nematic LC to align parallel to the metal surface. As a combination of electrical dipoles and current loops, providing simultaneously negative permittivity and permeability, a fishnet structure can operate under normal incidence. The frequency dependence of the transmission, measured under various bias voltages has been compared with full wave calculations (Figure 1.16). As shown in this figure, for the initial alignment with the LC director parallel to the fishnet surface, there is a well resolved peak with a relatively high intensity transmission peak around 9.01 GHz, which is separated from a quasi-unit transmission shoulder, starting from 11.0 GHz, by a shallow dip. As the LC director is orientated from 0º to 90º, it is shown that the ground transmission peak is shifted downward 8.60 GHz, accounting for 400 MHz frequency variation, whereas the second passband is nearly unchanged.

1.4.2. *Terahertz subwavelength holes arrays*

Primarily, subwavelength hole arrays were introduced for the observation of the so-called extraordinary transmission defined in the literature by the acronym EOT [EBB 98]. The term “extraordinary transmission” characterizes the fact that the transmission through a screen perforated by subwavelength apertures may exceed the ratio between the surface of the holes and the whole illuminated area. It is now well-established that the transmission through a hole in a metal plate exhibits a cutoff frequency that is related, in a first approximation, to the condition that the whole diameter fits half the wavelength. This cutoff was predicted theoretically by Bethe. Under the EOT

condition, it can be shown that a device made of a single hole or of a hole array enhances transmission levels with respect to the values predicted by direct geometrical considerations. As a result, much higher transmittance values than those predicted in the framework of the Bethe diffraction theory are achieved. This enhancement in transmissivity is observed at specific frequencies involving complex transmission mechanisms. Notably, surface waves called surface plasmon polaritons are evidenced in optics (spoofs plasmon waves at terahertz) between the upper and lower interfaces, between the metal and its background medium (air for instance).

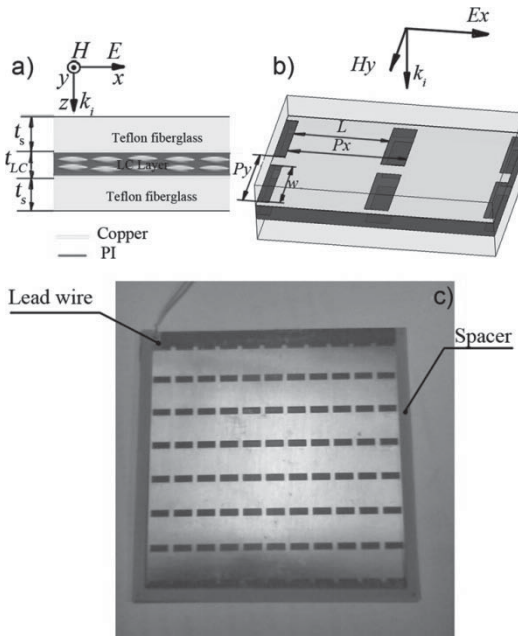

Figure 1.15. *Schematic of the basic cell of a fishnet metamaterial operating at microwave and consisting of two staked rectangular aperture arrays (side view a), 3D view b) and image c)). The top layer was removed for clarity. The metal dielectric stack creates a current loop under normal incidence of the incident wave*

To the best of our knowledge, one of the first experiments, showing that a stack of subwavelength holes arrays may involve left-handed transmission, was conducted at the Spanish Public University of Navarra [BER 05, BER 06, BER 07]. The authors showed that a stack of aluminum plates drilled with subwavelength holes arrays can be compared to a double negative media with backward propagation for a wave normally impinging to the stack. Since this

first article, numerous papers have been published in this field by determining the necessary conditions for designing a negative index material. Notably, it was recognized that a minimum of two layers have to be stacked, a single layer behaving as a conventional frequency selective surface (FSS).

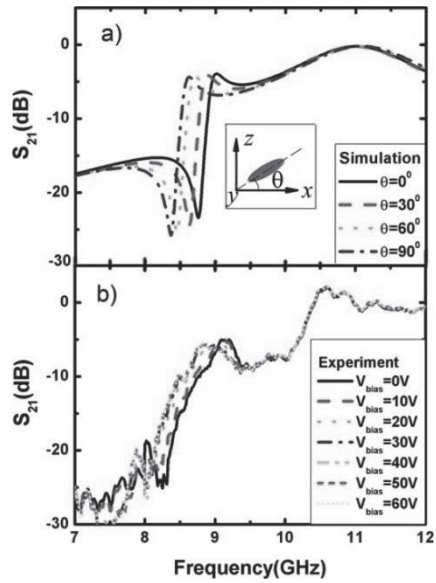

Figure 1.16. *Frequency dependence of the transmission coefficient (calculated a) and measured b)). Tunability of the dispersion characteristics is achieved with liquid crystal technology infiltrated between the two large area parallel metal plates*

In the following, we present another example based on the stacking of subwavelength hole arrays for terahertz frequencies. Figure 1.17 illustrates the various issues that have been solved toward this goal from the point of view of the fabrication and experiments. As exemplified in the first part of this chapter, devoted to the omega-shaped basic cell, the first challenge was to choose a monolithic integration of the structures, whereas manual assembling of individual drilled aluminum plates was performed in the aforementioned works. For this terahertz design, submicron gold films embedded in BCB dielectric layers have been used. In addition, in order to avoid the influence of the GaAs substrate, a membrane-like structure was fabricated in the last stage. For the cell design, full wave analysis shows that an elliptical-shaped aperture with an aspect ratio close to 2:1 allows high transmission levels in the left-handed dispersion branch. These specific features are illustrated in Figure 1.17(a) that depicts (1) the top layer of a

stack with elliptical apertures patterned by optical lithography, (2) the inset of this figure that shows an image of the free-standing array fabricated by deep selective chemical etching and (3) an SEM of the cross-section of a stack of four metal films (their thickness is typically 0.4 μm for a BCB layer of thickness around 30 μm). These devices were subsequently characterized by TDS, which the pump-probe scheme outlined in the previous section. The typical frequency dependences of the magnitude and the phase of the transmission are displayed in Figure 1.18.

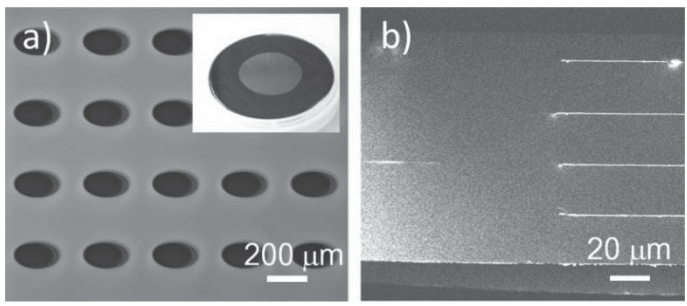

Figure 1.17. *a) Image of a membrane fishnet-like prototype fabricated by stacking subwavelength hole arrays with elliptical-shaped apertures, image of the 2 inch wafer in inset. b) Scanning electron micrograph of the 0.4 μm thick metal/26 μm thick dielectric stacking*

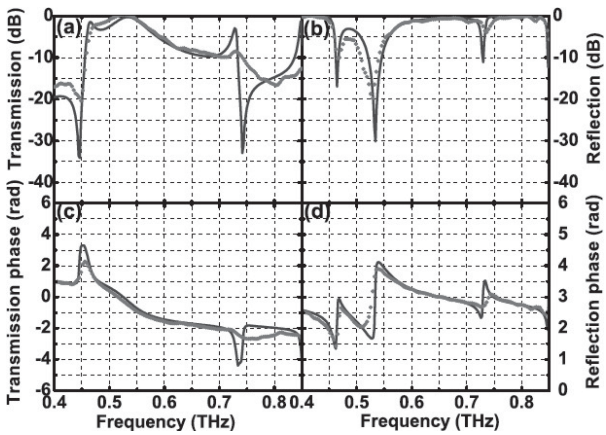

Figure 1.18. *Comparison of the scattering parameters measured by time domain spectroscopy (shadow symbols) and calculated using HFSS ™ (black line) of stacked subwavelength hole metal layers operating at terahertz frequencies. Propagation is backward (phase advance) for the first transmission peak*

The retrieval of the effective permittivity and permeability parameters confirms that the first peak in the transmission, at about 450 GHz, corresponds to negative index values. In contrast, the second peak can be attributed to a right-handed dispersion branch located at higher frequencies. These conclusions are corroborated by full wave analysis [CRO 09] and by lumped element approaches [CAR 10]. In addition, a parametric study as a function of the number of layers first confirms that the canonical structure for negative index must integrate at least two metal layers and also illustrates the possibility of achieving a balanced CRLH regime [WAN 10a]. Comparing the transmission spectra of fishnet structures and subwavelength hole arrays shows similar trends. In fact, both structures operate on the same basic principle, notably artificial magnetism via the creation of a current loop between adjacent metal layers.

In the previous section, we have considered a slab made up of hole arrays. In this case, the demonstration of negative index regime is not direct and uses Fresnel relation inversion techniques. How can we directly assess that such a structure refracts negatively? The most straightforward experiment is a measurement of the refracted angle for a wedge-type device. This is considered in the following.

1.4.3. *Wedge-type devices*

Figure 1.19 illustrates the set-up used toward this goal [WAN 10b]. It is based on angle-resolved measurement of the transmitted beam through a wedge-type device. In practice, the device was monolithically integrated using the technological process described in the previous section (0.3 μm gold films between 26 μm BCB interlayers). The main difference arises from the step-like structure for implementing the slanting side of the prism (see Figure 1.20).

Unlike the measurement of the complex scattering parameters (magnitude and phase of S_{ij}), only the magnitude of the transmission was measured at various angles. This analysis is similar to the one performed in the study of the refraction properties by omega chain arrays. Indeed, the refracted angle is deduced from the Snell–Descartes law by keeping a normal incidence on the first interface. The time domain variations of the transmitted signal are recorded for each detector rotation. Then, by Fourier transform, it is possible to deduce the frequency dependence of the transmitted beam. The application of this experimental procedure gives the results displayed in Figure 1.20. The measured frequency dependence of the effective index was compared to the values deduced from the radiation pattern in the far field and retrieved numerically from a slab structure.

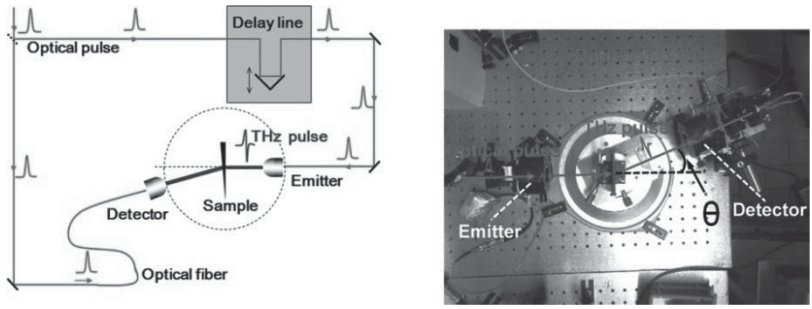

Figure 1.19. *a) Schematic of the angle-resolved TDS set-up (goniometric configuration) aimed at experimentally determining the effective refractive index from the Snell–Descartes law. b) Image of the experimental set-up of the University of Savoy*

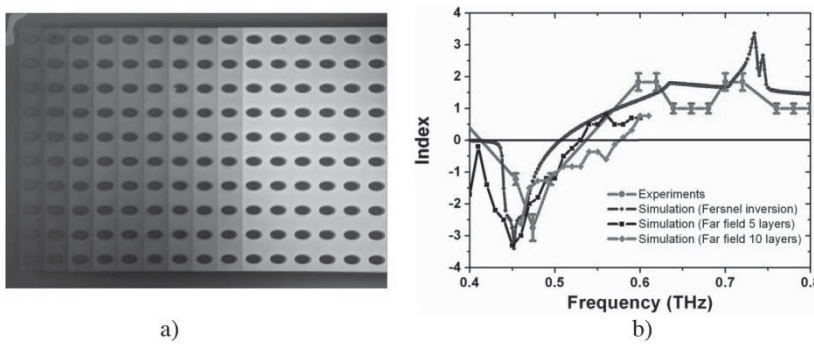

Figure 1.20. *a) Image of a wedge-type metamaterial fabricated by stacking subwavelength hole arrays in a step like prism configuration. b) Frequency dependence of the refractive index measured by using a goniometer and retrieved from the so-called Fresnel inversion technique and by using far-field numerical simulations*

The main goal of the studies presented so far is the control of the dispersion. This means the possibility of switching the operation conditions between left- and right-handed regimes by shifting the operation frequency or tuning by means of ferroelectrics or LC technologies. Are there some novel possibilities afforded by metamaterials to control the polarization of waves and not solely the phase and magnitude? Such prospects have been proposed quite recently with the emergence of chiral metamaterials. In the following, we consider a chiral metamaterial designed from a fishnet arrangement.

1.4.4. *Fishnet with twisted apertures: chiral device*

Chiral devices for achieving double negative media have received widespread attention [PEN 04, PLU 07, TRE 03, PLU 09]. Figure 1.21 shows an image of a prototype aimed at operating at approximately 500 GHz [WAN 13]. The main difference with respect to the previous array of holes is the twisted aperture structure. This topology allows the rotation of the electric field. In fact, the use of an elliptical-shaped aperture, introduced to optimize the level of transmission, involves a sensitivity of the device to the polarization of the electric field. Therefore, it can be shown that the highest transmission level is achieved for an electric field polarized along the small axis of the ellipse. As a consequence, by rotating step-by-step the orientation of the elliptical aperture, we can think that the electric field direction will similarly rotate its orientation. For experimental assessment of this concept, a three-layer prototype is presented. Further details about the TDS experimental method, developed in order to measure the rotary power, can be found in [WAN 13]. In the present experiment, the intensity of the transmitted level is analyzed as a function of the angle between the incident and transmitted beam by a polarized detector. This detector is a dipole antenna integrated with a polarizer on the same rotating stage. From this experimental protocol, we can get the rotation angle θ, which is directly related to the chirality factor, and the ellipticity angle η. For the present device, the orientation of the elliptical aperture has been twisted a 45° step along the three-layered structures. Starting from $\theta = 0$, we thus obtained a rotation of 90° for the last metal plane.

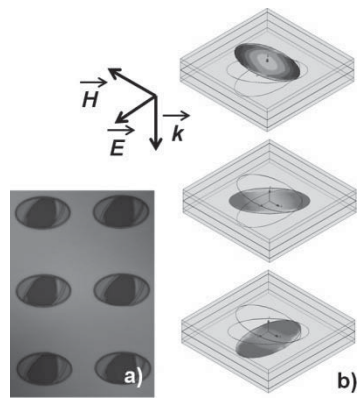

Figure 1.21. *a) Image of a three-layer chiral metamaterial operating at 0.5 THz. A rotary power of 1,000° per wavelength is achieved by twisting the elliptical aperture of a subwavelength hole array prototype by 45° during the stacking. b) Illustration of the rotation of the polarization direction by field mapping at the various metal plates*

The analysis of the different intensity of the transmitted beam as a function of frequency gives the frequency dependence of the rotation angle displayed in Figure 1.22(a). We can note that a rotation magnitude of 90° can be achieved over a distance corresponding to the total thickness of the stack. We can then deduce that the rotary power is as high as 1,000° per wavelength and hence much more efficient than conventional polarization rotators. The other key characteristic is the ellipticity that describes the difference in the attenuation between the right and left circularly polarized waves, denoted as RCP and LCP, respectively. The difference in the attenuation figures for LCP and RCP leads to a deformation of the transmitted beam.

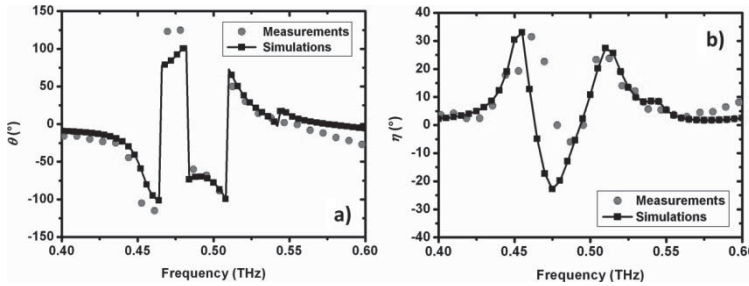

Figure 1.22. *Frequency dependence of the azimuthal rotation a) and of the ellipticity b) angles measured by TDS*

Many features of the propagation of electromagnetic waves are now mastered through the engineering of metal/dielectric artificial material structures on a subwavelength scale. Made up of planar or stratified media, the devices are, however, highly anisotropic as exemplified by the omega-type structures from which the diagonal elements of the permittivity and permeability tensors have been retrieved. The basic concepts, in particular for artificial magnetism, are theoretically irrelevant to the frequency range in which the device operates, but the constitutive elements and more precisely the metal layers are highly dispersive. In the following, we will show that a full dielectric approach also permits us to target artificial magnetism in order to synthesize negative index media.

1.5. Full dielectric approach: Mie resonance-based devices

Most of the concepts used in this section are drawn from the review article published in the journal *Material Today* [ZHA 09b]. We will mainly show here how a magnetic moment can be induced in a dielectric layer. In

addition, we will define the conditions for satisfying the long wavelength regime, which means that the wavelength of the incident wave is much larger than the relevant dimensions used for dielectric structuring.

Basically, the underlying principle for negative permeability values is similar to the aforementioned principle, i.e. an out-of-phase component of the induced field B with respect to the H-field excitation owing to resonance effects originally described by Mie [MIE 08]. By using high-permittivity (κ) dielectrics, two important conclusions can be drawn. First, high displacement current (J_d) can be achieved ($J_d = \varepsilon.\partial E/\partial t$) and the scale over which the resonance takes place is dramatically decreased, owing to the reduction of the wavelength in this high-permittivity media. To sum up, Mie resonance-type devices are generally made up of high κ ferroelectrics cubes or spheres thus with a high degree of symmetry, so that isotropic characteristics can be expected.

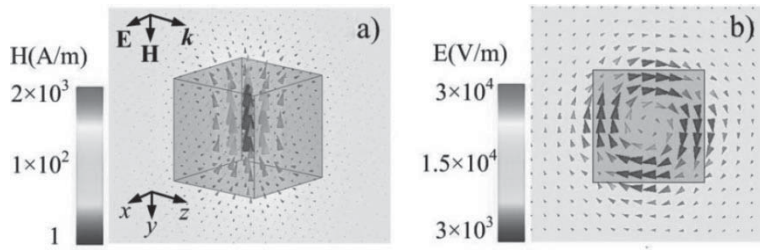

Figure 1.23. *Basic principle of a full dielectric approach by using high permittivity (ferroelectrics BST-cubes). The incident H-field induces a strong circular displacement at the resonance frequency (ground magnetic Mie resonance with an out-of-phase inductive response (B = –1 /μ / H) above the resonance)*

In order to check these assumptions, Figure 1.24 gives the frequency dependence of the effective permeability for barium strontium titanate (BST) ($BaSrTiO_3$) cubes, with dimensions on a millimeter scale. From the electric field mapping shown in Figure 1.23, it can be checked that a displacement current loop is induced within the cube. This displacement current is responsible for an induced magnetic moment.

The retrieval of the effective permeability by Fresnel inversion, via the calculation of the reflection and transmission coefficients, shows a Lorentz-like dispersion profile with negative values of the permeability μ_{eff} above the resonance frequency. The electric response characterized by the effective permittivity is almost flat. As a result, the BST cube array behaves as a single negative medium (MNG).

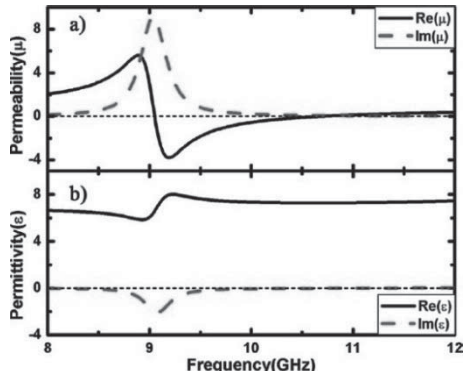

Figure 1.24. *Frequency dependence of μ_{eff} for a high-permittivity cube array. μ_{eff} obeys a Lorentz-type dispersion characteristic similar to the one exhibited by SRR patterns*

The strength of the resonance will depend on the loss tangent (tan $\delta = \varepsilon''/\varepsilon'$ for a complex permittivity $\varepsilon^* = \varepsilon' - j\varepsilon''$). At microwaves, ferroelectric cubes exhibit a typical loss tangent of 1%. In contrast, increasing the operating frequency up to 100 GHz notably degrades the value of $\tan\delta$ up to 10%. There is another drawback in the use of ferroelectric particles, which can be understood from Figure 1.24 in the sense that there is no significant electrical activity at the magnetic resonant frequency. Nevertheless, an electrical Mie resonance exists at higher frequencies. Therefore, more complex structures have to be designed, targeting the achievement of a double negative media and notably those making use of a dual-size super-cell in order to simultaneously fit the magnetic and electric Mie resonances of the cube.

1.5.1. *BST cube technology*

Experimentally, the insensitivity to the incidence can be evidenced with the help of a scattering chamber made up of a parallel plate wave guide whose set-up is illustrated in Figure 1.25 along with an image of the cube arrays characterized for the transverse electric (TE) and transverse magnetic (TM) polarizations. The corresponding measurements are given in the two bottom panels of the right-hand side figure while the results of the calculations by full wave are displayed above.

The first dip in the transmission characteristics, recorded for both TE and TM polarizations, corresponds to the ground magnetic Mie resonance. The insensitivity to the polarization and to the incidence angle is verified.

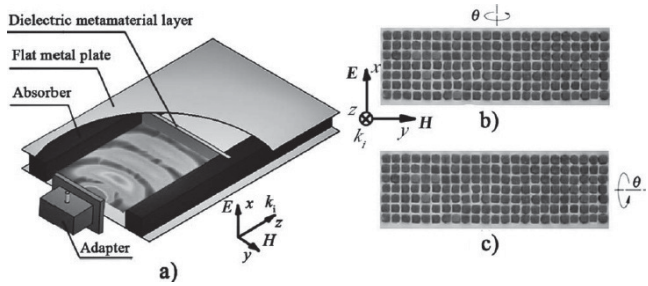

Figure 1.25. *Experimental assessment of artificial magnetism of high-permittivity basic cell (ferroelectrics BST cube with a relative real permittivity of 200). a) Schematic of a scattering chamber with two parallel plates and feeding of the electromagnetic energy via a coaxial to wave guide adapter. b) and c) Image of the ferroelectric cube array for the TE and TM polarization conditions*

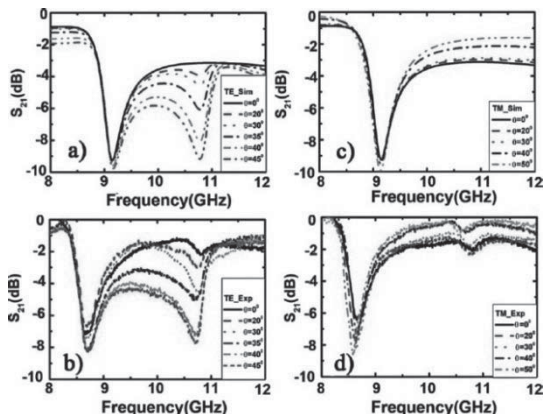

Figure 1.26. *Experimental verification of the isotropy of the dispersion characteristics via full wave analysis (upper panel), by means of incidence field angle scattering parameters measurements (bottom panel)*

1.6. Photonic crystal technology

For telecommunications wavelengths, approximately 1.55 μm, implementing metal-based (plasmonics) metamaterials becomes troublesome owing notably to the high loss level and to the technological difficulties. These conclusions have motivated the search for a full dielectric route.

Among the various possibilities, photonic crystals [LOU 06] based on semiconductor technologies have become very popular and have been widely used for all-angle negative refraction [PER 05, FAB 06].

1.6.1. *Principle*

The underlying concept can be understood from Figure 1.27 showing the band structure calculated for a two-dimensional photonic crystal.

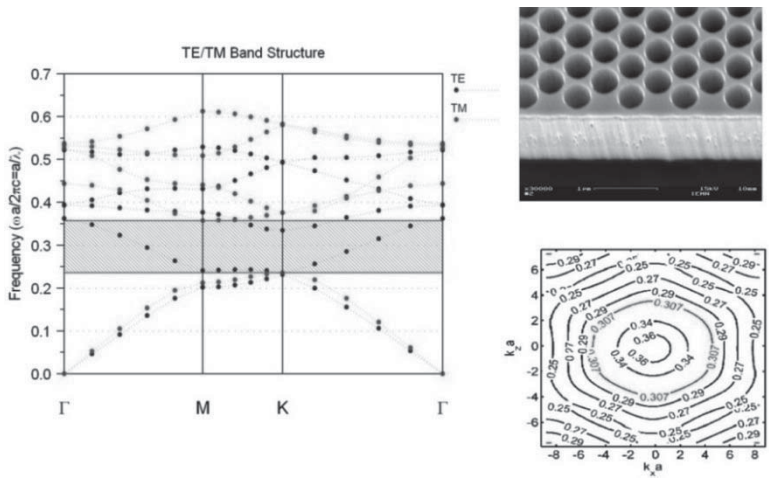

Figure 1.27. *Illustration of the basic principle for negative refraction in photonic crystal microstructures: dispersion diagram in the main symmetry axis of a hexagonal-shaped hole array in a GaAs semiconductor substrate (SEM in inset) for the TE (E perpendicular to the hole axis (y)) and TM mode (E parallel to the y direction). For a TE mode, a second band with a negative curvature (negative index value) is calculated for a reduced frequency between 0.24 and 0.36. The light ($\omega = c.k$) cone where c is the light velocity and k is the wave-vector is crossing this upper-frequency lying dispersion branch around a reduced frequency of 0.3. For this value, the iso-frequency characteristic in the transverse direction k_x and k_z (displayed on the right hand side) is round shaped. All angle refraction can be envisaged for this operating frequency with an effective index n= –1*

This structure consists of a hole array etched in a semiconductor slab. The eigenstates are shown for the high-symmetry directions and for the two polarizations TE and TM, depending on the orientation of the electric and magnetic fields with respect to the hole axis. This band structure shows, in particular, the possibility of propagating TE backward waves in the frequency band between the reduced frequencies 0.24 and 0.36 (shaded region). Indeed,

in this frequency band, we can note that group velocity (v_g) defined as the derivative of the angular frequency (ω) relative to the k vector $v_g = \partial\omega/\partial k$ and the phase velocity $v_p = \omega/k$ are of opposite signs. The iso-frequencies (see Figure 1.27) show round-shaped contours around 0.3 (reduced frequency), which correspond to an effective refractive index equal to –1. Under this condition, it can be expected that the effective value of the refractive index will not depend on the k vector.

1.6.2. *Flat lens*

The fact of having an isotropic value of the effective refractive index permits us to envisage the fabrication and subsequent experimental verification of the so-called Veselago lens [FAB 08, SCH 10]. Let us recall that Veselago first proposed the idea of focusing a point source by means of a flat lens in 1968. The principle of such a focusing can be easily understood with the ray tracing superimposed on the scanning electron microphotograph (SEM) of a photonic crystal (PC) flat lens integrating hole arrays as previously discussed (see Figure 1.29). The light radiated from a ridge optical wave guide in front of the lens refracts negatively at the first and second interfaces with the air embedding medium. A virtual focus within the lens and the formation of an image spot at the back of the lens result from this double negative refraction effect. The frequency operation is chosen according to $n_{eff} = -1$ as discussed earlier, whatever the incidence angle of the ray impinging onto the various interfaces. Under these conditions, the refracted beams converge within and outside the lens. The resolution is mainly determined by the structuring dimensions. Strictly speaking, the condition of deep subwavelength sizing is not fully encountered in the case of PC since the diameter of the holes and period of the array are 347 and 470 nm, respectively, for a wavelength of 1,550 nm. The ability to focus the light radiated from the optical wave guide with a subwavelength resolution was assessed experimentally by SNOM. Without interface engineering, the transfer of light onto the image spot is relatively poor owing to a strong mismatch at the interface. It is worth mentioning that the matching of the index value $n = 1$ for the embedding medium and $n_{eff} = -1$ for the flat lens is non-sufficient for satisfying impedance matching condition. The reduced impedance defined by $z = (\mu_r/\varepsilon_r)^{1/2}$ is not equal to unity like the modulus of $n = (\mu_r.\varepsilon_r)^{1/2}$ that is equal to 1. It can be shown that a dramatic improvement of the transmissivity can be achieved by implementing an anti-reflection coating (ARC) on the two interfaces with air in front of and behind the lens [SCH 10]. Figure 1.29 illustrates the focusing effect by using a flat PC lens via the mapping of the fields

calculated by full wave analysis and displays the image recorded by SNOM experiments. The experimental verification confirms the success of light transfer into the image with a resolution comparable to the Rayleigh limit after the de-convolution of the influence of the tip probe. This limitation is explained by the use of PC technology rather than a true metamaterial technology for which super-resolution could be expected. Experimentally, two differences with the simulation assumptions have to be taken into account. For guiding the wave into a plane inside the lens, it is necessary to develop, by molecular epitaxy, a three-layered InP/InGaAsP/InP confining structure. Numerically, we thus assume an effective medium index value of 3.26 (average of 3.36 for InGaAsP and 3.16 for InP at the thickness pro rata).

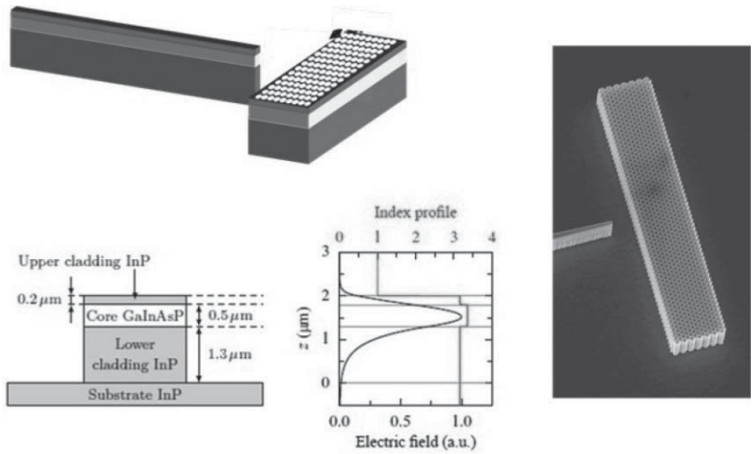

Figure 1.28. *Illustrations of focusing by means of the so-called Veselago flat lens (photonic crystal PC technology) with (1) a schematic of the PC-based device integrating a flat lens and a ridge optical waveguide, (2) a scanning electron micrograph of a prototype that consists of arrayed (hexagonal lattice) holes etched in a three-layered InP/InGaAsP/InP semiconductor hetero-structure and (3) a field mapping in a cross-section*

For an extended control of electromagnetic waves, numerous ideas have recently been proposed on the basis of transformation optics. A survey of these various ideas is beyond the scope of this chapter and the readers will find several examples of transformation optics-based devices in Chapters 6 and 7. However, with a main emphasis on photonic crystal technology applied to dispersion control, it seems interesting to consider the so-called carpet cloaking scheme, also called the ground carpet cloak, as another example.

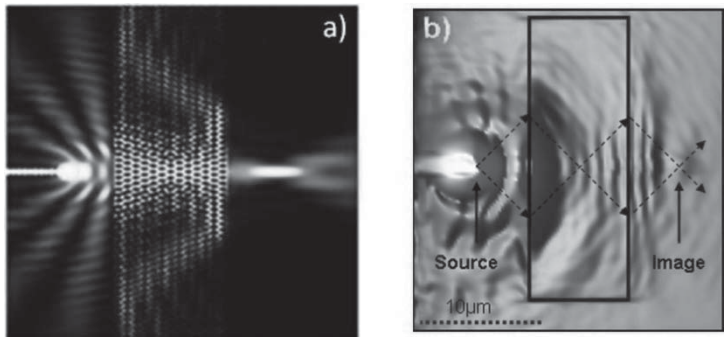

Figure 1.29. *a) Illustration of focusing by using an n = –1 flat lens with a field mapping calculated by FDTD (Rsoft code ™), showing double focusing within and out of the lens after double negative refraction. b) Experimental evidence by scanning near-field optical microscopy (SNOM) imaging. A ray tracing was superimposed onto the SNOM image for illustrating the basic principle of focusing in a negative index medium first proposed by Veselago*

1.6.3. *Carpet cloaking devices*

Basically, a carpet cloak is a reflecting device [LI 08, VAL 09]. In a full cloak [GAI 08], beyond the reconstruction of the phase front of the incident wave in front and behind a potential scatterer, the main goal is to avoid any reflection that could induce standing waves. In contrast, in a carpet cloak, the invisibility device gives the illusion that the scatter does not exist while it is physically placed onto a plane reflecting surface. For illustration of this stealth principle, we consider in the following the case of a carpet cloak fabricated using a photonic crystal technology. By using SNOM measurements, we show that a bump of trapezoidal shape onto a photonic crystal reflecting surface can be invisible with respect to a plane wave impinging onto this irregular surface. Several demonstrations of this invisibility principle use a metallic mirror and a cloak structure made up of PCs.

For the results reported below, the whole set-up is made up of dielectric. In other words, the mirror is made up of a PC semiconductor slab operating in the band gap (hole array). The carpet, which includes an index gradient in order to manipulate the phase front, is fabricated from pillar arrays. The last component of this carpet-on chip device is the integration of an enlarged wave guide, which serves for quasi-plane wave excitation. Figure 1.30 illustrates the design of the cloak via transformation optics techniques and we give a schematic of the SNOM experiment with arrows that depict the

impinging waves. The positions of the pillars, defining the cloak, are set at the nodes of an optical space transformation illustrated in Figure 1.30. Their unequal spacing is used for compensating the phase difference between the incident wave reflected (1) on the top of the trapezoidal-shaped bump, (2) by the slanted interfaces on each side of the bump and (3) the flat back-side interfaces.

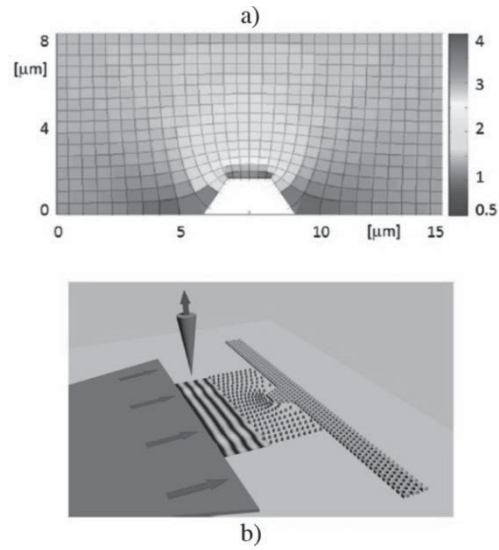

Figure 1.30. *a) Illustration of optical transformation techniques used for a ground carpet invisibility cloak. b) Schematic of the SNOM experiment for assessing plane wave reconstruction in front of a trapezoidal-shaped PC mirror*

Figure 1.31 illustrates the semiconductor-based technologies used to fabricate the mirror PC with a hole array (let us mention that we are using here the band gap regime in a TM mode (see the band structure in Figure 1.25). Figure 1.31 also shows a zoomed view of the cloak fabricated in a single-mask and single-etching stages by the induced coupled plasma (ICP) technique. For verifying the efficiency of such a cloaking scheme under normal incidence, a comparison between a flat mirror, a bare bumped surface and a device dressed with a carpet cloak is displayed in Figure 1.32, which shows topographical images and the optical near-field intensity images recorded by SNOM. From this comparison, it can be noted that the phase fronts are almost flat for the device dressed with a carpet cloak, similarly to a flat reflected surface, whereas some scatterings can be evidenced in the standing wave pattern displayed in the central column.

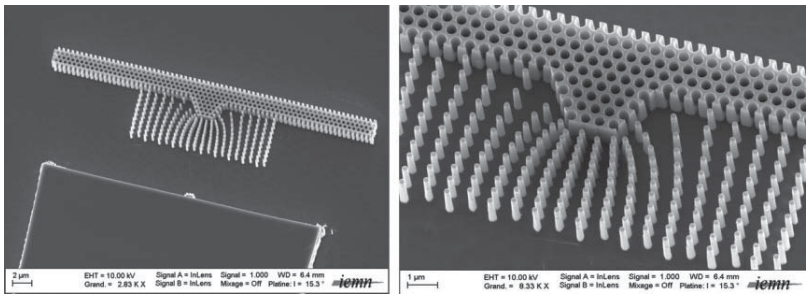

Figure 1.31. *Scanning electron microphotograph of a device operating at telecommunications wavelengths (mid-infrared λ~1.55μm). Illumination of the structure is achieved via a trumpet-shaped ridge wave guide apparent on the top of the left-hand side image. A hole array photonic crystal was designed to operate as a mirror at the wavelength of interest. A pillar array, designed from optical transformations, is integrated in front of a trapezoidal mirror-like scatterer*

1.7. Conclusion and prospects

The possibilities for spatially manipulating the phase fronts and engineering the material dispersion afforded by artificial materials (metamaterials and photonics crystals) have been extended to great extent. In this chapter, it has been shown that several configurations can be chosen as a function of the targeted applications with a clear distinction between a full dielectric approach (high κ Mie resonance media and PCs), which exhibits isotropic properties, and the plasmonic approach resulting in highly anisotropic effective parameters. Beyond the possibility of scaling, at different frequencies, the general basic concepts with the prospect of covering a frequency band from microwave to visible optics, it appears that the dispersion of the constitutive materials gives some frequency limitations. Moreover, and as a general rule, strong dispersion effects require the use of resonance enhancement. As a consequence, the second important limitation is narrow bandwidth related to sharp resonance effects. In addition, this resonance effect increases dramatically the losses in the vicinity of the resonance frequencies. This point is detailed in Chapter 5. What could be the future stages in the development of metamaterial technology?

With respect to the material issue, we can envisage the development of graphene and superconductors with expected cutoff frequencies in the terahertz domain.

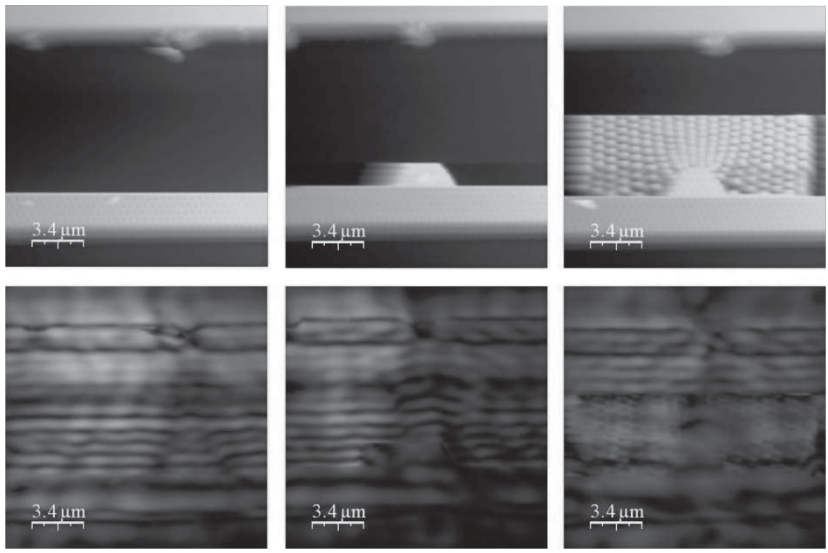

Figure 1.32. *Experimental verification of a mirage effect. The non-flat PC mirror appears as a flat mirror owing to the reflected wave control via the invisibility cloak. For comparison, SNOM imaging of a perfect flat photonic crystal and of a bare scattering surface is also shown in the first and central columns*

From the concept side, quantum metamaterials, which combine electronic confinement in quantum wells and the singular electromagnetic properties of metamaterials, should involve considerable development in the future with a convergence of nanoelectronics and nanophotonics quantum size effects.

Also the so-called hyperbolic metamaterials are considered as a promising route toward a better dispersion control.

From the application side, the number of potentialities is numerous and the main requirement is to overcome the intrinsic losses.

1.8. Acknowledgments

D. Lippens would like to thank all the permanent staff of the DOME group along with the PhD students and post-docs for their contribution to this chapter: L. Burgnies, A.L. Borja, C. Croënne, N. Fabre, M. Hoffman, G. Houzet, L. Kang, É. Lheurette, X. Mélique, V. Sadaune, O. Vanbésien, S. Wang, F. Zhang, J.F. Lampin and X. Wallart of the THz photonics and

Epitaxy groups at IEMN. Special thanks go to J.- L. Coutaz and F. Garet from the University of Savoy, J. Carbonell from the Polytechnic University of Valencia (Spain) , B. Gralak and S. Guenneau from the Fresnel Institute in Marseille (France), F. de Fornel and B. Cluzel from the University of Burgundy in Dijon (France).

1.9. Bibliography

[BER 05] BERUETE M., SOROLLA M., CAMPILLO I., *et al.*, "Enhanced millimeter wave transmission through quasioptical subwavelength perforated plates", *IEEE Transactions on Antennas and Propagation*, vol. 53, pp. 1897–1903, 2005.

[BER 06] BERUETE M., SOROLLA M., CAMPILLO I., "Left-handed extraordinary optical transmission through a photonic crystal of subwavelength hole arrays", *Optics Express*, vol.14, pp. 5445–5455, 2006.

[BER 07] BERUETE M., SOROLLA M., NAVARRO-CIA M., *et al.*, "Extraordinary transmission and left-handed propagation in miniaturized stacks of doubly periodic subwavelength hole arrays", *Optics Express*, vol. 15, pp. 1107–1114, 2007.

[CAI 09] CAI W., SHALAEV V., *Optical Metamaterials: Fundamentals and Applications*, Springer, 2009.

[CAL 04] CALOZ C., ITOH T., "Transmission line approach of left-handed (lh) materials and microstrip implementation of an artificial lh transmission line", *IEEE Transactions on Antennas and Propagation*, vol. 52, pp. 1159–1166, 2004.

[CAL 06] CALOZ C., ITOH T., *Electromagnetic Metamaterials: Transmission Line Theory and Microwave Application*, Wiley Interscience, 2006.

[CAR 10] CARBONELL J., CROENNE C., GARET F., *et al.*, "Lumped elements circuit of terahertz fishnet-like arrays with composite dispersion", *Journal of Applied Physics*, vol. 108, pp. 014907–014913, 2010.

[CRÉ 05] CRÉPIN T., LAMPIN J.-F., DECOOPMAN T., *et al.*, "Experimental evidence of backward waves on terahertz left-handed transmission lines", *Applied Physics Letters*, vol. 87, pp. 104105–104108, 2005.

[CRO 08a] CROENNE C., FOULON M.F., LHEURETTE É., *et al.*, "Negative index metamaterial at 100 GHz", *Proceedings of the European Microwave Association*, vol. 4, pp. 95–101, 2008.

[CRO 08b] CROENNE C., FABRE N., GAILLOT D.P., *et al.*, "Bloch impedance in negative index photonic crystals", *Physical Review B*, vol. 77, pp. 125333–125339, 2008.

[CRO 09] CROENNE C., GARET F., LHEURETTE É., *et al.*, "Left handed dispersion of a stack of subwavelength hole metal arrays at terahertz frequencies", *Applied Physics Letters*, vol. 94, pp. 133112–133115, 2009.

[EBB 98] EBBESSEN T., LEZEC H.J., GHAEMI H.F., *et al.*, "Extraordinary optical transmission through sub-wavelength hole arrays", *Nature*, vol. 391, pp. 667–669, 1998.

[ELE 05] ELEFTHERIADES G.W., BALMAIN K.G., *Negative-refraction Metamaterials: Fundamentals Principles and Applications*, Wiley Interscience, 2005.

[FAB 06] FABRE N., FASQUEL S., LEGRAND C., *et al.*, "Towards focusing using photonic crystal flat lens", *Opto-Electronics Review*, vol. 14, pp. 225–232, 2006.

[FAB 08] FABRE N., LALOUAT L., CLUZEL B., *et al.*, "Optical near-field microscopy of light focusing through a photonic crystal flat lens", *Physical Review Letters*, vol. 101, pp. 073901–073904, 2008.

[GAI 08] GAILLOT D.P., CROENNE C., ZHANG F., *et al.*, "Transformation optics for the full dielectric electromagnetic cloak and metal–dielectric planar hyperlens", *New Journal of Physics*, vol. 10, pp. 115039–115054, 2008.

[GOK 06] GOKKAVAS M., GUVEN K., BULU I., *et al.*, "Experimental demonstration of a left-handed metamaterial operating at 100 GHz", *Physical Review B*, vol. 73, pp. 193103–193107, 2006.

[HUA 04] HUANGFU J., RAN L., CHEN H., *et al.*, "Experimental confirmation of negative refractive index of a metamaterial composed of Omega-like metallic patterns", *Applied Physics Letters*, vol. 84, pp. 1537–1539, 2004.

[JOA 08] JOANNOPOULOS J.D., JOHNSON S.G., WINN J.N., *et al.*, *Photonic Crystals: Molding the Flow of Light*, 2nd ed., Princeton University Press, 2008.

[KAN 11] KANG L., LIPPENS D., "Mie resonance based left-handed metamaterial in the visible frequency range", *Physical Review B*, vol. 83, pp. 195125–195131, 2011.

[LEW 47] LEWIN L., "Electrical constants of a material loaded with spherical particles", *Journal of the Institution of Electrical Engineers*, vol. 94, no. 3, pp. 65–68, 1947.

[LHE 07] LHEURETTE É., VANBÉSIEN O., LIPPENS D., "Double negative media using interconnected omega-type metallic particles", *Microwave and Optical Technology Letters*, vol. 49, pp. 84–90, 2007.

[LI 08] LI J., PENDRY J.B., "Hiding under the carpet: a new strategy for cloaking", *Physical Review Letters*, vol. 101, pp. 203901–203904, 2008.

[LIN 04] LINDEN S., ENKRICH C., WEGENER M., *et al.*, "Magnetic response of metamaterials at 100 terahertz", *Science*, vol. 19, pp. 1351–1353, 2004.

[LIN 06] LINDEN S., ENKRICH C., DOLLING G., WEGENER M., "Photonic metamaterials: magnetism at optical frequencies", *IEEE Journal of Selected Topics in Quantum Electronics*, vol. 12, pp. 1097–1105, 2006.

[LIP 09] LIPPENS D., "Phase-shift, refraction and focusing based on the metamaterial technologies", *Comptes rendus de Physique de l'Académie des Sciences*, vol. 10, no. 5, pp. 400–413, 2009.

[LIU 08] LIU N., GUO H., FU L., *et al.*, "Three-dimensional photonic metamaterials at optical frequencies", *Nature Materials*, vol. 7, pp. 31–37, 2008.

[LIU 09] LIU R., JI C., MOCK J.J., *et al.*, "Broadband ground-plane cloak", *Science*, vol. 323, pp. 366–369, 2009.

[LOU 06] LOURTIOZ J.M., *Photonic Crystals*, Spinger-Verlag, Berlin, Heidelberg, 2006.

[MAR 08] MARQUÉS R., MARTIN F., SOROLLA M., *Metamaterials with Negative Parameters: Theory, Design and Microwave Applications*, Wiley, 2008.

[MAR 09] MARTEAU A., VELU G., HOUZET G., *et al.*, "Ferroelectric tunable balanced right- and left-handed transmission lines", *Applied Physics Letters*, vol. 94, pp. 023507–023510, 2009.

[MIE 08] MIE G., "Beiträge zur optik trüber medien, speziell kolloidaler metallösungen", *Annalen der Physik*, vol. 330, pp. 377–445, 1908.

[OLI 02] OLI A.A., "A periodic structure negative refractive index medium without resonant element", *URSI Digest, IEEE AP-S/URSI International Symposium*, San Antonio, 16–21 June 2002.

[PEN 96] PENDRY J.B., HOLDEN A.J., STEWART W.J., "Extremely low-frequency plasmons in metallic mesostructures", *Physical Review Letters*, vol. 76, pp. 4773–4776, 1996.

[PEN 99] PENDRY J.B., HOLDEN A.J., ROBBINS D.J., *et al.*, "Magnetism from conductors and enhanced nonlinear phenomena", *IEEE Transactions on Microwave Theory and Techniques*, vol. 47, pp. 2075–2084, 1999.

[PEN 04] PENDRY J.B., "A chiral route to negative refraction", *Science*, vol. 306, pp. 1353–1355, 2004.

[PER 05] PERRIN M., FASQUEL S., DECOOPMAN T., *et al.*, "Left-handed electromagnetism obtained via nanostructured metamaterials: comparison with that from microstructured photonic crystals", *Journal of Optics A: Pure and Applied Optics*, vol. 7, p. S3, 2005.

[PLU 07] PLUM E., FEDOTOV V., SCHWANECKE A.S., *et al.*, "Giant optical gyrotropy due to electromagnetic coupling", *Applied Physics Letters*, vol. 90, pp. 223113–223116, 2007.

[PLU 09] PLUM E., ZHOU J., DONG J., *et al.*,"Metamaterial with negative index due to chirality", *Physical Review B*, vol. 79, pp. 035407–035414, 2009.

[RAM 08] RAMAKRISHNA S.A., GRZEGORCZYK T.M., *Physics and Applications of Negative Refractive Index Materials*, SPIE Press, Bellingham, WA, 2008.

[SIM 03] SIMOVSKI C.R., "Plane-wave reflection and transmission by grids of conducting omega-particles and dispersion of omega electromagnetic crystals", *AEU – International Journal of Electronics and Communications*, vol. 57, pp. 358–364, 2003.

[SCH 10] SCHERRER G., HOFMAN M., SMIGAJ W., *et al.*, "Interface engineering for improved light transmittance through photonic crystal flat lenses", *Applied Physics Letters*, vol. 97, pp. 071119–07121, 2010.

[SMI 02] SMITH D.R., SCHULTZ S., MARKOS P., *et al.*, "Determination of effective permittivity and permeability of metamaterials from reflection and transmission coefficients", *Physical Review B*, vol. 65, pp. 195104–195109, 2002.

[SOL 09] SOLYMAR L., SHAMONINA E., *Waves in Metamaterials*, Oxford University Press, 2009.

[SOU 07] SOUKOULIS C.M., LINDEN S., WEGENER M., "Negative refractive index at optical wavelengths", *Science*, vol. 315, pp. 47–49, 2007.

[TRE 03] TRETYAKOV S., NEFEDOV I., SIHVOLA A., *et al.*, "Waves and energy in chiral nihility", *Journal of Electromagnetic Waves and Applications*, vol. 17, pp. 695–706, 2003.

[VAL 09] VALENTINE J., LI J., ZENTGRAF T., *et al.*, "An optical cloak made of dielectric", *Nature Materials*, vol. 8, p. 568, 2009.

[VEL 06] VELU G., BLARY K., BURGNIES L., *et al.*, "A 310 deg;/3.6-dB K-band phaseshifter using paraelectric BST thin films", *IEEE Microwave and Wireless Components Letters*, vol. 16, pp.87–89, 2006.

[WAN 10a] WANG S., GARET F., BLARY K., *et al.*, "Composite left/right-handed stacked hole arrays at submillimeter wavelengths", *Journal of Applied Physics*, vol. 107, pp. 074510–074516, 2010.

[WAN 10b] WANG S., GARET F., BLARY K., LIPPENS D., *et al.*, "Experimental verification of negative refraction for a wedge-type negative index metamaterial operating at terahertz", *Applied Physics Letters*, vol. 97, pp. 181902–181903, 2010.

[WAN 13] WANG S., GARET F. LHEURETTE É. ASTIC M., *et al.*, "Optical activity of twisted fishnet-like subwavelength holes arrays", *Applied Physics Materials*, in press, 2013.

[ZHA 08a] ZHANG F., HOUZET G., LHEURETTE É., *et al.*, "Negative-zero-positive metamaterial with omega-type metal inclusions", *Journal of Applied Physics*, vol. 103, pp. 084312–084320, 2008.

[ZHA 08b] ZHANG F., POTET S., CARBONELL J., *et al.*, "Negative-zero-positive refractive index in a prism-like omega-type metamaterial", *IEEE Transactions on Microwave Theory and Techniques*, vol. 56, pp. 2566–2573, 2008.

[ZHA 08c] ZHANG F., ZHAO Q., KANG L., *et al.*, "Magnetic control of negative permeability metamaterials based on liquid crystals", *Applied Physics Letters*, vol. 92, pp. 193104–193107, 2008.

[ZHA 08d] ZHANG F., ZHAO Q., GAILLOT D.P., *et al.*, "Numerical investigation of metamaterials infiltrated by liquid crystal", *Journal of the Optical Society of America B*, vol. 25, pp. 1920–1925, 2008.

[ZHA 08e] ZHANG F., GAILLOT D.P., CROENNE C., *et al.*, "Low-loss left-handed metamaterials at millimeter waves", *Applied Physics Letters*, vol. 93, pp. 083104–083106, 2008.

[ZHA 09a] ZHANG F., KANG L., QIAN Z., *et al.*, "Magnetically tunable left handed metamaterials by liquid crystal orientation, *Optics Express*, vol. 17, pp. 4360–4366, 2009.

[ZHA 09b] ZHAO Q., ZHOU J., ZHANG F., *et al.*, "Mie resonance-based dielectric metamaterials", *Materials Today*, vol. 12, pp. 60–69, 2009.

[ZHA 11] ZHANG F., ZHANG W., ZHAO Q., *et al.*, "Electrically controllable fishnet metamaterial based on nematic liquid crystal", *Optics Express*, vol. 19, pp. 1553–1568, 2011.

Chapter 2

MetaLines: Transmission Line Approach for the Design of Metamaterial Devices

2.1. Introduction

As presented in Chapter 1, applications of left-handed materials (LHMs) are characterized by simultaneous negative permittivity and permeability in various microwave applications. This concept was extended to the field of transmission lines (TL) by the UCLA group [CAL 02]. An equivalent circuit approach was also developed by Eleftheriades *et al*. [ELE 02]. As a result, the concept of a left-handed transmission line (a line with a negative phase velocity) was proposed. For practical applications, the parasitic right-handed (RH) effects naturally occurring in a left-handed (LH) structure must be taken into account. Thus, the various proposals have led to the concept of a composite right/left-handed (CRLH) line. The CRLH notation is now the usual designation of these artificial lines since the name clearly describes the fundamentally RH and LH nature of metamaterial lines [CAL 06].

2.2. Historical concepts of transmission lines and homogenization

2.2.1. *Electrical model*

The concept of electric transmission lines dates back to the 19th Century. The strength of this innovation is certainly its use for the electric telegraph,

---

Chapter written by Bruno SAUVIAC.

marking the beginning of the development of modern communications. Scientists then worked hard to model the physical phenomenon involved in the "singing wires". From Heaviside's pioneering work, via Brillouin's [BRI 56] propagation in periodic electric circuits to recent metamaterial transmission lines [CAL 06], models have changed little. The idea is to represent the propagation line as a succession of electrical elementary cells. In the generalized theory, the basic quadrupole is represented by a series impedance followed by a shunt admittance (Figure 2.1).

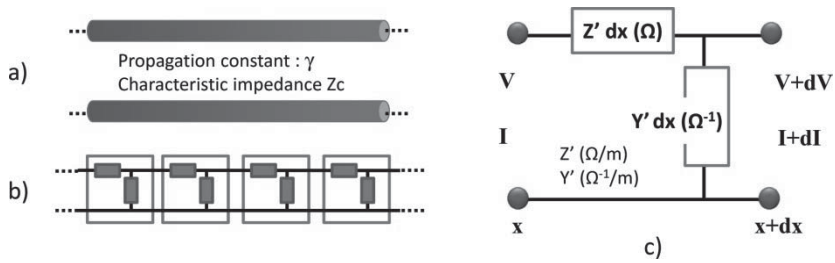

Figure 2.1. *General electrical model for the transmission line. a) Real transmission line characterized by its propagation constant and characteristic impedance. b) Equivalent circuit model composed of an infinite number of elementary cells. c) Schematic representation of the elementary cell. Note that Z' and Y' are respectively per unit length impedance and per unit length admittance*

As a result of this modeling, the characteristics of the transmission line can be derived. The main results are as follows:

$$Z_c = \sqrt{\frac{Z'}{Y'}} \qquad [2.1]$$

$$\gamma = \alpha + j\beta = \sqrt{Z'Y'} \qquad [2.2]$$

$$v_\varphi = \frac{\omega}{\Im m(\gamma)} \qquad [2.3]$$

$$v_g = \left[\frac{\partial \Im m(\gamma)}{\partial \omega}\right]^{-1} \qquad [2.4]$$

In these equations, Z_c is the characteristic impedance of the transmission line and γ is its propagation constant. In general, γ is a complex number where α and β are, respectively, the real and imaginary parts, attenuation and phase constants. v_φ is the phase velocity and v_g is the group velocity.

This modeling principle is theoretically valid if cells whose size tends to zero are considered. However, the question of its validity must be considered as the practical realization is discrete and of finite size.

2.2.2. *Homogenization*

For illustrative purposes, a coplanar line without losses of physical length between 4 and 5 cm is considered. It is engraved on an alumina substrate. For a line of this kind, the series impedance Z is a pure inductance while the parallel admittance is an ideal capacitance. Geometry of the line allows an effective dielectric constant of approximately 5.1 to be determined. The test frequency is 2 GHz. Of course, as the elementary cell is a low-pass filter, it is obvious that this behavior is not present in the real transmission line. Nevertheless, the problem will appear at high frequency. So the main question is the validity around the operating frequency. Transmission along this line is simulated by a series of electrical cells LC (each cell is composed of a series inductance and a parallel capacitance – Figure 2.2(a)) whose number increases at the same time as the size decreases, in order to keep a quasi-constant equivalent physical length [ZER 09]. The results (Figure 2.2) are compared with an analytical model suitable for this type of coplanar line [HEI 93]; the analytical model will be considered as the reference. First, it can be noted that the agreement between the two results is always better at low frequencies. In Figure 2.2(c), the observed difference below 2 GHz can reach 0.2 dB. In Figure 2.2(d), the difference between the results is no more than 10^{-3} dB. When cells get smaller (Figures 2.2(d) and (e)), the agreement gets better for higher frequencies.

In conclusion, it can be assessed that the electric model is a good representation of the behavior of the transmission line. Changing perspective, it can be also said that the cascade of elementary electric cells can behave like a transmission line. This observation, which is not new, opens the way to a powerful tool that can help in engineering transmission lines. Thus, by changing the nature of electrical components in the elementary cell [BRI 56, MAL 51], it is possible to obtain properties that do not exist in conventional lines. In recent literature, this concept has been revisited in the context of metamaterials studies, theoretically [CAL 02, ELE 02] and experimentally [IYE 03].

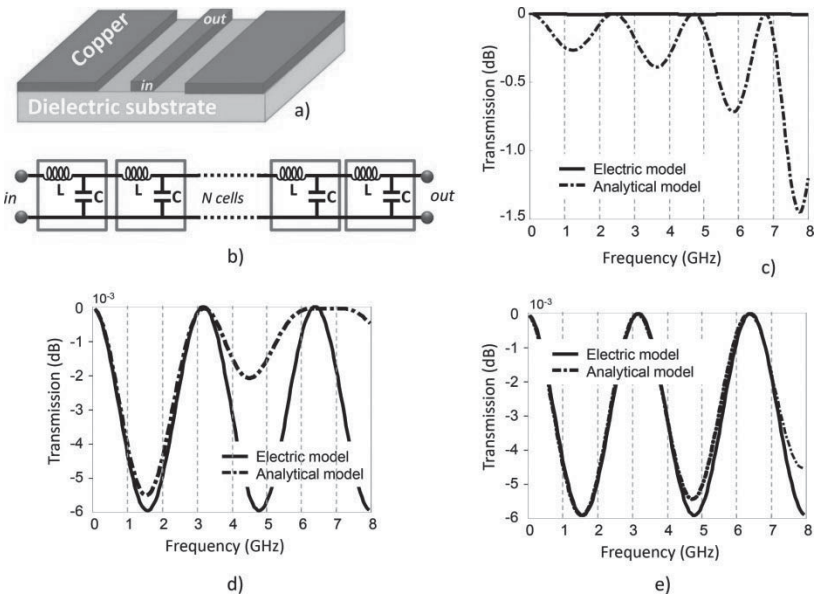

Figure 2.2. *Homogenization of a coplanar transmission line. a) Structure of the coplanar line. b) Equivalent periodic network. c) Comparison of the obtained transmission between a physical model of the line and the electric equivalent model – seven cells of size of λg/4 (λg is the guided wavelength along the line). d) Thirteen cells of size of λg/8. e) Forty cells of size of λg/26*

For example, in the case where Z' becomes a capacitance and Y' an inductance, LH propagation can be created. In this theoretical case, using equations [2.1–2.4] with $Z' = jC'\omega$ and $Y' = 1/jL'\omega$ will give unusual characteristics. Compared with the standard lossless transmission line, the characteristic impedance and the propagation constant are the same except that the phase constant changes sign. In addition, the phase velocity is negative while the group velocity remains positive. These properties are characteristic of a "left-handed" transmission line.

2.3. CRLH transmission lines

2.3.1. *MetaLine cell*

The big advantage of the concept of artificial lines (also called "MetaLines" [MAR 08]) is to allow the creation of propagation structures that will lead to properties specified in advance. The artificial lines or

MetaLines can thus be considered as a design tool to control the electromagnetic properties of propagation lines.

The principle therefore consists of cascading electrical elementary cells, in order to obtain the desired electromagnetic propagation. Unfortunately, not everything is feasible. For example, the previous case (lossless LH transmission line) cannot be achieved practically. This is due to the inevitable occurrence of RH parasitic effects. In the literature, various proposals have led to the concept of CRLH line. The CRLH notation is now the usual designation of these artificial lines since the name clearly describes the fundamentally RH and LH nature of the MetaLines. The second limitation in the range of possibilities comes from losses. It is obvious that there must be losses in the device, and only the low-loss case is possible.

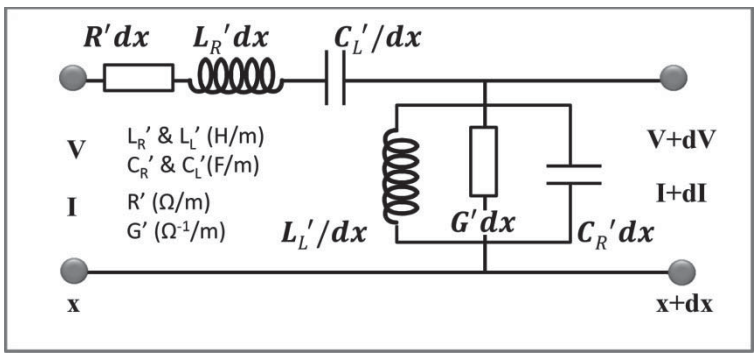

Figure 2.3. *Elementary cell of type CRLH. Subscript "R" refers to right-handed component and "L" to left-handed component*

Figure 2.3 shows the simplest case of a CRLH transmission line (the ideal non-lossy case will be obtained considering R′=G′=0). Considering this elementary cell, it can easily be derived that:

$$Z' = R' + j\left(L_R'\omega - \frac{1}{C_L'\omega}\right) = R' + j\frac{\frac{\omega^2}{\omega_s^2} - 1}{C_L'\omega} \quad [2.5]$$

$$Y' = G' + j\left(C_R'\omega - \frac{1}{L_L'\omega}\right) = G' + j\frac{\frac{\omega^2}{\omega_p^2} - 1}{L_L'\omega} \quad [2.6]$$

where ω_s and ω_p are, respectively, series and parallel resonances:

$$\omega_s = 1/\sqrt{L_R^{'} C_L^{'}} \quad [2.7]$$

$$\omega_p = 1/\sqrt{L_L^{'} C_R^{'}} \quad [2.8]$$

These relations can subsequently be used in equations [2.1–2.4] to obtain the equivalent properties of the MetaLine. All relationships have been derived in [CAL 06] and here, we will focus on dispersion graphs for the propagation constant and the characteristic impedance. Considering equations [2.7] and [2.8], different cases can be analyzed depending on the respective values of ω_S and ω_p.

2.3.2. *Case with* $\omega_S < \omega_p$

This case is illustrated in Figures 2.4(a) and (b). In the lower frequency band, it can be noted that the phase constant is negative under the series resonance. The propagation is LH in this frequency band. Whatever the level of losses, for frequencies higher than the parallel resonance, the phase constant is positive and a normal RH propagation can be observed. This transition is at ω_p for the lossless case and between the two resonance frequencies for the lossy case. In the lossless case, it can be noted that the propagation constant is no longer purely imaginary between the series and parallel resonances and becomes real to create a stop band. In this band, the characteristic impedance is purely reactive. With the increase of losses, this gap closes and tends to disappear.

The characteristic impedance varies between two real values: $\sqrt{L_L^{'} / C_L^{'}}$ when the frequency tends to zero and $\sqrt{L_R^{'} / C_R^{'}}$ for very high frequencies. Between these two limits, the characteristic impedance is complex. The lower the losses will be, the greater the reactive part will be in the frequency band between the two resonant frequencies.

2.3.3. *Case with* $\omega_S > \omega_p$

This situation is described in Figures 2.4(c) and (d). The observations that can be made are quite similar. The difference lies in the positioning of the LH and RH frequency bands. For the lossless case, the propagation is LH only up to the parallel resonant frequency; for the lossy case, the LH effect exists higher in frequency, up to the series resonance.

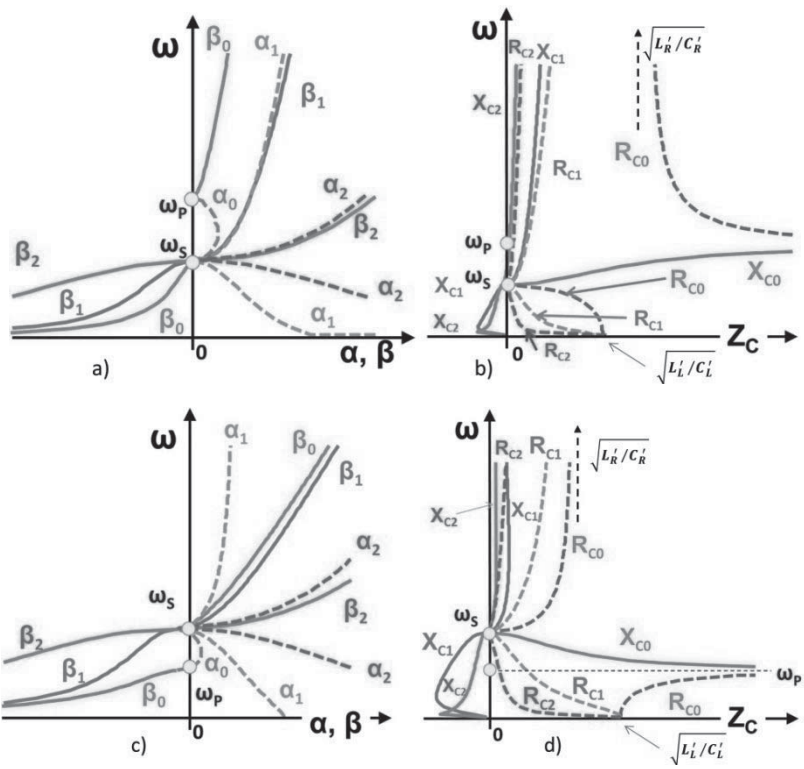

Figure 2.4. *a) and b) Case $\omega_S < \omega_p$. c) and d) Case $\omega_S > \omega_p$. Indexes refer to level of losses: 0 = no losses; 1 = weak losses; 2 = high losses. (a) and (c) Dispersion of the propagation constant: solid line is for imaginary part of the propagation constant and dashed lines for attenuation or real part of the propagation constant. (b) and (d) Dispersion of the characteristic impedance. Dashed and solid lines refer, respectively, to real and imaginary parts of Z_c*

Considering equations [2.5], [2.6] and [2.1], it is clear that the series resonance is a zero for the characteristic impedance while the parallel resonance frequency is a pole. So in all cases, the characteristic impedance goes to zero for ω_S and to infinity for ω_p.

2.3.4. *Balanced case with $\omega_S = \omega_p$*

The case where $\boldsymbol{\omega_S = \omega_p = \omega_o}$ is called the balanced case (Figure 2.5). There is no gap between RH and LH parts and the transition point is given

by $\boldsymbol{\omega_o}$. Regardless of the level of losses, the phase constant is zero for the latter frequency. Then, the wavelength tends to infinity. For the lossless case, the group velocity takes the value $1/2\sqrt{L_R^{'} C_R^{'}}$ for the frequency $\boldsymbol{\omega_o}$. As soon as losses appear, the group velocity collapses without completely reaching zero. This situation is quite remarkable, since the wave can propagate and the line has an electrical length equal to zero.

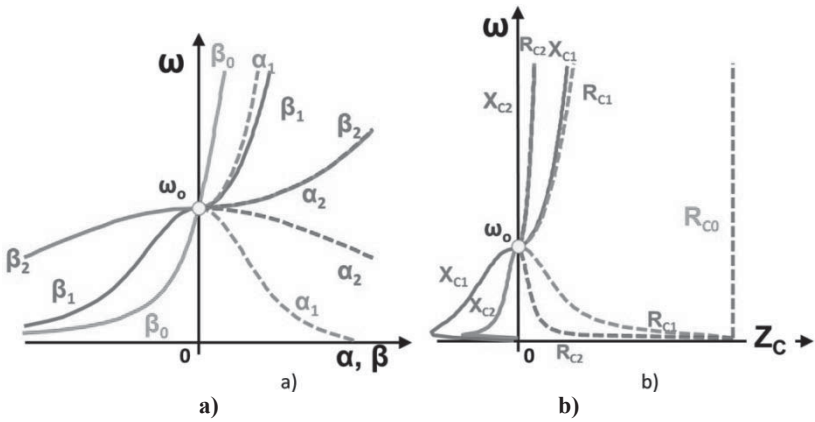

Figure 2.5. *Balanced case. Indexes refer to level of losses: 0 = no losses; 1 = weak losses; 2 = high losses. a) Dispersion of the propagation constant: solid line is for imaginary part of the propagation constant and dashed lines for attenuation or real part of the propagation constant. b) Dispersion of the characteristic impedance. Dashed and solid lines refer, respectively, to real and imaginary parts of* Z_c

On the characteristic impedance, the lossless case gives a real impedance that does not vary with frequency. In the real case with losses, the characteristic impedance becomes real for $\boldsymbol{\omega_o}$ and tends to the value $\sqrt{R'/G'}$.

2.4. Some technical approaches to realize MetaLines

2.4.1. *Context*

We have seen that cascading electrical elementary cells is a tool for designing structures with propagation properties specified in advance. In addition, by choosing particular cells, it is possible to create propagation properties that do not exist naturally. Thus, it remains to find practical ways to realize this MetaLine approach.

A lot of work has been done on this subject, previously, studying the elementary cell. For instance, the question of symmetric elementary cells has been addressed [CAL 06]. This point can be important in order to make reciprocal devices. Regarding technological achievements, they can be classified into two main categories. The first category, sometimes called the dual transmission line approach, consists of locally structuring the propagation lines, while the second category uses resonant elements that are coupling with a normal transmission line. In the remainder of this section, we will illustrate the principles of realization using examples drawn from the literature. The most commonly used technology was planar.

2.4.2. *Discrete component approach*

One of the first realizations of the planar MetaLine was proposed by Iyer *et al.* [IYE 03]. In fact, the main objective was to make a 2D negative refractive index lens using a 2D microstrip transmission line loaded with reactances (Figure 2.6(a)). The elementary cell is shown in Figure 2.6(b) and is realized with surface-mount components. The unit cell consists of a line on which the series capacitors are soldered. An inductor is soldered to the center of the junction and connected to the lower ground plane through the substrate. The size of the cell is 5 mm × 5 mm. The dispersion characteristic is measured along one line; the result is reported in Figure 2.6(b). Only the LH part is shown. The LH propagation can be observed from 0.96 to 2.5 GHz; between 1.2 and 2 GHz theoretical and measurement results are in very good agreement. It is interesting to note the measurement problems at low frequency. Indeed, and this is not a usual way of thinking, in the LH part, when the frequency decreases, the wavelength decreases also. Thus, below 1.2 GHz, the size of the unit cell becomes larger than $\lambda g/4$. Then, the boundaries of homogenization are reached as discussed in section 2.2.2; it then becomes difficult to consider the device as a homogeneous transmission line.

This first example, historically one of the first achievements of a MetaLine with LH propagation, shows the expected properties over a wide frequency range. The principle of the use of discrete lumped elements is therefore a possible way for the fabrication of artificial lines. The main advantage is the ease of manufacture since the desired components simply have to be bought and soldered. Regarding defects, the fact that the components are often limited in frequency and that it is not possible to find any desired value of components in supplier catalogs may be mentioned.

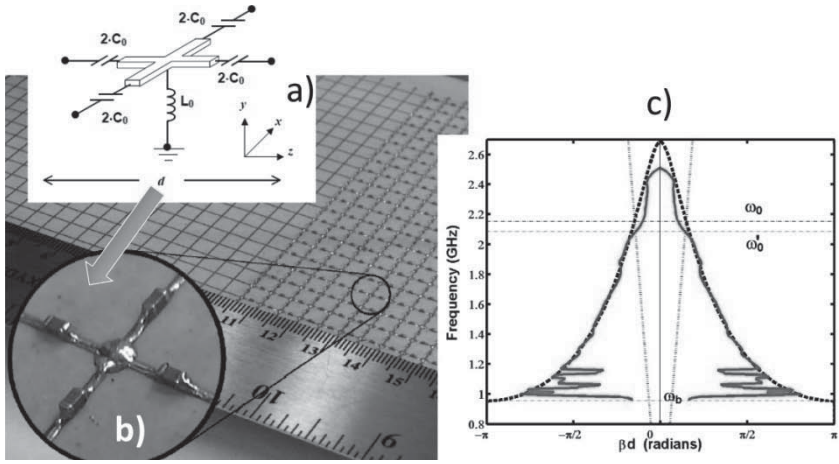

Figure 2.6. *Extract from [IYE 03] – 2D microstrip transmission MetaLine. a) Unit cell for the 2D transmission line. b) Prototype with a zoom on a unit cell. c) Measurements of the dispersion relation*

2.4.3. *Distributed or semi-lumped element approach in microstrip technology*

As in the previous section, the objective is to add parallel inductances and series capacitances to a classical microstrip line. In this technique, the additional components are made directly by structuring the line. The appropriate term should be semi-lumped elements as proposed by Marqués *et al.* [MAR 11], but in the following, the term "distributed element" will be used with the meaning of planar elements opposed to discrete or resonant elements. The first achievements in microstrip technology were proposed by Caloz and Itoh [CAL 02] and Lai *et al.* [LAI 04].

The elementary cell is composed of a series interdigital capacitor (with five digits) connected to a parallel shorted stub inductor (Figure 2.7(a)). These two parts give the LH contribution (C_L and L_L, respectively). But at the same time, these components provide parasitic elements that are RH (Figure 2.7(b)). Indeed, the current flow into the fingers of the capacitance induces a parasitic series inductance (L_R), while the stub brings a parallel capacitance (C_R) created by the proximity of the ground plane. The values of these four components are set to obtain a balanced situation. As a result, the prototype is a balanced CRLH transmission line. The complete line is composed of 24 unit cells (Figure 2.7(c)). Measurements have been made and compared to

theory (Figure 2.7(d)). We may note firstly that the line is well balanced since, at approximately 4 GHz, the propagation passes continuously from LH propagation to RH propagation. At very low frequencies, there is a shift between measurement and theory. This clearly shows the region where the transmission line can no longer be considered as homogeneous. For similar reasons, the difference will grow at high frequencies.

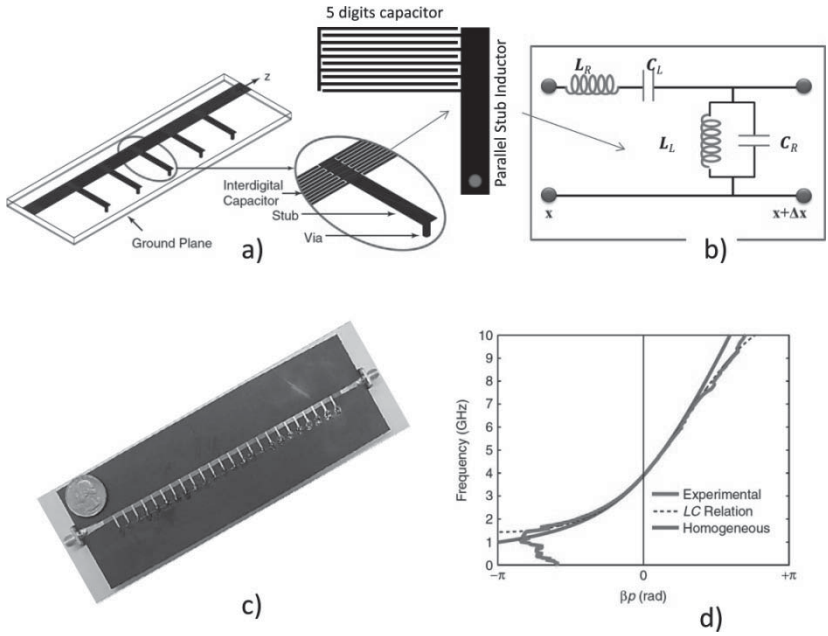

Figure 2.7. *Microstrip CRLH transmission line from [CAL 06] and [LAI 04]. a) Design of the transmission line. The inset presents a zoom on the unit cell. b) The equivalent electric circuit of the unit cell. C_L and L_L come, respectively, from the five digits capacitor and the stub inductor. L_R and C_R are parasitic elements of the unit cell. Design and size of the unit cell lead to the balanced case. Δx is about 6.1 mm. c) Picture of the CRLH microstrip line realized with 24 cells on a substrate with dielectric constant εr = 2.2 and thickness of 1.575 mm. d) Measured dispersion diagram compared with theory*

2.4.4. *Distributed element approach in coplanar waveguide technology*

Compared to the microstrip, coplanar waveguides (CPWs) have several advantages for monolithic microwave integrated circuits (ease of shunt and series connections, low radiation, low dispersion and simpler fabrication). So,

naturally, the possibility of the coplanar line has been explored. The first proposition was made by Grbic and Eleftheriades [GRB 02] for antenna purposes, but, in this section, the transmission line applications will be focused on, with the example of [GAO 05a] and [GAO 05b].

The proposed approach is to locally structure the trace of the CPW, in order to implement the required components in the equivalent circuit. The layout is shown in Figure 2.8(b), and the equivalent circuit is in Figure 2.8(a). On the left of the unit cell (Figure 2.8(b)), the slit in the central conductor not only gives the series capacitance but also the parasitic capacitances. To the right, a small length of line connects to the parallel short circuited stub, which gives the parallel inductance. This is not a pure inductance and parasitic series inductances must be taken into account. After that, another length of line allows the next unit cell to be connected. The prototype is shown in Figure 2.8(c). It is achieved with nine unit cells.

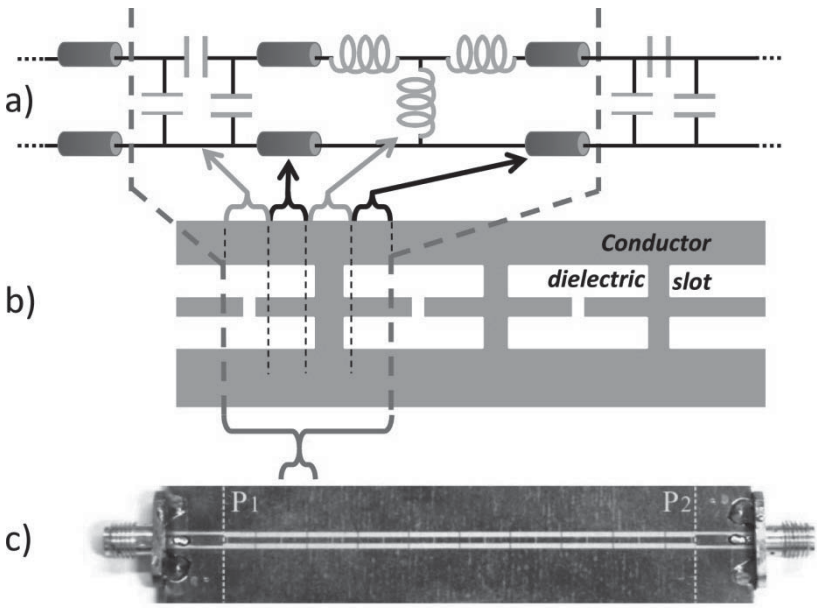

Figure 2.8. *CRLH coplanar transmission line [GAO 05a, GAO 05b]. Dotted lines define the unit cell. a) Equivalent circuit model with distributed elements. b) Trace of the CPW. Blank parts represent the slots of the line while grey parts are conductors. c) Prototype realized with nine unit cells*

The transmission results are shown in Figure 2.9. Four regions can be observed. The first one goes up to 5 GHz and is an LH stop band. The phase constant is negative but the attenuation part of the propagation constant is very high, resulting in a stop band. Next, from 5 GHz up to 5.75 GHz, the LH propagation band appears, since the attenuation constant drops to very low values. As the proposed prototype is not balanced, a gap is present in the response of the line (7.75–7 GHz). Subsequently, in the range 7–8.75 GHz, the propagation becomes RH. For higher frequencies, the attenuation increases and the transmission is stopped. It can be noted that in the two passbands, the level of transmission is quite low. This is often a difficulty for the design.

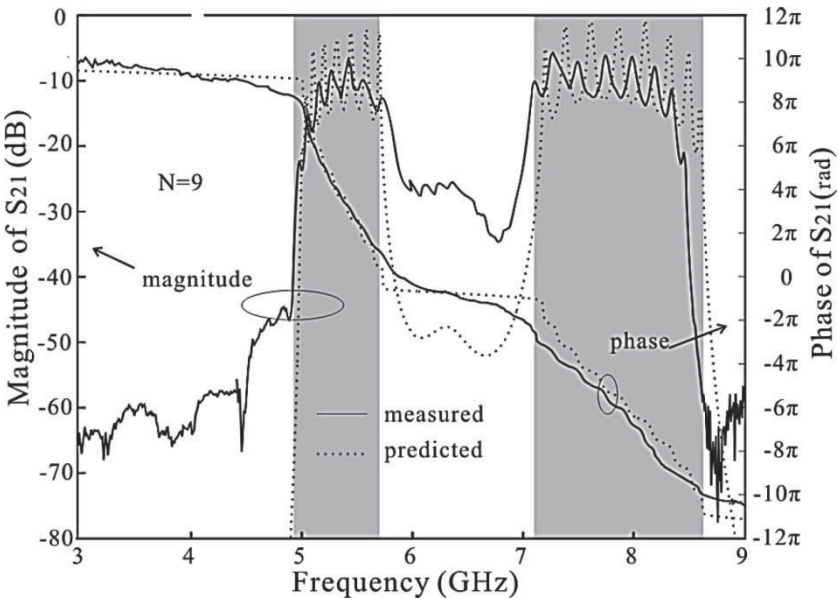

Figure 2.9. *Results for the unbalanced CRLH CPW [GAO 05a, GAO 05b]. Left axis is for S21 (dB) while the right axis is for the phase of S21 in radians*

Other prototypes of unbalanced coplanar lines are shown in Figure 2.10. The observed behavior is globally similar (LH stop band, LH passband, band gap, RH passband and RH stop band). The reported designs can emphasize different properties such as the width of the LH passband, high level of transmission in the LH passband, high compactness of the layout and strong rejection in the band gap for filter purposes.

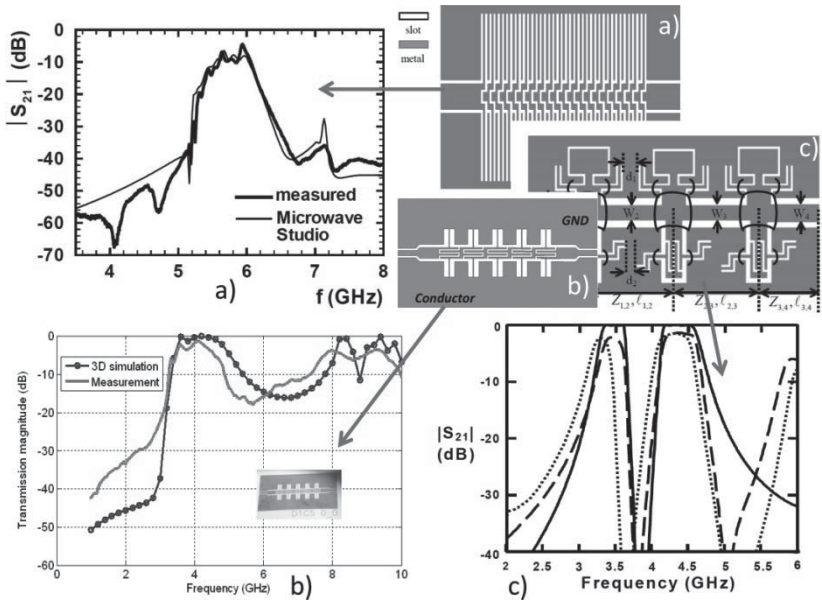

Figure 2.10. *Several prototypes of coplanar MetaLines. a) The unbalanced CRLH TL is composed of 20 unit cells [MAC 05]. Only the LH frequency band is shown. b) This unbalanced MetaLine is realized with five compact unit cells [ZER 10]. Left and right bands are shown. (c) Very compact stubs (50%) are used in this unbalanced TL [WU 07]. Continuous line: equivalent circuit modeling; dashed line: full-wave simulation; dotted line: measured results*

2.4.5. *The resonant approach*

The resonant approach is to periodically load a transmission line with resonators. These resonators were initially split ring resonators (SRRs) that were used during the first achievements of bulk metamaterials [SHE 01]. This approach is different from the dual lines previously presented but substantially equivalent to that used in making bulk metamaterials with negative index. The line must be structured (for example periodic shunt connections) so as to reproduce the equivalent of a negative permittivity medium up to a certain frequency, which depends on the shunt and the spatial period. The added resonators are responsible for creating a magnetic resonance. If everything is set properly, the resonance of SRR provides the negative part of the effective permeability while the remainder of the line behaves as an equivalent negative effective permittivity. The effective index of the line is then negative and LH propagation can be obtained.

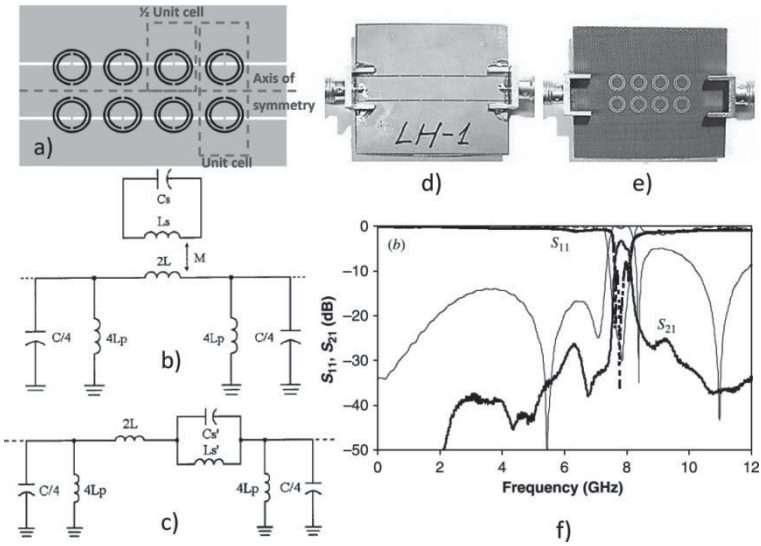

Figure 2.11. *Resonant-type MetaLine [MAR 03]. a) Alignment of the line and the SRRs. Gray color for the metallic part of the CPW. Metallic SRRs are drawn with black lines. This view is seen in transparency since the line and the SRRs are not in the same plane. b) Equivalent circuit of one-half of the unit cell. c) Simplified equivalent circuit. d) Upper side of the prototype. Shunts in the slots of the line are visible. e) Underside of the prototype with the etched SRRs. f) Simulated (thin line) and measured (bold line) results of S parameters for the prototype*

The first realization was proposed by Martin *et al.* [MAR 03]. The device is based on a host CPW. Resonators are placed beneath the substrate of the line. They are centered on the slots of the line and placed symmetrically with respect to the central metal strip. On the side of the strips of the CPW, thin metal shunts connect the signal to the ground. These shunts are aligned with the center of the SRR (Figure 2.11(a)). Although the approach is different, the whole thing can be considered as an equivalent periodic circuit (Figure 2.11(b)). In this schematic, L and C are the per unit length inductance and capacitance of the line. Lp represents the inductance of shunt, and Ls and Cs are the equivalent circuit parameters of the SRR. M is the coupling factor with the CPW. In view of the structure, a magnetic wall can be considered as a symmetry plane and Figure 2.11(b) only represents one-half of the unit cell. This equivalent circuit can be simplified to the one given in Figure 2.11(c). Looking at this configuration, we find that all the components necessary to obtain a CRLH are present (series and parallel capacitances and inductances). Figure 2.11(d) shows the upper side of the prototype (note the shunts in the

slots) and Figure 2.11(e) shows the opposite side where the SRRs are etched. The resonant frequency of SRRs has been set to 7.7 GHz.

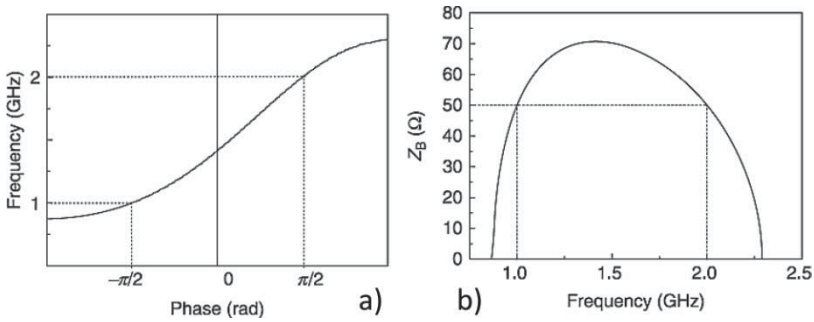

Figure 2.12. *Illustration of the dual-band behavior with e CRLH transmission line. Figures are from [MAR 11]. The two operation frequencies are of 1 and 2 GHz. a) Dispersion diagram with left- and right-handed bands. b) Corresponding characteristic impedance*

The results are shown in Figure 2.11(f). As can be seen, the device does not transmit the signal, but close to the resonant frequency, a narrow passband appears. This frequency band is LH and corresponds to the fact that permittivity and permeability are simultaneously negative.

The resonant approach is another tool for the control of transmission line properties. This concept is similar to that developed for the realization of bulk metamaterials, which implies a certain complexity in modeling the electromagnetic interactions between the resonators and the line. However, a great advantage lies in the fact that it is easier to control the characteristic impedance, and that the size of the line remains unchanged. Moreover, the relatively simple method of fabrication has led to many versions and applications [MAR 11].

2.5. Toward tunability

With increases in the number of communication systems, microwave functions must be realized on several frequency bands. One way is to multiply the number of devices, each one specialized on one frequency band. Another way is to develop components that can operate at different frequencies, with components that enable the desired functionality on multiple discrete and fixed frequencies or with components that can change the operating frequency by an external command.

2.5.1. *The dual-band behavior*

Martín and Bonache [MAR 08] propose a good example to illustrate the potentialities of the CRLH transmission line. The example is based on the realization of a dual-band inverter (a line of length of $\lambda g/4$); as the sign of the phase shift is not important, two functioning frequencies can be used with a CRLH line, one in the LH band (–90°) and one in the RH band (+90°). However, there is an additional criterion that should be taken into account to make the device operational: the characteristic impedance must be equal to 50 Ω. So, with four constraints (two frequencies, a phase shift and Z_c) and four degrees of freedom (L_L, C_L, L_R and C_R), the problem can be solved, with a CRLH transmission line (Figure 2.12). As can be seen, for two distinct frequencies, the CRLH device is an impedance inverter and simultaneously, the characteristic impedance is matched to 50 Ω.

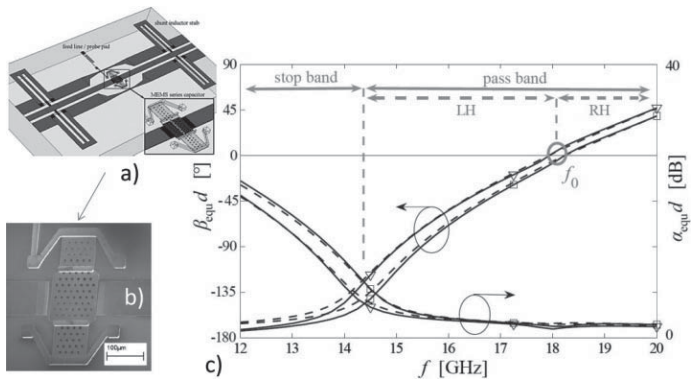

Figure 2.13. *MEMs-controlled CRLH transmission line from [PER 06]. a) Unit cell of the MetaLine with the MEMs series capacitor. b) Zoom of the MEMs capacitor. c) Measured results. Left axis: phase constant in degrees; right axis: attenuation constant in decibels. The two curves are for two different positions of the MEMs*

2.5.2. *Mechanical agility*

A possible method to dynamically modify the properties of the CRLH line is to drive the value of one or more components of the unit cell (typically L_L, C_L, L_R or C_R). In the design of the unit cell of the MetaLine proposed in [PER 06], the authors have introduced a series capacitor realized with Microelectromechanical systems (MEMs). As a result, the dispersion diagram can be controlled by means of an MEMs device and therefore an actuation voltage (Figure 2.13). This mechanical approach has also been proposed for the MetaLine of resonant type [VÉL 08a].

2.5.3. *CRLH line controlled with active components*

Another approach is to use active components in the elementary cell. For example, Vélez *et al.* [VÉL 08b] proposed to tune a resonant-type microstrip MetaLine. The signal line (Figure 2.14(a)) is split to make the necessary series capacitance. In this application, the resonant particle is a complementary split ring resonator (CSRR), which is the dual version of an SRR since it is etched in the ground plane (Figure 2.14(b)). The CSRR particle is loaded with a varactor capacitor (Figures 2.14(a) and (b)). As a result, the applied voltage on the capacitor will change the value of the capacitance that is involved in the equivalent circuit of the CSRR, driving the resonant frequency of the particle. The results are shown in Figure 2.14(c). Different bands can be spotted. The lower band is a stop band due to the effect of series capacitance for low frequencies. Next, a narrow LH passband followed with a band gap can be spotted. Finally, at higher frequencies, an LH passband is followed by an RH passband. With the variation of the bias voltage on the varactor diode, the different bands are shifted.

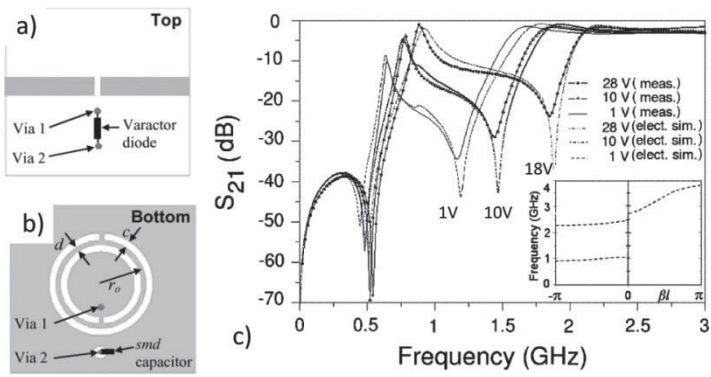

Figure 2.14. *Tunable resonant CRLH transmission line by means of varactor capacitor [VÉL 08a, VÉL 08b]. The line is loaded with only one CSRR particle. a) Top side of the line. Gray color is for metallic part; white is for dielectric. A slit has been made in the signal line. b) Bottom face of the device. The SRR is in white since it is etched in the ground plane (CSRR). c) Frequency response of the transmission through the device for several voltages applied on the varactor*

2.5.4. *Ferroelectric agility*

The ferroelectric thin films are one of the possible applications for agility. This route has been explored in the context of MetaLines by Marteau *et al.* [MAR 09]. The authors want two simultaneous properties for the device:

agility on the operating frequencies and balanced properties for the CRLH line. The design is fabricated in coplanar technology (Figure 2.15(a)). The prototype is realized on a ferroelectric thin film ($Ba_{0.5}Sr_{0.5}TiO_3$, BST) deposited on a sapphire substrate. The series capacitance is obtained because of an interdigital capacitance etched in the signal line. The parallel inductance is obtained through a short-circuited parallel stub. To validate the balanced condition more easily, an interdigital capacitance is introduced in parallel with the previous stub. In this way, once the balanced condition is obtained without external bias, when the ferroelectric layer is polarized, both capacities vary simultaneously, which maintains the balanced case. Pictures of the prototype are shown in Figures 2.15(b) and (c). The first one shows a microscope view of the series capacitance. The second one presents two unit cells of the MetaLine. In the latter, metal strips and connecting pads are visible above the line. Their function is to polarize the ferroelectric capacitances. The measurements of the propagation constant for three different values of the bias field are shown in Figure 2.15(d). The first thing to note is that the line remains balanced when the applied voltage changes, so the band gap in the long wavelength regime stays closed (inset in Figure 2.15(d)). The second thing is the shift of the dispersion characteristic with the variation in the bias voltage. When the voltage increases, the dielectric constant of the BST decreases. As a consequence, the value of the series capacitance decreases and the transition frequency between LH and RH bands increases (see equation [2.7]).

Ferroelectric films were also used in the case of the resonant MetaLine [HOU 10]. In this case, a C-shaped resonator is loaded with an interdigital capacitance in order to tune the resonance frequency. A microstrip transmission line is coupled with the resonant particle. The complete device is etched on a BST film. For a bias of 30 V, the resonance is shifted to higher frequencies (approximately 7% of the resonance).

2.5.5. *Ferrimagnetic agility*

Ferrite material has also been used in the general field of metamaterials and in MetaLine too. The key idea is to use the possibility of varying the permeability of a ferrite with an external magnetic bias. The use of ferrite is often preferred to other magnetic families since it is not a conductor. In [TSU 04], the authors propose a non-reciprocal LH transmission line in microstrip configuration over a ferrite substrate. In [ABD 07] and also in several following papers, the authors demonstrate theoretically the non-reciprocal effect of the CRLH transmission line over a ferrite substrate in

CPW configuration. Compared to previous approaches, the magnetic one is more complicated for two main reasons. The first is the non-reciprocal properties of transmission induced by the ferrite. The second reason lies in the difficulty of modeling the magnetic response of the ferrite, especially when the material is not in complete and homogeneous saturation.

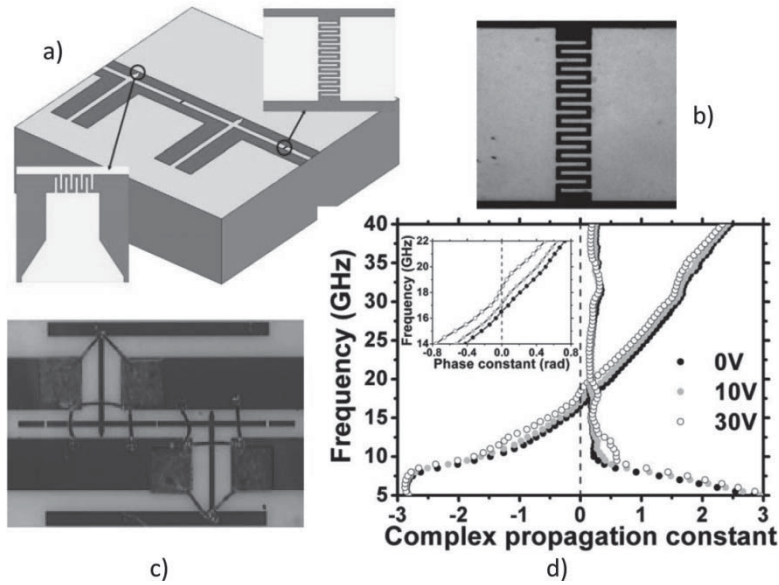

Figure 2.15. *Ferroelectric tunable balanced CRLH transmission line [MAR 09]. a) Design of the MetaLine. The line is etched on a ferroelectric thin film. The insets are showing the interdigital capacitors. On the right: the series capacitance. On the left: the additional parallel capacitance to obtain balanced conditions. b) Microscope photo of the series capacitance. c) Prototype with two unit cells. The connectors for the bias field on the ferroelectric film are visible above the line. d) Measurement results for three values of applied voltage*

The following example of CRLH transmission line with ferrite material is extracted from [ZER 10] and [ZER 11]. The line is realized on a bulk ferrite substrate (composed of Yttrium iron garnet – YIG) with five unit cells (see Figure 2.16(a)). The device is biased with an external field whose direction is in the plane perpendicular to the propagation and in the metal plane (Figure 2.16(a)). So far, two propagation bands and a band gap have been commonly observed. The ferrite is a highly dispersive material and changes in the permeability are important. There is even a band around the resonance

frequency of the material in which the permeability becomes negative. In addition, around the resonance frequency, the medium becomes strongly anisotropic and, above all, non-reciprocal. These magnetic effects are frequency-shifted depending on the intensity of the static field applied; the higher the intensity, the greater the gyromagnetic resonance frequency shifts to high frequencies. The study of the design of the line allows the values of inductances and capacitances of the line to be evaluated. These data are used to extract (without regard to losses) dispersion diagrams as a function of the applied external field (Figures 2.16(b) and (d)). In Figure 2.16(b), the applied static field puts the resonance frequency in the middle of the LH band, which has the effect of splitting the LH band into two. Between these two LH bands, the non-reciprocal magnetic effects take over and the propagation becomes clearly non-reciprocal. At higher frequencies, the line has the normal behavior of an unbalanced CRLH line: a band gap followed by an RH band. Figure 2.16(c) shows the measurement results. The first thing to note is that the magnetic losses in the structure are relatively strong in the bulk substrate. The second important point is that the YIG is certainly not homogeneously magnetized, which increases the level of losses. Nevertheless, it is possible to find the successive behaviors provided by theoretical modeling. For results in Figures 2.16(d) and 2.16(e), the static field is stronger, which shifts the gyromagnetic frequency up. Under these conditions, the gyromagnetic resonance is now in the RH band. The successive behaviors are now: LH band, band gap, RH band, non-reciprocal effects due to gyromagnetic resonance. The expected behaviors can be found in measurements (although in the case of measurements, the static field could not be set as high as planned theoretically).

2.6. Conclusion

The concept of the discrete line or artificial line is now a reality. This concept originates with the electrical model of a classical transmission line, which is attempted to achieve with discrete assembling. Based on this observation, it became possible to imagine unit cells of the line, different from those of the historical classical line. Thus, the concept of the dual line appeared, directly inspired by the works on metamaterials. It confirmed the concept of the discrete line and brought new unnatural electromagnetic properties in the propagation lines such as LH propagation. No matter whether we call these structures metamaterial lines or MetaLines, different research works led first to the concept of the CRLH line since the name clearly describes the fundamentally RH and LH nature of MetaLines.

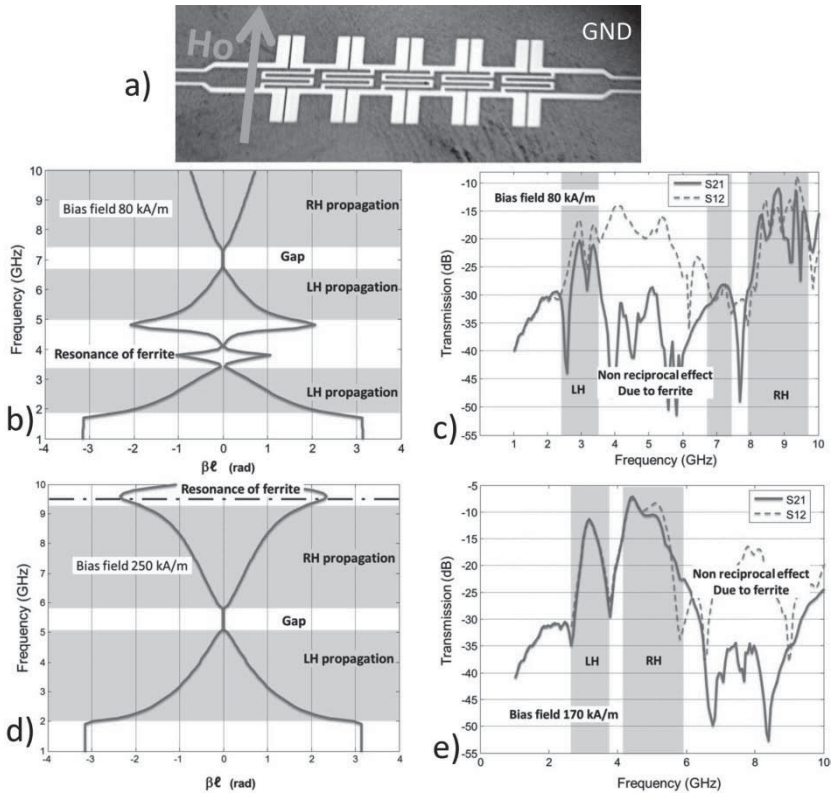

Figure 2.16. *CRLH transmission line on a biased ferrite substrate. a) Picture of the prototype composed of five unit cells. Direction of magnetic polarization is shown. b) Theoretical dispersion diagram, in lossless case and with a saturated ferrite under a static magnetic field of 80 kA/m. c) Measured transmission (S21 and S12) under a static field of 80 kA/m. d) Theoretical dispersion diagram, in lossless case and with a saturated ferrite (250 kA/m). e) Measurement of transmission in the case of 170 kA/m*

The key idea is thus to find the basic physical structure to obtain the desired electromagnetic effect. Among the proven benefits, miniaturization, the ability to achieve the desired function on several frequency bands, improving the performance of certain functions with equivalent size circuits, can be mentioned.

The artificial lines are therefore a powerful design tool, which will increase the number of tuning parameters for structures and thus increase the scope of possibilities in terms of electromagnetic properties and functions.

2.7. Bibliography

[ABD 07] ABDALLA M.A., HU Z., "On the study of CPW dual band left handed propagation with reciprocal and nonreciprocal characteristics over ferrite substrates", *IEEE Antennas and Propagation Society International Symposium*, Honolulu, pp. 2578–2581, June 2007.

[BRI 56] BRILLOUIN L., PARODI M., *Propagation des ondes dans les milieux périodiques*, Masson-Dunod, Paris, 1956.

[CAL 02] CALOZ C., ITOH T., "Application of the transmission line theory of left-handed (LH) materials to the realization of a microstrip LH transmission line", *Proceedings of the IEEE-AP-S USNC/URSI National Radio Science Meeting*, vol. 2, San Antonio, pp. 412–415, June 2002.

[CAL 06] CALOZ C., ITOH T., *Electromagnetic Metamaterials: Transmission Line Theory and Microwave Applications: The Engineering Approach*, Wiley, 2006.

[ELE 02] ELEFTHERIADES G.V., IYER A.K., KREMER P.C., "Planar negative refractive index media using periodically L-C loaded transmission lines", *IEEE Transactions on Microwave Theory and Techniques*, vol. 50, pp. 2702–2712, 2002.

[GAO 05a] GAO J., ZHU L., "Characterization of infinite- and finite-extent coplanar waveguide metamaterials with varied left- and right-handed passbands", *IEEE Microwave and Wireless Components Letters*, vol. 15, no. 11, pp. 805–807, November 2005.

[GAO 05b] GAO J., ZHU L., "Per-unit-length parameters of 1-D CPW metamaterials with simultaneously series-C and shunt-L loading", *Microwave Conference Proceedings, APMC 2005, Asia-Pacific Conference Proceedings*, vol. 1, pp. 4, 4–7 December 2005.

[GRB 02] GRBIC A., ELEFTHERIADES G.V., "Experimental verification of backward wave radiation from a negative refractive index metamaterial", *Journal of Applied Physics*, vol. 92, pp. 5930–5935, 2002.

[HEI 93] HEINRICH W., "Quasi-TEM description of MMIC coplanar lines including conductor loss effects" *IEEE Transactions on Microwave Theory and Techniques*, vol. 41, pp. 45–52, 1993.

[HOU 09] HOUZET G., Déphasage composite accordable et routage spatial par la technologie des métamatériaux, PhD Thesis, University of Lille 1, October 2009.

[HOU 10] HOUZET G., MÉLIQUE X., LIPPENS D., *et al.*, "Microstrip transmission line loaded by split-ring resonators tuned by ferroelectric thin film", *Progress in Electromagnetics Research C*, vol. 12, pp. 225–236, 2010.

[IYE 03] IYER A., KREMER P., ELEFTHERIADES G., "Experimental and theoretical verification of focusing in a large, periodically loaded transmission line negative refractive index metamaterial", *Optics Express*, vol. 11, pp. 696–708, 2003.

[LAI 04] LAI A., CALOZ C., ITOH T., "Composite right/left-handed transmission line metamaterials", *IEEE Microwave Magazine*, vol. 5, no. 3, pp. 34–50, September 2004.

[MAC 05] MACHAE J., HUDLIEKA M., ZEHENTNER J., *et al.*, "Left-handed coplanar waveguide", *IEEE MTT-S International Microwave Symposium Digest, 2005*, pp. 1957–1960, 12–17 June 2005.

[MAL 51] MALYUZHINETS G.D., "A note on the radiation principle", *Zhurnal Tekhnicheskoi Fiziki*, vol. 21, pp. 940–942, 1951.

[MAR 03] MARTIN F., BONACHE J., FALCONE F., *et al.*, "Split ring resonator-based left-handed coplanar waveguide", *Applied Physics Letters*, vol. 83, pp. 4652–4654, 2003.

[MAR 08] MARTÍN F., BONACHE J., "Beyond the state-of-the-art microwave components by using metamaterial transmission lines", *Metamaterials: a scientific revolution*, European Summer University, Saint-Etienne, France, September 2008.

[MAR 09] MARTEAU A., VELU G., HOUZET G., *et al.*, "Ferroelectric tunable balanced right- and left-handed transmission lines", *Applied Physics Letters*, vol. 94, p. 023507, 2009.

[MAR 11] MARQUÉS R., MARTÍN F., SOROLLA M., *Metamaterials with Negative Parameters: Theory, Design and Microwave Applications*, John Wiley & Sons, 2011.

[PER 06] PERRUISSEAU-CARRIER J., LISECAND T., SKRIVERVIK A.K., "Circuit model and design of silicon-integrated CRLH-TLS analogically controlled by MEMS", *Microwave and Optical Technology Letters*, vol. 48, pp. 2496–2499, 2006.

[SHE 01] SHELBY R., SMITH D.R., SCHULTZ S., "Experimental verification of a negative index of refraction", *Science*, vol. 292, pp. 77–79, 2001.

[TSU 04] TSUTSUMI M., UEDA T., "Nonreciprocal left-handed microstrip lines using ferrite substrate", *IEEE MTT-S International Microwave Symposium Digest*, vol. 1, pp. 249–252, 2004.

[VÉL 08a] VÉLEZ A., BONACHE J., ROTTENBERG X., *et al.*, "Tunable metamaterial transmission lines based on complementary split ring resonators (CSRRs): two approaches", *NATO Adwanced Research Workshop & Metamaterials for Secure Information and Communication Technologies (META'08)*, Marrakesh, Morocco, 7–10 May 2008.

[VÉL 08b] VÉLEZ A., BONACHE J., MARTÍN F., "Varactor-loaded complementary split ring resonators (VLCSRR) and their application to tunable metamaterial transmission lines", *Microwave and Wireless Components Letters, IEEE*, vol. 18, no. 1, pp. 28–30, January 2008.

[WU 07] WU M.S., MAO S.G., "Dispersion characteristics of compact composite right/left-handed and electromagnetic bandgap coplanar waveguide stubs", *Metamaterials'2007*, Rome, Italy, 22–26 October 2007.

[ZER 09] ZERMANE A., SAUVIAC B., BAYARD B., *et al.*, "Etude comparative d'une ligne coplanaire par l'utilisation de trois méthodes", *Proceedings of SETIT 2009*, Hammamet, Tunisia, 22–26 March 2009.

[ZER 10] ZERMANE A., SAUVIAC B., BAYARD B., *et al.*, "Modeling and measurement of a zeroth-order resonator and a composite right-left-handed transmission line in coplanar technology", *Progress in Electromagnetics Research C*, vol. 14, pp. 33–43, 2010.

[ZER 11] ZERMANE A., Contribution à l'étude et la faisabilité de micro-résonateurs en structures planaires, PhD Thesis, University of Saint-Etienne, 2011.

Chapter 3

Metamaterials for Non-Radiative Microwave Functions and Antennas

3.1. Introduction

Current and future wireless communications systems have to be smart while proposing an acceptable Quality of Service for given applications and optimized resource management in terms of energy consumption and spectral occupation. Moreover, the demand for nomadic devices is growing, thus requiring light, low-profile and miniaturized microwave components that can easily integrate into complex systems. All these requirements can be contradictory for the conventional microwave engineer since, for instance, miniaturization is usually achieved with a non-negligible impact on overall performances.

Since metamaterials can be designed to present required electromagnetic properties, they should definitely provide a higher degree of freedom in the design of both radiative and non-radiative components for wireless systems. The potential of metamaterial to improve the performances of microwave devices should also be considered.

This chapter is divided in two main parts: the first part deals with metamaterial applications for non-radiative microwave components and the

---

Chapter written by Divitha SEETHARAMDOO and Bruno SAUVIAC.

second part describes the potential and applications of metamaterials to microwave antennas.

3.2. Metamaterials for non-radiative applications

Early studies on metamaterials showed that the use of discrete electrical components in propagation structures allowed the appearance of new properties to be demonstrated (see Chapter 2). Thus, many studies were carried out to apply this approach to microwave components and functions. As the properties depend on the base transmission line and on the added electrical elements, the number of setting parameters increases, which allows the number of degrees of freedom in design to be increased. Thus, the advantages of this approach are revealed in works on different types of circuits: improved bandwidth, reduced size of the devices or dual band functionality.

3.2.1. *Miniaturization*

To reduce the size of components, it is of course possible to reduce the size of the unit cell but also to adjust the electrical length of some elements used in the device. An obvious example is that of a phase shifter made using a simple line section. Assuming that somebody wants to achieve a 270° phase shift, a classical right-handed transmission line of length $3\lambda/4$ can be used. With a MetaLine operating in the left-handed band (where the phase constant is negative), it is then sufficient to use a line of length $\lambda/4$ in order to obtain an equivalent phase shift of –90°. If both versions use the same guided wavelength, then the left-handed approach allows the length of the line to be divided by three.

Another way to miniaturize a circuit is to reduce the size of the unit cells that constitute the device and/or to reduce the number of cells used in cascade. This is one of the paths explored with the resonant-type approach (see Chapter 2). In [GIL 07], the authors propose to realize a Y-junction power divider. The device is based on two connected impedance inverters achieved with lines with characteristic impedance of $\sqrt{2}Z_o$ (Z_o is supposed to be the reference impedance; usually $Z_o = 50\ \Omega$). The first version is realized with classical right-handed lines (see Figure 3.1(a)). The second version is made with a resonant-type MetaLine based on the complementary split ring resonator (CSRR) particle (see Chapter 2). In the latter, the two impedance

inverters are realized with a phase shift of –90° with a single unit cell (see Figure 3.1(b)). In Figure 3.1, the layouts of the two versions are shown. Compared to the classical approach, the size reduction is obvious in the images; the ratio of miniaturization is about 50%.

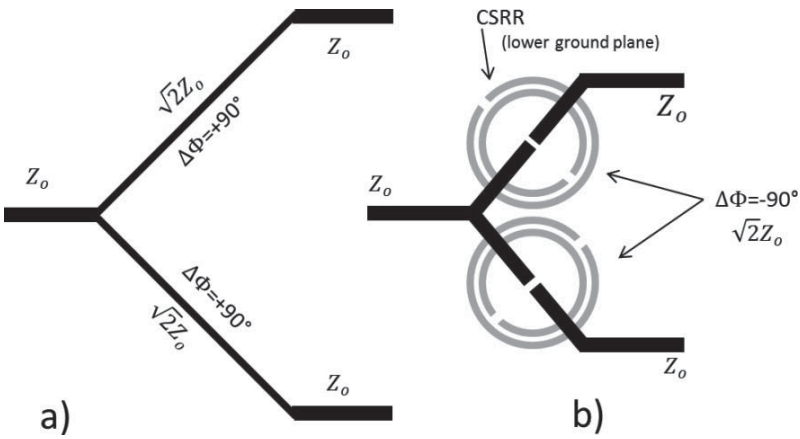

Figure 3.1. *Compared layouts to realize a Y-junction power divider. a) Conventional version with right-handed transmission lines. b) Version with resonant MetaLines using the left-handed band. Layouts are extracted from [GIL 07]. Images of layouts have been redone but the size ratio was observed*

Mobility has become a very important factor in the development of communications applications. The need arising from this development is to use smaller and smaller devices. In conclusion, we can say that the metamaterial tool can be a good way to work on the size of microwave devices.

3.2.2. *Bandwidth improvement*

Usually, microwave devices are adjusted for a specific central frequency and the bandwidth is defined around this central frequency. In this bandwidth, the required function or operation of the device can be considered to be stable with respect to the frequency shift. The main cause of the limitation of this bandwidth arises from the variation of the phase depending on the frequency. Once again, the fact that MetaLines increase the number of setting

parameters allows work on the enhancement of the bandwidth to be possible. To illustrate the purpose, a simple example will be studied. After a power divider, a signal is separated into two equal parts and transmitted through two separate lines. As an example, for IQ demodulation, the two signals must be finally mixed with ±90° phase difference. Using two similar transmission lines (same phase velocity v_φ), in order to realize this operation, implies that the second line (length ℓ_2) is longer that the first line (length ℓ_1). For the central frequency ω_o, the difference of length between the two lines can be expressed as:

$$\Delta\varphi_o = \frac{\omega_o}{v_\varphi}(\ell_2 - \ell_1) = \frac{\pi}{2} \quad [3.1]$$

When the two lines are set, the phase difference between the two lines is 90° for ω_o. When the frequency deviates from the central frequency, the phase difference also changes. The deviation from the required phase difference can be written as:

$$\Delta\varphi = \Delta\varphi_o + \frac{\omega-\omega_o}{\omega_o}\Delta\varphi_o \quad [3.2]$$

The phase variations are shown in Figure 3.2(a); the increasing difference between the phases of the two RH lines can be observed when the angular frequency increases. Using MetaLines, it is possible to design the dispersion diagram of the CRLH transmission line in order to control the phase variation. The proposed MetaLine is supposed to be balanced, and the behavior of this line is supposed to be equivalent in the right-handed propagation band. As a result, the characteristic impedance is compatible with the reference line and the slope of the phase is nearly parallel to the reference line (Figure 3.2(a)). The phase difference between the lines is shown in Figure 3.2(b). The limit of the phase deviation from the required phase difference is set to a maximum of π/8. The graph shows that the CRLH approach allows the bandwidth to be multiplied by 4. Moreover, it can be noticed that the CRLH line has been set with a transition frequency ($\beta = 0$) that corresponds to the central frequency. As a result, the length of the line is smaller than the classical line. In this example, the RH line must be twice as long as the reference line while the CRLH is 37% smaller than the reference line. Hence, this example shows that both size and bandwidth can be improved simultaneously.

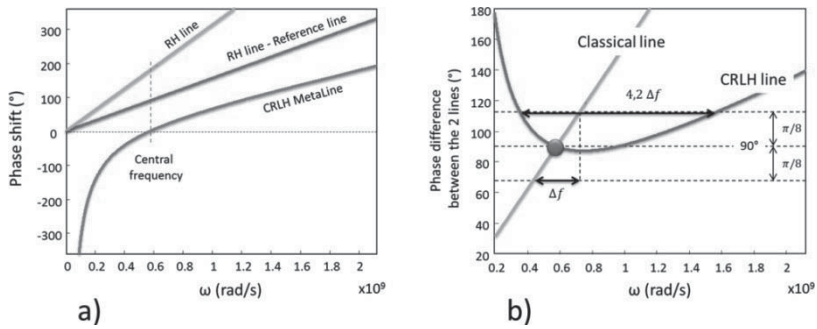

Figure 3.2. *a) Compared variation of the phase versus frequency for different lines. b) Variation of the phase difference with frequency. The big point shows the nominal operating frequency. Classical line refers to the case where the second line is standard while CRLH line refers to the case where the second line is a MetaLine*

Many other works in the literature lead to the same conclusion: MetaLines allow the functionality of the device to be obtained over broader bandwidths and at the same time allow the overall dimensions to be reduced. For example, in [ANT 05], the improvements are made on a power divider; in [LIU 08], the bandwidth of a microstrip balun is enhanced; and in [SIS 08], the authors improved a rat-race coupler with resonant-type MetaLines.

In this section, it has been pointed out that the metamaterials can be a good tool to work on the bandwidth of devices. The most interesting result comes from the fact that size reduction can be obtained simultaneously.

3.2.3. *Dual band*

For some applications, the bandwidth is not the most important point. Another interesting property provided by MetaLines is the ability to achieve the desired functionality on more than one frequency band (see also Chapter 2).

Even if it is not a practical application, the previous example can be modified in order to illustrate the dual-band capability. The length of the previous CRLH line is increased. As a result, the phase shift produced by the CRLH is modified and the curve crosses the curve of the reference line (Figure 3.3(a)). Now looking at the phase difference in Figure 3.3(b), another functional point appears before the next frequency value where the phase

difference will be increased by 360°. The first frequency point gives –90° while the next frequency point gives +90°.

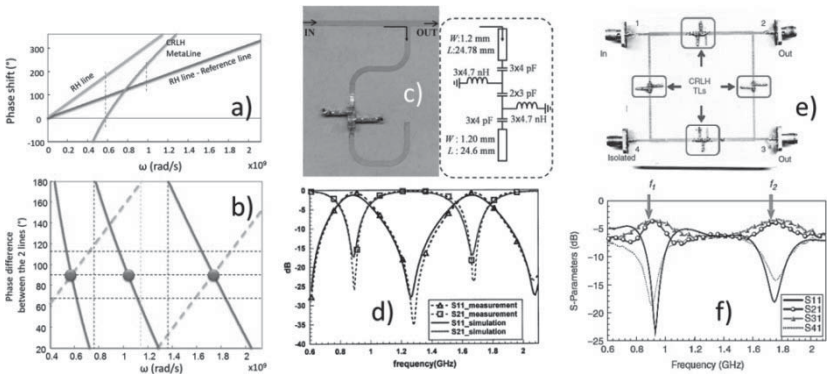

Figure 3.3. *Illustrations of the dual-band advantage. a) Teaching example. Phase variation of different lines. Length of RH line and CRLH line is twice long as the length of the reference line. b) Identification of operating frequency points. Dashed line represents the classical RH line and solid line represents the CRLH transmission line. c) Image of the CRLH open-stub [LIN 04]. d) Frequency response of the line loaded by the stub [LIN 04]. e) Image of the branch line coupler [LAI 04]. f) Frequency response of the branch line coupler [LIN 04, LAI 04]*

Using this principle, dual-band components have been proposed. In [LIN 04], the authors worked on a dual-band quarter wave transmission line, a dual-band stub, a branch-line coupler and a rat-race coupler. In Figure 3.3(c), an image of the λg/4 open-stub circuit is presented; it can be noticed that the device is realized with discrete surface-mounted devices (SMD). The proposed CRLH line is designed in order to have a phase response of –90° at 890 MHz and +90° at 1,670 MHz. The response of the classical line loaded by the stub is shown in Figure 3.3(d). Two similar stop bands can be observed on the response showing the dual-band functionality. An image of a branch line coupler realized with CRLH lines is shown in Figure 3.3(e). Usually, for a classical (right-handed) device, the functionality is obtained for the design frequency and for the odd harmonics of the latter. Replacing the RH lines with CRLH lines allows two non-harmonic frequencies to be possible to implement the coupler functionalities (Figure 3.3(f)). Of course, the harmonics of these two frequencies are also valuable to make the coupler efficient.

The metamaterial approach can give flexibility in the design of multiband components. The previous examples were realized with discrete SMD components. Of course, MetaLines with distributed or resonant elements also allow dual-band behavior to be obtained. In [VÉL 11], CRLH lines of the resonant type are used to design a duplexer. In addition to the dual-band behavior, it is shown that the reduction in the size of the device can be simultaneously obtained.

3.2.4. *Zeroth-order resonator (ZOR)*

In section 3.2.3, it has been shown that MetaLines could improve different characteristics of the usual microwave components. In addition to the different interests presented, it is possible to manufacture new components such as zeroth-order resonator (ZOR), which did not exist before. On the basis of a transmission line with a short or open termination, a resonator can be obtained. In a right-handed line, the resonance frequencies of the resonator are obtained when the electrical length of the piece of line (physical length ℓ) is a multiple of π:

$$\beta\ell = 2\pi\ell/\lambda g = p.\pi \qquad [3.3]$$

As a result, for a given length, there is an infinite number of resonant frequencies, from $p = 1$ to $p = +\infty$. Unlike the classical transmission line, the balanced CRLH transmission line can have a zero phase constant to a non-zero frequency. Moreover, for lower frequencies, the phase constant is negative in the band where the propagation is left handed. Therefore, the relationship [3.3] can be fulfilled with negative values of p (Figure 3.4) but also with the specific value of $p = 0$ ($p = 0, \pm1, \pm2, \ldots, \pm\infty$.). When the electrical length is zero, the resonance condition no longer depends on the physical length of the line. This can be helpful to miniaturize resonators. Moreover, as each positive resonant mode has its dual negative resonant mode with similar impedance, dual-band functions can be achieved.

The approach using a CRLH transmission line therefore can give unusual but very interesting properties. These resonators are named ZORs. The first ZOR was proposed by [SAN 03]; it was realized in microstrip configuration. On the basis of the proposed unit cell, a practical application is realized for antennas [ITO 08]. A coplanar waveguide (CPW) has the advantage that the line and the ground plane are located on the same plane, and that it can be easily fabricated at low cost by using a simple lithography process. Some researchers studied and realized ZORs in a CPW technology [LI 07, ZER 10].

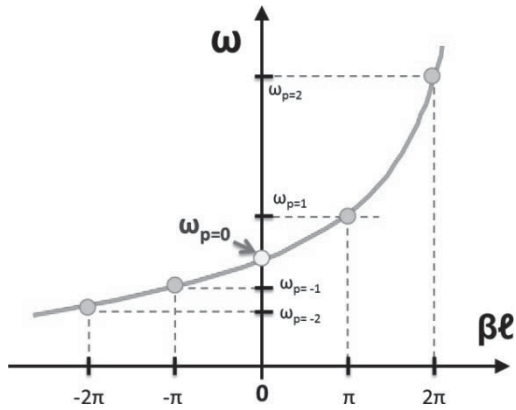

Figure 3.4. *Typical dispersion diagram of a CRLH balanced transmission line. Points on the curve correspond to half wavelength resonance frequencies*

In [SAN 03] and [CAL 03], a microstrip ZOR is realized with seven unit cells (see Figure 3.5(a)). The zero order of resonance is shown in the figure. The authors show that this special resonance does not depend on the number of cells used to make the resonator. With a study of the field repartition along the line, the authors also show that each peak in the scattering parameter S_{21} can be related to its corresponding order. In [LI 07], a ZOR with capacitive coupling is realized, based on a CPW loaded by three cells that cause the left-handed effects (Figure 3.5(b)). The objective of the work is to synthesize a band-pass filter with compact size, using the CRLH approach. The proposed design of the unit cell gives an unbalanced CRLH line (left-handed band from 3 to 4.7 GHz, band gap from 4.7 to 5.8 GHz and right-handed band from 5.8 to 9 GHz). The authors are only interested in the zeroth-order resonance, so the central frequency of the band-pass filter is set to 5.8 GHz. The three cells give a third-order Chebyshev response (Figure 3.5(b)). The size of the proposed filter is reduced (more than 60%) as compared to a conventional device. In [ZER 10, ZER 11], a CPW ZOR designed on alumina substrate is proposed. The series capacitance is composed of an interdigital capacitor and the parallel inductance is obtained with a short-circuited stub inductor. In the case presented, the coupling is inductive. Measurement results are shown in Figure 3.5(c). The resonator has a band-pass filter response of approximately 1.6 GHz with a 3 dB bandwidth of 17%. It can be noted that the phase value of the transmission coefficient for the central frequency is zero. In this case, the reduction of the size is more than 70%, including the access tapers.

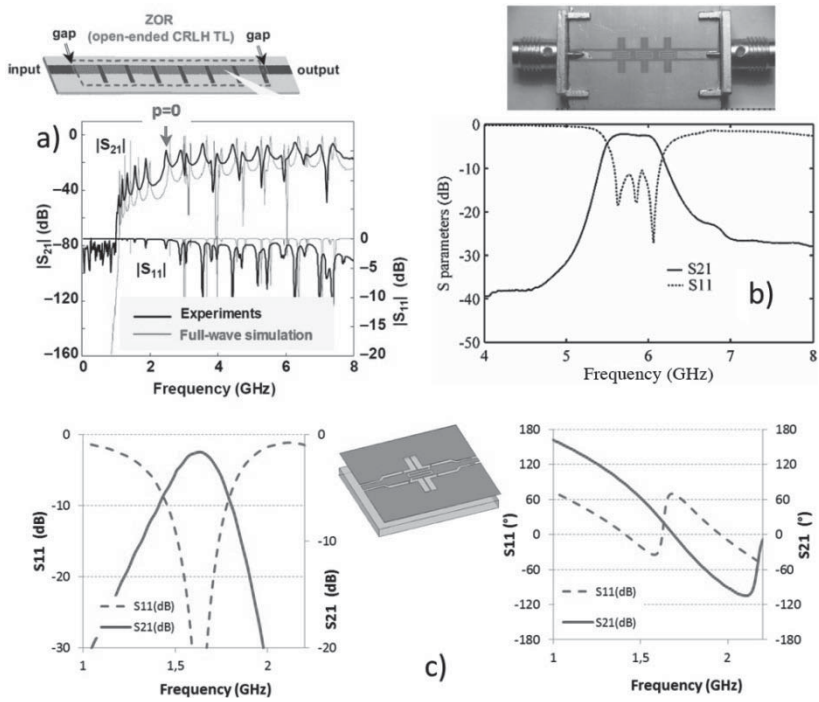

Figure 3.5. *Response of several ZOR. a) Microstrip ZOR with seven unit S parameters with respect to frequency for cells [SAN 03]. The order zero is pointed out on the transmission. b) CPW ZOR with capacitive coupling based on an unbalanced MetaLine with three unit cells [LI 07]. Measured response of the created band-pass filter. c) Measured results of a CPW ZOR with inductive coupling with a single cell [ZER 10]. Measured results: left: values (dB) of transmission and reflection coefficients; right: phase of transmission and reflection coefficients.*

The example of the ZOR component shows the potentialities of MetaLines. In this component, the obtained functionality is unique since only MetaLines can achieve the condition $\beta = 0$ at a non-zero frequency.

3.3. Metamaterials for antennas at microwave frequencies

Since metamaterials can propose an equivalent medium with electric and magnetic characteristics beyond the properties of readily available materials, their capacity to enhance the performances of antennas, namely in terms of miniaturization, bandwidth, efficiency and directivity, is sought. Although

many metamaterial antennas can be found in the literature for applications such as directivity enhancement [OUR 06, GER 13], one of the most appealing and challenging applications is antenna miniaturization.

3.3.1. *Antenna miniaturization*

The requirements of current and future telecommunications systems involve miniaturized devices. Miniaturization of antennas without deterring radiation performances is a real challenge. There are indeed fundamental limitations on the radiating performances of electrically small antennas (ESAs) and studies on these limitations can be traced back to Chu's and Wheeler's work [CHU 48, WHE 47] and were revisited more recently [MCL 96, YAG 05]. The minimum radiation quality factor Q of a vertically polarized omnidirectional antenna within a spherical surface of radius r is given by [MCL 96]:

$$Q = \frac{1}{(kr)^3} + \frac{1}{kr} \qquad [3.4]$$

where k is the wave number for the corresponding operating frequency. Equation [3.4] gives an indication of the maximal fractional bandwidth (1/Q) and radiation efficiency that can be obtained for an antenna size at a given frequency. For ESAs, the bandwidth and the radiation resistance shrink and the efficiency is decreased. The advent of metamaterials raised the hope that these limitations might be abrogated. These limitations have indeed been re-examined more recently to consider the potential contributions of metamaterial.

3.3.2. *Efficient electrically small antennas with metamaterials*

Sohl *et al.* [SOH 07a] demonstrate, using the forward dispersion relation for the extinction cross-section [SOH 07b], that ESAs consisting of metamaterial media are of limited use to overcome radiation fundamental limitations. However, Ziolkowski *et al.* [ZIO 07] show from both analytical and numerical results that the presence of homogeneous, isotropic metamaterials around an ESA such as an infinitesimal dipole presenting either a negative refractive index [ZIO 03] or a negative permittivity [ZIO 06] can improve the radiation efficiency beyond the limitation described in [3.4].

There have been, in the microwave antenna community, several approaches to achieve ESA by an appropriate packing of resonant antenna elements into the antenna volume using natural geometrical configurations [BES 04]; fractal curve antenna [WER 03] is used to reach performances beyond the fundamental limitations. Along the same lines, a metamaterial shell of negative permittivity can improve the radiated power of an infinitesimal electric dipole. Ziolkowski *et al*. [ZIO 06] considered an electric dipole in enclosed in a metamaterial shell [Figure 3.6(a)] of inner radius, $r_1 = 10$ mm of real permittivity, and realistic values of loss tangent, $\epsilon_r = -3$. The radiated power ratio (RPR) is calculated for this metamaterial shell dipole for an input current of 1 A:

$$RPR = 10\log_{10}\left(\frac{P_{with\ metamaterial}}{P_{without\ metamateril}}\right) \text{ in dB} \qquad [3.5]$$

and shown in Figure 3.6(b). A peak value of RPR is obtained for an outer shell radius of 18.79 mm. The high values of RPR even when a loss tangent is considered show the potential of metamaterials to improve the radiated power of small dipoles.

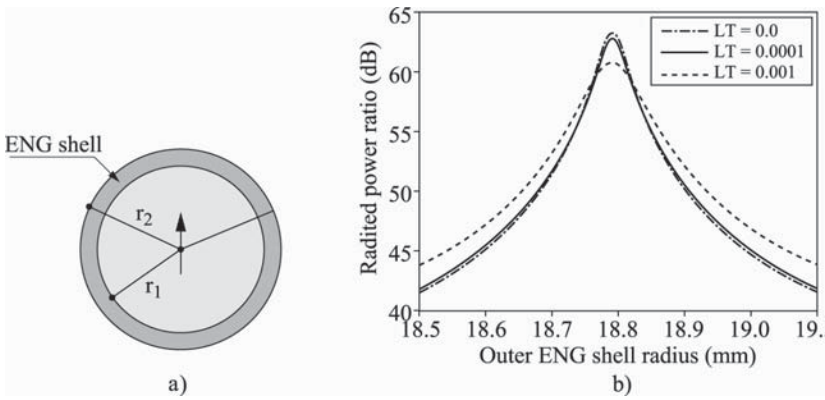

Figure 3.6. *a) Electric dipole enclosed in a shell ($r_1 = 10$ mm) made up of metamaterial of frequency-independent negative permittivity (ϵ_r),). b) Associated radiated power ratio for different values of loss tangent of the permittivity (LT) of the metamaterial shell [ZIO 06]*

More realistic values of permittivity of the metamaterial shell accounting mainly for dispersion have been considered in [ZIO 07] and dispersion-related limits have been defined. If these solutions for efficient ESA are very

interesting, realization can prove to be much harder: sub-wavelength low-loss unit cells have yet to be designed and assembled to realize a bulk metamaterial.

On the basis of these studies and to ensure practical realizations, a novel approach has been proposed by Erentok *et al.* [ERE 08]. The authors propose to insert a single designed metamaterial inclusion as a parasitic element in the extreme near-field of an ESA to enhance the input impedance matching and radiation efficiency. The term "metamaterial-inspired antennas" has been coined for this approach to differentiate it from "metamaterial-based antennas" where bulk homogeneous metamaterials are considered.

3.3.3. *Patch antenna miniaturization considering metamaterial substrate*

Hansen *et al.* [HAN 00] consider the potential of metamaterials for the miniaturization of patch antennas with improved radiating performances. Let us consider a square metallic patch antenna printed on a magneto-dielectric substrate with electromagnetic characteristics (ϵ_r, μ_r). If the values of the permittivity ϵ_r or the permeability μ_r are increased, the patch dimensions get smaller for identical operating frequencies. However, it is difficult to guess how the bandwidth and radiating performances change. Since metamaterials can be designed to present arbitrary values of ϵ and μ, a physical understanding of the role or each parameter is essential. Hansen *et al.* propose a zero-order approach to draw simple rules. A transmission line analysis and cavity model are used; the bandwidth of a square patch antenna is given by:

$$BW = \frac{96\sqrt{\frac{\mu_r}{\epsilon_r}}\frac{t}{\lambda_0}}{\sqrt{2}(4+17\sqrt{\mu_r\epsilon_r}} \qquad [3.6]$$

where λ_0 is the operating wavelength and ϵ_r and μ_r are, respectively, the permittivity and permeability of the substrate on which the square patch antenna is printed. Equation [3.6] is valid for values of $\epsilon_r\mu_r$ extending from 1 to 10. First, the authors can conclude that a significant bandwidth improvement together with patch shortening results only when μ_r is large and ϵ_r is close to one. Second, unlike high values of ϵ_r, increasing μ_r results in smaller patch antennas together without decreasing the bandwidth. These results have been confirmed in other works [NIA 11]. The radiation

efficiency for square patch antennas of width W printed on lossy magneto-dielectric substrate of thickness *d* is given by [NIA 11]:

$$\eta_{rad} = \frac{1}{\frac{\tan\delta_\epsilon \tan\delta_\mu}{240\,G}\frac{W}{d}\sqrt{\epsilon_r/\mu_r}} \qquad [3.7]$$

where G is the radiation conductance of a patch antenna. The efficiencies calculated from equation [3.6] and simulated for a patch antenna printed on a dielectric and magnetic substrate are shown in Figures 3.7(a) and (b), respectively.

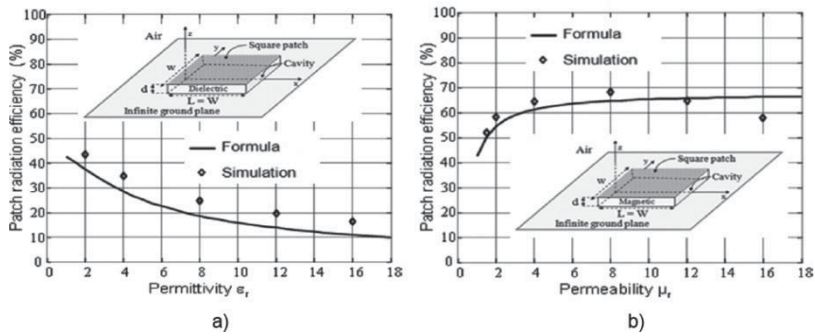

Figure 3.7. *a) Radiation efficiency for a patch antenna for* $\epsilon_r = [1-16]$, $\mu_r = 1$ *, tan* $\delta_\epsilon = 0.05$ *and tan* $\delta_\mu = 0, b)$ *Radiation efficiency for a patch antenna for* $\mu_r = [1-16]$, $\epsilon_r = 1$, *tan* $\delta_\epsilon = 0$ *and tan* $\delta_\mu = 0.05$ *[NIA 11]*

The radiation efficiency for magneto-dielectric antennas is indeed greater for high-permeability substrates compared to high-permittivity substrates.

3.3.4. *Miniature metamaterial antennas: numerical and experimental attempts*

At quite low frequencies, magnetic materials can be useful to provide permeability with reasonable losses. Mosallaei *et al*. [MOS 04a] proposed an antenna with a metamaterial substrate made up of a stack of magnetic and dielectric materials as shown in Figures 3.8(a) and (b). The metamaterial antenna was then studied by a numerical model based on the finite-difference time-domain (FDTD) technique. The resulting reflection coefficient of the metamaterial antenna is shown Figure 3.8(c). It is compared to a reference

patch antenna of identical size on a dielectric substrate of permittivity adjusted to yield the same resonance frequency. The bandwidth enhancement is shown to be relatively high. Moreover, the radiation pattern shown in Figure 3.8(d) confirms that no distortion is induced by the metamaterial substrate.

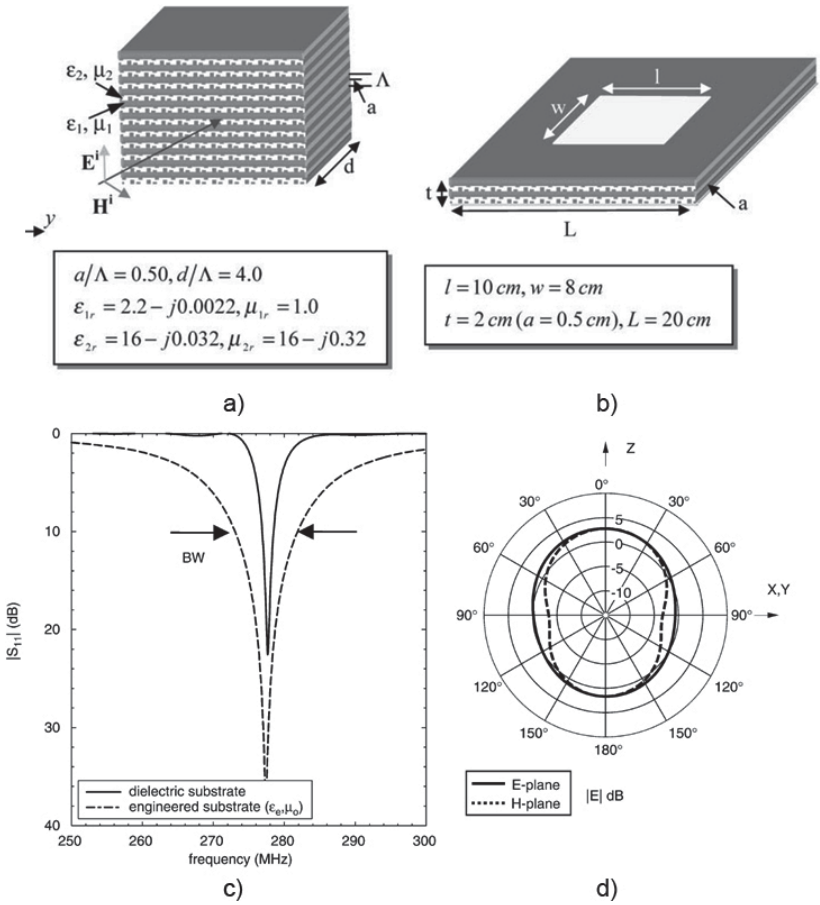

Figure 3.8. *a) Bulk periodic metamaterial. b) Patch antenna with metamaterial substrate. c) Reflection coefficient of the metamaterial antenna and the reference antenna with respect to frequency. d) Radiation pattern of the metamaterial antenna for the E and H planes [MOS 04a]*

At higher frequencies when low-loss magnetic materials are not readily available, artificial magnetic metamaterial can be useful. The effect of artificial magneto-dielectric substrates on the impedance bandwidth properties of patch antennas has been evaluated [KAR 05, IKO 06] both numerically and experimentally. The effective permittivity and permeability of the metamaterial are shown in Figure 3.9(a). The artificial magnetic metamaterial is described in Figure 3.9(b). The real part of the permeability shows a resonance (2.3 GHz) as expected for a metamaterial consisting of split-ring resonators. This metamaterial is then used as the substrate of a patch antenna as shown in the inset of Figure 3.9(a). The measured reflection coefficient of the patch antenna with metamaterial substrate is shown in Figure 3.9(c).

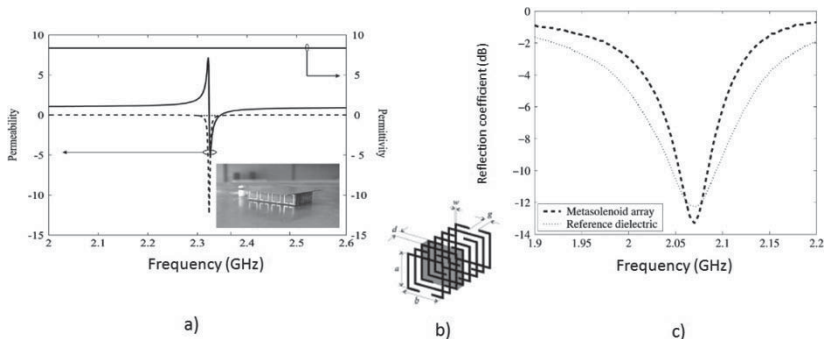

Figure 3.9. *a) Permittivity and permeability of the metamaterial with respect to frequency. The dashed lines represent the imaginary part and solid lines represent the real parts. The inset shows an image of the antenna with the metamaterial substrate. b) Schematic of the metasolenoid metamaterial. c) Reflection coefficient of the metamaterial and reference antenna with respect to frequency [IKO 06]*

The bandwidth of the metamaterial is shown to be smaller than the reference dielectric antenna. The authors demonstrate that this is due to the dispersive behavior of the permeability. These results demonstrate the limits of this approach to miniaturize patch antennas.

Frequency dispersion, high value of losses and fabrication issues make bulk metamaterials less appealing for antenna miniaturization applications. Surfaces made up of metamaterials have been proposed for patch antenna miniaturization. For instance, reactive impedance metamaterial surfaces have been studied [MOS 04b]. The metamaterial is shown in Figure 3.10(a) and the corresponding surface impedance is shown in Figure 3.10(b). This

metamaterial is termed reactive impedance metamaterial since its real part of the effective impedance is zero such that the magnitude of the reflection coefficient is equal to one and its phase is different from π as for metallic surfaces. Figure 3.10(c) shows the metamaterial antenna designed and fabricated and its reflection coefficient is shown in Figure 3.10(d).

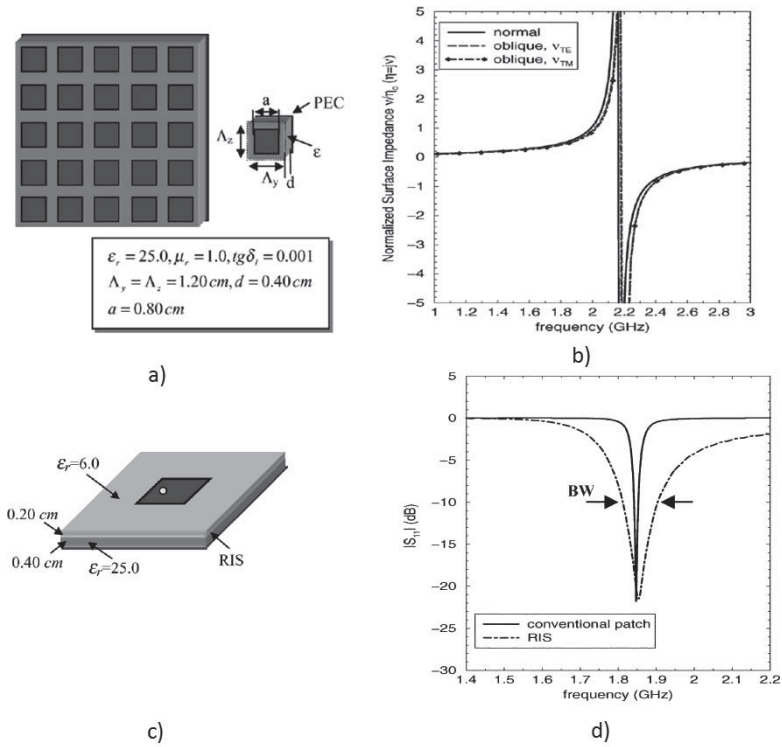

Figure 3.10. *a) Metamaterial reactive impedance surface. b) Normalized surface impedance with respect to frequency. c) Patch antenna on a reactive impedance substrate. d) Reflection coefficient with respect to frequency for a conventional patch antenna and the reactive impedance metamaterial antenna*

Compared to a conventional antenna of same surface and resonating at the same frequency, the bandwidth is much higher. The antenna is miniature (almost $\frac{\lambda}{10}$). The measured bandwidth is 6.7% and the radiation efficiency is 90%. These results are very promising for antennas based on metamaterial surfaces.

3.4. Conclusion

The application and interest of metamaterials for both radiative and non-radiative applications have been described. In non-radiative applications, metamaterials can lead to filter and transmission line miniaturization, multiband operation, as well as bandwidth improvement. For antennas, the challenging topic of radiating element miniaturization without deterring the performances has been tackled. The potential of metamaterials to overcome fundamental limitations on the performances of antennas, namely size, with respect to efficiency has been discussed. Theoretical, analytical and numerical models, as well as experimental attempts, have been described and analyzed.

3.5. Bibliography

[ANT 05] ANTONIADES M.A., ELEFTHERIADES G.V., "A broadband series power divider using zero-degree metamaterial phase-shifting lines", *Microwave and Wireless Components Letters*, vol. 15, no. 11, pp. 808–810, November 2005.

[BES 04] BEST S.R., "The radiation properties of electrically small folded spherical helix antennas", *IEEE Transactions on Antennas and Propagation*, vol. 52, no. 4, pp. 953–960, April 2004.

[CAL 03] CALOZ C., SANADA A., ITOH T., "Microwave circuits based on negative refractive index material structures", *Gallium Arsenide Applications Symposium (GAAS 2003)*, Munich, 6–10 October 2003.

[CHU 48] CHU L.J., "Physical limitations of omnidirectional antennas", *Journal of Applied Physics*, vol. 19, pp. 1163–1175, December 1948.

[ERE 08] ERENTOK A., ZIOLKOWSKI R.W., "Metamaterial-inspired efficient electrically small antennas", *IEEE Transactions on Antennas and Propagation*, vol. 56, pp. 691–707, March 2008.

[GER 13] GERMAIN D., SEETHARAMDOO D., BUROKUR S.N., *et al.*, "Thin conformal directive Fabry–Pérot cavity antenna", *Antennas and Wireless Propagation Letters*, vol. 12, pp. 926–929, 2013.

[GIL 07] GIL M., BONACHE J., GIL I., *et al.*, "Miniaturisation of planar microwave circuits by using resonant-type left-handed transmission lines", *Microwaves, Antennas and Propagation*, vol. 1, no. 1, pp. 73–79, February 2007.

[HAN 00] HANSEN R.C., BURKE M., "Antennas with magneto-dielectrics", *Microwave and Optical Technology Letters*, vol. 26, pp. 75–78, July 2000.

[IKO 06] IKONEN P.M.T, MASLOVSKI S.I., SIMOVSKI C.R., *et al.*, "On artificial magnetodielectric loading for improving the impedance bandwidth properties of microstrip antennas", *IEEE Transactions on Antennas and Propagation*, vol. 54, no. 6, pp. 1654–1662, June 2006.

[ITO 08] ITOH T., RENNING A., "CRLH metamaterial leaky-wave and resonant antennas", *IEEE Antennas and Propagation Magazine*, vol. 50, pp. 25−39, 2008.

[KAR 05] KARKKAINEN M., ERMUTLU M., MASLOVSKI S., *et al.*, "Numerical simulations of patch antennas with stacked split-ring resonators as artificial magnetic substrates", *IEEE International Workshop on Antenna Technology: Small Antennas and Novel Metamaterials, 2005 (IWAT 2005)*, Singapore, pp. 395–398, 7–9 March 2005.

[LAI 04] LAI A., CALOZ C., ITOH T., "Composite right/left-handed transmission line metamaterials", *IEEE Microwave Magazine*, vol. 5, no. 3, pp. 34–50, September 2004.

[LI 07] LI C., LIU K.Y., LI F., "Analysis of composite right/left-handed coplanar waveguide zeroth-order resonators with application to a band-pass filter", *PIERS Online*, vol. 3, no. 5, pp. 599–602, 2007.

[LIN 04] LIN I.H., DE VINCENTIS M., CALOZ C., *et al.*, "Arbitrary dual-band components using composite right/left-handed transmission lines", *IEEE Transactions on Microwave Theory and Techniques*, vol. 52, pp. 1142–1149, April 2004.

[LIU 08] LIU C., MENZEL W., "Broadband via-free microstrip balun using metamaterial transmission lines", *Microwave and Wireless Components Letters*, vol. 18, no. 7, pp. 437–439, July 2008.

[MCL 96] MCLEAN J.S., "A re-examination of the fundamental limits on the radiation Q of electrically small antennas", *IEEE Transactions on Antennas and Propagation*, vol. 44, pp. 672–676, May 1996.

[MOS 04a] MOSALLAEI H., SARABANDI K., "Magneto-dielectrics in electromagnetics: concept and applications", *IEEE Transactions on Antennas and Propagation*, vol. 52, no. 6, pp. 1558–1567, June 2004.

[MOS 04b] MOSALLAEI H., SARABANDI K., "Antenna miniaturization and bandwidth enhancement using a reactive impedance substrate", *IEEE Transactions on Antennas and Propagation*, vol. 52, no. 9, pp. 2403–2414, September 2004.

[NIA 11] NIAMIEN C., COLLARDEY S., SHARAIHA A., *et al.*, "Compact expressions for efficiency and bandwidth of patch antennas over lossy magneto-dielectric materials", *Antennas and Wireless Propagation Letters*, vol. 10, pp. 63–66, 2011.

[OUR 06] OURIR A., DE LUSTRAC A., LOURTIOZ J.-M., "All-metamaterial-based subwavelength cavities (λ/60) for ultrathin directive antennas", *Applied Physics Letters*, vol. 88, no. 8, pp. 08103-(1–3), February 2006.

[SAN 03] SANADA A., CALOZ C., ITOH T., "Novel zeroth-order resonance in composite right/left-handed transmission line resonators", *Asia Pacific Microwave Conference*, vol. 3, Seoul, Korea, pp. 1588–1591, November 4–7 2003.

[SIS 08] SISO G., GIL M., BONACHE J., Martin F., "Applications of resonant-type metamaterial transmission lines to the design of enhanced bandwidth components with compact dimensions", *Microwave and Optical Technology Letters*, vol. 50, no. 1, pp. 127–134, January 2008.

[SOH 07a] SOHL C., GUSTAFSSON M., KRISTENSSON G., "Physical limitations on antennas—isoperimetric inequalities and the effect of metamaterials", *19th International Conference on Applied Electromagnetics and Communications (ICECom 2007)*, Dubrovnik, Croatia, pp. 1–5, September 24–26 2007.

[SOH 07b] SOHL C., GUSTAFSSON M., KRISTENSSON G., "Physical limitations on broadband scattering by heterogeneous obstacles", *Journal of Physics A: Mathematical and Theoretical*, *vol.* 40, pp. 11165–11182, 2007.

[VÉL 11] VÉLEZ A., SISÓ G., CAMPO A., *et al.*, "Dual-band microwave duplexer based on spiral resonators (SR) and complementary split ring resonators (CSRR)", *Journal of Applied Physics A*, vol. 103, no. 3, pp. 911–914, 2011.

[WER 03] WERNER D.H., GANGULY S., "An overview of fractal antenna engineering research", *IEEE Antennas and Propagation Magazine*, vol. 45, no. 1, pp. 38–56, February 2003.

[WHE 47] WHEELER H.A., "Fundamental limitations of small antennas", *Proceedings of the IRE,* vol. 35, pp. 1479–1484, December 1947.

[YAG 05] YAGHJIAN A.D., BEST S.R., "Impedance, bandwidth, and Q of antennas", *IEEE Transactions on Antennas and Propagation*, vol. 53, pp. 1298–1324, April 2005.

[ZER 10] ZERMANE A., SAUVIAC B., BAYARD B., *et al.*, "Modeling and measurement of a zeroth-order-resonator and a composite right-left-handed transmission line in coplanar technology", *Progress in Electromagnetic Research C*, vol. 14, pp. 33−43, 2010.

[ZER 11] ZERMANE A., Contribution à l'étude et la faisabilité de micro-résonateurs en structures planaires, PhD Thesis, University of Saint-Etienne, July 2011.

[ZIO 03] ZIOLKOWSKI R.W., KIPPLE A., "Application of double negative metamaterials to increase the power radiated by electrically small antennas", *IEEE Transactions on Antennas and Propagation*, vol. 51, pp. 2626–2640, October 2003.

[ZIO 06] ZIOLKOWSKI R.W., ERENTOK A., "Metamaterial-based efficient electrically small antennas", *IEEE Transactions on Antennas and Propagation*, vol. 54, pp. 2113–2118, July 2006.

[ZIO 07] ZIOLKOWSKI R.W., ERENTOK A., "At and below the Chu limit: passive and active broad bandwidth metamaterial-based electrically small antennas", *IET Microwave, Antennas and Propagation*, vol. 1, pp. 116–128, 2007.

Chapter 4

Toward New Prospects for Electromagnetic Compatibility

4.1. Introduction

Studies in electromagnetic compatibility (EMC) are mainly based on the unintentional generation, propagation and reception of electromagnetic (EM) waves with respect to undesired effects that may be induced such as EM interference (EMI). A common viewpoint of EMC, originating from the number of practical problems challenging engineers in all fields related to electromagnetism, is that it is based on a collection of recipes and rules of thumb relying on theory and practical experience [CHR 07]. These recipes do indeed work within given limits and under certain circumstances. However, with the growing complexity of both the current systems and the surrounding EM environments in which they should function, understanding and analyzing predominant EM interactions is important. Modeling and designing systems by taking into account EMC constraints at design level is becoming popular. The need for EMC depends not only on the fact that the system has to function satisfactorily but also on the compliance with standards fixing the limits of emission or immunity for various classes of apparatus and systems [CHA 05]. Strict regulations together with the growing complexity of systems and EM environments call for new technological solutions in EMC engineering. In this context, recent advances in the field of wave–matter interaction suggest that metamaterials that are designed to present chosen EM

Chapter written by Divitha SEETHARAMDOO.

properties for given applications should provide an additional degree of freedom to solve EMC problems related to state-of-the-art systems.

This chapter focuses on the potential of metamaterials in EMC applications. It is organized as follows. In section 4.2, a short overview of EMC is given. To highlight the relevance of metamaterials in EMC problems, current trends in industrial applications as well as the consequent challenges arising in EMC are described. The cases of the transport and telecommunications industries are considered. The two main applications envisaged are filtering and shielding. Section 4.3 focuses on EM shielding. The performance of shields depends on both their geometric and electrical parameters, and on the characteristics of the incident EM field. Figures of merit to evaluate these performances are given. Examples of three published one-dimensional (1D) metamaterial shields based on reflection or absorption are given. In section 4.4, a detailed analysis of a three-dimensional (3D) metamaterial cavity is proposed. The contribution of metamaterials is highlighted in the concept of subwavelength cavities. The design steps of an appropriate metamaterial for this particular application are given. Finally, the metamaterials designed are applied to the walls of a regular reverberation chamber (RC) generally used for EMC tests.

4.2. Electromagnetic compatibility

EMC is the ability of a piece of equipment or a system to function satisfactorily in its EM environment without introducing intolerable EM disturbances to anything in that environment. In certain parts of the spectrum, a strict international regulatory framework has been set up to ensure the immunity of equipment to EMI. Equipment, such as electronic devices for information technology, vehicles or engineering systems, both emit EM disturbances (behaving as EMI sources) and are subject to external EM fields (Figure 4.1(a) and (b)).

Figure 4.1. *Electromagnetic compatibility of an IT electronic device from an interference source and victim point of view. a) Electromagnetic interference (EMI): EM noise emission and b) electromagnetic susceptibility or immunity to noise*

A given system or device should not emit EM disturbances more than the levels determined in limits established by regulatory bodies, and at the same time it should be able to withstand an expected level of EM disturbances from various sources of transient phenomena and continuous radio frequency phenomena that are present in its intended *EM environment*. EMI sources can be classified as natural (lightning and low-frequency electric and magnetic fields), man-made (switching transients, fault surges, etc.) as well as intentional and non-intentional sources. The basic mechanisms by which the EMI source affects the victim are termed *coupling mechanisms*. The main coupling mechanisms include far-field radiation, near-field coupling (inductive and capacitive) and conduction.

EMC engineering mainly focuses on four main fields. The first challenge is the determination of potential EMI sources of the environment. The understanding of the coupling mechanisms by which the device can be affected by these EMI sources is the second challenge that can be solved by simple to complex analytical numerical models. The third challenge is the testing of these devices according to standards defined by regulatory bodies, thus ensuring interchangeability and compatibility between devices. Finally, the last challenge is the design of components such as filters and shields to enhance the immunity of devices and systems and reduce their emission levels.

Current trends in EMC engineering promote the consideration of EMC constraints on a given system from the design level. Indeed, product development processes tend to neglect EMC constraints, thus resulting in a longer time to market, either when the products do not comply with standards or when the proper operation of the system is not achieved despite complying with standards. Identifying the possible interference sources in the environment as well as the most probable coupling mechanisms because of the modeling approaches is, for instance, one of the solutions considered. Research in EMC is also driven by trends in industries such as the transport and telecommunications industries, to name but a few. These trends and the consequent EMC challenges are briefly described in sections 4.2.1 and 4.2.2, respectively.

4.2.1. *Trends in the transport and telecommunications industries*

In the transport industry, advances in the field of mechanics, thermal and material engineering have led to the use of novel composite materials in the manufacture of vehicle bodies. Indeed, the quest to decrease the weight of

vehicles and the cost of maintenance, as well as to optimize energy consumption, has resulted in an increasing acceptance in the replacement of metal crafts by composites. Figure 4.2(a) depicts an example of a railway car body in composite developed by Voith Turbo Scharfenberg. The existing heavy steel systems have been replaced by a lightweight structure mainly from fiber composite materials [INN 12]. In the field of aeronautical engineering, the same strategy has been adopted and the Boeing 787 Dreamliner shown in Figure 4.2(b) is the world's first major long-range airliner to use composite materials as the primary material in the construction of its airframe [NOR 09].

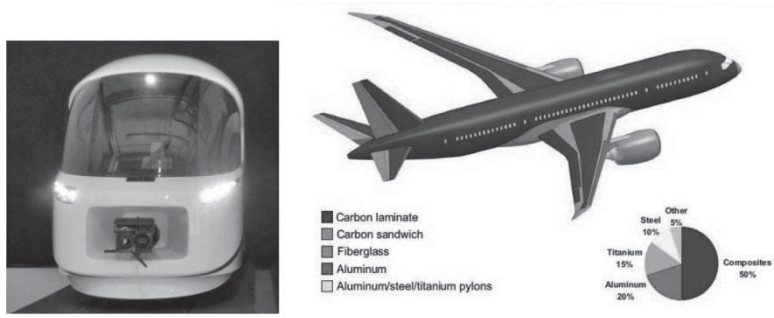

Figure 4.2. *a) Railway vehicle head GALEA developed for intercity passenger trains by Voith Turbo Scharfenberg and presented at InnoTrans 2012 [INN 12]. This lightweight vehicle structure is made mainly from fiber composite materials. b) Boeing 787 Dreamliner, the first long-range airliner to use at least 50% of composite in its airframe. The pie chart and color codes give the material composition of the frame of the plane [NOR 09]*

In the telecommunications industry, nomad devices are more and more common – these devices should be as small and light as possible. This results in a miniaturization of communication systems as well as strong collocation due to the multiplication of systems (Wi-Fi, global positioning system (GPS), global system for mobile communications (GSM), etc.).

4.2.2. *EMC challenges induced by recent industrial trends – metamaterials for EMC*

In the railway industry, as far as rolling stock vehicles are concerned, the definition of needs and EMC constraints has up to now been based on

characteristic features of metallurgical work [CAM 06]. Nowadays, the introduction of composites having lower conductivity than metals has resulted in poorer shielding of sensitive devices from EM pollution. In the aeronautical industry, lower conductivity of the airframe due to the use of composites creates challenges for shielding in the case of lightning. Since metamaterials are actually designed to control the flow of EM waves, we believe they should be able to provide solutions to these problems.

More generally in all fields of transport, the nature of EM pollution is changing and protecting sensitive systems is getting more and more difficult. For instance, if we consider the evolution in technologies used in high power electronics, EM pollution is now defined by broadband transients that can reach telecommunications frequencies.

Moreover, in the telecommunications industry, high integration, miniaturization and multiplication of the number of collocated systems call for new solutions in terms of *shielding* and *filtering*. Indeed, metamaterials provide a higher degree of freedom for design since the flow of EM waves is considered and specific application-oriented designing of the metamaterial can be performed. Moreover, coupled to advances in numerical modeling, metamaterials should be able to enable the EMC considerations at design level. The potential of metamaterials for filtering applications has been described in Chapter 3. Shielding applications are detailed in section 4.3.

4.3. Electromagnetic shielding – potential of metamaterials

There are several strategies involved in basic shielding mechanisms. The most commonly used strategies are one of the following or a combination of them [CEL 08]:

– Adding an obstacle between the source and the volume to be protected.

– Introduction of a medium capable of diverging the EM field from the volume to be protected.

– Introduction of an additional source whose effect is the reduction of the EM field levels in the volume to be protected.

Divergence of the EM field from the volume to be protected is typically realized by highly conducting media or magnetic materials. In this context, cloaking mechanisms (described in Chapter 6) based on the use of metamaterials can propose good solutions for shielding. Adding an obstacle

is particularly effective in reducing the EM field levels when the shield is characterized by constitutive parameters resulting in a high level of attenuation of the field propagating through the shield.

4.3.1. *Figures of merit for shielding configurations*

The definition of adequate figures of merit for shielding configurations is important in setting up analysis and design problems and in comparing the performance of existing shielding structures. There is no consensus in the definition of the effectiveness of shielding configurations [BUT 97]. In the following, a few figures of merit such as the local, global and statistical shielding effectiveness as well as their relevance for metamaterial shielding configurations will be discussed.

The local shield effectiveness is defined as the ratio between the absolute value of the electric $\vec{E}(\vec{r})$ or magnetic field $\vec{H}(\vec{r})$ present at a given point $\vec{r}$ in the presence or absence of a given shield [IEE 07]:

$$\mathrm{SE}_{\mathrm{eletrical}} = 20\log\frac{|\overrightarrow{E_{inc}}(\vec{r})|}{|\vec{E}(\vec{r})|} \qquad [4.1]$$

$$\mathrm{SE}_{\mathrm{magnetic}} = 20\log\frac{|\overrightarrow{H_{inc}}(\vec{r})|}{|\vec{H}(\vec{r})|} \qquad [4.2]$$

For plane waves incident on planar shields, $\mathrm{SE}_{\mathrm{electrical}}$ and $\mathrm{SE}_{\mathrm{magnetic}}$ are identical. If metamaterials are considered, the reflection and transmission coefficients as well as the absorption factor can be used to evaluate the local shielding effectiveness. Klinkenbusch [KLI 05] proposed a more general expression for the transient shielding effectiveness, SE_T, to consider a transient plane wave with a given spectral density distribution $S(\omega)$:

$$\mathrm{SE}_T = 10\log\frac{2\int_0^\infty |S(\omega)|^2\omega\,d\omega}{\int_0^\infty |S(\omega)|^2\left(\left|\frac{\vec{E}\mathrm{shielded}(\vec{r})}{\vec{E}\mathrm{unshielded}(\vec{r})}\right|^2 + \left|\frac{\vec{H}\mathrm{shielded}(\vec{r})}{\vec{H}\mathrm{unshielded}(\vec{r})}\right|^2\right)\omega\,d\omega} \qquad [4.3]$$

Other figures of merit based on a global point of view and statistical approaches have been proposed and can be used for metamaterial-based structures. Their detailed description lies beyond the scope of this book but can be found in [CEL 08].

4.3.2. *One-dimensional metamaterial shield*

A few examples of metamaterial shields are described in this section. The shielding mechanisms on which they are based rely either on reflection or on absorption. The advantages of using metamaterial shields instead of conventional metallic screens are that they can provide the same reflective properties but with a lower density and reduced weight and they can be designed to exhibit the required frequency-selective properties. In some applications, absorption can be preferred to reflection to limit the level of EM emissions; the transmission coefficient should anyway be minimized at the frequency of interest.

In Figure 4.3 [PON 12, DE 11], a frequency selective surface (FSS) is shown together with the transmission coefficient as a function of frequency for different angles of incidence.

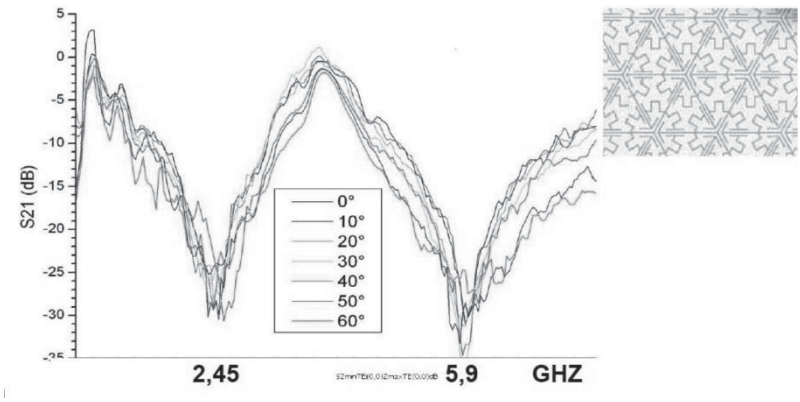

Figure 4.3. *Transmission coefficient with respect to frequency for several incident angles. Inset depicts the frequency selective surface [PON 12]*

The two frequency bands around Wi-Fi frequencies, namely 2.45 and 5.9 GHz, are shielded. The transmission coefficient is minimized and the predominant phenomenon is reflected. This FSS has been proposed for wall paper printing to ensure secure Wi-Fi communications buildings. FSSs are periodic structures consisting of a unit cell designed to resonate at the frequencies of interest. Maximum shielding effectiveness is obtained at this frequency. A complete description of the design principles and analysis of FSS for shielding is beyond the scope of this book but can be found in Chapter 10 of Celozzi *et al*. [CEL 08]. In applications where absorption is

preferred, the use of FSS can become difficult to analyze. However, metamaterials can propose interesting solutions. A metamaterial absorber solution is shown in Figure 4.4 [BIN 09]. The absorbance of the metamaterial is close to unity at the frequency of interest. This is realized because of the resonance of the split-ring.

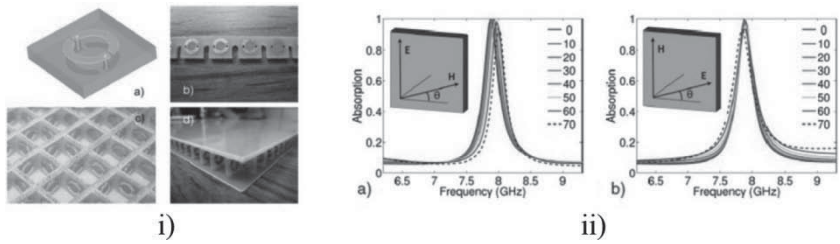

Figure 4.4. *i) Metamaterial unit cell and 3D lattice. ii) Absorption coefficient of the metamaterial lattice for the two polarizations [BIN 09]*

One of the main advantages of using metamaterials is that scalability to much higher frequencies such as in terahertz, where telecommunications applications and devices are proposed, is possible. Figure 4.5 shows an example of such another metamaterial [TAO 08] with an absorption coefficient both in simulation and measurements.

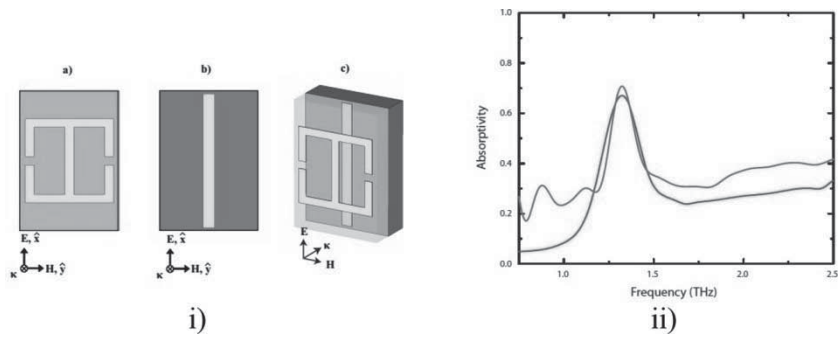

Figure 4.5. *i) Description of the metamaterial unit cell, overview in (c) with the incident wave polarization and detailed description of the split-ring and wire media in (a) and (b). ii) Absorbance as a function of frequency, comparison of simulations and measurement [TAO 08]*

4.4. Metamaterials for 3D shielded cavities – application to electromagnetic reverberation chambers

4.4.1. *General case of a 3D shielded cavity*

A 3D shielded cavity at microwave frequencies generally consists of six reflectors. If perfect reflectors are considered, the reflection coefficient for a given polarization is given by:

$$\frac{E_{ref}}{E_{inc}} = \exp j\phi_{\vec{r}} \qquad [4.4]$$

where $\vec{r} = x\hat{x} + y\hat{y} + z\hat{z}$. The phase $\varphi_{\vec{r}}$ depends on the reflectors used. For common metallic conductors readily found in nature, $\phi_{\vec{r}} = \pi$. Metamaterial surfaces can however be engineered to present a reflection coefficient with an arbitrary phase in the range extending from $-\pi$ to $+\pi$.

Let us consider a 3D cavity of dimensions $L_x \times L_y \times L_z$ consisting of six reflectors having a reflection coefficient of arbitrary phase given by [4.4]. For a transverse magnetic (TM) mode, the general form of the E_z [LI 06] is given by:

$$E_z = \frac{1}{8}\sum_{i=1}^{8} A\left(\overrightarrow{k_\iota}\right) exp(jk_i\vec{r}) exp(j\omega t) \qquad [4.5]$$

where $\overrightarrow{k_\iota} = \pm k_x, \pm k_y, \pm k_z$, ω is the angular frequency and the expansion parameters $A\left(\overrightarrow{k_\iota}\right)$ are determined by matching boundary conditions. For the x-axis, they are defined for the reflector at $x = 0$ and $x = L_x$ by equations [4.6] and [4.7], respectively:

$$\frac{A(k_x,k_y,k_z)\exp(jk_yL_y+jk_zL_z)}{A(-k_x,k_y,k_z)\exp(jk_yL_y+jk_zL_z)} = \exp(j\phi_{-x}), \qquad [4.6]$$

$$\frac{A(-k_x,k_y,k_z)\exp(-jk_xL_x+jk_yL_y+jk_zL_z)}{A(k_x,k_y,k_z)\exp(jk_xL_x+jk_yL_y+jk_zL_z)} = \exp(j\phi_{-x}). \qquad [4.7]$$

Substituting equation [4.6] into equation [4.7] yields the following condition:

$$-2k_xL_x - (\phi_{+x} + \phi_{-x}) = 2m_x\pi. \qquad [4.8]$$

If the two surfaces are metallic reflectors, the phase conditions $\phi_{+x} = \phi_{-x} = \pi$. The condition for resonance is $L_x = \frac{\lambda}{2}$ for $m_x = 0$ and

$L_x = m_x \frac{\lambda}{2}$, which corresponds to the classical electric dimension at resonance for a 1D resonator. To ensure that there is no resonance along the *x*-axis requires $m_x = -1$. Thus, to map m_x onto the mode index of a 3D cavity, $m_x \in \mathbf{Z}$ with $m_x \geq 1$.

The resonance condition along the *x*-axis given by equation [4.8] can also be derived in the same way for the *y*- and *z*- axes. Then, given that:

$$k_x^2 + k_y^2 + k_z^2 = \frac{\omega^2}{c^2} \quad [4.9]$$

c being light velocity, the resonant frequencies of such a 3D cavity can be expressed as:

$$\omega_{mnp} = c \sqrt{\frac{\Delta \phi_x^2}{4L_x^2} + \frac{\Delta \phi_x^2}{4L_x^2} + \frac{\Delta \phi_x^2}{4L_x^2}} \quad [4.10]$$

where the phase difference $\Delta \phi_{x,y,z}$ is defined as:

$$\Delta \phi_{x,y,z} = \phi_{x,y,z} + \phi_{-x,-y,-z} + 2\pi m_{x,y,z}, \quad [4.11]$$

and $m = m_x + 1$, $n = m_y + 1$ and $p = m_z + 1$.

Equation [4.10] can be used to predict the resonant frequencies of a cavity given the phase of the reflection coefficient of each wall. In the case of a perfect metallic 3D cavity, equation [4.10] shows that its resonant frequencies depend only on its physical dimensions, while if an arbitrary value of $\phi_{x,y,z}$ is engineered, the resonant frequencies for characteristic dimensions smaller than $\frac{\lambda_g}{2}$ can be achieved.

4.4.2. *Concept of subwavelength cavities*

The concept of subwavelength cavities based on metamaterials was first suggested to create low-profile antennas [SIE 99]. The concept of a resonant cavity independent of physical dimensions is an attractive approach for any microwave device [ENG 02]. These concepts are often based on the use of a bilayer of material of positive refractive index and negative refractive index. However, high-performance (in terms of bandwidth and losses), negative refractive index metamaterials are difficult to manufacture. In waveguides, metamaterials have also been used to induce wave propagation for frequencies lower than the cutoff frequencies [CAR 06]. In this case, a waveguide under the cutoff frequency is considered as an electric plasma

with negative permittivity and propagation is obtained by coupling this media with a negative permeability one such as a periodic array of split-ring resonators [PEN 99].

An alternative approach based on the use of a cavity with reactive impedance metamaterials (RIMs) on the wall surfaces has been proposed for antennas [MOS 04]. A reflective surface with specific properties is used as ground plane for patch antennas, thus reducing the substrate thickness with respect to a patch antenna backed by a metallic ground plane. This is achieved by engineering the phase of the reflection coefficient of the plate so that resonance occurs for wavelengths smaller than the common $\frac{\lambda_g}{2}$, where λ_g is the guided wavelength in the substrate.

4.4.3. *Design of a metamaterial surface of reflection coefficient with arbitrary phase*

An engineered surface having a reflection coefficient close to 1 and the phase different from π as well as dimensions much smaller compared to the operating wavelength can be termed RIM. Indeed, the phase ϕ of the reflection coefficient is related to the surface impedance Z_s by:

$$\frac{E_{ref}}{E_{inc}} = \exp\{j\phi\} = \frac{Z_s - Z_0}{Z_s + Z_0}, \quad [4.12]$$

where Z_0 is the wave impedance of free space.

The unit cell of such a metamaterial or RIM and its equivalent circuit are shown in Figure 4.6.

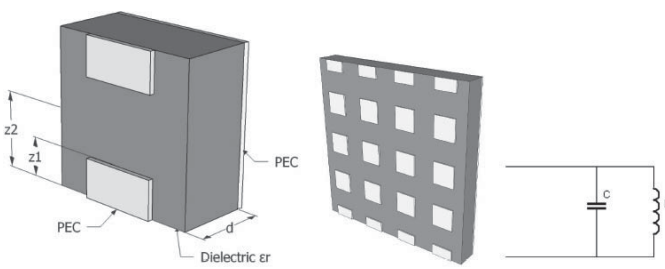

Figure 4.6. *Unit cell of the reactive impedance metamaterial consisting of a metal backed dielectric* (ϵ_r, d) *with two rectangular identical metallic patches, overall two-dimensional view of the periodic RIM and the equivalent circuit representation of the unit cell*

An analytical model can be given for the unit cell of the RIM based on the equivalent circuit described in Figure 4.6. The surface impedance can thus be written as:

$$Z_s = j\frac{X_C X_L}{X_C - X_L}, \quad [4.13]$$

and ϕ, which is the phase of the reflection coefficient, can be written as:

$$\phi = 2\arctan\left(\frac{1}{Z_0}\frac{X_C X_L}{X_C - X_L}\right). \quad [4.14]$$

The phase of the reflection coefficient is plotted for different values of X_L and X_C at the frequency of 100 MHz as shown in Figure 4.7.

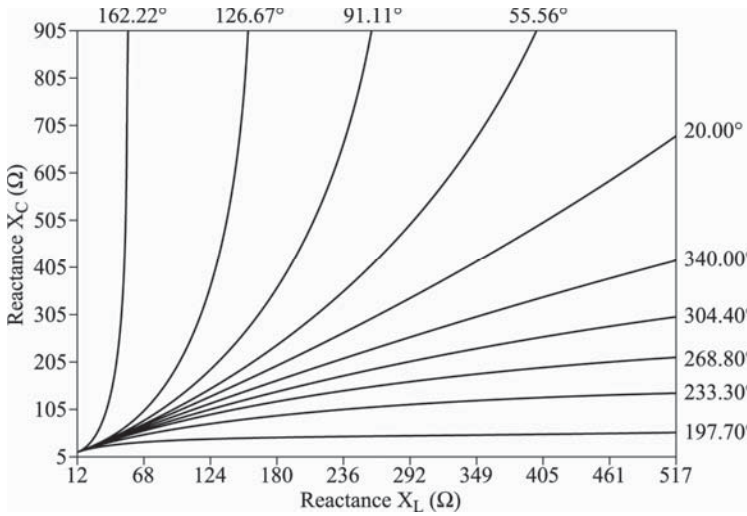

Figure 4.7. *Phase of the reflection coefficient as a function of the inductance and capacitance*

The inductive reactance X_L is given by the dielectric layer and defined as:

$$X_L = \frac{Z_0}{\sqrt{\epsilon_r}}\tan\left(\frac{2\pi f\sqrt{\epsilon_r}}{c}d\right). \quad [4.15]$$

This equation is valid only for plane incident waves and normal incidence. The inductance X_L is plotted as a function of the two parameters: permittivity and substrate thickness (Figure 4.8).

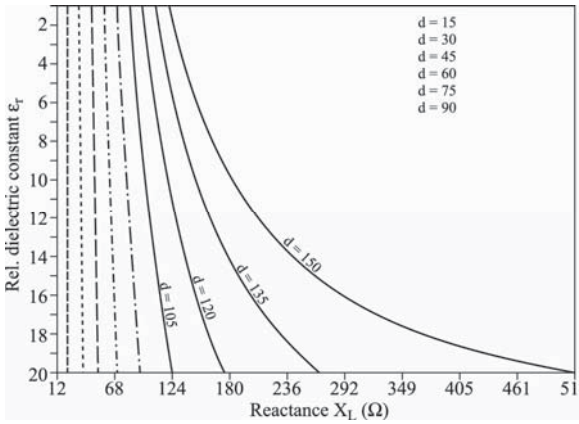

Figure 4.8. *Variation of inductance for different values of dielectric constant and substrate thickness*

The capacitive reactance is given by:

$$X_C = \frac{1}{2\pi f C} \quad [4.16]$$

and an upper estimation of the capacitance C can be calculated by considering the two metal patches as a coplanar stripline; therefore, the capacitance per meter can be given by:

$$C_0 = \frac{\tilde{\epsilon}\, K\left(\sqrt{1-\frac{z_1}{z_2}}\right)^2}{\left(\frac{z_1}{z_2}\right)} \quad [4.17]$$

where K is the complete elliptic integral of the first kind and $\tilde{\epsilon_r}$ is the effective dielectric constant, which should account for the fact that the electric field is distributed partly in the dielectric and partly in the free space:

$$\tilde{\epsilon} = \epsilon_0 \frac{\epsilon_r + 1}{2} \quad [4.18]$$

C_0 must then be multiplied by the length of the patch $a = 2z_1$. It should be noted that finite size edge effects are not taken into account, thus leading to a slightly higher estimation of the capacitance.

The capacitance X_C is plotted as a function of the geometrical parameter defined by the ratio of the length of the square metallic patch to the periodicity of the unit cell of the RIM and the permittivity of the substrate (Figure 4.9).

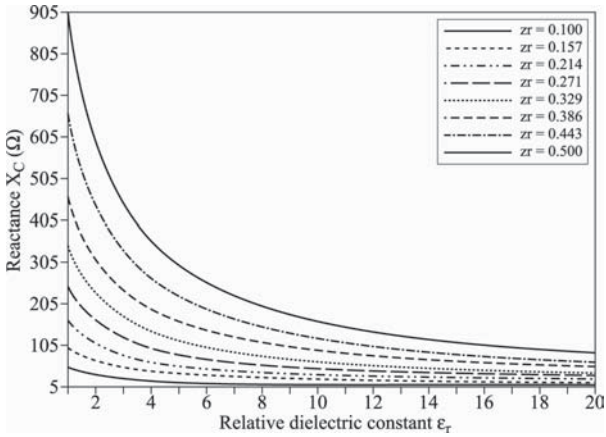

Figure 4.9. *Variation of the capacitance with the dielectric constant and the geometrical parameter z_r ($z_1 = 75$ mm)*

These analytical models provide us with the necessary physical insight and guidelines to design RIMs. The phase of the reflection depends on both geometrical and electrical parameters of the metamaterial. To engineer a subwavelength cavity, from equation [4.10], the value of ϕ required for a given cavity physical dimension at a given frequency has to be calculated. Then, from Figure 4.7, for the calculated value of φ, the corresponding reactances X_C and X_L can be chosen. For the value of X_L retained, ε_r is determined with respect to the parameter *d*. Finally, the capacitive reactance X_C provides the possible values of $z_r = \frac{z_1}{z_2}$ as shown in Figure 4.9.

Let us consider the example of a RIM shown in Figure 4.6 with the parameters defined in Table 4.1.

Dielectric substrate $(\epsilon_r, \tan\delta)$	(10.75, 0)
Geometrical parameter, $z_r = \frac{z_1}{z_2}$	0.5
Substrate thickness, *d* (mm)	130
Conductivity of metallic strips (S.m^{-1})	5.9×10^6

Table 4.1. *Electromagnetic and geometrical parameters of the reactive impedance metamaterial unit cell considered*

The resulting equivalent capacitive and inductive reactances of the metamaterial as well as the phase of its reflection coefficient are presented in Table 4.2 at a frequency of 100 MHz.

Equivalent inductive reactance, X_L (Ω)	143
Equivalent capacitance reactance, X_C (Ω)	159
Phase of reflection coefficient, φ (°)	28

Table 4.2. *Resulting inductive and capacitive reactances and phase of the reflection coefficient given the electromagnetic and geometrical parameters defined in Table 4.1*

The metamaterial described above is also modeled numerically with Floquet-Bloch periodic boundary conditions. Only the first propagation mode is calculated and within a monomodal assumption, the S_{11} parameter can be considered as the complex reflection coefficient. Figure 4.10 shows a comparison of the phase of the reflection coefficient calculated by the numerical and analytical models for a metamaterial defined by the geometrical data presented in Table 4.1.

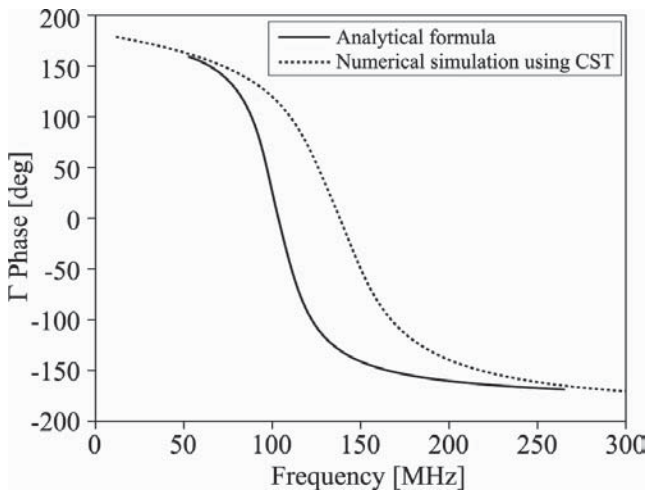

Figure 4.10. *The phase of the designed metamaterial for a metamaterial defined by the data given in Table 4.1*

The results between the two approaches are in quite good agreement except for the resonance frequency. The difference is due to the fact that finite size edge effects were not accounted for in our formula of the total effective capacitance.

This phase variation with frequency of both curves follows the same trend and this variation is very typical for a RIM. Note the interesting points which are the values $\phi = \pm\pi$, representative of a perfect metallic conductor, and $\phi = 0$, which is an artificial magnetic conductor.

4.4.4. *Application of subwavelength metamaterial cavity to reverberation chambers for EMC tests*

The RC is a multimode 3D metallic cavity with its smallest dimension much larger than the operating wavelength at which it provides an EMC test environment exhibiting a statistically homogeneous, isotropic, incoherent and randomly polarized cavity field within acceptable limits. One of the crucial parameters for determining the proper operation of an RC is the lowest usable frequency (LUF). The mode density at lower frequencies is generally dependent on the chamber geometry, quality factor and stirrer effectiveness [CHA 05, ARN 01]. With the aim of increasing the number of cavity modes generated at low frequencies, the use of metamaterials has been proposed [SEE 11b] to create subwavelength intrinsic resonant modes in a cavity.

The principle of subwavelength cavities described earlier can indeed be considered to modify the resonant frequencies of an RC. To illustrate the potential of metamaterials for such applications, three different 3D cavities have been considered as shown in Figure 4.11.

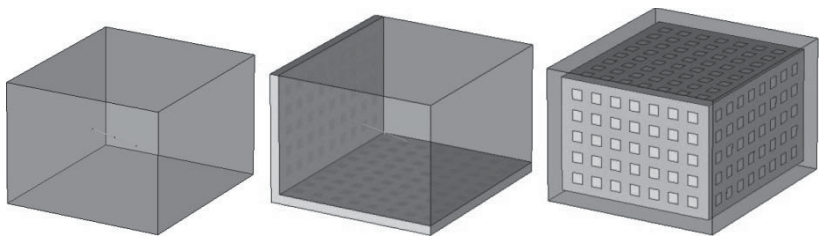

Figure 4.11. *Classical reverberation chamber, reverberation chamber with two metamaterial walls and reverberation chamber with six metamaterial walls*

The dimensions of the RCs considered are $L_x = 2.58$ m, $L_y = 1.90$ m and $L_z = 2.91$ m. The first 100 eigenmodes of the three different RCs are calculated using a finite element eigenmode solver. The approximate number of modes or resonant frequencies, *N*, of a classical six metallic wall RC is given by [HIL 09]:

$$N = \frac{8\pi}{3} L_x L_y L_z \frac{f^3}{c^3} - \left(L_x + L_y + L_z\right)\frac{f}{c} + \frac{1}{2}, \qquad [4.19]$$

where *f* is the frequency and c is the light velocity.

The number of modes evaluated by [4.19] is compared to the numerically calculated eigenmodes of the three RCs with and without metamaterial walls. The results are shown in Figure 4.12.

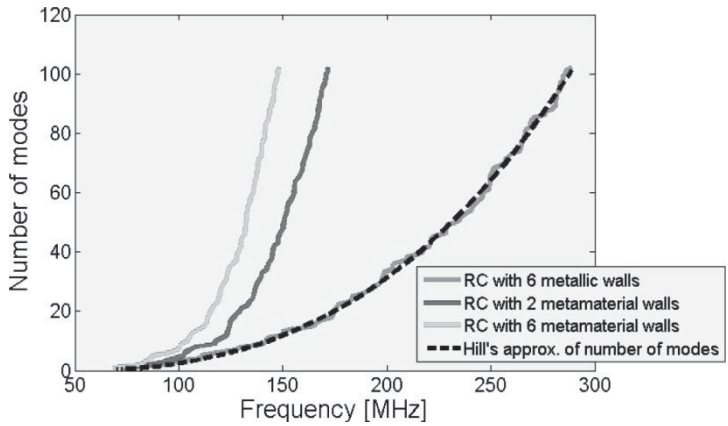

Figure 4.12. *Number of modes with respect to frequency for the reverberation chambers described in Figure 4.11*

The number of modes with respect to frequency for the metallic RC agrees with the approximation given in equation [4.19]. The two metamaterial wall RC proves to present a much higher modal density than the traditional metallic RC. The six metamaterial walls present an even higher modal density. These first results are promising. The value of φ chosen was arbitrary. A criterion can be developed to choose the value of φ, thus ensuring the highest modal density at a particular frequency.

In order to verify the approach, the phase required by the RIM to create a resonance is extracted from the resonant frequency of a given mode obtained

through numerical computation; this phase is then compared to the numerically calculated one of a unit cell. This verification has been performed only for 40 modes for the six metamaterial wall RC. This comparison is shown in Figure 4.13.

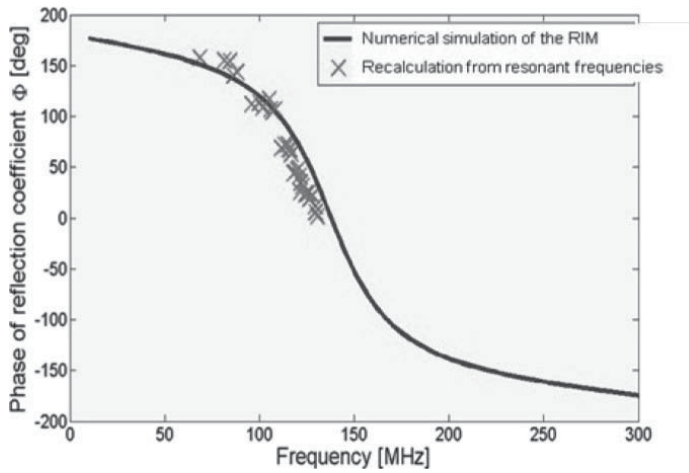

Figure 4.13. *Phase of reflection coefficient calculated during the design step compared to phase recovered by using [4.10] in the case of a six metamaterial walls chamber*

A good agreement is observed, suggesting that our analytical expressions for the resonant frequencies of the 3D metamaterial cavity based on the phase of the reflection coefficient of the wall surfaces are appropriate. The results obtained for the metamaterial wall RC are interesting since a great increase in modal density is observed and furthermore the analytical formula proposed to analyze the resonant frequencies and to design the RIM complies with the results obtained. This shows that the increase in resonant modes is really due to the subwavelength cavity phenomenon induced by metamaterials as described previously.

These preliminary results are promising for RCs used for EMC tests. However, to further analyze the relevance of using metamaterials for an RC, the statistical properties of the fields in the test volume must be studied. Indeed, the LUF is generally defined, in the IEC 61000-4-21 standard, as the lowest frequency above which the field uniformity requirements are met [CHA 05]. If the statistical properties are identical for a classical RC and an

RC with metamaterial walls, then we can conclude that polarization is not an issue and that metamaterials are indeed good candidates to reduce the LUF.

A numerical validation is then performed. A dipole antenna is used to excite the metallic wall RC (with metallic losses, $\sigma = 5.9 \times 10^6$ S.m^{-1}) and the E-field is calculated in the working volume using the transient finite integral technique (FIT) solver of CST microwave studio with a filtered white Gaussian noise as excitation [SEE 11a]. The frequency is allowed to vary over a narrow interval about some center frequency. The contribution of each mode to a given spatial point in the chamber, in that narrow band of frequency, is averaged to provide the field homogeneity [LOU 91]. A frequency window of 40 MHz, centered around 520 MHz, was used. The cumulative density functions of the absolute value of electric field obtained using computer simulation technology (CST) and WIPL-D (based on the method of moments) are compared for validation [GHY 11, SEE 11a].

In Figure 4.14, the probability density functions of the *z*-component of the electric field are shown.

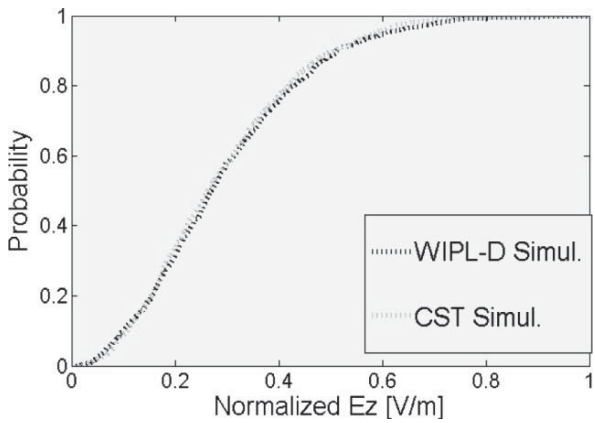

Figure 4.14. *Cumulative density functions of the absolute values of the z-component of the electric field at a frequency of 520 MHz. WIPL-D and CST simulation data are plotted on the same graph*

The results obtained by the transient solver of CST microwave studio and WIPL-D are in good agreement. The same metamaterial wall RC as the previously described one is modeled and analyzed with an identical procedure. The cumulative density functions are calculated and shown in Figure 4.15.

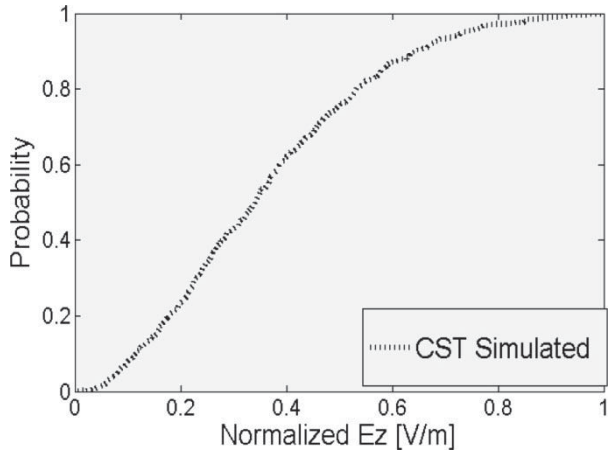

Figure 4.15. *Cumulative density functions of the absolute values of the z-component of the electric field, in case of an RC with six metamaterial walls at a frequency of 350 MHz*

For approximately the same number of modes, i.e. 625 modes with around 1.2 modes per MHz, for the metallic RC the operating frequency is 520 MHz and for the metamaterial wall RC the operating frequency is 350 MHz. For a given RC, the same properties and mode density can be obtained at lower frequencies for a metamaterial wall RC compared to a metallic wall RC.

4.5. Conclusion

Strict regulations together with the growing complexity of systems and EM environments call for new technological solutions in EMC engineering. The synthesis of new materials being an active field of research, in this chapter, the potential of metamaterials for applications in EMC has been described. To highlight the relevance of metamaterials in EMC applications, current trends in the transport and telecommunications industries, as well as the consequent challenges they give rise to, have been described. The shielding application has been dealt with through the description of three examples of 1D metamaterial shields. The first metamaterial shield is mostly based on the reflection of waves; the second metamaterial shield relies on absorption. Both of them are designed to operate at frequencies used in current telecommunications applications. The third metamaterial shield is

the one relying on absorption designed to function at terahertz frequencies; frequency band where there is an active field of research for future telecommunications applications. Finally, the use of metamaterials for subwavelength 3D shielded cavities has been detailed. The design rules of the metamaterial wall have been given and the metamaterial-based solution has been evaluated for its use in an RC, common test facility for EMC measurements.

4.6. Bibliography

[ARN 01] ARNAUT L., "Operation of electromagnetic reverberation chambers with wave diffractors at relatively low frequencies", *IEEE Transactions on Electromagnetic Compatibility*, vol. 43, no. 4, pp. 637–653, November 2001.

[BIN 09] BINGNAN W., THOMAS K., SOUKOULIS C.M., "Wide-angle and polarization-independent chiral metamaterial absorber", *Physical Review B*, vol. 80, no. 3, pp. 033108–033112, July 2009.

[BRU 05] BRUNS C., Three-dimensional simulation and experimental verification of a reverberation camber, PhD Dissertation, Dipl.-Ing, Universität Fridericiana Karlsruhe (TH), Germany, 2005.

[BUT 97] BUTLER J., "Shielding effectiveness – why don't we have a consensus industry standard?", *Proceedings of the 1997 IEEE International Symposium on Electromagnetic Compatibility*, Austin, TX, pp. 29–35, 18–22 August 1997.

[CAM 06] CAMPUS E., ROURRE B., "Use of composites in railway applications", *7th World Congress on Railway Research*, Montreal, Canada, 2006.

[CAR 06] CARBONELL J., ROGLA L., BORIA V., *et al.*, "Coaxial probe excitation of evanescent waveguides loaded with split ring resonators", *36th European Microwave Conference 2006*, Manchester, UK, pp. 336–339, September 2006.

[CEL 08] CELOZZI S., ARANEO R., LOVAT G., *Electromagnetic Shielding*, IEEE Press, Wiley, 2008.

[CHA 05] CHANG K., (ed.), *Encyclopedia of RF and Microwave Engineering*, Wiley, 2005.

[CHR 07] CHRISTOPOULOS C., *Principles and Techniques of Electromagnetic Compatibility*, CRC Press, 2007.

[DE 11] DE BARROS F., FEYMIN-PETOT-TOURTOLLET G., LEMAITRE-AUGER P., *et al.*, Surface for filtering a plurality of frequency bands, Patent WO/2011/135224, 2011.

[ENG 02] ENGHETA N., "An idea for thin subwavelength cavity resonators using metamaterials with negative permittivity and permeability," *Antennas and Wireless Propagation Letters*, vol. 1, no. 1, pp. 10–13, January 2002.

[GHY 11] GHYS J.-P., SEETHARAMDOO D., COCCATO I., *et al.*, "Numerical modeling for the analysis of Vivaldi antenna as transmitter in a reverberation chamber", *International Review of Progress in Applied Computational Electromagnetics*, Virginia, USA, pp. 1–6, March 2011.

[HIL 09] HILL D., *Electromagnetic Fields in Cavities: Deterministic and Statistical Theories*, IEEE Press Series on Electromagnetic Wave Theory, 2009.

[IEC 06] IEC 61000-4-21, "Electromagnetic compatibility (EMC) – 61000-4-21: Testing and measurement techniques – Reverberation chamber test methods", *International Electrotechnical Commission Std*, 3rd ed., 2006.

[IEE 07] IEEE Std-299-2006, "IEEE Standard method for measuring the effectiveness of electromagnetic shielding enclosures", Institute of Electrical and Electronics Engineers (IEEE), Piscataway, NJ, 2007.

[INN 12] INNOTRANS, International industry showplace focusing on Railway Technology, Berlin, Germany, September 2012.

[KLI 05] KLINKENBUSCH L., "On the shielding effectiveness of enclosures", *IEEE Transactions on Electromagnetic Compatibility*, vol. 47, no. 3, pp. 589–601, August 2005.

[LI 06] LI H., HAO J., ZHOU L., *et al.*, "All-dimensional subwavelength cavities made with metamaterials," *Applied Physics Letters*, vol. 89, no. 10, 2006.

[LOU 91] LOUGHRY T.A., Frequency stirring: an alternate approach to mechanical, mode-stirring for the conduct of electromagnetic susceptibility testing, April 90–April 91, Final Report, November 1991.

[MOS 04] MOSALLAEI H., SARABANDI K., "Antenna miniaturization and bandwidth enhancement using a reactive impedance substrate", *IEEE Transactions on Antennas and Propagation*, vol. 52, no. 9, pp. 2403–2414, September 2004.

[NOR 09] NORRIS G., WAGNER M., *Boeing 787 Dreamliner*, Zenith Press, 2009.

[OUR 06] OURIR A., DE LUSTRAC A., LOURTIOZ J.-M., "All-metamaterial-based subwavelength cavities for ultra-thin directive antennas", *Applied Physics Letters*, vol. 88, no. 8, pp. 084103–(1–3), February 2006.

[PEN 99] PENDRY J., HOLDEN A., ROBBINS D., *et al.*, "Magnetism from conductors and enhanced nonlinear phenomena", *IEEE Transactions on Microwave Theory and Techniques*, vol. 47, no. 11, pp. 2075–2084, 1999.

[PON 12] PONCET-PAPPINI S., La tranquillité électromagnétique (GSM and Wi-Fi) grâce à un papier peint révolutionnaire, Press Kit, Metapapier Technical Centre paper, March 2012.

[SEE 11a] SEETHARAMDOO D., "Numerical modeling of a reverberation chamber using CST microwave studio and WIPL-D and statistical post-processing", IFSTTAR Internal report, 2011.

[SEE 11b] SEETHARAMDOO D., COCCATO I.M., "Investigation on the use of metamaterials to lower the operating frequency of reverberation chamber", *EMC Europe 2011*, York, UK, 2011

[SIE 99] SIEVENPIPER D., ZHANG L., BROAS R., *et al.*, "High-impedance electromagnetic surfaces with a forbidden frequency band", *IEEE Transactions on Microwave Theory and Techniques*, vol. 47, no. 11, pp. 2059–2074, November 1999.

[TAO 08] TAO H., LANDY N., BINGHAM C., *et al.*, "A metamaterial absorber for the terahertz regime: design, fabrication and characterization", *Optics Express*, vol. 16, pp. 7181–7188, 2008.

Chapter 5

Dissipative Loss in Resonant Metamaterials

Metamaterials allow for the creation of electromagnetic media with properties that are not found in or, are much weaker in, natural materials. However, many of these properties require meta-atoms with strong electric or magnetic dipole moments, for which resonant constituents made from conducting materials must be used. We discuss how these resonances influence dissipative loss in metamaterials and we compare a number of conducting materials that can be used in the fabrication of metamaterials, including noble and transition metals, alkali metals, conducting oxides and graphene. Subsequently, we discuss design methods to minimize dissipative loss and the use of gain to compensate dissipation.

5.1. Introduction

In the previous chapters, many different metamaterials have been discussed. The majority of these metamaterials require large electric or magnetic dipole moments. In most metamaterials, this is implemented with metallic constituents supporting the flow of large electric currents [SMI 04, ENG 06, SHA 06, SOU 10, LIU 11]. Unfortunately, this results in significant Joule heating in the metal (particularly, at higher frequencies) and in relaxation loss in dielectrics (typically the dominant loss mechanism at

---

Chapter written by Philippe TASSIN, Thomas KOSCHNY and Costas M. SOUKOULIS.

microwave frequencies, except if substrates of very high quality are being used). The dissipation is exacerbated by the resonances; indeed, even if the loss tangent of the constituent materials is small, significant losses can still occur because the loss channels are driven by large resonant fields. Focusing on terahertz and higher frequencies, loss is dominated by dissipation in the conducting elements, even if noble metals with relatively good electrical properties (for example silver or gold) are used. This is reflected in the power loss when signals propagate through a metamaterial (Figure 5.1). For microwave metamaterials, the power loss can be less than a few decibels per wavelength, but when metamaterials are scaled down for operation in the terahertz and optical domains, power losses increase to more than 20 dB per wavelength [SOU 08]. This amounts to an extinction coefficient[1] of 3×10^4 cm^{-1}, to be compared with the extinction coefficient of 1×10^4 cm^{-1} for a direct bandgap conductor like gallium arsenide.

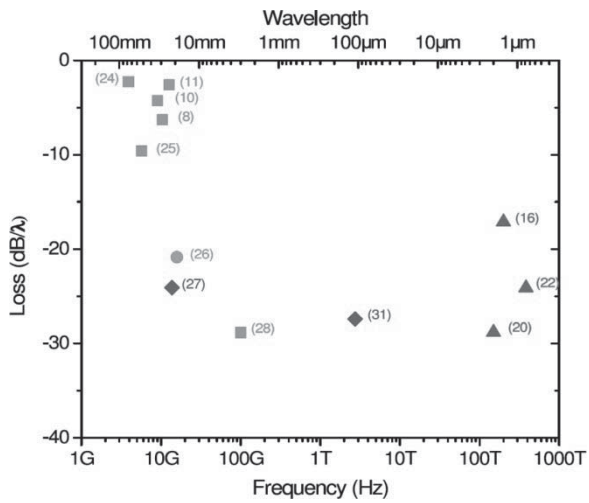

Figure 5.1. *Power loss in decibel per wavelength of propagation for a number of typical metamaterials in the microwave, terahertz and optical domains (from [SOU 08])*

Dissipative loss is not only a problem because it reduces signal power. More importantly, dissipative loss dampens resonance so that the large

1 When an electromagnetic wave propagates in a lossy medium, its amplitude will decay. The extinction coefficient is the inverse of the distance the wave propagates until its amplitude has decayed to 1/e of its original amplitude.

electric or magnetic dipole moments eventually disappear. This is illustrated with the response function of a negative permeability metamaterial in Figure 5.2 [TAS 12]. Metamaterials made from high-quality metallic constituents have a sharp resonance and can achieve negative permeability. When the metal gets lossier, the resonance is dampened and becomes shallower. We will see below that dissipation in the metamaterial gets worse, because we have to work closer to the resonance frequency to obtain the desired value of the permeability. Eventually, the resonance gets so highly dampened that it becomes impossible to obtain negative permeability at all. This is particularly relevant to optical metamaterials.

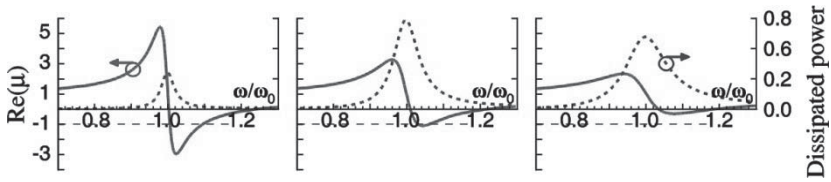

Figure 5.2. *Permeability and dissipated power for magnetic metamaterials with low (left) to high (right) dissipative loss (from [TAS 12])*

In addition to dissipative loss, metals exhibit another problem when we try to scale down metamaterials for operation at higher frequencies – kinetic inductance. At the lowest frequencies, the resonance frequency of, say, a split-ring resonator (SRR) scales inversely proportional to the unit cell size, but this simple scaling ceases to be valid in the infrared due to a saturation of the magnetic response and, eventually, the magnetic response becomes too weak to result in negative permeability. This effect is due to the finite mass of the charge carriers, which yields an additional contribution to the inductance of the SRR. Let us consider the SRR of Figure 5.3 as an example. A current $I = q\,N\,w\,t\,v_e$ flows in the ring, where $w\,t$ is the cross-section of the ring (see Figure 5.3 for the definition of the dimensions of the split ring), q is the electron charge, v_e is the average velocity of electrons in the wire and N is the density of the charge carriers in the metal. Besides the energy contained in the magnetic fields, $E_m = L\,I^2/2$, the electrons also have kinetic energy $E_k = N\,V\,m_e v_e^2$, where V is the volume of the metal of the ring. We can rewrite the kinetic energy as $E_k = L_k\,I^2/2$, with

$$L_k = \frac{V m_e}{q^2 w^2 t^2 N} \qquad [5.1]$$

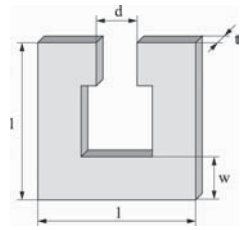

Figure 5.3. *Single-gap split-ring resonator used as an example (from [LIN 04])*

This "kinetic" inductance scales reciprocally with the size of the ring, in contrast to the geometrical inductance L that scales linearly with the size. Therefore, at low frequencies (microwaves), the kinetic inductance is negligible with respect to the geometrical inductance. However, at higher frequencies, the kinetic contribution starts to dominate and the resonance frequency $\omega_r^2 = 1/(LC)$ must eventually be replaced by

$$\omega_r = \frac{1}{\sqrt{L_k C}} = \sqrt{\frac{q^2 w^2 t^2 N}{m_e V} \frac{d}{\epsilon_0 wt}} = \sqrt{\frac{q^2 N}{m_e \epsilon_0}} \sqrt{\frac{wtd}{V}} \qquad [5.2]$$

so that the resonance frequency becomes constant under further downscaling (see Figure 5.4 for the resonance frequency of various types of wire pairs and fishnets). Minor changes in the configuration of the metallic resonators, e.g. split rings with two or four gaps or fishnets with large neck inductance, can push the saturation frequency somewhat higher, but the fundamental problem remains.

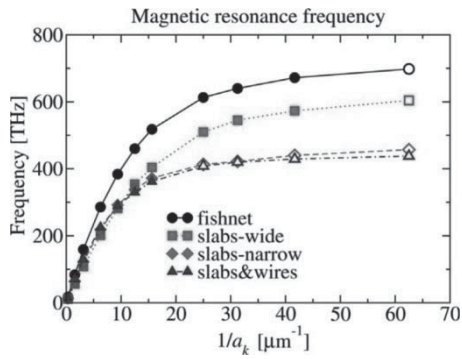

Figure 5.4. *Saturation of the resonance frequency when the size a_k of the meta-atom is decreased for a few different types of meta-atoms (from [PEN 10])*

The kinetic inductance is encoded in the imaginary part of the resistivity of the metal, as we will see in section 5.2, and therefore it must be considered when other conducting materials are considered for use in building metamaterial constituents.

Returning to the loss problem, there are basically three approaches that we can follow to reduce the impact of dissipative loss in metamaterials:

1) Use better constituent materials. This will be considered in section 5.2, where we will discuss a model to compare different conducting materials, including graphene at optical frequencies, transparent conducting oxides, noble metals and alkali metals.

2) Pursue passive reduction of dissipation, i.e. optimize the geometry of meta-atoms to minimize dissipation loss. A few methods to achieve this will be discussed in section 5.2.

3) Introduce gain in the meta-atoms to counteract the dissipation. The gain must be strongly coupled to the resonance to ensure that the resonance is undampened rather than simply amplifying the output signal. Examples of gain inclusions will be given in section 5.3.

5.2. What is the best conducting material?

The metamaterials we will consider here consist of an array of subwavelength conducting elements, such as SRRs, wire pairs or fishnet cells. It is exactly for this type of metamaterial that an effective permittivity and permeability makes sense [GOR 02, KOS 04]. This enables us to model each individual element as a quasistatic electrical circuit. Here, we consider that the resonant response of these circuits can be described by that of a simple RLC circuit. This is not the most general case, as some phenomena such as electromagnetically induced transparency (see also Chapter 8) require more intricate circuits to be explained [ZHA 08, PAP 08, TAS 09, LIU 09], but it has been proven that it can successfully capture the physics of the most popular elements, such as split rings and wire pairs, and even provide quantitative results [PEN 10]. Below we will derive a model for negative permeability metamaterials, but similar models can be constructed for other resonant metamaterials.

Our analysis[2] starts with Kirchhoff's equation describing the electrical current, I, flowing in the metallic circuit of each meta-atom, driven by the external time-dependent magnetic field of an electromagnetic incident wave:

$$L\frac{\mathrm{d}^2 I}{\mathrm{d}t^2}+\left(R+R_{rad}\right)\frac{\mathrm{d}I}{\mathrm{d}t}+\frac{1}{C}I=-\frac{\mathrm{d}^2}{\mathrm{d}t^2}\left(\mu_0 H_0 A\cos(\omega t)\right) \qquad [5.3]$$

where A is the area enclosed by the circuit, H_0 is the magnetic field amplitude of the incident wave, R_{rad} is the radiation resistance[3] and ω is the frequency of the incident wave. The inductance L and capacitance C must be interpreted as effective values that encompass coupling between neighboring circuits [GOR 02]. The right-hand term in equation 5.3 is, of course, nothing other than the electromotive force induced in the circuit. Once we solve this equation, we know the currents and can calculate the magnetic susceptibility of the metamaterial. In addition, we can calculate the dissipated power by summing the Joule heat loss for each circuit [LUA 09].

To arrive at a straightforward comparison of conducting materials, we need to work with dimensionless variables. For this purpose, we introduce the dimensionless frequency $\tilde{\omega}=\omega/\omega_0$, where $\omega_0 = (LC)^{-1/2}$ is the (geometric) resonance frequency of the quasistatic circuit. Using this definition and explicitly calculating the radiation resistance yields the following expression for the magnetic susceptibility:

$$\chi=-\frac{F\tilde{\omega}^2}{\tilde{\omega}^2\left(1+\xi\right)-1+\mathrm{i}\left(\tilde{\omega}\zeta+\kappa\tilde{\omega}^5\right)} \qquad [5.4]$$

where F is the filling factor of the metallic element within the metamaterial unit cell, have $\zeta = \mathrm{Re}(R)/\sqrt{L/C}$ is called the "dissipation factor", $\xi = -\mathrm{Im}(R)/(\tilde{\omega}\sqrt{L/C})$ is called the "kinetic inductance factor", and κ is a parameter describing radiation losses. We will discuss the physical significance of these parameters in the following. The dissipated power as a

2 Here, we give a summary of the analysis from [TAS 12]. The technical details can be found in the supplementary material of this publication.

3 The radiation resistance is the equivalent resistance in the circuit representing the radiated power.

fraction of the incident power can be cast in the following non-dimensionalized form:

$$\Pi = \frac{\text{dissipated power per unit cell}}{\text{incident power per unit cell}} = 2\pi\left(\frac{a_k}{\lambda_0}\right)\frac{F\tilde{\omega}^4\zeta}{\left[\tilde{\omega}^2(1+\xi)-1\right]^2+\left(\tilde{\omega}\zeta+\kappa\tilde{\omega}^5\right)^2} \quad [5.5]$$

where a_k is the metamaterial's unit cell size along the propagation direction and λ_0 is the free-space wavelength.

We argue that the effective susceptibility and the dissipated power fraction are the two variables of interest – the susceptibility tells us something about the strength of the effective magnetic behavior of the metamaterial, whereas the dissipated power fraction quantifies the dissipative loss. It is interesting to note that both depend on the following four independent, dimensionless parameters:

1) the filling factor F;

2) the radiation loss parameter κ;

3) the dissipation factor ζ (proportional to the real part of the resistivity);

4) the kinetic inductance factor ξ (proportional to the imaginary part of the resistivity).

The filling factor and the radiation loss parameter depend only on purely geometric variables, such as the area of the circuit and the geometric inductance, but not on the material properties of the conductor. In other words, for a certain geometry (say, split rings or fishnets), F and κ are fixed. This somewhat simplifies the analysis, because we can limit our discussion to how the susceptibility and the dissipated power depend on the other two parameters, ζ and ξ, which do depend on the resistivity, i.e. on the specific conducting material used. In Figure 5.5, we show the dissipated power fraction as a function of these two parameters of interest. Since our aim is to design metamaterials with negative permeability, we have calculated the dissipated power at the frequency where $\mu(\omega) = -1$.

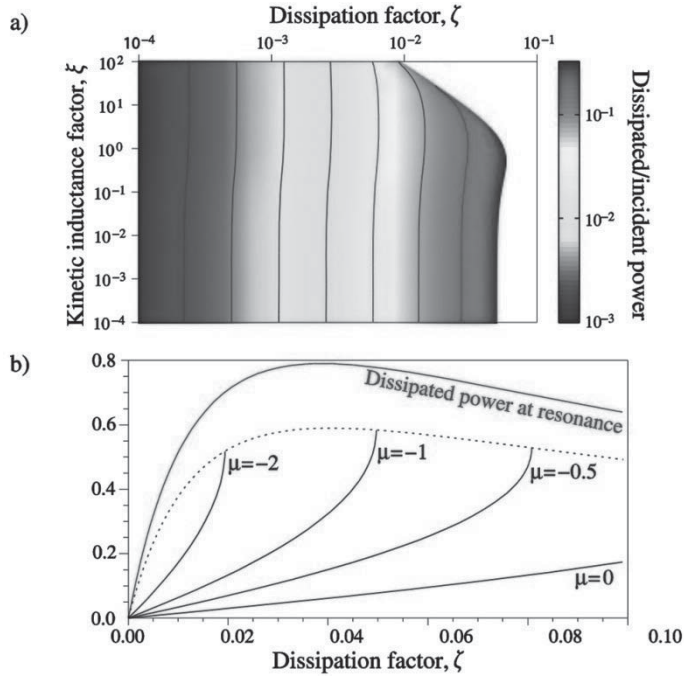

Figure 5.5. *a) Contour plot of the dissipated power as a function of the loss factor and the kinetic inductance factor. b) Dissipated power as a function of the loss factor (from [TAS 12])*

Apart from the uninteresting regions with high dissipation factors and/or high kinetic inductance factors (top and rightmost regions in Figure 5.5(a)), we see that the contours of equal dissipated power are almost vertical, i.e. the dissipative loss depends on good approximation only with the dissipation factor and not with the kinetic inductance factor. (This also explains why we named ζ the dissipation factor.) Let us now replot the dissipated power fraction as a function of the dissipation factor, as in Figure 5.5(b); in this figure, the curves enumerated by different values of μ represent the dissipated power fraction for several values of the achieved permeability. It might come as a surprise that smaller ζ – i.e. smaller real part of the resistivity – leads to lower power dissipation, since smaller resistivity implies quasistatic circuits with higher quality factors and, hence, much more pronounced resonances. This behavior can be understood from Figure 5.2, where we have shown the permeability for three different values of the dissipation factor. For large dissipation factors (metamaterials made from high-resistivity materials), the

resonance is highly damped; the peak loss at the resonance frequency (topmost curve in Figure 5.5(b)) is relatively low and the resonance is too shallow to allow for a permeability $\mu = -1$. With a decreasing dissipation factor, the resonance becomes sharper; the dissipated power at the resonance frequency increases, but for a given permeability design goal (e.g. $\mu = -1$), the resonance may be probed further from the resonance peak, effectively leading to smaller dissipated power if the dissipation factor ζ is decreased. When the dissipation factor is further decreased, the linewidth becomes limited by the radiation loss of the circuit, which implies that the induced current in the circuit does not increase further; from this point on, the resonance does not become any stronger when the dissipation factor is further decreased (i.e. when a better conductor is used). This means that we cannot achieve arbitrarily low permeability, but, on the contrary, that there is a geometrical limit on the strongest negative permeability that can be achieved with a certain structure. Since the induced current in the circuit now becomes constant when further decreasing the dissipation factor, the dissipated power at the working frequency continues to decrease linearly with the dissipation factor, because the Joule heating is proportional to the resistivity.

From the discussion above, we can identify the loss factor ζ as a good figure of merit to compare different conducting materials when used in resonant metamaterials. It is important to note that the loss factor is the product of a material parameter (the real part of the resistivity at the frequency of operation) and a geometric term. For most materials, metamaterials with the same dimensions can be made and it suffices to compare the resistivity. However, when comparing metals to certain two-dimensional materials such as graphene, it is essential to take into account the geometric term. Below we will compare a number of different potential conducting materials, including noble metals, transition metals, graphene and transparent conducting oxides.

In Figure 5.6, we compare a number of different conductors: noble and transition metals (e.g. silver, gold, copper, aluminum and iridium) and alternative conductors (alkali metals, alkali-noble intermetallics and conducting oxides). Silver is, at this time, still the best conducting metal in all frequency domains [TAS 12]. Copper is almost as good at microwave frequencies and has the advantage of easier experimental handling, but its losses increase dramatically in the optical domain due to interband scattering. Gold is a good alternative in infrared, where it is only slightly less good than silver, but again easier to use in fabrication processes. Zirconium nitride performs almost as well as gold in infrared.

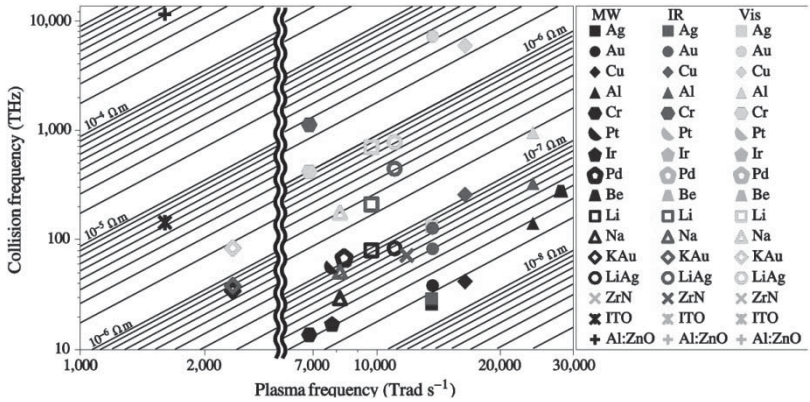

Figure 5.6. *Comparison of conductors for metamaterials. The oblique lines are lines of constant resistivity, so the best conductors for metamaterials are in the bottom-right corner (from [TAS 12])*

It was shown recently that there is a fundamental connection between the subwavelengthness of meta-atoms and loss when displacement current dominates over conduction current [KHU 11, KHU 12]. This happens in metals for frequencies larger than the intraband collision frequency. Thus, it is advantageous to search for conductors with a small intraband collision frequency. Two examples of such metals are chromium and iridium. Unfortunately, they have a smaller plasma frequency, increasing the average energy lost in each collision. This offsets the lower collision frequency, and, in the microwave domain, chromium and iridium turn out to be of similar quality as silver/copper.

When we go to higher frequencies (infrared and up), all of the above-mentioned metals begin to suffer from scattering by interband transitions with transition frequencies in the visible or the UV band. Alkali metals suffer less from interband transitions (compare in Figure 5.6 the change in collision frequency for lithium or sodium when going from microwaves to infrared to optical frequencies). Unfortunately, their intraband collision frequency is significantly larger and they tend to have a smaller plasma frequency. There has also recently been interest in alkali-noble intermetallics with the motivation of combining the low intraband resistivity of the noble metals with the reduced interband transition contribution of the alkali metals [BLA 10]. Two characteristic examples are KAu and LiAg. KAu (open diamond symbols in Figure 5.6) has its interband transitions far in the ultraviolet and its resistivity

increases only slightly from the microwave through the visible; however, its small plasma frequency leads to a relatively large resistivity. However, LiAg (open circles in Figure 5.6) has a larger plasma frequency, but performs badly at higher frequencies because of significant interband scattering. These examples show, nevertheless, the possibility of band engineering to tune the resistivity of alloys [BOB 09].

In addition, a few other conductor systems have recently been proposed as alternatives for metals: transparent conducting oxides, transition-metal nitrides and graphene (see, for example, [RHO 06, SCH 10, BOL 11]). Transparent conducting oxides, such as indium tin oxide (ITO) and aluminum-doped or gallium-doped zinc oxide, are semiconductors. For frequencies below their bandgap (i.e. near-IR and lower) and at sufficiently high doping levels, they act as conductors [RHO 06, NAI 11]. However, the dopants introduce significant scattering and they also have smaller plasma frequencies than noble metals. The result is that their resistivity values are of larger orders of magnitude than silver. Non-stoichiometric nitrides of transition metals such as titanium, hafnium and zirconium also have metallic properties up to the visible, but, similar to the conducting oxides, they cannot outperform the noble metals in the construction of resonant metamaterials. One interesting possibility is to use an applied electric field to create high carrier concentrations at the oxide/dielectric interface of a metal/ITO/ dielectric heterostructure [FEI 10]. As far as we know, creating resonant metamaterials out of such a two-dimensional electron gas has not yet been attempted.

We have investigated another two-dimensional conducting system: charge-neutral graphene [TAS 12]. As mentioned earlier, we must now carefully consider the geometric term in the loss figure of merit. This is what we have done when calculating the dissipation factor for graphene and for a gold film in Figure 5.7. The dissipation factor of graphene is 1,200, which is deep into the cutoff region of Figure 5.5(a), where the losses are tremendous and the magnetic resonance is highly damped. In addition, the dissipation factor of graphene is scale-invariant; graphene cannot be made a better conductor by making the slab-wire pair larger. We must conclude that graphene does not conduct well enough for use in resonant metamaterials at infrared and visible frequencies. This observation might not be so surprising given that recent results have demonstrated the optical transmittance through a free-standing graphene sheet to be more than 97%, i.e. graphene has a fairly small interaction cross-section with optical radiation. At terahertz frequencies, we could electrically bias graphene to create a large intraband conductivity. It remains to be seen whether high

enough carrier densities can be achieved in this way to obtain metamaterial response from patterned graphene flakes. One very interesting property, however, is that the bias voltage allows for control over the conduction properties – something that is difficult to achieve with metals – which is useful for tunable metamaterials [PAP 10, ZOU 12].

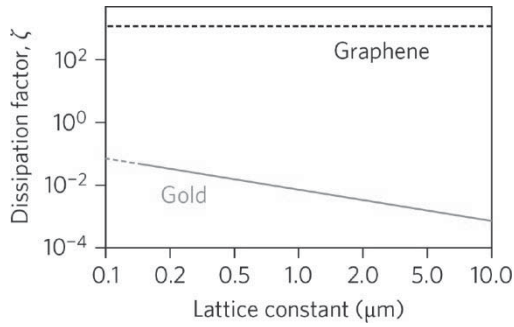

Figure 5.7. *Comparison of graphene and a gold film as conductors in resonant metamaterials (from [TAS 12])*

5.3. Optimize the geometry of meta-atoms

Apart from choosing an appropriate conductor with small resistivity, we may also try to optimize the geometry of the meta-atom to reduce dissipative loss.

5.3.1. *Increase RLC inductance*

A principle method used to reduce dissipative loss in meta-atoms such as SRRs, cut wires or fishnets is to increase the inductance of the RLC circuit equivalent of the meta-atom [ZHO 08]. Indeed, the quality factor of an RLC circuit equals

$$Q = \frac{\omega_0 L}{R} = \frac{1}{R}\sqrt{\frac{L}{C}} \qquad [5.6]$$

In fishnets, for example, the inductance can be increased with a thicker spacer between the two metallic layers of the fishnet. Simulation results for fishnets with different spacers are shown in Figure 5.8. A fishnet with a thin

spacer (dashed curves) has a shallow resonance in the permeability, resulting in a poor figure of merit |Re(*n*)/Im(*n*)|, where *n* is the index of refraction. With a thicker spacer (solid curves), we obtain a much stronger resonance and dramatically increased figure of merit. We must remind the reader that the dissipation factor was the product of the real part of the resistivity and a geometrical term. When we increase the inductance-to-capacitance ratio, we are effectively influencing the geometrical term. However, there is a limit to how much we can increase the inductance. For the fishnet, a spacer that is too thick will eventually break the subwavelengthness of the meta-atom, resulting in periodicity effects arising from the lack of homogenizability. This is, by the way, visible in the solid curve in Figure 5.8.

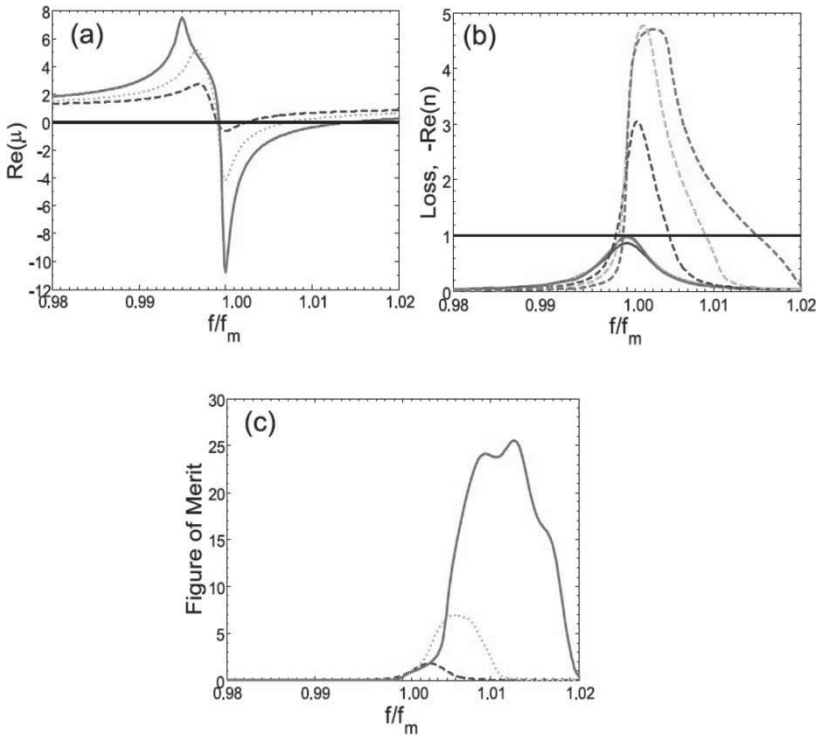

Figure 5.8. *Simulation results for fishnet metamaterials with spacers of different thickness. Dashed curves = thin spacer; dotted curves = intermediate spacer; solid curves = thick spacer (from [ZHO 08])*

5.3.2. *Geometric tailoring of corners and filling fraction*

It is also possible to engineer the metallic circuits to make the resistance R as small as possible. Guney *et al.* have investigated SRR with varying amounts of sharp corners: a circular SRR with a square cross-section, a circular SRR with a circular cross-section and a square SRR with a square cross-section [GÜN 09]. At microwave frequencies, they observe that the SRRs with sharp corners or bends exhibit higher losses. This is because sharp features result in hotspots in the current density distribution. It is in general advantageous to optimize meta-atom design so that the current is distributed as uniformly as possible over the cross-section of the structure.

At higher frequencies, the current density is much less sensitive to sharp edges and corners, because the skin depth is much larger relative to the size of the meta-atom and the current is not confined to the surface. Now, it is important to create bulky metallic structures with large filling factor F. Bulkier structures tend to have a larger skin depth, decreasing the current density and reducing ohmic loss.

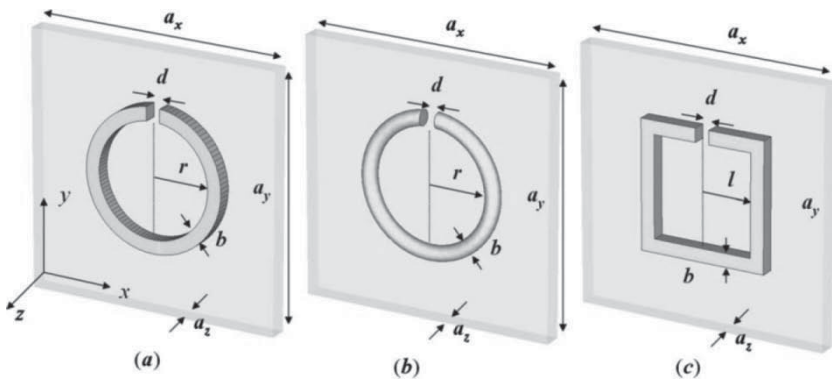

Figure 5.9. *Split-ring resonators with varying amounts of sharp corners: a) a circular SRR with square cross-section, b) a circular SRR with circular cross-section and c) a square SRR with square cross-section (from [GÜN 09])*

5.3.3. *Benefits from periodicity effects*

It is also possible to reduce absorption by working close to the limit of the effective-medium approximation. This is not possible for all applications, but if our only concern is for the scattering parameters (transmission and reflection)

of an incident beam, it may be a reasonable method to increase the transmission of a metamaterial sample. Periodicity effects may reshape the dispersion curve of the index of refraction, resulting in a very small extinction coefficient [Re(n)] and a large figure of merit |Re(n)/Im(n)|. This effect can be seen in Figure 5.10. In Figure 5.10(a), we see Lorentzian-shaped curves for a metamaterial with a sufficiently subwavelength unit cell – the figure of merit is maximally 4. In Figure 5.10(b), we see the effective medium parameters for a much thicker unit cell. The curves are significantly deformed from the Lorentzian shapes due to periodicity effects, but a much larger figure of merit of 25 can be obtained.

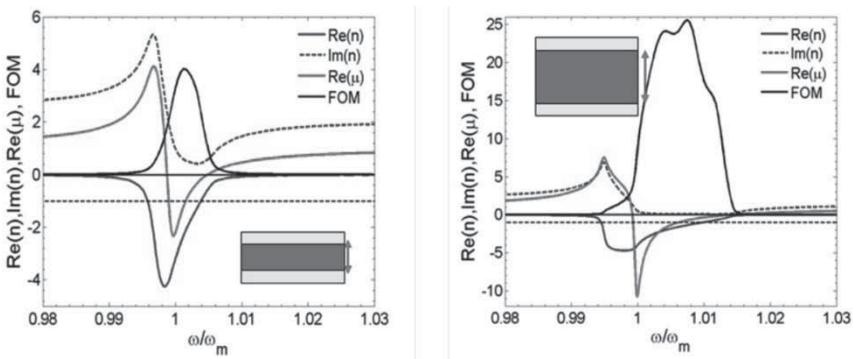

Figure 5.10. *Properties of metamaterials with a) a short unit cell and b) a long unit cell (from [ZHO 09])*

5.3.4. *Suppress internal resonant currents in strongly coupled fishnets*

Finally, we can go to the limit of strongly coupled fishnets. When multiple fishnet layers are closely stacked, their interacting evanescent fields will renormalize the circuit parameters in equation [5.3] and the fishnet resonance splits into two different modes: an antisymmetric mode in which the currents from each fishnet pair reinforce each other in the metallic layers (Figure 5.11(a)) and a symmetric mode in which the currents from each fishnet pair destructively interfere (Figure 5.11(b)). This effectively cancels the current in the center of the film and decreases the current density in the metallic sheets except for the sheets at the ends of the stack. The smaller current densities lead to reduced dissipative loss in the metamaterial.

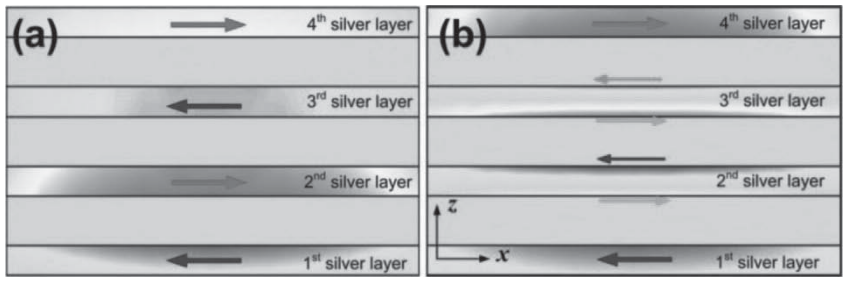

Figure 5.11. *Current distributions in strongly coupled fishnet metamaterials. a) Antisymmetric mode and b) symmetric mode (from [ZHO 09])*

5.4. Use gain to offset the impact of dissipative loss

5.4.1. *Introduction*

When dissipative loss cannot be reduced sufficiently by choice of a good conductor and by using the geometrical tailoring methods described in the previous section 5.3, we can try to add gain to the metamaterial to offset the dissipation. Adding gain to metamaterials is an active and rapidly evolving research topic [SOU 10, HES 12]. We will, therefore, only briefly outline the challenges of gain in metamaterials and we will show some early numerical and experimental work demonstrating the feasibility of compensating loss with gain.

When adding gain, it is not sufficient simply to amplify the transmitted signal. Indeed, as we have seen in section 5.2, dissipative loss is also broadening the resonance of the meta-atom, which in turn strongly increases the dissipation in the metamaterial (see Figure 5.2) because we need to set the working frequency close to the resonance frequency to obtain desired effective constitutive parameters like $\mathrm{Re}(\mu) = -1$. If the resonance is too shallow to allow negative permeability at all, amplifying the transmitted signal would obviously not be helpful. Consequently, it is important that the gain material is interacts strongly with the resonance of the metamaterials, in order to narrow the linewidth of the resonance and undo the broadening by dissipation. Preferably, the gain material is placed in the regions of the resonance's high evanescent fields. The development of novel meta-atom designs with optimal gain placement is currently an open problem.

5.4.2. *Self-consistent simulations of loss compensation in metamaterials*

The possibility of achieving loss compensation with gain was first shown in self-consistent simulations for SRRs [FAN 09] and fishnets [FAN 10, WUE 10]. These simulations implement the gain as spatially distributed pumped four-level oscillators coupled to the electromagnetic field through a source term in the polarization field. This is important, because the strongly inhomogeneous fields in meta-atoms lead to nonlinear effects, such as gain saturation, gain depletion and spatial hole burning, and they must be accounted for in simulations.

In Figure 5.12, we show the permeability of an SRR with gain material in the gap of the split ring. First of all, we have observed that for small enough signal amplitudes, the response is still linear in the signal field, which is desirable and essential for most applications. From the figure, we also see that the linewidth of the magnetic dipole resonance is significantly narrowed, indicating that the gain material is indeed undampening the resonance of the metamaterial.

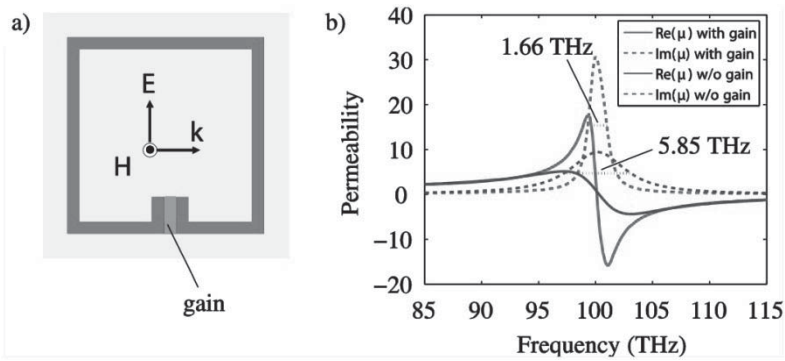

Figure 5.12. *a) Gain in a split-ring resonator. b) Narrowing of the linewidth of a negative permeability metamaterial (from [FAN 09])*

With gain present, there is now a frequency with a negative real part of the permeability, but a vanishing imaginary part. At this frequency, the extinction coefficient is also reduced. An interesting observation is that the improvement of the extinction coefficient due to the gain material in the gap of the SRR is larger than the gain coefficient of the bulk gain medium. This aspect is due to the strong local-field enhancement inside the SRR gap. It is important to benefit from this effect as much as possible when tailoring

metamaterials with gain. The linewidth narrowing and the decreased extinction coefficient demonstrate that the dissipation factor ζ of the metamaterial is reduced by the gain material.

5.4.3. *Experimental evidence for loss compensation in metamaterials*

Experimental evidence for loss compensation in metamaterials has come from photoluminescence measurements of inverse SRRs on top of a polymethylmethacrylate (PMMA) substrate in which PbS quantum dots have been dispersed [TAN 10]. In Figure 5.13, the photoluminescence spectra are shown. In the bottom row, the resonance frequency of the metamaterial is not matched with the emission frequency of the quantum dots (vertical gray band in the figure) and the resonance is dampened. For metamaterials with the resonance frequency closer to the quantum dot emission frequency (second to fifth row from the bottom in the figure), the resonance is undampened. The linewidth decreases and the peak photoluminescence signal is enhanced dramatically.

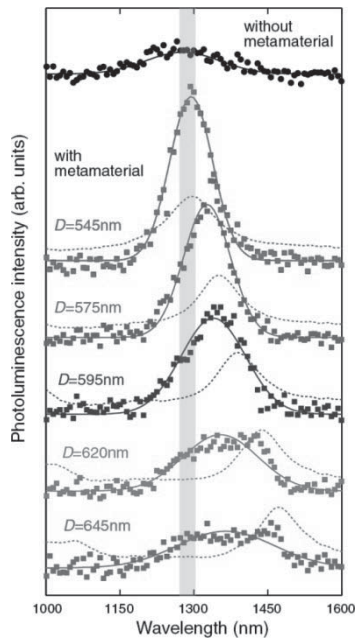

Figure 5.13. *Photoluminescence signals from inverse split-ring resonators on a substrate of PbS quantum dots dispersed in PMMA (From [TAN 10])*

Meinzer *et al.* have seen large differential transmission in pump-probe measurements on SRRs deposited on an InGaAs/InAlAs/InGaAs quantum well (see Figure 5.14(a)) [MEI 10]. Somewhat counter-intuitively, the differential transmission, due to pumping the quantum well with the SRRs, is negative, whereas the differential transmission due to pumping the quantum well by itself is positive (see Figure 5.14(b)). It was recently found that this is due to a stronger impedance mismatch and that the resonance is indeed undampened by interaction with the quantum well [HUA 12]. This highlights the importance of impedance matching in the design of metamaterials.

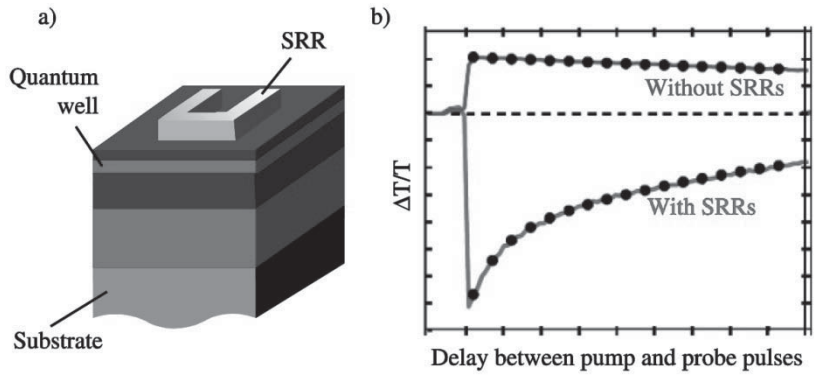

Figure 5.14. *a) Split-ring resonator metamaterial on a quantum well structure. b) Differential transmission from pump-probe experiments on this metamaterial (the gray line is the differential transmission for the quantum well with SRRs; the black line is the differential transmission for the quantum well without SRRs) (From [MEI 10])*

The experiments discussed in this section show that gain in metamaterials does allow for the compensation dissipative loss with gain media, e.g. dyes, quantum wells or quantum dots, but, at the time of writing this chapter, metamaterials with gain still need to be improved in order to make them a practical alternative for metamaterial applications.

5.5. Bibliography

[BLA 10] BLABER M.G., ARNOLD M.D., FORD M.J., "Tailoring materials for plasmonic systems: the alkali-noble intermetallics", *Journal of Physics: Condensed Matter*, vol. 22, p. 095501, 2010.

[BOB 09] BOBB D.A., ZHU G., MAYY M., *et al.*, "Engineering of low-loss metal for nanoplasmonic and metamaterials applications", *Applied Physics Letters*, vol. 95, p. 151102, 2009.

[BOL 11] BOLTASSEVA A., ATWATER H.A., "Low-loss plasmonic metamaterials", *Science*, vol. 331, pp. 290–291, 2011.

[ENG 06] ENGHETA N., ZIOLKOWSKI R.W., *Metamaterials: Physics and Engineering Explorations*, Wiley-IEEE Press, New York, 2006.

[FAN 09] FANG A., KOSCHNY T., WEGENER M., *et al.*, "Self-consistent calculation of metamaterials with gain", *Physical Review B*, vol. 79, p. 241104(R), 2009.

[FAN 10] FANG A., KOSCHNY T., SOUKOULIS C.M., "Self-consistent calculations of loss-compensated fishnet metamaterials", *Physical Review B*, vol. 82, p. 121102(R), 2010.

[FEI 10] FEIGENBAUM E., DIEST K., ATWATER H.A., "Unity-order index change in transparent conducting oxides at visible frequencies", *Nano Letter*, vol. 10, pp. 2111–2116, 2010.

[GOR 02] GORKUNOV M., LAPINE M., SHAMONINA E., *et al.*, "Effective magnetic properties of a composite material with circular conductive elements", *European Physical Journal B*, vol. 28, pp. 263–269, 2002.

[GÜN 09] GÜNEY D.Ö., KOSCHNY T., SOUKOULIS C.M., "Reducing ohmic losses in metamaterials by geometric tailoring", *Physical Review B*, vol. 80, p. 125129, 2009.

[HES 12] HESS O., PENDRY J.B., MAIER S.A., *et al.*, "Active nanoplasmonic metamaterials", *Nature Material*, vol. 11, pp. 573–584, 2012.

[HUA 12] HUANG Z., KOSCHNY T., SOUKOULIS C.M., "Theory of pump-probe experiments of metallic metamaterials coupled to a gain medium", *Physical Review Letters*, vol. 108, p. 187402, 2012.

[KOS 04] KOSCHNY T., KAFESKI M., ECONOMOU E.N., *et al.*, "Effective medium theory of left-handed materials", *Physical Review Letters*, vol. 93, p. 107402, 2004.

[KHU 11] KHURGIN J.B., SUN G., "Scaling of losses with size and wavelength in nanoplasmonics and metamaterials", *Applied Physics Letters*, vol. 99, p. 211106, 2011.

[KHU 12] KHURGIN J.B., BOLTASSEVA A., "Reflecting upon the losses in plasmonics and metamaterials", *MRS Bulletin*, vol. 37, p. 768, 2012.

[LIN 04] LINDEN S., ENKRICH C., WEGENER M., *et al.*, "Magnetic response of metamaterials at 100 terahertz", *Science*, vol. 306, pp. 1351–1353, 2004.

[LIU 09] LIU N., LANGGUTH L., WEISS T., *et al.*, "Plasmonic analogue of electromagnetically induced transparency at the Drude damping limit", *Nature Material*, vol. 8, pp. 758–762, 2009.

[LIU 11] LIU Y., ZHANG X., "Metamaterials: a new frontier of science and technology", *Chemical Society Reviews*, vol. 40, pp. 2494–2507, 2011.

[LUA 09] LUAN P., "Power loss and electromagnetic energy density in a dispersive metamaterial medium", *Physical Review B*, vol. 80, p. 046601, 2009.

[MEI 10] MEINZER N., RUTHER M., LINDEN S., *et al.*, "Arrays of Ag split-ring resonators coupled to InGaAs single-quantum-well gain", *Optics Express*, vol. 18, pp. 24140–24151, 2010.

[NAI 11] NAIK G.V., KIM J., BOLTASSEVA A., "Oxides and nitrides as alternative plasmonic materials in the optical range", *Optical Materials Express*, vol. 1, pp. 1090–1099, 2011.

[PAP 08] PAPASIMAKIS N., FEDOTOV V.A., ZHELUDEV N.I., *et al.*, "Metamaterial analog of electromagnetically induced transparency", *Applied Physics Letters*, vol. 101, p. 253903, 2008.

[PAP 10] PAPASIMAKIS N., LUO Z., SHEN Z.X., *et al.*, "Graphene in a photonic metamaterial", *Optics Express*, vol. 18, pp. 8353–8358, 2010.

[PEN 10] PENCIU R.S., KAFESAKI M., KOSCHNY T., *et al.*, "Magnetic response of nanoscale left-handed metamaterials", *Physical Review B*, vol. 81, p. 235111, 2010.

[RHO 06] RHODES C., FRANZENA S., MARIA J.-P., *et al.*, "Surface plasmon resonance in conducting metal oxides", *Journal of Applied Physics*, vol. 100, p. 054905, 2006.

[SCH 10] SCHULLER J.A., BARNARD E.S., CAI W., *et al.*, "Plasmonics for extreme light concentration and manipulation", *Nature Material*, vol. 9, pp. 193–204, 2010.

[SHA 06] SHALAEV V.M., "Optical negative-index metamaterials", *Nature Photonics*, vol. 1, pp. 788–792, 2006.

[SMI 04] SMITH D.R., PENDRY J.B., WILTSHIRE M.C.K., "Metamaterials and negative refractive index", *Science*, vol. 305, pp. 41–48, 2004.

[SOU 08] SOUKOULIS C.M., ZHOU J., KOSCHNY T., *et al.*, "The science of negative index materials", *Journal of Physics: Condensed Matter*, vol. 20, p. 304217, 2008.

[SOU 10] SOUKOULIS C.M., WEGENER M., "Optical metamaterials–more bulky and less lossy", *Science*, vol. 330, pp. 1633–1634, 2010.

[TAN 10] TANAKA K., PLUM E., OU J.Y., *et al.*, "Multifold enhancement of quantum dot luminescence in plasmonic metamaterials", *Physical Review Letters*, vol. 105, p. 227403, 2010.

[TAS 09] TASSIN P., ZHANG L., KOSCHNY T., *et al.*, "Low-loss metamaterials based on classical electromagnetically induced transparency", *Physical Review Letters*, vol. 102, p. 053901, 2009.

[TAS 12] TASSIN P., KOSCHNY T., KAFESAKI M., *et al.*, "A comparison of graphene, superconductors and metals as conductors for metamaterials and plasmonics", *Nature Photonics*, vol. 6, pp. 259–264, 2012.

[VAL 08] VALENTINE J., ZHANG S., ZENTGRAF T., *et al.*, "Three dimensional optical metamaterial exhibiting negative refractive index", *Nature*, vol. 455, pp. 376–379, 2008.

[WUE 10] WUESTNER S., PUSCH A., TSAKMAKIDIS K.L., *et al.*, "Overcoming losses with gain in a negative refractive index metamaterial", *Physical Review Letters*, vol. 105, p. 127401, 2010.

[ZHA 08] ZHANG S., GENOV D.A., WANG Y., *et al.*, "Plasmon-induced transparency in metamaterials", *Physical Review Letters*, vol. 101, p. 047401, 2008.

[ZHO 08] ZHOU J., KOSCHNY T., SOUKOULIS C.M., "An efficient way to reduce losses of left-handed metamaterials", *Optics Express*, vol. 16, pp. 11147–11152, 2008.

[ZHO 09] ZHOU J., KOSCHNY T., KAFESAKI M., *et al.*, "Negative refractive index response of weakly and strongly coupled optical metamaterials", *Physical Review B*, vol. 80, p. 035109, 2009.

[ZOU 12] ZOU Y., TASSIN P., KOSCHNY T., *et al.*, "Interaction between graphene and metamaterials: split rings vs. wire pairs", *Optics Express*, vol. 20, pp. 12198–12204, 2012.

Chapter 6

Transformation Optics and Antennas

6.1. Transformation optics

6.1.1. *Principle*

In a letter in 1662, Pierre de Fermat expounded the principle that leads to geometrical optics [TAN 91]. The path of light between two points is stationary. Generally, the path taker between the two points is the shortest one. In a few cases, this path can be the longest one. As shown in Figure 6.1, Pierre de Fermat wrote a very general and philosophical principle which states that nature always takes the easiest way. This principle has influenced modern physics with the principle of least action, which is the foundation of mechanics (Newton laws), electromagnetism, quantum field theory, relativity and particle physics. With the works of Leonhard Euler and Joseph-Louis Lagrange in the 18th Century, the principle of least action took the form of a variational principle where the action must be stationary (the action is an extremum). In fact, the modern way to write Fermat's principle is to define the action as the optical path, which is defined by the relation [6.1], where n is the refraction index that can depend on the spatial coordinates, and dl is an elementary distance:

$$s = \int ndl \qquad [6.1]$$

Chapter written by André de LUSTRAC, Shah Nawaz BUROKUR and Paul-Henri TICHIT.

Figure 6.1 shows an extract of the letter from Pierre de Fermat to Marin Cureau de la Chambre (1662), the King's adviser, where Fermat explains his principle of the stationary path for light.

Dès que j'ai voulu entreprendre cette analyse, j'ai eu deux obstacles à surmonter : le premier, que, bien que je fusse assuré de la vérité de mon principe, qui est qu'il n'y ait rien de si probable ni de si apparent que cette supposition, que la nature agit toujours par les moyens les plus aisés, c'est-à-dire ou par les lignes les plus courtes, lorsqu'elles n'emportent pas plus de temps, ou en tout cas par le temps le plus court, afin d'accourcir son travail et de venir plus tôt à bout de son opération (ce que le précédent calcul confirme, d'autant plus qu'il paroit que la lumière a plus de difficulté à traverser les milieux denses que les rares, puisque vous voyez que la réfraction vise vers la perpendiculaire dans mon exemple, ainsi que l'expérience le confirme, ce qui pourtant est contraire à la supposition de M. Descartes), néanmoins j'ai été averti de tous côtés, et principalement par M. Petit, que j'estime infiniment, que les expériences s'accordent exactement avec la proportion que M. Descartes a donnée aux réfractions, et que, bien que sa démonstration soit fautive, il est à craindre que je tenterai inutilement d'introduire une proportion différente de la sienne, et que les expériences qui se feront après que j'aurai publié mon invention la pourront détruire sur l'heure.

Figure 6.1. *Extract of the letter from P. de Fermat to M. Cureau de la Chambre (1662)*

If n varies with spatial position, a light path can be curved instead of being linear according to Euler–Lagrange equations. This happens, for example, above a hot road in summer when the optical index of the air layers above this road varies with temperature. In this case, we observe the curvature of light that gives the impression that the road is covered with water. Figure 6.2 gives a schematic idea of the deformation of a light ray when the space in which this ray propagates is distorted (Figure 6.2(a) and (b)). Hence, we can see that a variation of optical index can be equivalent to a distortion of space, and so we can conclude that a material containing this variation of optical index can simulate a distorted space. What does a distorted space mean? In fact, it is well known nowadays with Albert Einstein's general relativity that space and time are not absolute and are brought together in a space–time continuum. This continuum can be distorted with mass and energy, and all free objects in this space will always follow the shortest path, and if the space is curved, this path is not a line. This is the case for light rays or free photons, which are not propagating in straight line as, for example, for a gravitational

lens. Thus, in a free curved space, light follows geodesics that are defined as the shortest route between two points. What happens now if we assure the covariance of the Maxwell equations with a curved free space where light does not travel in straight line and a flat space with a material? In other words, is it possible to make an equivalence between a curved free space and a material? Pendry [PEN 06] and Leonhardt [LEO 06] answered this question in their papers published in 2006, calling the method "transformation optics". Pendry concluded that it was possible to hide a region of space by a conformation of light rays around this region (Figure 6.2(c)) – this was the first demonstration of the invisibility cloak.

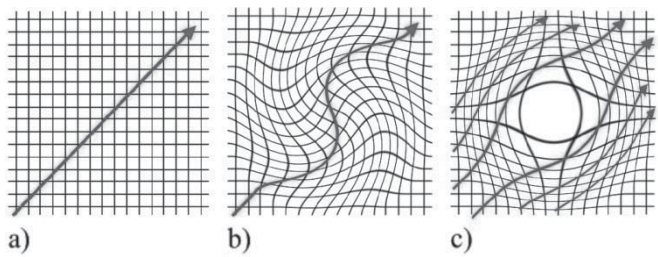

Figure 6.2. *a) Propagation of a light ray in a non-distorted space. b) Propagation of the same light ray in a distorted space. c) Cloaking of a region of space for incoming light rays*

The principle of the transformation optics method is relatively simple (Figure 6.3). If we are in a Cartesian space, where each point is designed by three coordinates (x, y, z), we can define a novel space where each point is designed by three new coordinates (u, v, w). These new coordinates must be a function of the three original coordinates:

$$u(x, y, z), v(x, y, z) \text{ and } w(x, y, z) \qquad [6.2]$$

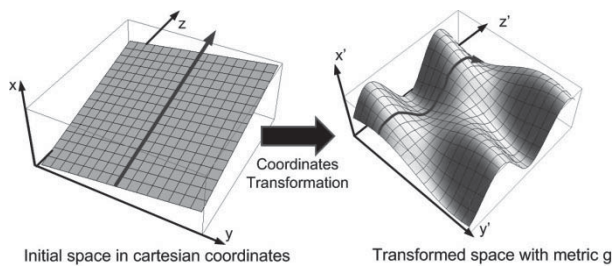

Figure 6.3. *Initial space and transformed space*

To ensure the equivalence, the new material must be written as:

$$\varepsilon^{i'j'} = \mu^{i'j'} = \frac{J_i^{i'} J_j^{j'} \varepsilon^{ij}}{\det(J)} \qquad [6.3]$$

with the Jacobian transformation matrix:

$$\overline{\overline{J}} = \begin{pmatrix} \frac{\partial x'}{\partial x} & \frac{\partial x'}{\partial y} & \frac{\partial x'}{\partial z} \\ \frac{\partial y'}{\partial x} & \frac{\partial y'}{\partial y} & \frac{\partial y'}{\partial z} \\ \frac{\partial z'}{\partial x} & \frac{\partial z'}{\partial y} & \frac{\partial z'}{\partial z} \end{pmatrix}$$

or be developed as:

$$\overline{\overline{\varepsilon}} = \overline{\overline{\mu}} = \begin{pmatrix} \varepsilon_{xx} & \varepsilon_{xy} & \varepsilon_{xz} \\ \varepsilon_{xy} & \varepsilon_{yy} & \varepsilon_{yz} \\ \varepsilon_{xz} & \varepsilon_{yz} & \varepsilon_{zz} \end{pmatrix}$$

$$\varepsilon^{xx} = \frac{\left(\frac{\partial x'}{\partial x}\right)^2 + \left(\frac{\partial x'}{\partial y}\right)^2 + \left(\frac{\partial x'}{\partial z}\right)^2}{\det\left(\overline{\overline{J}}\right)}$$

$$\varepsilon^{xy} = \frac{\left(\frac{\partial x'}{\partial x}\right)\left(\frac{\partial y'}{\partial x}\right) + \left(\frac{\partial x'}{\partial y}\right)\left(\frac{\partial y'}{\partial y}\right) + \left(\frac{\partial x'}{\partial z}\right)\left(\frac{\partial y'}{\partial z}\right)}{\det\left(\overline{\overline{J}}\right)}$$

$$\varepsilon^{yy} = \frac{\left(\frac{\partial y'}{\partial x}\right)^2 + \left(\frac{\partial y'}{\partial y}\right)^2 + \left(\frac{\partial y'}{\partial z}\right)^2}{\det\left(\overline{\overline{J}}\right)}$$

$$\varepsilon^{xz} = \frac{\left(\frac{\partial x'}{\partial x}\right)\left(\frac{\partial z'}{\partial x}\right) + \left(\frac{\partial x'}{\partial y}\right)\left(\frac{\partial z'}{\partial y}\right) + \left(\frac{\partial x'}{\partial z}\right)\left(\frac{\partial z'}{\partial z}\right)}{\det\left(\overline{\overline{J}}\right)}$$

$$\varepsilon^{yz} = \frac{\left(\frac{\partial y'}{\partial x}\right)\left(\frac{\partial z'}{\partial x}\right) + \left(\frac{\partial z'}{\partial y}\right)\left(\frac{\partial y'}{\partial y}\right) + \left(\frac{\partial y'}{\partial z}\right)\left(\frac{\partial z'}{\partial z}\right)}{\det\left(\overline{\overline{J}}\right)} \qquad [6.4]$$

$$\varepsilon^{zz} = \frac{\left(\frac{\partial z'}{\partial x}\right)^2 + \left(\frac{\partial z'}{\partial y}\right)^2 + \left(\frac{\partial z'}{\partial z}\right)^2}{\det\left(\overline{\overline{J}}\right)}$$

Because of the covariance, the classical electromagnetic relations are conserved in this new space:

$$\vec{B}' = \mu_0 \mu' \vec{H}' \text{ and } \vec{E} = \varepsilon_0 \varepsilon' \vec{E}' \quad [6.5]$$

In these relations, μ' and ε' are tensors where the components depend on the spatial coordinates *u, v* and *w*. Generally, the new material corresponding to this new space is anisotropic.

6.1.2. *First example: waveguide taper*

6.1.2.1. *Design*

We will see in this example that the design stage is very important: firstly, because the theoretical values of electromagnetic parameters calculated by transformation optics [6.3] are often too extreme to be practically achieved, even with metamaterials. Therefore, a careful design should allow a simplification of these values. Moreover, in some cases, the permittivity and permeability tensors have non-diagonal terms that are difficult to implement. To facilitate the realization of structures, it is important to minimize or cancel these terms. In all cases, for a real device, the parameter values should be achievable with available electromagnetic metamaterials. Secondly, a practical implementation requires a discretization of the theoretical material. This discretization, which is often accompanied by performance degradation, must maintain the degradation at an acceptable level. A trade-off is necessary between the level of discretization and the degradation of structure performance due to this discretization. The space transformation technique can also be used to transform the profile of an isotropic material with a singularity into an equivalent anisotropic material, leading to a more easily realizable device. For example, dielectric singularities are points where the refractive index *n* tends toward infinity or zero and where electromagnetic waves travel infinitely slowly or infinitely fast. Such singularities cannot be realized in practice over a broad spectral range, but the index profile can be transformed into an anisotropic tensor of permittivity and permeability. Thus, bounded values of the permittivity and permeability components allow the realization of the device. After the discretization of a theoretical profile, the next metamaterial engineering step is to approach and implement the target device. Based on electric and magnetic resonances, subwavelength metamaterial cells must be properly engineered such that the effective electromagnetic parameters can reach the desired values. In the following

example, we will see an application of this method and how the values of electromagnetic parameters depend on the initial analytical relations.

In this example, we consider two rectangular waveguides with different widths, 10 and 2 cm [TIC 10]. We will design a taper between these two waveguides by transformation optics respecting a good impedance matching (Figure 6.4). This example shows that the output parameters given by transformation optics are often unrealistic and that they need a careful optimization to allow a possible realization. Each waveguide is represented by black lines in its respective space given in Cartesian coordinates. The aim is to connect the horizontal lines between the spaces to allow for the transmission of electromagnetic waves. Thus, in the geometric approximation, each ray of light in the first waveguide is guided into the second waveguide by the taper. For the first formulation, a linear transformation may be assumed by connecting the two spaces with straight lines as shown in Figure 6.4(a). The second formulation uses a parabolic transformation to achieve the connection (Figure 6.4(b)). For the third formulation, an exponential transformation is defined as shown in Figure 6.4(c). In all three cases, the geometrical properties of the schema under analysis remain unchanged. The widths of the input and output waveguides are denoted by a and b, respectively, and the length of the taper in all three cases is taken to be l. Mathematical expressions defining each formulation of the transformation approaches are given in Figure 6.4. x', y' and z' are the coordinates in the transformed (new) space and x, y and z are those in the initial space. As can be observed from the mathematical expressions, the different formulations depend on the geometric parameters (a, b, l).

These three profiles correspond to the analytical relations of Figure 6.4. Applying the procedure described in [6.3] gives the electromagnetic parameters of the material corresponding to the transformed space between the two waveguides that are given by the following relations:

$$\overline{\overline{\varepsilon}} = \overline{\overline{\theta}}\varepsilon_0, \overline{\overline{\mu}} = \overline{\overline{\theta}}\mu_0 \text{ and } \frac{J_i^{i'} J_j^{j'} \delta^{ij}}{\det(J)} = \theta^{i'j'} \quad [6.6]$$

with:

$$\overline{\overline{\theta}} = \begin{pmatrix} \theta_{xx}(x') & \theta_{xy}(x', y') & 0 \\ \theta_{xy}(x', y') & \theta_{yy}(x', y') & 0 \\ 0 & 0 & \theta_{zz}(x') \end{pmatrix} \quad [6.7]$$

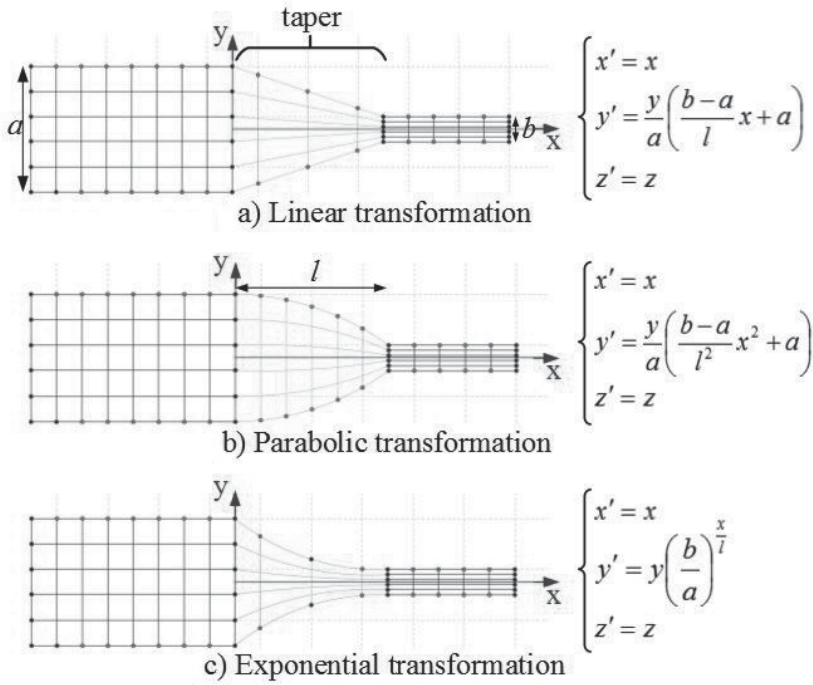

Figure 6.4. *Three possible transformed taper profiles between two rectangular waveguides with different cross-sections. a) Linear, b) parabolic and c) exponential transformation formulation*

Figure 6.5 shows the variation of the electromagnetic parameters calculated with [6.6]. We can observe that the values of the extrema are very high in the first case (linear) and the second case (parabolic). These values are much lower in the third case (exponential). In fact, only the third case is really achievable. This first calculation illustrates how the choice of shape of the transformed space determines the final values of electromagnetic parameters to be realized. We must also note in this example that the values of the permittivity and permeability are identical, given a perfect impedance matching between the theoretical material and the surrounding vacuum.

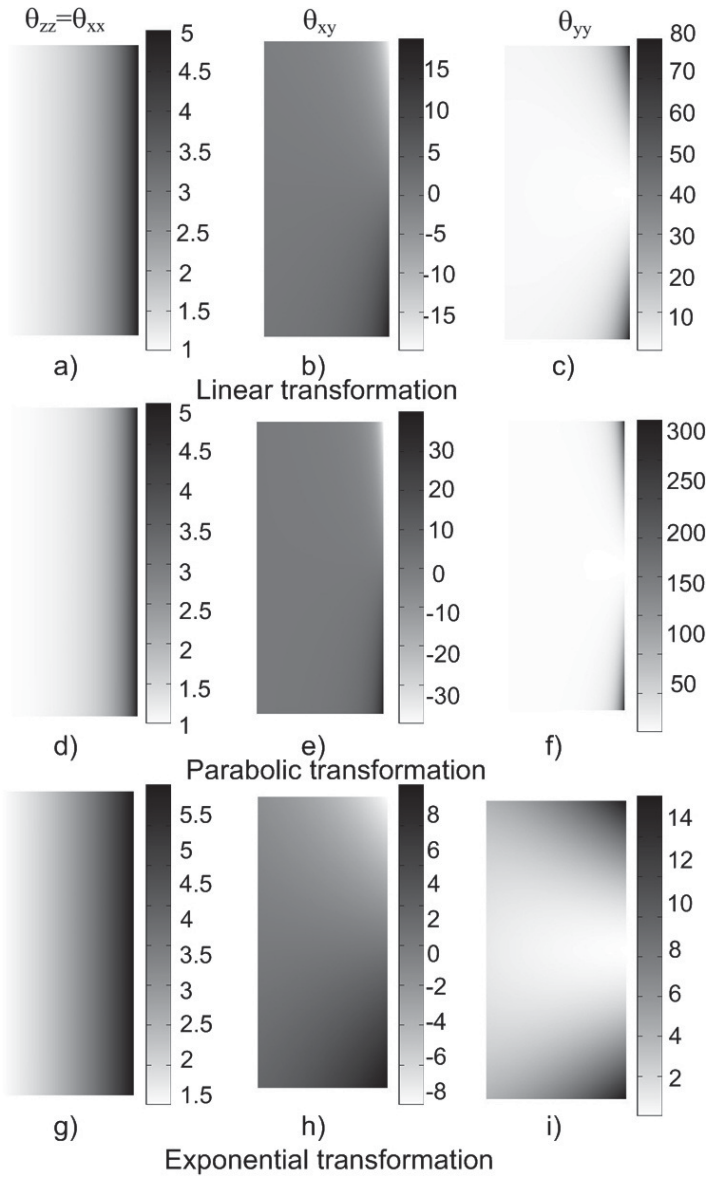

Figure 6.5. *Variation of the electromagnetic components of the tensors ε and μ. The exponential transformation is the most suitable because it leads to values achievable with metamaterials*

6.1.2.2. *Simulations*

To verify the results expressed in the previous section, the finite element based commercial software Comsol MULTIPHYSICS is used to simulate the described waveguide taper. Two-dimensional simulations are performed for the validation of the proposed material parameters. Ports are used to excite the first and third transverse electric (TE_1 and TE_3) modes of the input waveguide, with the E-field directed along the *z*-axis to verify the conservation of modes through the taper. The waveguide boundaries are assumed to be perfect electric conductors (PECs) and matched boundary conditions are applied to the taper. Verifications are made in the microwave domain for a possible future physical prototype based on metamaterials. The waveguide widths are chosen to be a = 10 cm and b = 2 cm with 1.5 and 7.5 GHz cutoff frequencies, respectively. The length of the taper is chosen as l = 5 cm, thus allowing the generation of the entire spatial dependence of the material parameters $\theta_{xx}(x')$, $\theta_{zz}(x')$, $\theta_{xy}(x',y')$ and $\theta_{yy}(x',y')$ as shown in Figure 6.5. These distributions are plotted from the expressions given in Table 6.1. Values of permittivity and permeability shown in Figure 6.5 account for the control of the electromagnetic field in the taper and the conservation of the propagating modes from the first large waveguide to the second narrow waveguide.

Transformation	$\theta_{xx}(x')= \theta_{zz}(x')$	$\theta_{xy}(x',y')$	$\theta_{yy}(x',y')$
Linear	$\frac{al}{a\,(l-x')+b\,x'}$	$\theta_{xx}^2\,\frac{b-a}{al}\,y'$	$\frac{1}{\theta_{xx}}+\frac{\theta_{xy}^2}{\theta_{xx}}$
Parabolic	$\frac{al^2}{(al^2-a\,x'^2+b\,x'^2)}$	$\frac{2\theta_{xx}^2(b-a)\,x'y'}{al^2}$	$\frac{1}{\theta_{xx}}+\frac{\theta_{xy}^2}{\theta_{xx}}$
Exponential	$\left(\frac{b}{a}\right)^{-\frac{x'}{l}}$	$\frac{\theta_{xx}y'\ln\left(\frac{b}{a}\right)}{l}$	$\frac{1}{\theta_{xx}}+\frac{\theta_{xy}^2}{\theta_{xx}}$

Table 6.1. *Analytical expressions of the different components of the electromagnetic tensors*

Although the same spatial distribution profile can be observed for the three different formulations, the parameter values are completely different.

For the linear and parabolic transformations, values of μ_{yy} are too high to be physically achievable with existing metamaterials. However, it is clear that the exponential transformation leads to values more easily achievable with metamaterials. Moreover, the physical realization of such a metamaterial taper will be facilitated by the slow variation of the material parameters, implying a gradual variation in the geometric parameters of metamaterial inclusions. Note that the components are calculated in the Cartesian system and respect the following dispersion relation in the *TE* mode:

$$\varepsilon_{zz}\left(\mu_{xy}{}^{2}-\mu_{xx}\mu_{yy}\right)+\mu_{xx}k_{x}{}^{2}+k_{y}\left(\mu_{yy}k_{y}-2\mu_{xy}k_{x}\right)=0 \qquad [6.8]$$

This relation is obtained from the propagation equation and describes the control of electromagnetic waves in the material. This relation is also important for future reduction of parameters, which can be done by simplifying the non-diagonal parameter θ_{xy} to a closed interval near zero when choosing the appropriate length of the taper. For example, by bounding the non-diagonal term of the exponential formulation in Table 6.1, the condition $l > \frac{a^2}{b}\frac{\left|\ln\left(\frac{b}{a}\right)\right|}{2\Delta}$ leads to $-\Delta < \mu_{xy} < \Delta$ where Δ can be very close to zero. We can then minimize this non-diagonal term.

Simulation results for the E-field distribution of the structure under study for all three transformations are shown in Figure 6.6. The distributions in the tapered waveguides are compared to a non-tapered case at 10 GHz for the fundamental (TE_1) excitation mode and at 30 GHz for the third (TE_3) excitation mode. Concerning the non-tapered junction waveguides, phase distortions may be observed due to reflections at the junction from the larger waveguide to the smaller waveguide (Figure 6.6(a) – (c)). These distortions become more severe at higher frequencies (30 GHz). However, simulations performed on the tapered waveguides (Figure 6.6(d) – (l)) illustrate that electromagnetic waves are properly guided from one waveguide to the other, without any impact on the guided mode when the transformed medium is embedded between the two waveguides. The difference in the transformation formulations indicates a change in the path of electromagnetic waves in the tapered section, highlighted by the shaded gray area in Figure 6.6.

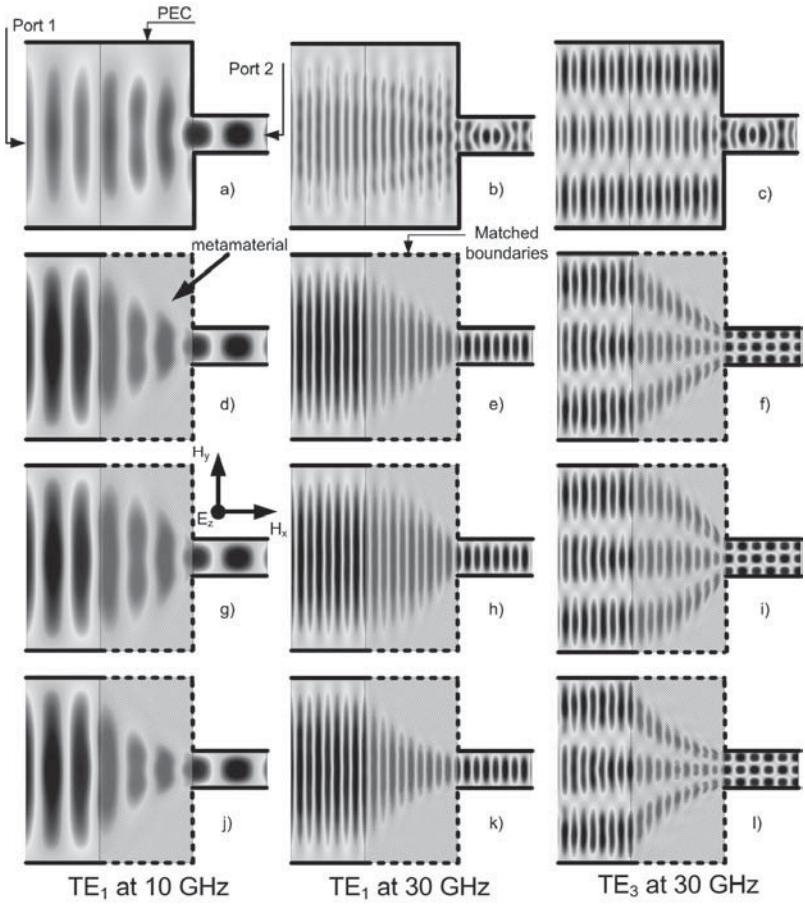

Figure 6.6. *Normalized E-field distribution for TE polarization. a)–c) Non-tapered junction waveguides, d)–f) Tapered junction waveguides with linear transformation. g)–i) Tapered junction waveguides with parabolic transformation. j)–l) Tapered junction waveguides with exponential transformation*

Increasing the frequency improves the transmission between the two waveguides through the tapered section. This phenomenon can be observed when the E-field distributions are compared at 10 and 30 GHz. At 10 GHz, a slight impedance mismatch between the taper output and the small waveguide input can be observed. This phenomenon decreases at higher frequencies, as illustrated for 30 GHz.

6.2. Applications to antennas

6.2.1. *Directive antenna*

This second example describes the design of a highly directive antenna based on the transformation of an isotropic source, radiating in a cylindrical space, into a directive antenna radiating in a rectangular space [TIC 11a]. In this example, we physically realize the proposed theoretical design after a discretization of the theoretical material obtained by transformation optics. We begin by deriving the permeability and permittivity tensors of a metamaterial able to transform the isotropic source into a compact highly directive antenna in the microwave domain. The aim is to show how a judiciously engineered metamaterial allows the emission direction of a source to be controlled in order to collect all the energy in a small angular domain around the surface normal, with good impedance matching between the radiating source and the material obtained by transformation optics.

6.2.1.1. *Theoretical formulation*

For the theoretical formulation of the highly directive emission, we consider a line source radiating in a cylindrical vacuum space (Figure 6.7). The line source is placed along the cylindrical axis. Wave fronts represented by cylinders at r = constants and polar coordinates (r, θ) are appropriate to describe such a problem. To transform the cylindrical space, a physical space where lines θ = constant become horizontal is generated, as illustrated by the schematic principle in Figure 6.7. Each circle of the initial cylindrical space becomes a vertical line in the final rectangular space, whereas each radial line becomes a horizontal line. Finally, the right half-cylinder of diameter d is transformed into a rectangular region with width e and length L. The line source in the center of the cylinder becomes the left black vertical radiating surface in the rectangular space. The transformation can then be expressed as:

$$\begin{cases} x' = \dfrac{2L}{d}\sqrt{x^2+y^2} \\ y' = \dfrac{e}{\pi}\arctan\left(\dfrac{y}{x}\right) \text{ with } -\dfrac{\pi}{2} \le \arctan\left(\dfrac{y}{x}\right) \le \dfrac{\pi}{2} \\ z' = z \end{cases} \qquad [6.9]$$

where x', y' and z' are the coordinates in the transformed rectangular space and x, y, z are those in the initial cylindrical space. Free space is assumed in the cylinder, with isotropic permeability and permittivity tensors ε_0 and μ_0. The following transformations are used to obtain the material parameters of the rectangular space:

$$\varepsilon^{i'j'} = \frac{J_i^{i'} J_j^{j'} \varepsilon_0 \delta^{ij}}{\det(J)} \text{ and } \mu^{i'j'} = \frac{J_i^{i'} J_j^{j'} \mu_0 \delta^{ij}}{\det(J)} \text{ with } J_\alpha^{\alpha'} = \frac{\partial x'^{\alpha}}{\partial x^{\alpha}} \qquad [6.10]$$

where $J_\alpha^{\alpha'}$ and δ^{ij} are, respectively, the Jacobian transformation matrix of the transformation of [6.9] and the Kronecker symbol ($\delta^{ij} = 1$ if $i = j$ and 0 otherwise). The Jacobian matrix between the transformed and the original coordinates has four non-zero parameters that depend on the distance from the origin. J_{xx}, J_{yy} and J_{xy} are assumed to be z-independent with $J_{zz} = 1$. The divergence of J_{yy} can be explained by the non-bijection of the initial coordinates y-lines transformation. The inverse transformation is obtained from the initial transformation [6.9] and derived by a substitution method, enabling the metamaterial design, which leads to anisotropic permittivity and permeability tensors. Both electromagnetic parameters μ and ε have the same behavior. Also, note that the equality of permittivity and permeability tensors implies a perfect impedance which matches with no reflection at the interface with vacuum.

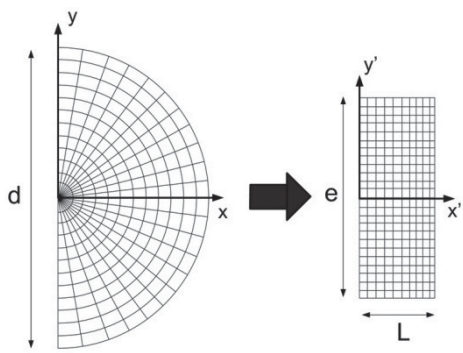

Figure 6.7. *Representation of the transformation of the initial space into the desired space. Each radius line of the cylindrical space is transformed into a horizontal line of the right rectangular space. Each circular line is transformed into a vertical line*

Using equation [6.10] and substituting the new coordinate system in the tensor components, the following material parameters are derived:

$$\overline{\overline{\varepsilon}} = \begin{pmatrix} \varepsilon_{xx}(x',y') & 0 & 0 \\ 0 & \varepsilon_{yy}(x',y') & 0 \\ 0 & 0 & \varepsilon_{zz}(x',y') \end{pmatrix} \varepsilon_0 \text{ and}$$
$$\overline{\overline{\mu}} = \begin{pmatrix} \mu_{xx}(x',y') & 0 & 0 \\ 0 & \mu_{yy}(x',y') & 0 \\ 0 & 0 & \mu_{zz}(x',y') \end{pmatrix} \mu_0 \qquad [6.11]$$

where:

$$\varepsilon_{xx}(x',y') = \mu_{xx}(x',y') = \frac{\pi}{e}x'; \varepsilon_{yy}(x',y') = \mu_{yy}(x',y') = \frac{1}{\varepsilon_{xx}(x',y')}; \ \varepsilon_{zz} = \mu_{zz} = \frac{d^2\pi}{4eL^2}x' \qquad [6.12]$$

The appropriate choice of the transformation thus assures an absence of non-diagonal components, giving rise to a practical implementation of the device using metamaterials.

Figure 6.8 shows the variation of the permittivity tensor components in the transformed rectangular space. The different geometrical dimensions of the initial and transformed space are, respectively, d = 15 cm, e = 15 cm and L = 15 cm. Note that the three components of the permittivity depend only on the coordinate x'. This is due to the invariance of the initial space with θ, with respect to the distance from the source in the cylindrical space. This distance is represented by x' in the transformed rectangular space.

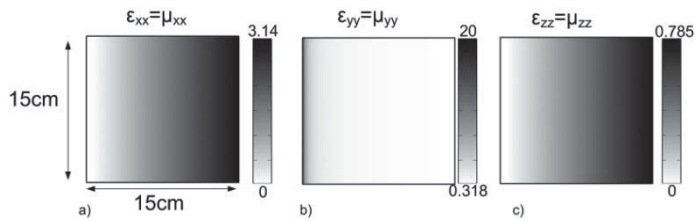

Figure 6.8. *Variation of the permittivity tensor components: a) ε_{xx}, b) ε_{yy}, and c) ε_{zz}*

The divergence of ε_{yy} near $x' = 0$ creates an "electromagnetic wall" with ε_{yy} tending toward infinity on the left side of the rectangular area. This left side also corresponds to the radiating source transformed from the center line

source of the initial cylindrical space. Note the simplicity of the ε_{xx} and ε_{zz} terms that present only a linear variation.

6.2.1.2. *Simulations*

Finite element method (FEM) based numerical simulations with Comsol Multiphysics are used to simulate this theoretical transformed directive antenna. As the line source of the right half-cylindrical space becomes a radiating plane in the transformed rectangular space, an excitation is inserted at the left side of the rectangular space as shown in Figure 6.9(a). This space is delimited by metallic boundaries on the upper and lower sides and at the left side of the rectangular space representing the metamaterial with dimensions of 15 cm × 5 cm. The radiating properties of the antenna are calculated and shown in Figure 6.10.

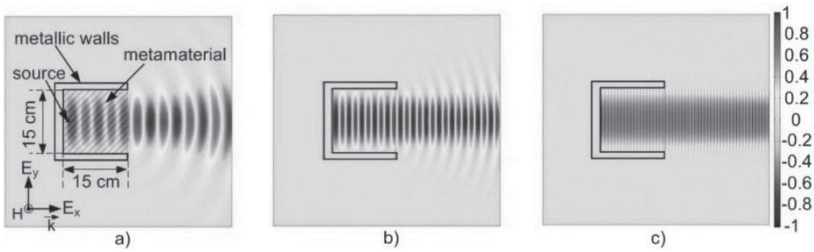

Figure 6.9. *a) Magnetic field distribution for a TM wave polarization at a) 5 GHz, b) 10 GHz and c) 40 GHz*

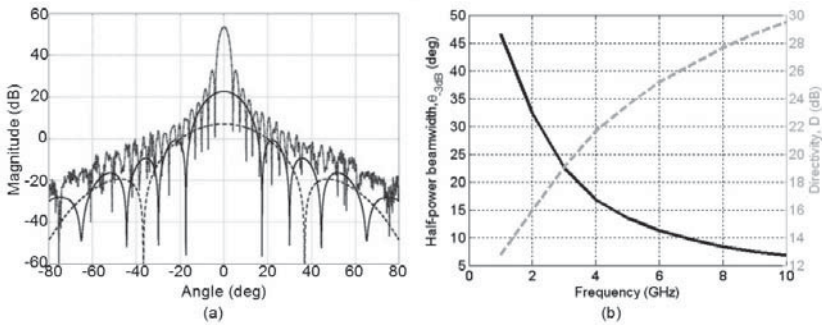

Figure 6.10. *a) Far field radiation patterns at 5 GHz (dashed), 10 GHz (continuous) and 40 GHz (dashed–dotted). b) Half-power beamwidth (continuous) and directivity (dashed) versus frequency*

Three operating frequencies have been considered here; 5, 10 and 40 GHz, corresponding, respectively, to e/λ = 2.5, 5 and 20. A directive emission can be observed as illustrated by the magnetic field radiations of the antenna for a TM wave polarization. A very high directivity is noted and can be calculated using the expression given in [BAL 97]:

$$D = 41253 / (\theta_1 \theta_2) \quad [6.13]$$

where θ_1 and θ_2 are, respectively, the half-power beamwidths (in degrees) for the H-plane and E-plane patterns. Here, we assume $\theta_1 = \theta_2$. Then, for a half-power beamwidth of 13.5° at 10 GHz, a directivity of 23.6 dB is obtained, implying a ratio e/λ = 5. This directivity is comparable with that of a parabolic reflector antenna of the same size [BAL 97] and is greater than that of a wideband (2–18 GHz) dual-polarized FLANN® horn antenna where the directivity varies from 10 to 23 dB. The far-field radiation patterns of the antenna are calculated at different frequencies to assess the variation of the directivity. The dimensions of the rectangular box remain the same as above (e = 15 cm and L = 5 cm). Figure 6.10(a) shows the radiation patterns for the cases e/λ = 2.5 (5 GHz), 5 (10 GHz) and 20 (40 GHz). The directivity strongly increases as the frequency increases. In fact, increasing the frequency allows us to approach geometric optics and thus ensures that the signal perfectly follows the geodesics of the transformed space. It goes from 23.6 dB at 5 GHz, to 29.5 dB at 10 GHz, and 42 dB at 40 GHz. The directivity enhancement is illustrated by the evolution of the half-power beamwidth versus frequency in Figure 6.10(b). This increase in the directivity is mainly due to the reduction of the diffraction of the wave by the antenna aperture.

6.2.1.3. *Parameter reduction and discrete metamaterial layers*

The metamaterial calculated above shows coordinate-dependent electromagnetic parameters following [6.12]. This dependency is identical for the permittivity and permeability, allowing an exact impedance matching with vacuum. It is proposed to simplify the calculated parameters of the highly directive antenna for a realistic experimental realization from achievable metamaterial structures. Choosing plane wave solutions for the electric field and magnetic field, with a wave vector $\boldsymbol{k}$ in the xy plane, and a *TM* or a *TE* polarization with, respectively, the magnetic or electric field polarized along the z-axis, a dispersion equation is obtained:

$$\det(F) = 0 \quad [6.14]$$

$$\text{with } F = \begin{pmatrix} \varepsilon_{xx} - \dfrac{k_y^2}{\mu_{zz}} & \dfrac{-k_x k_y}{\mu_{zz}} & 0 \\ \dfrac{-k_x k_y}{\mu_{zz}} & \varepsilon_{yy} - \dfrac{k_x^2}{\mu_{zz}} & 0 \\ 0 & 0 & \varepsilon_{zz} - \dfrac{k_x^2}{\mu_{yy}} - \dfrac{k_y^2}{\mu_{xx}} \end{pmatrix} \quad [6.15]$$

The determinant of this equation must be equal to zero. By solving it, one equation is obtained for each polarization. In the *TE* polarization, this equation can be written as:

$$\varepsilon_{zz} = \frac{k_x^2}{\mu_{yy}} = \frac{k_y^2}{\mu_{xx}} \quad [6.16]$$

whereas in the *TM* polarization, it becomes:

$$\mu_{zz} = \frac{k_x^2}{\varepsilon_{yy}} = \frac{k_y^2}{\varepsilon_{xx}} \quad [6.17]$$

For a possible realization, the dimensions of the semi-cylindrical space must be set so that $d^2/4L^2 = 4$ in order to obtain achievable values for the electromagnetic parameters. An additional simplification arises from the choice of the polarization of the emitted wave. Here, consider a polarized electromagnetic wave with an electric field pointing in the *z*-direction, which allows us to modify the dispersion equation in order to simplify the electromagnetic parameters, without changing Maxwell's equations and propagation in the structure. To obtain these electromagnetic parameter values that are suitable for the manufacturing technology, the same method is used as proposed in [SCH 06a]. The dispersion equation is multiplied by μ_{xx} and the metamaterial is thus simply described by:

$$\begin{cases} \mu_{xx} = 1 \\ \mu_{yy} = \dfrac{1}{\varepsilon_{xx}^2} \\ \varepsilon_{zz} = 4\varepsilon_{xx}^2 \end{cases} \quad [6.18]$$

Equation [6.18] describes the material parameters that can be achieved with existing metamaterial structures, for example split ring resonators (SRRs) [PEN 99] and electric-LC (ELC) resonators [SCH 06b]. The penalty of the above reduction is an imperfect impedance match at the outer boundary of the metamaterial at $Z = \sqrt{\frac{\mu_{yy}}{\varepsilon_{zz}}}\left(x = L\right) = \frac{9}{2\pi^2}$ with L = 5 cm and d = 15 cm. Thus, the transmission at the outer boundary is calculated classically with $T = \frac{4Z}{\left(1+Z\right)^2} = 0.85$, which assures a high level of radiated electromagnetic field. Further simplification consists of discretizing the desired variation of the parameters μ_{yy} and ε_{zz} to secure a practical realization that produces experimental performances close to theory.

Figure 6.11(a) shows the schematic structure of the directive emission antenna. A microstrip patch antenna on a dielectric substrate constitutes the radiating source. A surrounding material made up of alternating electric metamaterial and magnetic metamaterial layers transforms the isotropic emission of the patch antenna into a directive emission. The material is composed of five different regions where permittivity and permeability vary according to the profile of Figure 6.11(c). The corresponding reduced magnetic and electric properties of the metamaterial obtained from transformation optics are shown in Figure 6.11(b) and (c). The distribution of the theoretical material parameters satisfying relation [6.18] is shown in Figure 6.11(b). The distribution in Figure 6.11(c) presents the discrete values corresponding to the five regions of the metamaterial used for the experimental validation. To implement the material specifications in equation [6.18] using metamaterials, we must choose the overall dimensions, design the appropriate unit cells and specify their layout. For this implementation, the metamaterial unit cell is not periodic. It is advantageous to optimize the three design elements all at once since common parameters are shared. Equation [6.18] shows that the desired ultra-directive emission will have constant μ_{xx}, with ε_{zz} and μ_{yy} varying longitudinally throughout the structure. The axial permittivity ε_{zz} and permeability μ_{yy} show values ranging from 0.12 to 4.15 and from 1.58 to 15.3, respectively. We can note that this design is more complicated than the cloak structure of Pendry and Smith [SCH 06a] as the two parameters vary simultaneously whereas only the permeability vary in the cloak.

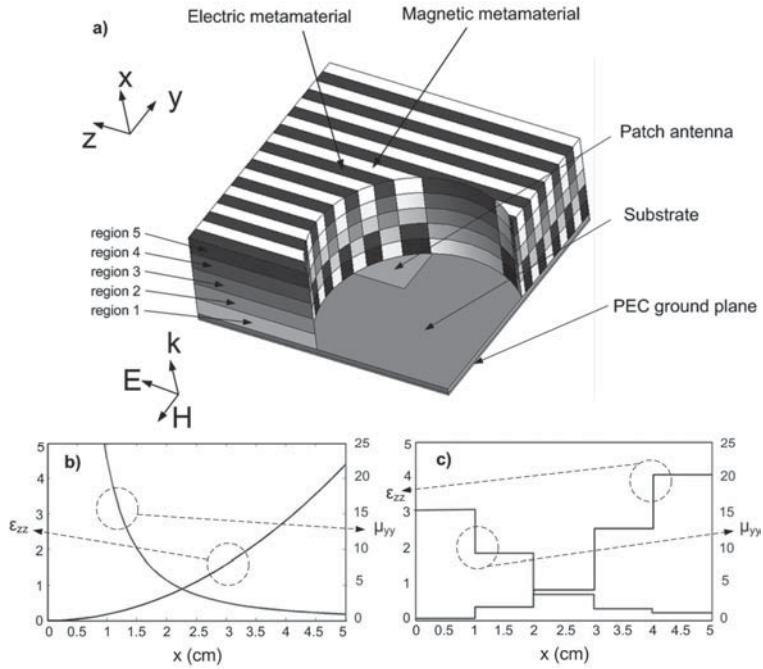

Figure 6.11. *a) Schematic structure of the proposed antenna with a cylindrical cut to show the internal structure of the material and the radiating source. This source is a microstrip patch antenna on a dielectric substrate. The metamaterial is composed of alternating vertical permittivity and permeability layers. Each layer is made up of five different material regions. b) Theoretical material parameters given by relation [6.18]. c) Discrete values of material parameters used in experimental realization*

6.2.1.4. *Realization*

As shown by the schematic structure of the antenna in Figure 6.11(a), a square copper patch is printed on a 0.787 mm thick low-loss dielectric substrate (Rogers RT/Duroid 5870^{TM} with 17.5 μm copper cladding, $\varepsilon_r = 2.33$ and tan $\delta = 0.0012$) and used as the feed source. The metamaterial the patch feed source to capture the emanating isotropic radiation and completely covers transform it into a directive pattern. The metamaterial is a discrete structure composed of alternating layers with anisotropic permeability and permittivity. Figure 6.12 shows photography of the fabricated antenna device. The bulk metamaterial was built from 56 layers of dielectric boards on which subwavelength resonant structures are printed. Twenty-eight layers contain

artificial magnetic resonators and 28 contain electric resonators. Each layer is made up of five regions of metamaterials corresponding to the discretized values of Figure 6.11(c). The layers are mounted 2 by 2 with a constant air spacing of 2.2 mm between each, in order to best represent the permeability and permittivity characteristics in the different regions. Overall dimensions of the antenna are 15 cm × 15 cm × 5 cm.

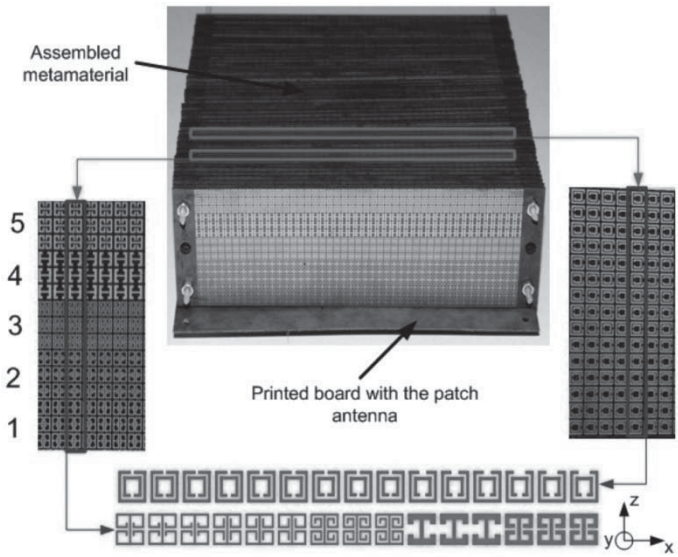

Figure 6.12. *Structure of the antenna: each magnetic and dielectric layer of the metamaterial is divided into five regions to assure the desired variations of electromagnetic parameters along the wave propagation direction. The dimensions of the antenna are 15 cm × 15 cm × 5 cm. The operating frequency is 10.6 GHz. Left and right inserts show details of the resonators used in the magnetic (right) and electric (left) metamaterial layers. Each level is made up of three rows of identical resonators*

The details of the metamaterial cells are illustrated in Figure 6.12. The left and right patterns show the designs of the resonators used in the magnetic (right) and electric (left) metamaterial layers. The layers are divided into five regions in the direction of wave propagation. Each region is composed of three rows of resonators with identical geometry and dimensions. Different resonators are used for electric and magnetic layers. Their schematic drawings are depicted at the bottom of Figure 6.12. The permeability (μ_{yy}) and permittivity (ε_{zz}) parameter sets plotted in Figure 6.11(c) can be, respectively, achieved in a composite metamaterial containing SRRs and

ELCs, known to provide, respectively, a magnetic response and an electric response that can be tailored (Figure 6.12).

Due to layout constraints, a rectangular unit cell with dimensions $p_x = p_z = 10/3$ mm was chosen for both resonators. These dimensions must be much lower than the wavelength at the designated frequency (f = 10 GHz, λ = 3 cm) to satisfy the condition of an equivalent effective material [DE 07]. The layout consisted of five regions, each of which was three unit cells long (10 mm). The desired ε_{zz} and μ_{yy} were obtained by tuning the resonators' geometric parameters. Using the Ansoft HFSS commercial full-wave finite element simulation software, a series of simulations were performed for the SRR and ELC unit cells separately over a discrete set of the geometric parameters covering the range of interest. A normally incident wave impinging on the unit cell is considered for simulations. Electric and magnetic symmetry planes are applied on the unit cell, respectively, for the faces normal to the electric and magnetic field vector. By calculating the unit cells separately, there is very low coupling between neighboring ELCs and SRRs. The influence of this coupling is even lower when the electric and magnetic layers are mounted 2 by 2. This mounting better satisfies the conditions for an effective material. A standard retrieval procedure was then performed to obtain the effective material properties ε_{zz} and μ_{yy} from the *S*-parameters [NIC 70].

The discrete set of simulations and extractions was interpolated to obtain the particular values of the geometric parameters that yielded the desired material properties plotted in Figure 6.11(c). Simulations were also performed using Comsol Multiphysics to assure the functionality of the metamaterial. An operating frequency of approximately 10 GHz was chosen, which yields a reasonable effective medium parameter $\lambda/p_x > 10$, where λ is the free-space wavelength.

6.2.1.5. *Experimental measurement of the ultra-directive antenna*

To validate the directive emission device performance, the far-field radiation pattern of the antenna is measured in an anechoic chamber. Figure 6.13(a) shows the far-field measurement system. In such an emission-reception set-up, the fabricated metamaterial antenna is used as an emitter and a wideband (2–18 GHz) dual-polarized horn antenna is used as the receiver to measure the radiated power level of the radiating antenna. The measurements are performed for computer-controlled elevation angles varying from –90° to +90°. The microwave source is a vector network analyzer (Agilent 8722 ES) that was also used for detection. The feeding port is connected to the

metamaterial antenna by means of a coaxial cable whereas the detecting port is connected to the horn antenna also by means of a coaxial cable. The measured far-field radiation pattern in the E-plane (plane containing E and k vectors) is shown in Figure 6.13(b). The antenna presents maximum radiated power at 10.6 GHz with a directive main beam and low parasitic secondary lobes, under –15 dB. The main lobe presents a 13° half-power beamwidth in the E-plane (x–y plane). This narrow beamwidth is less than that of a parabolic reflector antenna with similar dimensions (diameter equal to 15 cm), where the half-power beamwidth is approximately 16°. Measurements are found to be consistent with the predicted radiation patterns shown in Figure 6.13(c).

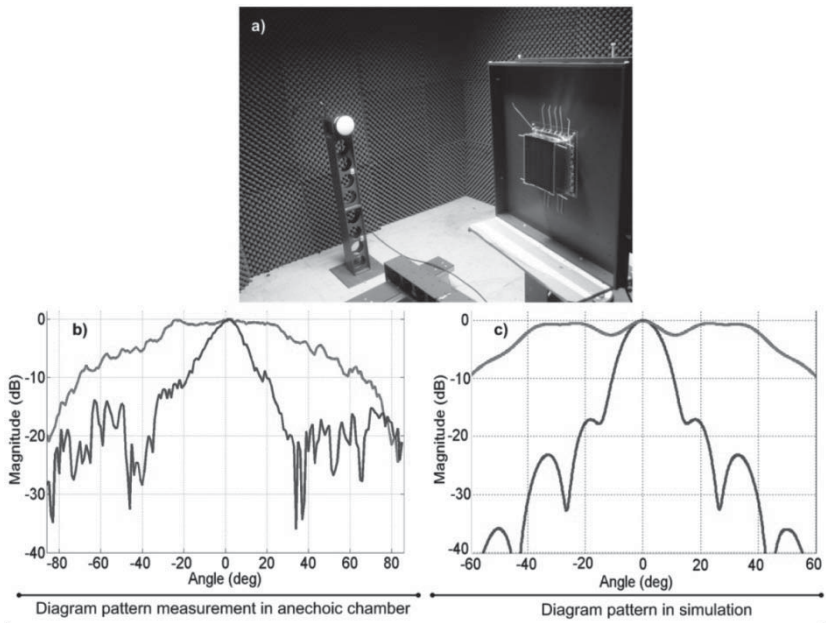

Figure 6.13 . *Far-field measurement in an anechoic chamber. a) Experimental set-up. b) Measurements. c) Simulations. Radiation patterns of the metamaterial antenna (____) and of the feeding microstrip patch antenna alone (--o--) are presented at 10.6 GHz*

This example shows that it is possible to design and realize a directive antenna application by transformation optics with magnetic and electric

metamaterials such as SRRs and ELCs. In the following section, we will study the inverse transformation.

6.2.2. *Isotropic antenna*

In contrast to the previous example where a quasi-isotropic emission was transformed into a directive emission, here we describe how coordinate transformation can be applied to transform a directive emission into an isotropic emission [TIC 11b]. We will also show how transformation electromagnetics can modify the apparent (electromagnetic) size of a radiating object. Here, we do not describe the realization of the practical antenna as the process is identical to the one presented in the previous section.

6.2.2.1. *Theoretical design*

An intuitive schematic principle used to illustrate the proposed method is given in Figure 6.14. Consider a source radiating in a circular space, as shown in Figure 6.14(a), where a circular region bounded by the black circle around this source limits the radiation zone. Here, a "space stretching" technique is applied. The "space stretching" coordinate transformation consists of exponentially stretching the central zone of this delimited circular region represented by the shaded circle as illustrated in Figure 6.14(b).

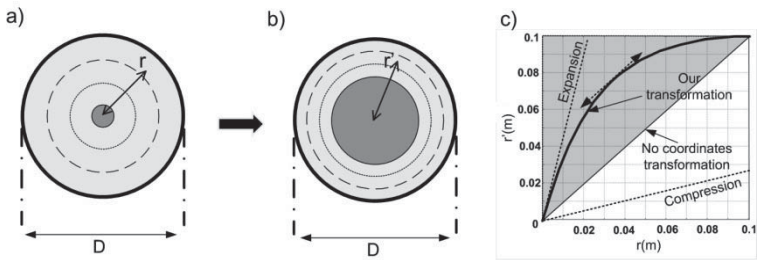

Figure 6.14. *a) Initial space, b) transformed space, c) the black curve shows the transformation rule made of an expansion followed by a compression*

However, a good impedance match must be preserved between the stretched space and the exterior vacuum. Thus, the expansion procedure is followed by a compression of the annular region formed between the shaded and black circles so as to secure an impedance match with free space. Figure 6.14(c) summarizes the exponential form of the coordinate transformation. The

diameter of the transformed circular medium is denoted by D. Mathematically, this transformation is expressed as [6.11]:

$$\begin{cases} r' = \alpha(1 - e^{qr}) \\ \theta' = \theta \\ z' = z \end{cases} \quad \text{with } \alpha = \frac{\mathrm{D}}{2}\frac{1}{1 - \mathrm{e}^{\frac{q\mathrm{D}}{2}}} \qquad [6.19]$$

where r', θ' and z' are the coordinates in the transformed cylindrical space, and r, θ and z are those in the initial cylindrical space. In the initial space, free-space conditions are assumed with isotropic permittivity and permeability tensors ε_0 and μ_0. Parameter q (in m^{-1}) appearing in equation [6.19] must be negative in order to achieve the impedance matching condition. This parameter is an expansion factor, which can be physically viewed as the degree of space expansion. A high (negative) value of q means high expansion, whereas a low (negative) value of q means nearly zero expansion. Calculations lead to permeability and permittivity tensors given in the diagonal base by:

$$\begin{aligned} \overline{\overline{\varepsilon}} = \overline{\overline{\psi}}\varepsilon_0 \text{ and } \overline{\overline{\mu}} = \overline{\overline{\psi}}\mu_0 \text{ with } \overline{\overline{\psi}} &= \begin{pmatrix} \psi_{rr} & 0 & 0 \\ 0 & \psi_{\theta\theta} & 0 \\ 0 & 0 & \psi_{zz} \end{pmatrix} \\ &= \begin{pmatrix} \dfrac{qr(r'-\alpha)}{r'} & 0 & 0 \\ 0 & \dfrac{r'}{qr(r'-\alpha)} & 0 \\ 0 & 0 & \dfrac{r}{r'q(r'-\alpha)} \end{pmatrix} \end{aligned} \qquad [6.20]$$

$$\text{where } \mathrm{r} = \frac{\ln\left(1 - \dfrac{\mathrm{r}'}{\alpha}\right)}{q}$$

The components in the Cartesian coordinate system are calculated and are as follows:

$$\begin{cases} \psi_{xx} = \psi_{\mathrm{rr}}\cos^2(\theta) + \psi_{\theta\theta}\sin^2(\theta) \\ \psi_{xy} = \psi_{yx} = (\psi_{\mathrm{rr}} - \psi_{\theta\theta})\sin(\theta)\cos(\theta) \\ \psi_{yy} = \psi_{\mathrm{rr}}\sin^2(\theta) + \psi_{\theta\theta}\cos^2(\theta) \end{cases} \qquad [6.21]$$

The ε and μ tensor components present the same behavior as given in equation [6.20]. Figure 6.15 shows the variation of the permittivity and permeability tensor components in the newly generated transformed space. The geometric dimension D is chosen to be 20 cm and parameter q is fixed at –40 m^{-1}. It can be noted that components ψ_{xx}, ψ_{yy} and ψ_{zz} present variations and an extremum that are simple to realize with commonly used metamaterials by reducing their inhomogeneous dependence. At the center of the transformed space, ε and μ present very low values (<<1).

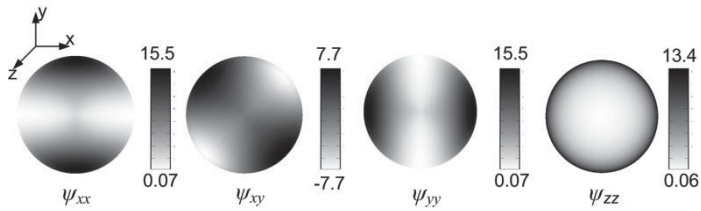

Figure 6.15. *Variation in the permeability and permittivity tensor components of the transformed space for D = 20 cm and q = –40 m^{-1}*

Consequently, light velocity and the corresponding wavelength are much higher than in vacuum. The width of the plane source then appears very small compared to wavelength and the source can then be regarded as a radiating wire, which is in fact an isotropic source. The merit of this transformation depends effectively on the expansion factor q value, and more generally, it can be applied to a wide range of electromagnetic objects, where the effective size can be reduced compared to a given wavelength. By fixing the electric field directed along the z-axis and by adjusting the dispersion equation without changing propagation in the structure, the following reduced parameters can be obtained:

$$\begin{cases} \mu_{rr} = 1 \\ \mu_{\theta\theta} = \left(\dfrac{r'}{qr(r'-\alpha)} \right)^2 \\ \varepsilon_{zz} = \left(\dfrac{r}{r'} \right)^2 \end{cases} \qquad [6.22]$$

In equation [6.22], the parameters present positive values (Figure 6.15), which can be easily achieved first by discretizing their continuous profile and second by using metamaterial resonators where magnetic and electric responses can be tailored and controlled.

6.2.2.2. *Simulations*

Figure 6.16 shows simulation results of the source radiating in the initial circular space at an operating frequency of 4 GHz for several values of q. The current direction of the source is supposed to be along the z-axis. Simulations are performed in a *TE* mode with the electric field polarized along the z-direction. The surface current source is considered to have a width of 10 cm, which is greater than the 7.5 cm wavelength at 4 GHz. Radiation boundary conditions are placed around the calculation domain in order to plot the radiation properties. Continuity of the field is assured in the interior boundaries. As previously stated and verified from the different electric field distribution patterns, a high negative value of q leads to a quasi-perfect isotropic emission since the space expansion is higher. This phenomenon can clearly be observed in Figure 6.16(d) for $q = -40\ \mathrm{m}^{-1}$.

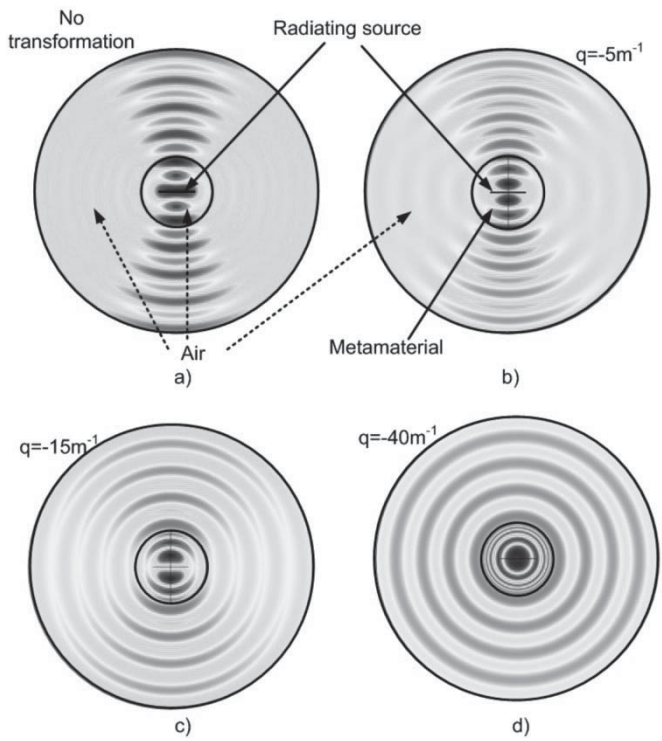

Figure 6.16. *Simulated electric field distribution for a TE wave polarization at 4 GHz. a) A planar current source is used as the excitation for the transformation. The current direction is perpendicular to the plane of the figure; b)–d) verification of the transformation for different values of expansion factor q*

6.3. Conclusions

We have presented three examples of transformation optics applications in the field of antennas. The first example showed that a careful choice of the transformation is necessary to obtain achievable values of the electromagnetic parameters. The second example gives the complete process necessary to realize a practical implementation of an antenna, calculated by transformation optics with commonly used metamaterial resonators. Finally, the third example shows that this method can be extended to the transformation of the apparent size of a source. These three examples are not exhaustive but they give an idea of the potential of this method and of its practical usage in the real world.

6.4. Acknowledgment

The authors thank the French National Research Agency for its financial support through the METAPHORT, METAVEST and METAPHOTONIQUE projects.

6.5. Bibliography

[BAL 97] BALANIS C.A., *Antenna Theory: Analysis and Design*, 2nd ed., Wiley, New York, 1997.

[DE 07] DE LUSTRAC A., *Métamatériaux, Techniques de l'Ingénieur,* vol. TIB186DUO, p. 14, 2007.

[LEO 06] LEONHARDT U., "Optical conformal mapping", *Science*, vol. 312, pp. 1777–1780, 2006.

[NIC 70] NICHOLSON A.M., ROSS G.F., "Measurement of the intrinsic properties of materials by time-domain techniques", *IEEE Transactions on Instrumentation and Measurement*, vol.19, pp. 377–382, 1970.

[PEN 99] PENDRY J.B., HOLDEN A.J., ROBBINS D.J., *et al.*, "Magnetism from conductors and enhanced nonlinear phenomena", *IEEE Transactions on Microwave Theory and Techniques*, vol. 47, pp. 2075–2084, 1999.

[PEN 06] PENDRY J.B., SCHURIG D., SMITH D.R., "Controlling electromagnetic fields", *Science*, vol. 312, pp. 1780–1782, 2006.

[SCH 06a] SCHURIG D., MOCK J.J., JUSTICE B.J., *et al.*, "Metamaterial electromagnetic cloak at microwave frequencies", *Science*, vol. 314, pp. 977–980, 2006.

[SCH 06b] SCHURIG D., MOCK J.J., SMITH D.R., "Electric-field-coupled resonators for negative permittivity metamaterials", *Applied Physics Letters*, vol. 88, p. 041109(3), 2006.

[TAN 91] TANNERY P., HENRY C., *Œuvres de Pierre de FERMAT*, vol. 2, Gauthier-Villars, 1891.

[TIC 10] TICHIT P.H., BUROKUR S.N., DE LUSTRAC A., "Waveguide taper engineering using coordinate transformation technology", *Optics Express*, vol. 18, pp. 767–772, 2010.

[TIC 11a] TICHIT P.H., BUROKUR S.N., GERMAIN D., *et al.*, "Design and experimental demonstration of a high-directive emission with transformation optics", *Physical Review B*, vol. 83, p. 155108(7), 2011.

[TIC 11b] TICHIT P.H., BUROKUR S.N., DE LUSTRAC A., "Transformation media producing quasi-perfect isotropic emission", *Optics Express*, vol. 19, pp. 20551–20556, 2011.

Chapter 7

Metamaterials for Control of Surface Electromagnetic and Liquid Waves

7.1. Introduction

During the past few years, research groups from all over the world have demonstrated the possibilities offered by metamaterials thanks to their ability to control electromagnetic waves (and other types of waves, e.g. acoustic and elastic, as well as diffusion phenomena). After negative refraction and subwavelength imaging, it has appeared possible to hide some objects from electromagnetic radiation and to make them invisible. A first path to invisibility was investigated by Engheta and Alù [ALÙ 05] in 2005 and is based on plasmonic materials designed in order to cloak dielectric or conducting objects. This technique relies heavily on a scattering cancellation phenomenon, based on the negative local polarizability of a cover made up of low electric permittivity materials. It appears to be relatively robust to changes in the design parameters, geometry and frequency of operation.

Experimental evidence of such invisibility devices was demonstrated recently in the microwave regime [EDW 09, RAI 12] and its requirement of *a priori* knowledge of electromagnetic properties of the objects to hide. The use of space-time transformations as a design tool for new materials was subsequently introduced as an alternative path toward invisibility. The basic

---

Chapter written by Sébastien GUENNEAU, Mohamed FARHAT, Muamer KADIC, Stefan ENOCH and Romain QUIDANT.

idea of this concept is that a metamaterial mimics a transformed empty space. The light rays follow straight trajectories according to Fermat's principle in this transformed (virtual electromagnetic) space, and are curved in a desired way in the (real) laboratory space. This allows us to design, in an efficient way, materials with various characteristics such as invisibility cloaks, whereby light is detoured smoothly around an object.

In 2006, Pendry *et al.* [PEN 06] theorized that a finite size object surrounded by a coating consisting of a metamaterial might become invisible for electromagnetic waves. An international team involving these authors subsequently implemented this idea using a metamaterial consisting of concentric layers of split ring resonantors (SRRs) [SCH 06], which makes a copper cylinder invisible to an incident plane wave at a specific microwave frequency (8.5 GHz). The smooth behavior of the electromagnetic field in the far field limit could be expected in view of the numerical evidence given [PEN 06] using a geometrical optics based software. Importantly, Leonhardt [LEO 06] proposed, in parallel to this development of transformational optics, a conformal optics route toward invisibility, which is however constrained by the two-dimensional (2D) geometry, as it relies heavily on complex analysis, and the ray optics limit, i.e. far field. To date, the only evidence that invisibility is preserved in the intense near field limit is purely numerical [ZOL 07].

A very different route to invisibility was proposed by McPhedran, Nicorovici and Milton [McP 94] in the same year. This grouping studied a countable set of line sources using anomalous resonance when the sources lie in the close neighborhood of a cylindrical coating filled with negative permittivity material, which is nothing but a cylindrical version of the "poor mans lens" of Pendry [PEN 00]. These researchers attribute this cloaking phenomenon to anomalous localized resonances [MIL 06a, NIC 07], which is reminiscent of the field of plasmonics.

One of the most famous paradigms of plasmonics is the extraordinary physics of the transmission of light through holes which are small compared with the wavelength publicized by Ebbesen *et al.* [EBB 98] in the late 1990s. However, some heralding earlier work is less well-known (for example combining both theory and experiment [BLI 80]). Pendry *et al.* [PEN 04] showed in 2004 that we can manipulate surface plasmon ad libitum via homogenization of structured surfaces. In the same vein, pioneering approaches to invisibility relying upon plasmonic metamaterials have already led to fascinating results [ALÙ 05, GAR 05, SMO 08, BAU 09]. These include plasmonic shells with a suitable out-of-phase polarizability in order to

compensate the scattering from the knowledge of the electromagnetic parameters of the object to be hidden, and external cloaking, whereby a plasmonic resonance cancels the external field at the location of a set of electric dipoles. In 2008, Smolyaninov *et al.* [SMO 08] achieved a noticeable reduction in the scattering of surface plasmon polaritons (SPPs) incident upon a cloak consisting of polymethylmethacrylate at a wavelength of 532 nm. More recently, Baumeier *et al.* [BAU 09] have demonstrated theoretically and experimentally that it is possible to significantly reduce the scattering of an object by an SPP at a wavelength of 632.8 nm when it is surrounded by two concentric rings of point scatterers. However, these two experiments rely upon the resonant features of the plasmonic cloak.

In the first section of this chapter, we show that it is possible to design a flat lens and a cylindrical acoustic cloak for linear surface liquid waves (LSWs). We construct two structured materials: a square array of circular cylinders bends surface waves in the wrong direction at a specific hertz frequency (via negative refraction upon resonance); and a concentric array of cylinders bends surface waves over a finite interval of hertz frequencies (via artificial anisotropy through averaging). The lens behaves as an effective fluid with a negative gravity and the cloak behaves as an effective fluid characterized by a transversely anisotropic shear viscosity. In the second section of this chapter, we design a structured metal plate that bends SPPs in the visible and near infrared spectrum. Such an invisibility carpet is deduced from a quasi-conformal grid and is therefore nearly isotropic. Such an enhanced control of water and electron wave trajectories, which used techniques developed in the emerging fields of transformational and conformal optics, opens new vistas in transformational surface physics.

7.1.1. *Prehistory of acoustic metamaterials*

At the beginning of this millennium, the group of Ping Sheng at the University of Hong Kong provided the first numerical and experimental evidence of a localized resonant structure for elastic waves propagating in 3D arrays of thin coated spheres [LIU 00]. This work paved the way toward acoustic analogs of electromagnetic metamaterials. Movchan and Guenneau [MOV 04] subsequently proposed to use arrays of cylinders with a split ring cross-section as building blocks for 2D localized resonant structures. Li and Chan [LI 04] independently proposed a similar type of negative acoustic metamaterial. In a recent work, Fang *et al.* [FAN 06] experimentally demonstrated a dynamic effective negative stiffness for a chain of water-filled SRRs for ultrasonic waves. Milton *et al.* [MIL 06] provided a mathematical

framework for such effects including cloaking whereby the elastic response of an obstacle subject to an applied field is suppressed.

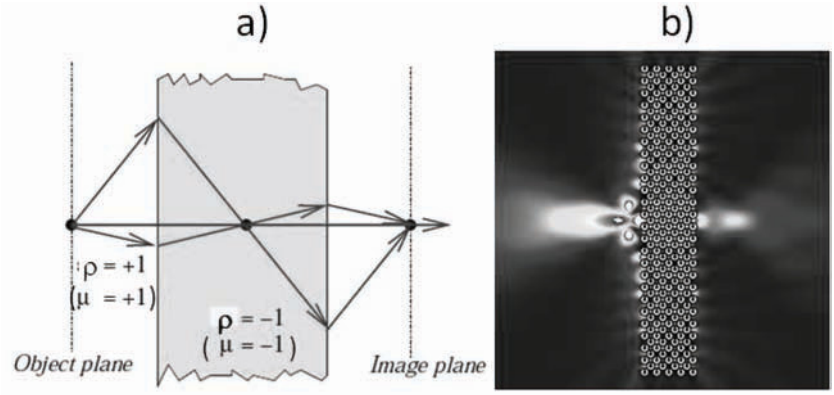

Figure 7.1. *Acoustic lens via negative refraction: a) schematic diagram depicting the focusing of rays by the acoustic counterpart of the Pendry–Veselago lens (the density ρ and the shear modulus μ for anti-plane shear waves play the role of the electric permittivity and the magnetic permeability – or vice-versa depending upon light polarization – in optics). A point source placed on one side will produce an image on the other side of the slab of negative density. The entire object plane is mapped point-wise onto the image plane; b) numerical simulation demonstrating the imaging effect for anti-plane shear waves (plot of field intensity). An acoustic source placed on the left side of an array of voids (with cross-sections shaped as split ring resonators (SRRs)) in an isotropic bulk (e.g. silica) is imaged on the right side (with subwavelength resolution, about one-third of the incident wavelength). The asymptotic formula [7.1] provides us with the resonant frequency of SRRs at which the effective density of the array turns negative, according to [7.2]*

Interestingly, similar localization effects with a markedly enhanced elastic response have also been observed experimentally by Russell *et al.* [RUS 03] at megahertz frequencies in sonic band gap crystal fiber preforms with dual core defects in 2003, see Figure 7.2: trapped modes appear in the stop band of the periodic cladding, and couple to light via photoelastic effects in the defects. This suggests that elastic metamaterials are in essence periodic structures within which wave localization occurs, thereby enhancing resonance effects (as well as light and sound interplay).

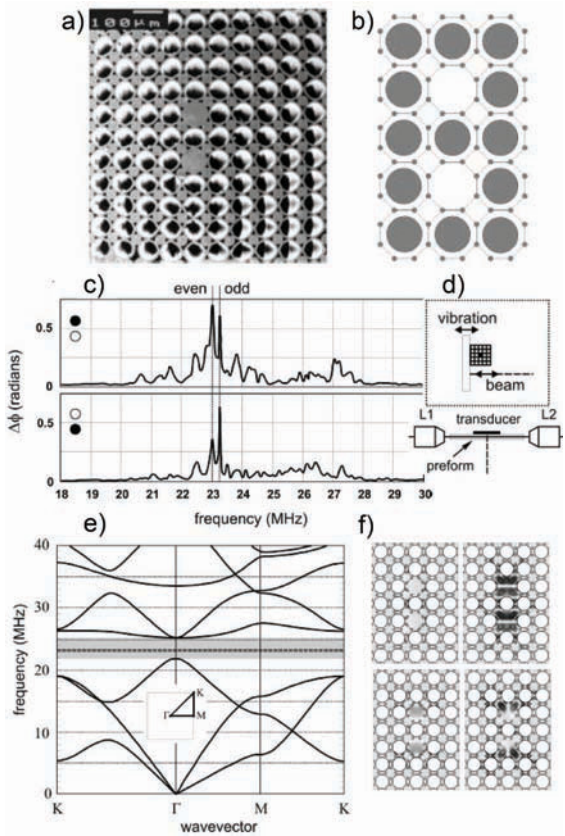

Figure 7.2. *Photonic crystal fiber preforms as a locally resonant elastic metamaterial: a) scanning electron micrograph of the preform used in the experiments of Philip Russell's optoelectronic group at Bath University in 2001–2003. It has two solid core defects, an interhole period of* $80\,\mu m$*, a hole diameter of* $59\,\mu m$ *and an interstitial hole diameter of* $80\,\mu m$*; b) a detail of the structure used in the numerical modeling (the lines are only guidelines); c) phase change of the light propagating in the cores of the PCF preform, induced by the acoustic wave, as a function of frequency. Two sharp resonances are apparent at* 23 *and* 23.25 *MHz; d) schematic diagram of the experimental setup. L1 and L2 are microscopic objectives. A piezoelectric transducer was used to create acoustic vibrations; e) sonic band structure for in-plane mixed-polarized shear and dilatational waves in the sonic crystal, with defects removed (Rayleigh method [GUE 03]). The experimentally observed resonances (at* 23 *and* 23.25 *MHz – the dashed lines) sit near the middle of the sonic band gap, which extends from 21.8 to 25 MHz; and f) field patterns for the acoustic resonances at* 23.47 *and* 24.15 *MHz (finite element simulations with Comsol Multiphysics) (source: adapted from [RUS 03] and reprinted with permission from OSA)*

7.1.2. *Correspondences between electromagnetic and acoustic metamaterials via locally resonant models*

Metamaterials are artificially structured composites that can be engineered to have desirable electromagnetic properties, such as focusing via negative refraction [VES 68] or spatially varying, anisotropic, refractive index. The former makes a high-resolution flat lens [PEN 00] while the latter leads to invisibility cloaks via transformation optics [LEO 06, PEN 06]. As such, they offer unique and previously unexplored features. A new branch of physics has emerged in the last decade, following the discovery by John Pendry [PEN 96a, PEN 96b] of new structures that lead to negative refraction of electromagnetic waves [SMI 00]. Negative refractive index materials (NRIM) consist of structured metamaterials such as arrays of thin straight wires [PEN 96a] and SRRs [PEN 96b]. SRRs are cylinders with capacitive splits that respond resonantly to radiation with the magnetic field along the cylindrical axes, see Figure 7.3(a). Circulating currents around the rings actually tends to shield the interior due to the inductance while the capacitance, due to the gaps, gives rise to a resonance associated with a negative refractive index, see, e.g., [GUE 09] for a comprehensive review. This resonant effect creates a narrow low-frequency stop band associated with artificial magnetism in the context of optics.

Using asymptotic methods for fields in multistructures [KOZ 99], it can be shown that (normalized) resonant frequencies ω_m, $m = 1, 2, ...$ are given by the transcendental equation [MOV 04]:

$$d\cot(\omega_m l) = \text{area}(\Xi)\omega_m, \qquad [7.1]$$

where Ξ denotes the region inside a split ring, a the pitch of the array, d the thickness of the slit, see Figure 7.3(a), and l its width. The analogy with the mass-spring model counterpart of the usual electrical circuit description of electromagnetic metamaterials, see Figure 7.3(c), first appears in [MOV 04].

The effective density ρ_{hom} at a frequency ω is then given in the form [FAR 09]:

$$\rho_{hom}(\omega) = 1 - \sum_{m=1}^{\infty} \frac{\omega^2}{\omega^2 - {\omega_m}^2} \|V_m\|^2_{L^2(0,l)}, \qquad [7.2]$$

where V_m is the eigenfield within the slit $(0, l)$ of the split ring and $\|V_m\|^2_{L^2(0,l)} = \int_0^l V_m^2(x)\, dx$. It is clear from [7.2] that $\rho_{hom}(\omega)$ can take

negative values near resonances $\omega = \omega_m$. In the context of electromagnetism, the expression for the effective permeability μ_{hom} is the same, and first appears in [PEN 96b], where ω_m was referred to as plasmon frequency. A similar expression holds for the so-called fishnet structures popularized by Soukoulis's group [DOL 07].

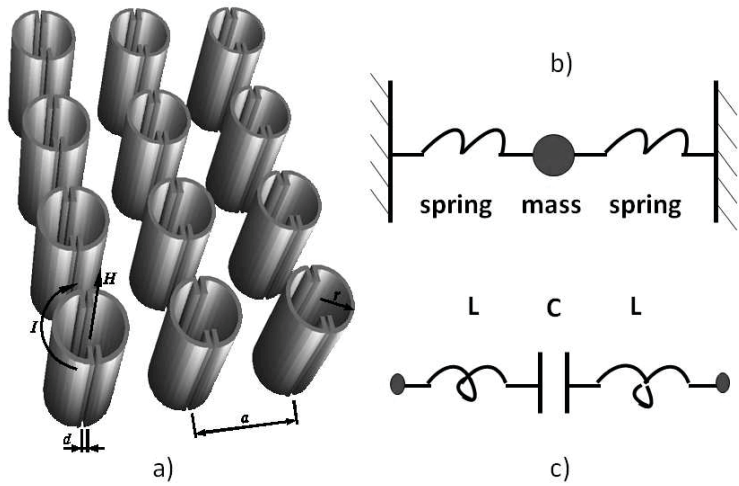

Figure 7.3. *a) Square array of cylinders with capacitive splits (so-called thin bridges of thickness d small compared to the pitch a) that responds resonantly to radiation with the (longitudinal) magnetic field along the cylindrical axes. Circulating currents I around the rings tend to shield the interior due to the inductance while the capacitance due to the gaps gives rise to a resonance, the so-called artificial magnetism (picture adapted from Guenneau and Ramakrishna [GUE 09]). b) A split ring acts as a Helmholtz resonator: a mass (counterpart of the capacitance C in electric circuits) is connected to walls via springs (counterparts of inductance L, say in solenoids) [MOV 04]. The mechanical interpretation is a negative effective density [FAR 09] upon resonance, counterpart of effective magnetism in electromagnetics [PEN 96b]. c) Resonant LC circuit counter part of a Hemholtz resonator*

Combined together, structural elements such as SRRs and thin straight wires (associated with an effective permittivity ε_{hom} described by a similar expression to equation [7.2] in the optical setting, and a negative stiffness in

the acoustical setting [GUE 07][1]) can bring about a (complex valued) negative effective refractive index for the Snell–Descartes law and result in negative refraction of radiation [SMI 00, GUE 07]. Indeed, a slab of NRIM with $n = -1$ can image both the far-field propagating modes [VES 68] and the near-field modes of a source [PEN 00], thus acting as a perfect lens. The resolution of this system is not limited by the wavelength, but only by the dissipation, dispersion and imperfections in the constituent materials. NRIM indeed support a host of surface plasmon states for both polarizations of light which conveys the subwavelength details from the source to the image. However, such surface waves also exist in acoustic settings. This opens up new horizons such as imaging with subwavelength image resolution through an acoustic counterpart of the Pendry–Veselago slab lens [FAR 09], already shown in Figure 7.1.

Figure 7.4 is an experimental proof of lensing via negative refraction, which is based on an analogy between acoustics, whereby anti-plane shear waves propagate within an array of voids with stress-free conditions (Neumann data), see Figure 7.1, and surface waves propagating within an array of rigid cylinders immersed in a liquid. The fact that the C-shaped inclusions have been replaced by circular inclusions shifts up the frequency at which negative refraction occurs, and this in turn spoils the subwavelength features of the image: we are in the presence of a phononic crystal rather than an acoustic metamaterial, and the imaging effect is due to multiple scattering between the cylinders (Bragg regime) rather than local resonances (homogenization regime); we return to this question of semantics later.

7.2. Acoustic cloaking for liquid surface waves

In this section, we describe an effective medium approach to cloaking for liquid surface waves (LSWs), which works over a finite frequency bandwidth, unlike for cloaking using resonant metamaterials, which displays spatially varying artificial magnetism [SCH 06]. Before we embark on our invisibility journey, we find it useful to recall under which hypotheses we can consider

1 Kohn and Shipman were the first mathematicians to retrieve Pendry's formula for artificial magnetism via two-scale homogenization of SRRs in 2008 [KOH 08]. However, Bouchitté and Schweizer [BOU 10] obtained a more general form for the tensor of effective permittivity in the case of a cubic array of toroidal SRRs with a thin slit of high contrast material in 2010. In the 2D case, Farhat *et al.* [FAR 09] retrieved Pendry's result in 2009, using a three-scale homogenization approach for SRRs with thin slits with Neumann data which model infinite conducting boundaries for transverse electromagnetic waves as in Figure 7.1 or rigid boundaries in the context of acoustics.

water waves satisfy governing equations reminiscent of those familiar to scientists working in the field of linear optics, or put in other words, how can we get rid of nonlinearities in Navier–Stokes equations?

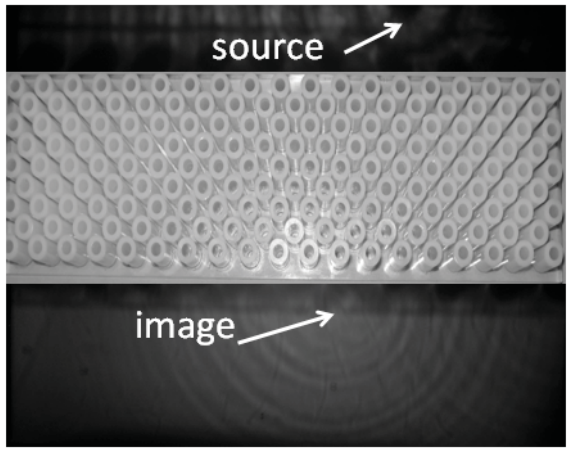

Figure 7.4. *Snapshot (cliché) of a surface liquid wave experiment with a surface wave generated on one side (dark region) of an array of rigid cylinders immersed in Methoxynonafluorobutane, which is a liquid that presents the advantage of combining a low-viscosity coefficient with a relatively high density. An image appears on the other side of the array, according to the laws of negative refraction, see Figure 7.1, though it is slightly shifted to the left. It should be noted that the image does not show subwavelength features as the structure works as a phononic crystal rather than an acoustic metamaterial: the wavelength is of the same order as the pitch of the array*

7.2.1. *From Navier–Stokes to Helmholtz*

Let us denote the open bounded domain in the space $\mathbb{R}^3$ occupied by a fluid by Ω . The conservation of momentum leads to the Navier–Stokes equation:

$$\frac{\partial \mathbf{u}}{\partial t} + (\mathbf{u} \cdot \nabla)\mathbf{u} + \frac{1}{\rho}\big(\nabla - \mu\nabla^2\mathbf{u}\big) = \mathbf{g} \quad \text{in } \Omega, \qquad [7.3]$$

where $\mathbf{u}$ is the velocity field, p is the pressure, ρ is the fluid density, $\mu\nabla^2\mathbf{u}$ accounts for the fluid's viscosity, and $\mathbf{g}$ is the vector of gravity force: $\mathbf{g} = -g\mathbf{e}_3$, where g denotes the acceleration caused by gravity and $\mathbf{e}_i$ are the basis vectors of the Euclidean space.

To start with the simplification process, we neglect the viscosity $\mu\nabla^2\mathbf{u}$. Such a hypothesis will bring a strong constraint on the choice of the liquid in the experimental setup. Further assuming that the velocity field $\mathbf{u}$ is curl free, we show in the sequel that it derives from a potential Φ which is related to the vertical displacement of the liquid surface ξ through a reduced potential ϕ such that $\Phi(x_1, x_2, x_3, t) = \Re\left(\phi(x_1, x_2)\cosh(\kappa x_3)e^{-i\omega t}\right)$ and $\xi(r, \theta, t) = \mathcal{R}(-\frac{i\omega}{g}\phi(r, \theta)e^{-i\omega t})$, where ω is the wave frequency and ϕ satisfies the Helmholtz's equation [7.12], with κ the spectral parameter [ACH 90].

Let $x_3 = \xi(x_1, x_2, t)$ be the equation of the free surface. The pressure is prescribed to be equal to the constant atmospheric pressure p_0 on $x_3 = \xi(x_1, x_2, t)$, and the surface tension is neglected. Hence, [7.3] leads to the well-known Bernoulli equation:

$$\frac{\partial\Phi}{\partial t} + \frac{|\nabla\Phi|^2}{2} + \frac{p_0}{\rho} + g\xi = f(t) \quad \text{on } x_3 = \xi. \tag{7.4}$$

Assuming that $f(t)$ is incorporated into ϕ and that liquid fluctuations are small, i.e. $|\xi - h| \ll 1$, where h denotes the mean value of ξ, and also $|\frac{\partial\xi}{\partial x_j}| \ll 1$, $j = 1, 2$, differentiation of [7.4] with respect to t leads to the linearized equation:

$$\frac{\partial^2\Phi}{\partial t^2} + g\frac{\partial\xi}{\partial t} = 0 \quad \text{on } x_3 = h. \tag{7.5}$$

Using the small-slope ansatz:

$$u_3 = \frac{dx_3}{dt} = \frac{\partial\xi}{\partial t} + \frac{\partial\xi}{\partial x_1}\frac{\partial x_1}{\partial t} + \frac{\partial\xi}{\partial x_2}\frac{\partial x_2}{\partial t} \sim \frac{\partial\xi}{\partial t}, \tag{7.6}$$

the divergence-free condition $\nabla \cdot \mathbf{u} = 0$ (i.e. incompressible fluid) and [7.5] lead to Poisson's condition:

$$\frac{\partial^2\phi}{\partial t^2} + g\frac{\partial\phi}{\partial x_3} = 0 \quad \text{on } x_3 = h. \tag{7.7}$$

Altogether, Φ is the solution of the following system:

$$\begin{cases} \nabla^2\Phi = 0 \quad \text{for } x_3 \in]0, h[, \\ \dfrac{\partial^2\Phi}{\partial t^2} + g\dfrac{\partial\Phi}{\partial x_3} = 0 \quad \text{for } x_3 = h, \\ \mathbf{n} \cdot \nabla\Phi = 0 \quad \text{for } x_3 = 0, \end{cases} \tag{7.8}$$

where the last boundary condition accounts for a no-flow condition through the plane $x_3 = 0$ (this stands for the fixed surface at the bottom of the water tank). If we look for a harmonic ansatz for the potential $\Phi(x_1, x_2, x_3, t) = f(x_3)e^{-i(\omega t - \kappa_1 x_1 - \kappa_2 x_2)}$, Laplace's equation in [7.8] gives $f''(x_3) - \kappa^2 f(x_3) = 0$, where $\kappa^2 = \kappa_1^2 + \kappa_2^2$ is by inspection of the Neumann boundary condition in [7.8], a parameter that forces the evanescence of the potential Φ away from the free boundary in the form $f(x_3) = \cosh(\kappa x_3)$. This means that the physics of the problem can be described by a governing equation on the free interface between liquid and air. Linear LSWs are indeed governed by the Helmholtz's equation:

$$\nabla^2\phi + \kappa^2\phi = 0, \qquad [7.9]$$

on the free surface, where ϕ is the reduced potential related to the potential Φ via $\Phi(x_1, x_2, x_3, t) = \Re\left(\phi(x_1, x_2)\cosh(\kappa x_3)e^{-i\omega t}\right)$. We note that if the free surface is perforated by rigid cylinders immersed in the liquid, this equation is valid in the liquid region outside the rigid cylinders and is supplied with a no-flow condition $\frac{\partial\phi}{\partial n}$ on each cylinder's boundary. This will be used in our model of a structured cloak for LSWs. Furthermore, from the Poisson's condition in [7.8], the spectral parameter κ in [7.9] is linked to the wave frequency via the dispersion relation [ACH 90]:

$$\omega^2 = g\kappa(1 + d_c^2\kappa^2)\tanh\kappa h, \qquad [7.10]$$

with $d_c = \sqrt{\sigma/(\rho g)}$ the liquid capillarity. Note that surface waves propagating at the liquid–air interface are thus always dispersive, unlike pressure waves within the liquid. This dispersive feature of surface waves is also found in the context of plasmonics, whereby electron waves propagate at a metal interface, and will be discussed in the next section.

7.2.2. *Effective anisotropic shear viscosity through homogenization*

Our aim is now to extend this principle to the LSW waves governed by the Helmholtz equation [7.9] and the Neumann boundary conditions. The goal is to homogenize the microstructured cloak shown in Figure 7.5 that reveals an effective anisotropic shear viscosity underpinning the cloaking effect. Bearing in mind that when the shear viscosity matrix is large enough in the tangential θ direction, LSW waves will be bent around the central region of the cloak and thus make its interior almost invisible to any exterior observer.

For this, we note that when the fluid penetrates the microstructure of Figure 7.5 (whose cross-section Ω_c is evenly divided into a large number of

small curved sectors ηY of radial length $\eta(R_2 - R_1)$ and azimuthal length $2\pi\eta$, where η is a small positive real parameter), it undergoes fast periodic oscillations. To filter these oscillations, we consider an asymptotic expansion of the potential field solution of the Helmhotz equation [7.9] in terms of a macroscopic (slow) variable $\mathbf{x} = (r, \theta)$ and a microscopic (fast) variable $\mathbf{x}/\eta$ [JIK 94]:

$$\forall \mathbf{x} \in \Omega_c, \quad \phi_\eta(\mathbf{x}) = \phi_0\left(\mathbf{x}, \frac{\mathbf{x}}{\eta}\right) + \eta\phi_1\left(\mathbf{x}, \frac{\mathbf{x}}{\eta}\right) + \eta^2\phi_2\left(\mathbf{x}, \frac{\mathbf{x}}{\eta}\right) + \cdots \quad [7.11]$$

where each term $\phi^{(i)}(\mathbf{x}, \cdot)$ is Y-periodic.

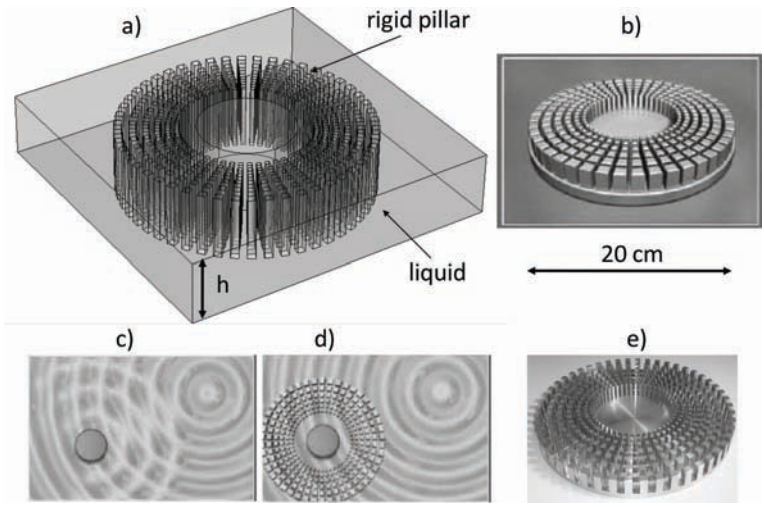

Figure 7.5. *Principle of water wave cloak: a) geometry of the structured cloak consisting of concentric arrays of rigid pillars immersed in a vessel of liquid of depth h; b) diagrammatic view of the cloak; c–d) scattering of water waves on a rigid obstacle (red disc) without c) and with d) the water wave cloak; e) photo of the micro-structured cloak used in experiments around* 10 *Hz*

The differential operator is rescaled accordingly as $\nabla = \nabla_{\mathbf{x}} + \frac{1}{\eta}\nabla_{\mathbf{y}}$, and collecting terms of same powers of η, we obtain the following homogenized problem in the limit when η tends to zero (see also [JIK 94]):

$$\nabla \cdot ([\mu_{hom}]\nabla\phi_{hom}(\mathbf{x})) = \kappa^2\phi_{hom}(\mathbf{x}) \qquad \text{in} \quad \Omega_c. \qquad [7.12]$$

This homogenized equation shows that the velocity field is now a solution of equation [7.9] with an anisotropic matrix of viscosity with non-trivial part (transverse shear):

$$[\mu_{hom}] = \frac{1}{\mathcal{A}(Y^*)} \begin{pmatrix} \mathcal{A}(Y^*) - \psi_{rr} & \psi_{r\theta} \\ \psi_{\theta r} & \mathcal{A}(Y^*) - \psi_{\theta\theta} \end{pmatrix}. \quad [7.13]$$

where $\mathcal{A}(Y^*)$ denotes the area of the region Y^* surrounding a rigid inclusion S (subject to Neumann boundary conditions) in an elementary cell Y of the periodic array, and ψ_{ij} represent corrective terms derived from an integral over the boundary ∂S:

$$\forall i, j \in \{r, \theta\},\ \psi_{ij} = -\int_{\partial S} \Psi_i n_j \, ds, \quad [7.14]$$

where $\mathbf{n}$ is the unit outward normal to ∂S, and Ψ_j , $j \in \{r, \theta\}$, are Y-periodic potentials, which are unique solutions (up to an additive constant) of the following two Laplace equations $(\mathcal{L}_j)$:

$$(\mathcal{L}_j):\ \nabla^2 \Psi_j = 0 \text{ in } Y^*. \quad [7.15]$$

These so-called annex problems are supplied with the effective boundary condition $\frac{\partial \Psi_j}{\partial n} = -\mathbf{n} \cdot \mathbf{e}_j$ on the boundary ∂S of the inclusion. Here, $\mathbf{e}_r$ and $\mathbf{e}_\theta$ denote the vectors of the basis in polar coordinates (r, θ).

Altogether, this shows that the velocity field is a solution of equation [7.3] with an anisotropic matrix of viscosity whose non-trivial part (transverse shear) could be calculated as:

$$[\mu_{hom}] = \frac{1}{\mathcal{A}(Y^*)} \begin{pmatrix} \mathcal{A}(Y^*) + 0.7 & 0 \\ 0 & \mathcal{A}(Y^*) + 7.2 \end{pmatrix}, \quad [7.16]$$

which shows that the effective fluid is strongly anisotropic along the θ-direction.

7.2.3. *Numerical analysis of LSW cloaking*

In this section, we give some numerical illustrative examples of cloaking of an acoustic vibration (radiated by a cylindrical point source) located close to an obstacle through the phononic crystal fiber making the cloak (see Figures 7.5 and 7.6). As detailed in the previous section, we first replace the

microstructured cloak immersed in the liquid by an effective transversely anisotropic fluid whose homogenized shear viscosity is deduced from the numerical solution [7.16] of the two annex problems [7.15]. This provides us with a qualitative picture of the cloaking mechanism shown in the lower right panel of Figure 7.6. We then compare this asymptotic theory against the numerical solutions of the same scattering problems when we model the complete microstructured cloak, as shown in the upper right panel of Figure 7.6. We note the strong similarities between the asymptotic solution and the numerical solution.

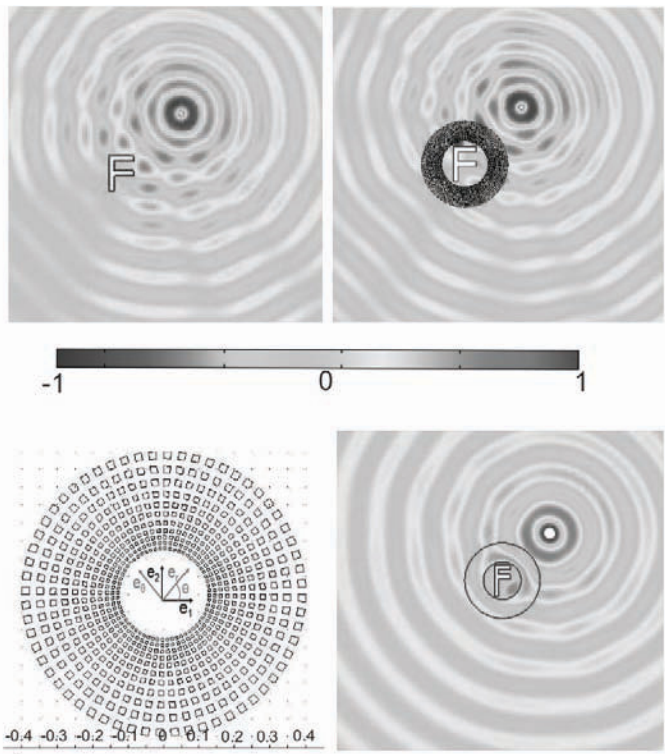

Figure 7.6. *Upper panel: 2D plot of the real part* $\mathcal{R}e(\phi)$ *of the potential of velocity* $\mathbf{u}$ *radiated by an acoustic point source of normalized wavelength ,* $\lambda = c/\nu = c/2.5$ *in presence of an F-shaped obstacle (left) and a microstructured cloak surrounding the obstacle (right); lower panel: zoom on the geometry of the microstructured cloak (left) and diffraction by a cloak (with inner and outer boundaries* $r = R_1 = 0.164$ *and* $r = R_2 = 0.4$*) whose parameters are given by [7.17]. The similarities between the upper right and lower right panels are noted. Importantly, the radii are normalized here and are related to those of Figure 7.7 through factor* 2.5 *(for meters)*

According to transformation acoustics, the effective fluid should be characterized by a varying density ρ, as well as a varying radial and azimuthal shear viscosities μ_{rr} and $\mu_{\theta\theta}$ (reduced parameters inspired by that of the groupings of Cummer and Shalaev [CUM 07, CAI 07]). These requirements seem to be beyond the actual experimental possibilities. Nevertheless, we can introduce some variation in the radial length of the sectors for which it seems reasonable to assume that the improved cloak is characterized by an effective anisotropic fluid whose shear viscosity (a diagonal matrix in polar basis) is:

$$\mu'_{rr} = \left(\frac{R_2(r-R_1)}{(R_2-R_1)r}\right)^2, \qquad \mu'_{\theta\theta} = \left(\frac{R_2}{R_2-R_1}\right)^2, \qquad [7.17]$$

where R_1 and R_2 are, respectively, the inner and outer radii of the ring. Importantly, the effective fluid's density is $\rho' = \rho$; i.e., it does not play any prominent role. Figure 7.7 shows simulations performed for the ideal case when the obstacle is cloaked and for a vacuum for comparison.

The upper right panel of Figure 7.7 clearly shows that the structured cloak consisting of a very large number (100) of identical curved sectors, small compared to the working wavelength and regularly arranged along the radial and azimuthal directions will enable us to gain control over surface waves. We have also verified the effect of varying the size of sectors along the radial direction and numerically checked that the cloaking is thus further improved. It is enough to design a cloak with identical sectors to gain a good control of the velocity field, but the azimuthal shear wave speed of liquid particles will linearly increase with their distance to the center of the cloak only in the case of sectors with increasing size. We numerically checked that in the case of a cloak with identical sectors, this shear wave speed does not vary; hence, a shadow region revealing the presence of the hidden object is observed behind the cloak (through phase shift). We also checked that such a structured cloak with 256 curved sectors (Figure 7.6 upper right panel) is more appropriate for the cloaking than one with 100 curved sectors. But we had to find a compromise between the realizable structures using conventional machining, the limits imposed by the viscosity of the liquids, and the constraints imposed by homogenization.

7.2.4. *Experimental measurements of LSW cloaking*

Regarding the experimental setup, we refer the reader to Figure 7.7, which clearly demonstrates a reduced backscattering for an acoustic source generating LSW at 10 Hz a couple of wavelengths away from a structured

cloak consisting of 100 rigid pillars arranged as in the lower left panel of Figure 7.6.

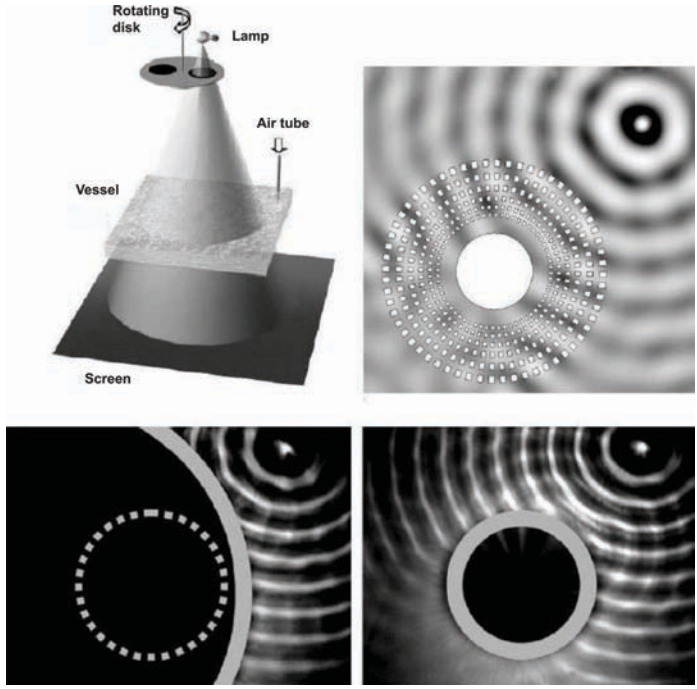

Figure 7.7. *a) (Experimental setup): a halogen lamp modulated by a perforated rotating disc illuminates a transparent vessel containing the liquid (Methoxynonafluorobutane). The surface waves are excited by a localized pressure thanks to air pulsed in a small tube at the same frequency as the modulation of the light (stroboscopic effect); b) (simulation): diffraction pattern of the surface waves generated by a harmonic acoustic source at frequency* 10 *Hz for a cloak with* 100 *rigid sectors. The depth of liquid in the vessel is* $h = 9$ *mm and its capillarity is* $d_c = 0.95$ *mm; c): snapshot of diffraction pattern by a rigid cylinder of radius* 38 *mm surrounded by the structured cloak (outlined as the gray coating) of Figure 7.6 with inner and outer radii* $R_1 = 41$ *mm and* $R_2 = 100$ *mm. d): snapshot of diffraction pattern by the rigid cylinder on its own (outlined by a dashed gray circle in the left panel for comparison) (Source: reprinted with permission from APS)*

The liquid used for the experiments was Methoxynonafluorobutane chosen for its physical properties and especially for having a low kinematic viscosity [ACH 90] ($\nu = \mu/\rho = 0.61$ mm^2/s) so that $\mu\nabla^2\mathbf{u}$ can be neglected outside the cloak in equation [7.3], a small surface tension $\sigma = 13.6$ N/cm

and a large density ($\rho = 1.529$ g/mL), ensuring a small capillarity length $d_c = \sqrt{\sigma/(\rho g)} = 0.95$ mm. The vessel is filled with a depth of liquid $h = 9$ mm.

The basic principle behind the experiments is very simple: the light of a halogen lamp modulated by a perforated rotating disc illuminates a transparent vessel containing the liquid. The surface waves are excited by a localized pressure thanks to air pulsed in a small tube at the same frequency as the modulation of the light (to take advantage of the stroboscopic effect for the observation). The surface waves create local curvatures of the liquid and the light is refracted when crossing the surface. Thus, on the screen the dark and light zones allow for visualizing the LSWs. Note that the low viscosity of the liquid is important for such experiments and we were unable to produce similar results with water: due to its larger viscosity, the water profile flattens within the microstructured cloak, much like in thin channels [ACH 90], and water cannot flow.

7.3. Optical cloaking for surface plasmon polaritons

In this section, we adapt the tools of transformational optics to SPPs propagating at the interface between two anisotropic media of opposite permittivity signs. We identify the role played by entries of anisotropic heterogeneous tensors of permittivity and permeability deduced from a coordinate transformation in the dispersion relation governing propagation of SPPs. Using this concept and the idea of quasi-conformal mapping, we apply this concept to mimic a flat Bragg mirror by a curved Bragg mirror with a heterogeneous structure, thereafter caller plasmonic carpet, in front of the curved one. This novel concept is verified by an experimental characterization using one-step lithography to realize the structure. The measurement of the propagation of the SPP in both structures has been achieved by the leakage radiation setup.

7.3.1. *Introduction to surface plasmon polaritons*

The Maxwell's theory shows that electromagnetic waves can propagate at the interface between a metal and a dielectric. These waves are associated with plasma oscillations of free electrons on the surface of the metal. They are known as surface plasmon polaritons (SPPs) [RAT 88]. The maximum intensity of the field associated with this wave is confined at the metal-dielectric interface. The electromagnetic field decreases exponentially in the two media in the direction perpendicular to the interface, which is a

characteristic of surface waves also encountered in very different physical contexts such as hydrodynamics (e.g. LSLWs as described in the previous section), or elastodynamics (e.g. Rayleigh seismic waves propagating at the surface of the Earth). Figure 7.8 is a schematic representation of the oscillations and the exponential dependence on the associated electric fields. These surface modes, introduced by Wood [WOO 02a] in the beginning of the last century, have been studied intensively by spectroscopic loss of energy (attenuated total reflection: ATR) of electrons [RIT 57, KRE 68]. The plasmons are extremely sensitive to the refractive index in contact with the metal surface or the roughness of the surfaces. For that reason, they find many applications in physics, chemistry and biology.

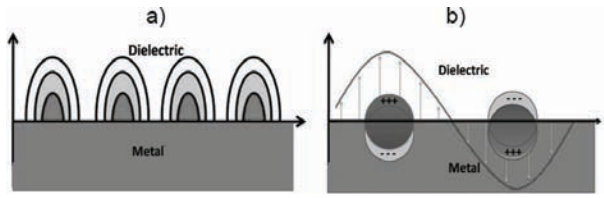

Figure 7.8. *Schematic representation of the electromagnetic field spreading at the metal-dielectric interface: a) the maxium intensity of the magnetic field corresponds to the dark gray, that is near the interface; b) polarization of the electric field and associated distribution of electric charges*

Considering the surface plasmons as an electromagnetic wave spreading at a plane interface between a dielectric and a metal, we will look at the relation between the energy of the oscillation and the wave vector. This wave is linked to the wave vector $\mathbf{k}$ by a dispersion relation. We consider two semi-infinite media (see Figure 7.8), one consisting of a dielectric environment and the other of a metal. The xy-plane is defined as the interface and the z-direction is perpendicular to the interface. The plasmon spreads along the x-direction, which means that the system is invariant to translation along the y-direction. We find the existence conditions of surface plasmons from the Maxwell equations and boundary conditions.

Under these circumstances, we show that SPPs can only exist for transverse magnetic (TM) polarized light. In this case, we have the general form of the magnetic field propagating along the x direction above and below the interface $z = 0$ is:

$$\begin{cases} \mathbf{H}_2 &= (0, H_{y2}, 0) \exp\{\mathrm{i}(k_{x2}x - \omega t) - k_{z2}z\}, z > 0, \\ \mathbf{H}_1 &= (0, H_{y1}, 0) \exp\{\mathrm{i}(k_{x1}x - \omega t) + k_{z1}z\}\ , z < 0, \end{cases} \quad [7.18]$$

with $\Re(k_{z1})$ and $\Re(k_{z1})$ strictly positive numbers in order to maintain evanescent fields above and below the interface $z = 0$. Here, ω denotes the

wave frequency, t the time variable and k_{xi} and k_{zi} the (possibly complex) components of the wavevector along x and z directions above ($i = 2$) and below ($i = 1$) the interface.

For this field to be a solution of Maxwell's equations, continuity of its tangential components is required across the interface $z = 0$ and this requires $k_{x1} = k_{x2} = k_x$ and the dispersion relations:

$$k_{zi} = \sqrt{k_x^2 - \varepsilon_i \left(\frac{\omega}{c}\right)^2}, \ \frac{k_{z1}}{\varepsilon_1} + \frac{k_{z2}}{\varepsilon_2} = 0 \,, \qquad [7.19]$$

where c is the celerity of light in vacuum, ε_1 is the permittivity in the upper-half plane (dielectric medium) and ε_2 is the permittivity in the lower-half plane (metal).

The dispersion relation of the propagative vector along the x-axis follows as:

$$k_x = \frac{\omega}{c} \left(\frac{\varepsilon_2 \varepsilon_1}{\varepsilon_2 + \varepsilon_1}\right)^{1/2}, \qquad [7.20]$$

and if we now consider the dielectric function of the metal as complex, it results in k_x being complex. We note that an SPP can only exist between a metal and a dielectric and for a finite range of frequencies and has to satisfy the existing relation $\Re(\varepsilon_1)\Re(\varepsilon_2) < 0$. Importantly, we note that the propagating length of SPPs can easily be computed from:

$$L = \frac{1}{2k_x^{"}} = \frac{c}{\omega} \left|\frac{\varepsilon_1' + \varepsilon_2}{\varepsilon_1' \varepsilon_2}\right|^{3/2} \frac{\varepsilon_1'^2}{\varepsilon_1^{"}} \qquad [7.21]$$

where c is the speed of light in vacuum, and primes (respectively double primes) denote real (respectively imaginary) parts of complex quantities. The evanescent behavior of the surface plasmon for each medium depends on the dielectric constants. The penetration length is given in the metal by:

$$z_m = \frac{\lambda}{2\pi} \left(\frac{|\varepsilon_1' + \varepsilon_2|}{\varepsilon_1'^2}\right)^{1/2}, \qquad [7.22]$$

and in the dielectric by:

$$z_d = \frac{\lambda}{2\pi} \left(\frac{|\varepsilon_1' + \varepsilon_2|}{\varepsilon_2'^2}\right)^{1/2}. \qquad [7.23]$$

Using these relations, we note that an SPP at $700 \text{ nm} < \lambda < 900$ nm propagating between an air-gold interface would have the following properties: penetration lengths respectively in metal and dielectric $20 \text{ nm} < z_m < 30$ nm, $500 < z_d < 800$ nm, and the propagation length $30{,}000 \text{ nm} < L < 50{,}000$ nm. It clearly appears that the main part of the electromagnetic energy is located in the dielectric region. We will make use of these properties in the last section of this chapter.

It should be noted that SPPs need to be generated using an incident electromagnetic field, and this is in itself a non-trivial task. Figure 7.9 shows the excitation of an SPP on a thin layer of metal by an incident plane wave at a critical angle depending upon the permittivity of the substrate. In this case, the critical angle of SPP excitation corresponds to a glass substrate and can easily be found in [MAI 07].

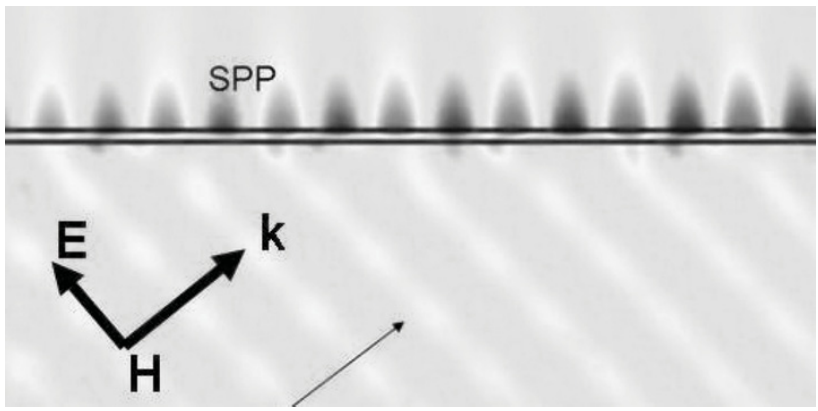

Figure 7.9. *Simulation of an SPP excitation on a thin metallic film with a plane electromagnetic wave incident through a glass substrate from below at a critical angle found using [MAI 07]*

Introduced in 2006, transformational optics was the pioneering idea of Sir John Pendry for electromagnetic waves [PEN 06]. This concept has been proposed for invisibility as has the idea of hiding under a carpet, which consists of mimicking a curved surface by a flat one. The basic idea consists of linking a space deformation to physical properties of that space (permittivity and permeability). This can be done by noting that Maxwell's equations are invariant through a change of system coordinates. In this way, we can obtain a relation between the change of coordinates and the physical properties (permittivity and permeability), which are encompassed in the Jacobian matrix [WAR 96, NIC 94]. This leads to anisotropic and

heterogeneous tensors of permittivity and permeability. An alternative route to the control of wave trajectories is that of optical conformal mapping, introduced by Ulf Leonhardt [LEO 06] in 2006, and published in the same issue of the *Science* magazine as the work of Pendry. Leonhardt's proposal, which was constrained to 2D geometries as it heavily relied upon the mathematical theory of complex analysis, has since been combined with the powerful tools of transformation optics by Li and Pendry [LI 08] using the concept of quasi-conformal mapping in order to design invisibility carpets in 2D [LI 08, REN 10, LIU 08, VAL 09] and 3D [ERG 10] geometries. In what follows, we extend this concept to plasmonics.

7.3.2. *From transformational optics to plasmonics*

In this section, we would like to extend the control of electromagnetic fields using tools of geometric transforms, to the area of SPPs. For this, we first recall that when the original permittivity and permeability matrices are scalars in the coordinate system (x, y, z), their transformed counterparts in the new coordinate system (u, v, w) are given by [NIC 94].

$$\underline{\underline{\varepsilon'_j}} = \varepsilon_j \mathbf{T}^{-1},\ \underline{\underline{\mu'_j}} = \mu_j \mathbf{T}^{-1},\ \text{ where } \mathbf{T} = \frac{\mathbf{J}^T \mathbf{J}}{\det(\mathbf{J})}, \qquad [7.24]$$

where $\det(\boldsymbol{J})$ is the determinant of the Jacobian matrix $\mathbf{J} = \partial(x, y, z)/\partial(u, v, w)$ of the map from coordinate system (u, v, w) to $(x(u, v, w), y(u, v, w), z(u, v, w))$. We emphasize the fact that it is the transformed domain and coordinate system that are mapped onto the initial domain with Cartesian coordinates, and not the opposite [NIC 94]. Moreover, in the context of plasmonics, $j = 1$ is the (transformed) metal region and $j = 2$ is the (transformed) dielectric region.

However, we have seen that the penetration depth in metal [7.22] is much smaller than in dielectric [7.23]. Therefore, we can simplify the problem by assuming that only the dielectric medium needs to be transformed. Let us thus derive the dispersion relation for a surface plasmon at the interface between metal and a transformed medium described by diagonal tensors of relative permittivity and permeability $\underline{\underline{\varepsilon'}} = \text{diag}(\varepsilon_{xx2}, \varepsilon_{yy2}, \varepsilon_{zz2})$ and $\underline{\underline{\mu'}} = \text{diag}(\mu_{xx2}, \mu_{yy2}, \mu_{zz2})$. From the first Maxwell equation, we know that:

$$\begin{cases} \nabla \times \mathbf{H}_2 &= -\mathrm{i}\omega\varepsilon_0 \underline{\underline{\varepsilon'}} \mathbf{E}_2, z > 0, \\ \nabla \times \mathbf{H}_1 &= -\mathrm{i}\omega\varepsilon_0\varepsilon_1 \mathbf{E}_1, z < 0, \end{cases} \qquad [7.25]$$

where $\varepsilon_0\mu_0 = c^{-2}$ and $\mathbf{H}_j$ is defined by:

$$\begin{cases} \mathbf{H}_2 & = (0, H_{y_2}, 0)\exp\{\mathrm{i}(k_{x2}x - \omega t) - k_{z2}z\}, z > 0, \\ \mathbf{H}_1 & = (0, H_{y_1}, 0)\exp\{\mathrm{i}(k_{x1}x - \omega t) + k_{z1}z\}, z < 0, \end{cases} \quad [7.26]$$

with $\Re(k_{z1})$ and $\Re(k_{z1})$ strictly positive in order to maintain evanescent fields above and below the interface $z = 0$. This leads to:

$$\begin{cases} \mathbf{E}_2 & = -\frac{c}{\omega}H_{y_2}(\frac{k_{z2}}{\varepsilon_{xx2}}, 0, \frac{k_{x2}}{\varepsilon_{zz2}})\exp\{\mathrm{i}(k_x x - \omega t) - k_{z2}z\}, z > 0, \\ \mathbf{E}_1 & = -\frac{c}{\omega}H_{y_1}(\frac{k_{z1}}{\varepsilon_1}, 0, \frac{k_{x2}}{\varepsilon_1})\exp\{\mathrm{i}(k_x x - \omega t) - k_{z1}z\}\ , z < 0, \end{cases} \quad [7.27]$$

with $\mathbf{E}_j = (E_{xj}, 0, E_{zj})$. The transverse wave numbers are found by invoking the other Maxwell equation:

$$\begin{cases} \nabla \times \mathbf{E}_2 & = \mathrm{i}\omega\mu_0\mu'\mathbf{H}_2, z > 0, \\ \nabla \times \mathbf{E}_1 & = \mathrm{i}\omega\mu_0\overline{\overline{\mathbf{H}}}_1, z < 0, \end{cases} \quad [7.28]$$

which leads to:

$$k_{zi} = \sqrt{\varepsilon_{xx2}\left(\frac{k_x^2}{\varepsilon_{zz2}} - \mu_{yy2}\left(\frac{\omega}{c}\right)^2\right)},\ j = 1, 2, \quad [7.29]$$

The boundary condition at the interface $z = 0$ requires continuity of the tangential components of the electromagnetic field, which brings:

$$\frac{k_{z1}}{\varepsilon_1} + \frac{k_{z2}}{\varepsilon_{xx2}} = 0\,. \quad [7.30]$$

Substituting [7.29] into [7.30], we obtain the local dispersion relation for a surface plasmon at the interface between a metal and transformed heterogeneous anisotropic medium.

For the sake of simplicity, $\varepsilon_1 = 1 - \frac{\omega_p^2}{\omega^2 + \mathrm{i}\gamma\omega}$ has the usual Drude form in the metal ($z < 0$), for which ω_p is the plasma frequency (2175 THz) of the *free electron gas* and γ is a characteristic collision frequency of about 4.35 THz.

We, therefore, have shown that in the simple case where the varying tensors of permittivity $\underline{\underline{\varepsilon'}}$ and permeability $\underline{\underline{\mu'}}$ are assumed to be represented

in a diagonal basis, i.e. $\underline{\underline{\varepsilon'}} = \mathrm{diag}(\varepsilon_{xx2}, \varepsilon_{yy2}, \varepsilon_{zz2})$ and $\underline{\underline{\mu'}} = \mathrm{diag}(\mu_{xx2}, \mu_{yy2}, \mu_{zz2})$, the dispersion relation for the surface polariton at such an anisotropic interface takes the form [REN 10]:

$$k_x = \frac{\omega}{c}\sqrt{\frac{\varepsilon_{zz2}\varepsilon_1(\mu_{yy2}\varepsilon_1 - \varepsilon_{xx2})}{\varepsilon_1^2 - \varepsilon_{xx2}\varepsilon_{zz2}}}. \qquad [7.31]$$

This necessary and sufficient condition for the existence of an SPP is richer than the usual one [7.20], and importantly only requires some magnetism along the y direction, which is parallel to the polarization of the magnetic component of the SPP field.

7.3.3. *Numerical analysis of plasmonic cloaking*

In this section, we wish to analyze the interaction of this SPP with a specific anisotropic heterogeneous structure, in the present case a 3D invisibility carpet [REN 10, ERG 10], deduced from the following geometric transformation:

$$\begin{cases} x' &= \frac{x_2(y)-x_1(y)}{x_2(y)}x + x_1(y),\ 0 < x < x_2(y), \\ y' &= y,\ a < y < b, \\ z' &= z,\ 0 < z < +\infty, \end{cases} \qquad [7.32]$$

where x' is a stretched vertical coordinate. It is easily seen that this linear geometric transform maps the segment (a, b) of the horizontal axis $x = 0$ onto the curve $x' = x_1(y)$, and it leaves the curve $x = x_2(y)$ unchanged. Importantly, there is a one-to-one correspondence between the segment and x_1. The curves x_1 and x_2 are assumed to be differentiable, and this ensures that the carpet would not display any singularity on its inner boundary.

The symmetric tensors $\underline{\underline{\varepsilon'}}$ and $\underline{\underline{\mu'}}$ are fully described by five non-vanishing entries in a Cartesian basis:

$$\underline{\underline{\varepsilon'}} = \underline{\underline{\mu'}} = \begin{pmatrix} \alpha\left(1 + \left(\frac{\partial x}{\partial y'}\right)^2\right) & -\frac{\partial x}{\partial y'} & 0 \\ -\frac{\partial x}{\partial y'} & \alpha^{-1} & 0 \\ 0 & 0 & \alpha^{-1} \end{pmatrix} \qquad [7.33]$$

where $\alpha = (x_2 - x_1)/x_2$ and with $\mathbf{J}$ the Jacobian matrix of the transformation. Furthermore, the derivative of x with respect to y' is given by:

$$\frac{\partial x}{\partial y'} = x_2\frac{x' - x_2}{(x_2 - x_1)^2}\frac{\partial x_1}{\partial y'} + x_1\frac{x_1 - x'}{(x_2 - x_1)^2}\frac{\partial x_2}{\partial y'}. \qquad [7.34]$$

We stress that such carpets work equally well for electromagnetic and plasmonic fields, as is intuitively the case when looking at the limit of ray optics, see Figures 7.10 and 7.11. The numerical simulation with finite elements is shown in Figure 7.12.

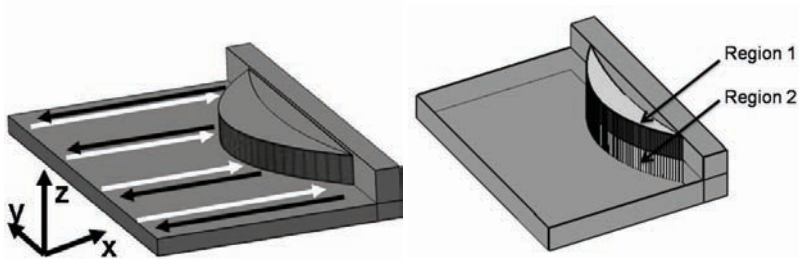

Figure 7.10. *a) Diagrammatic representation of the diffraction of an SPP incident from the left (white lines). The SPP hits the curved reflector and is reflected (black lines) as if it was a flat mirror through the transformed medium (gray and dark gray), which is the plasmonic carpet. b) diagrammatic representation of the different media needed to be transformed if we want a full control of SPP above and below the interface*

It is obvious that the wave front is exactly the same for a flat mirror (a) and a curved mirror dressed with a carpet (b). This is due to the fact that the transformed medium is valid for any field solution of the Maxwell equations. We note that new material inside the carpet is not only heterogeneous anisotropic, see Figure 7.13, but also magnetic, which seems far fetched regarding the current technological progress.

However, these constraints can be further relaxed using some quasi-conformal grids in the spirit of Li and Pendry's work for 2D carpets [LI 08]. We show in Figure 7.14 the quasi-conformal grid associated with the previous carpet. Then, keeping in mind an experimental realization requires a specific type of dielectric, in the present case TiO_2, we place particles on nodes of the quasi-grid and we optimize the size of these particles to minimize the scattering and to maximize the flatness of the reflected SPP wave front.

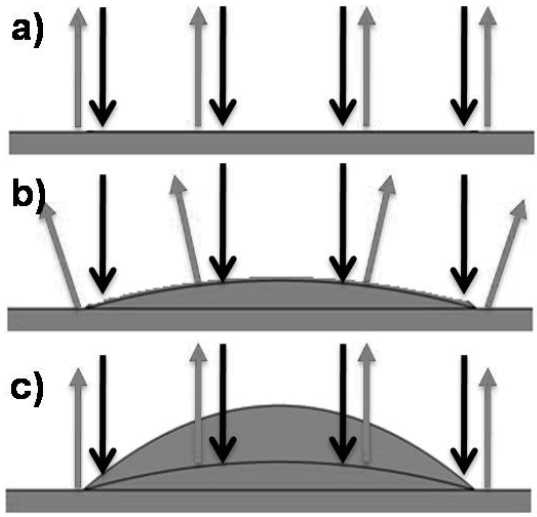

Figure 7.11. *Schematic diffraction of an SPP incident from the top: a) the SPP hits the straight reflector; b) cloak in front of the curved reflector compensates for the curved reflector; c) the SPP hits the curved reflector*

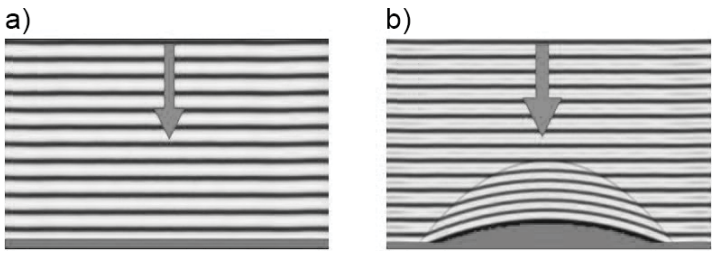

Figure 7.12. *Numerical simulation for the diffraction of an SPP incident from the top (magnetic field): a) the SPP hits the straight reflector; b) the SPP hits a carpet obtained by the geometrical transformation placed in front of the curved reflector*

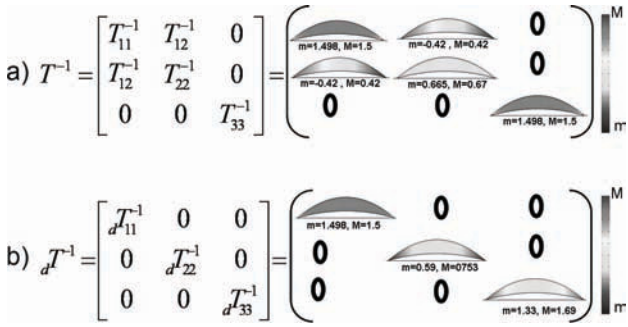

Figure 7.13. *a) Variation of the metric tensor in the plasmonic carpet; b) diagonalized metric tensor for the plasmonic carpet, which could be used in an experimental implementation*

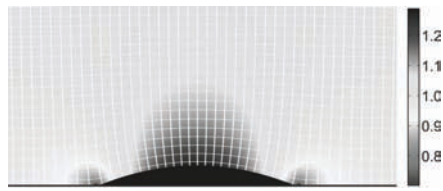

Figure 7.14. *Quasi-conformal grid associated with the geometrical transformation of the carpet. It should be noted that the right angles are preserved at the nodes of the mesh, which indicates that the associated transformed medium is nearly isotropic*

The numerical simulations in 2D, see Figure 7.15, and 3D, see Figure 7.16, validate our quasi-conformal approach to plasmonic cloaking.

Figure 7.15. *Two-dimensional numerical simulations for the diffraction of an SPP: a) on a flat mirror; b) on a curved mirror; c) on the curved mirror in presence of the metamaterial (cylindrical dielectric pillars of TiO_2) for a wavelength of 800 nm*

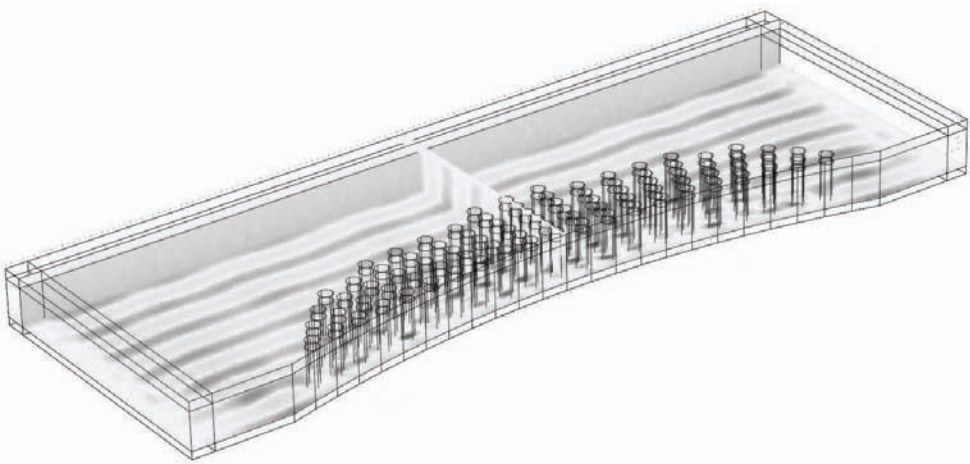

Figure 7.16. *Three-dimensional numerical simulation for the diffraction of an SPP on the curved mirror in presence of the metamaterial (cylindrical dielectric pillars of TiO_2) for a wavelength of 800 nm*

7.3.4. *Experimental measurements of plasmonic cloaking*

In order to experimentally meet the parameters found in our simulations, we chose a configuration in which a gold surface is structured with TiO_2 nanostructures. The TiO_2 pillars forming the crescent-moon-like carpet were first fabricated on top of a 60 nm thin Au film by combining electron-beam lithography and reactive ion etching. In a second lithography step, we added a curved Bragg-type reflector (formed by 15 gold lines (section = 150 nm $\times$ 150 nm) periodically separated by half the SPP wavelength), acting as the object to be hidden behind the carpet (see Figure 7.17, right panel). The shape of the obtained TiO_2 particles is conical ($h = 200$ nm, $r = 210$ nm) as a consequence of the etching anisotropy.

The SPP was launched at a ripple-like, 200 nm wide TiO_2-line placed 44 μm away from the reflector as shown in Figure 7.17, left panel. SPPs propagating on thin metal films deposited on dielectric substrate have radiative losses into the substrates. This leakage radiation was collected using a high-numerical aperture objective to map the SPP fields. Additionally for the sake of clarity, we employed spatial filtering in the conjugated (Fourier-) plane to suppress the direct transmitted light from the excitation spot and scattered light in order to isolate the carpet properties. Original attempts at reflecting SPPs with flat and curved homogeneous metallic step-like mirrors turned out to be inefficient because the SPPs tend to radiate in open space. We

therefore decided to consider flat and curved Bragg mirrors instead, formed by periodically arranged metal ridges, which show a much higher reflectivity.

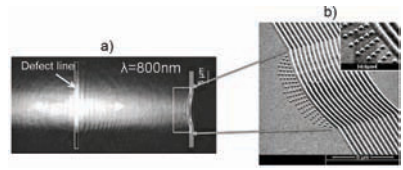

Figure 7.17. *SEM micrograph of the structure realized by single-step electron-beam-lithography: a) the defect line is used to launch the SPP from the left to the structure (bump with carpet); b) the carpet is made of TiO_2 cones as shown in the zoom*

The leakage radiation microscopy (LRM), images (see Figure 7.18) map the distribution of the SPPs propagating at the gold-air interface and interacting with the different structures fabricated at the gold surface. In the case of a bare curved Bragg-reflector, the reflected SPPs are propagating into different directions depending on their relative angle to the normal to the mirror lines (see upward pointing arrows in Figure 7.19(c)), thus leading to a curved wave front. Conversely, adding the crescent-moon-like TiO_2 carpet reestablishes a fringe pattern with a nearly straight wave front (see Figure 7.19(b)) very similar to the case of a flat Bragg-mirror. The remaining small lateral modulations are attributed to imperfections in the manufacturing. Further, data analysis has been used to quantify the modification in the wave front curvature induced by the presence of the crescent-moon-like TiO_2 carpet. Comparing the areas under the numerically averaged curves (b) (curved mirror with carpet) and (c) (curved mirror without carpet) leads to reduction by a factor 3.7 as shown in Figure 7.19(d).

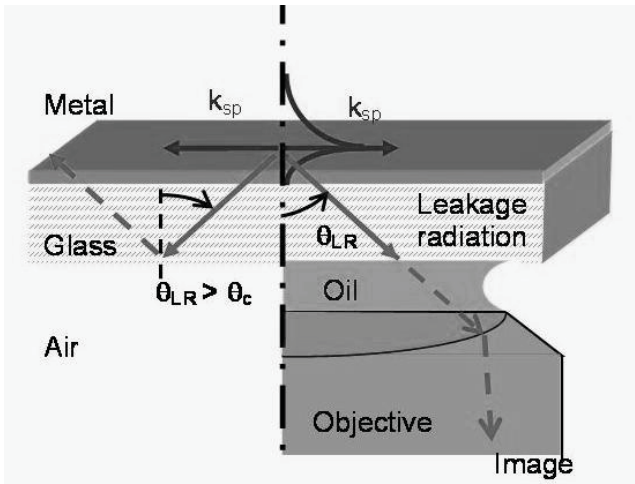

Figure 7.18. *Leakage radiation principle. By reciprocity, an SPP propagating at the surface of thin film leaks into the substrate. Mapping the leakage provides a direct information about the intensity of the surface field propagating at the interface*

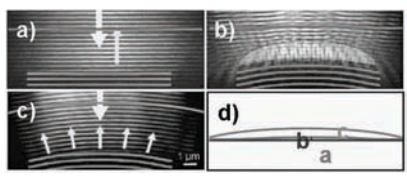

Figure 7.19. *Experimental diffraction of an SPP incident from the top (magnetic field): a) the SPP hits the straight reflector; b) cloak in front of the curved reflector nearly compensates for the curved reflector; c) the SPP hits the curved reflector d) comparison between cases a, b) and c) (source: reprinted with permission from OSA)*

7.4. Concluding remarks on LSW and SPP cloaking

In the first section, we have reviewed some lensing properties of LSWs propagating within arrays of rigid cylinders shaped as SRRs, using analogies with electromagnetic metamaterials. We then proposed an original route toward LSW cloaking. This is based on the extension of electromagnetic and acoustic cloaking mechanisms to the domain of waves propagating at the free interface between fluids and air. We have described a design of a broadband microstructured cloak consisting of a large number of small sectors arranged in a quasi-periodic manner on the surface of the liquid. For this, we have derived the homogenized linearized Navier–Stokes equations using a multi-scale asymptotic approach. We found that the homogenized fluid could be described by a rank 2 tensor (which could be interpreted as a generalized shear viscosity) and a scalar density that we took as constant to simplify the experiment realization. We then performed numerical computations based on the finite elements method, which proved that a rigid obstacle surrounded by a coating consisting of concentric layers with 100 and 200 periodic perforations is almost invisible for LSW waves. This design could be used to protect off-shore platforms or, on a larger scale, coastlines from ocean waves such as tsunamis.

In the second section, we have numerically and experimentally studied the extension of the invisibility carpet of Li and Pendry to SPPs. Our theoretical predictions, based on transformational plasmonics and quasi-conformal mapping, have been numerically and experimentally validated at visible and near infrared wavelengths for a metallic surface dressed with small (200 nm in diameter) dielectric pillars. Our results show that strong analogies exist between the physics of linear liquid waves at free air–fluid interfaces and electron waves at metal surfaces. Advances in one field might fuel research in the other one. Actually, it is cloaking for LSWs, which prompted the work on transformational plasmonics [REN 10, KAD 10, HUI 10, LIU 10, KAD 11, KAD 11].

We would like to finish this chapter as we started it: with a flat lens via negative refraction. In Figure 7.20, we dress a metallic surface with dielectric pillars forming a photonic crystal. We can see that this makes a flat lens in accordance with the inverted Snell–Descartes laws for an SPP at a visible wavelength.

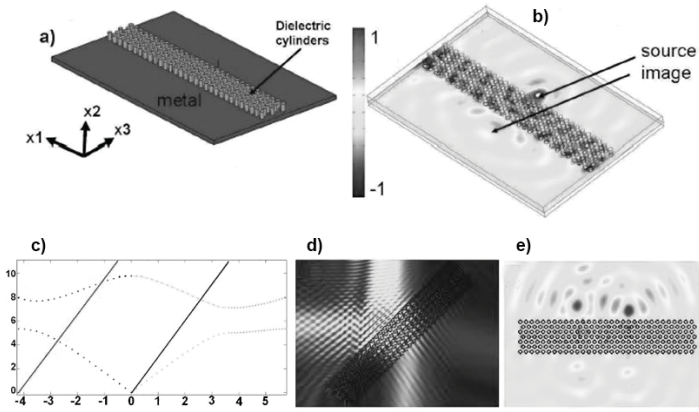

Figure 7.20. *Focusing through a plasmonic lens for an SPP line source at wavelength* $\lambda = 700$ *nm: a) schematic diagram of the flat SPP lens with a hexagonal lattice of dielectric cylinders (permittivity = 13, diameter d = 107 nm and height h = 700 nm) with center-to-center spacing of a = 180 nm, on a metal plate (Drude model with permittivity); b) 3D plot of the phase of the magnetic field; c) Band diagram of normalized frequency versus wave number showing intersection of light line with acoustic band leading to all-angle-negative refraction; d) negative refraction of an SPP beam through the slab (2D plot of the magnitude of magnetic field); e) two sources are imaged according to the laws of negative refraction*

7.5. Bibliography

[ACH 90] ACHESON D.J., *Elementary Fluid Dynamics*, Oxford University Press, Oxford, 1990.

[ALÙ 05] ALÙ A., ENGHETA N., "Achieving transparency with plasmonic and metamaterial coatings", *Physical Review E*, vol. 72, p. 016623, 2005.

[BAU 09] BAUMEIER B., LESKOVA T.A., MARADUDIN A.A., "Cloaking from surface plasmon polaritons by a circular array of point scatterers", *Physical Review Letters*, vol. 103, p. 246809, 2009.

[BLI 80] BLIEK P.J., DELEUIL R., BOTTEN L.C., *et al.*, "Inductive grids in the region of diffraction anomalies – theory, experiment, and applications", *IEEE Transactions on Microwave Theory and Techniques*, vol. 28, no. 10, pp. 1119–1125, 1980.

[BOU 10] BOUCHITTÉ G., SCHWEIZER B., "Homogenization of Maxwell's equations in a split ring geometry", *SIAM Journal of Multiscale Modeling and Simulation*, vol. 8, no. 3, pp. 717–750, 2010.

[CAI 07] CAI W., CHETTIAR U.K., KILDIEV A.V., *et al.*, "Optical cloaking with metamaterials", *Nature Photonics*, vol. 1, p. 224, 2007.

[CUM 07] CUMMER S.A., SCHURIG D., "One path to acoustic cloaking", *New Journal of Physics*, vol. 9, p. 45, 2007.

[DOL 07] DOLLING G., WEGENER M., SOUKOULIS C.M., *et al.*, "Design-related losses of double-fishnet negative-index photonic metamaterials", *Optics Express*, vol. 15, p. 11536, 2007.

[EBB 98] EBBESEN T.W., LEZEC H.J., GHAEMI H.F., *et al.*, "Extraordinary optical transmission through sub-wavelength hole arrays", *Nature*, vol. 391, pp. 667–669, 1998.

[EDW 09] EDWARDS B., ALÙ A., SILVEIRINHA M.G., *et al.*, *Physical Review Letters*, vol. 103, p. 153901, 2009.

[ERG 10] ERGIN T., STENGER N., BRENNER P., *et al.*, "Three-dimensional invisibility cloak at optical wavelengths", *Science*, vol. 328, pp. 337-339,, 2010.

[FAR 09] FARHAT M., GUENNEAU S., ENOCH S., *et al.*, "Negative refraction, surface modes, and superlensing effect via homogenization near resonances for a finite array of split-ring resonators", *Physical Review E*, vol. 80, p. 046309, 2009.

[FAN 06] FANG N., XI D., XU J., *et al.*, "Ultrasonic metamaterials with negative modulus", *Nature*, vol. 5, p. 452, 2006.

[GAR 05] GARCIA DE ABAJO F.J., GOMEZ-SANTOS G., BLANCO L.A., *et al.*, "Tunneling mechanism of light transmission through metallic films", *Physical Review Letters*, vol. 95, p. 067403, 2005.

[GUE 03] GUENNEAU S., POULTON C.G., MOVCHAN A.B., "Oblique propagation of electromagnetic and elastic waves for an array of cylindrical fibers", *Proceedings Royal Society London A*, vol. 459, pp. 2215–2263, 2003.

[GUE 07] GUENNEAU S., MOVCHAN A.B., RAMAKRISHNA S.A., *et al.*, "Acoustic meta-materials for sound focussing and confinement", *New Journal of Physics*, vol. 9, p. 399, 2007.

[GUE 09] GUENNEAU S., RAMAKRISHNA S.A., "Negative refractive index, perfect lenses and checkerboards: trapping and imaging effects in folded optical spaces", *Comptes Rendus Physique*, vol. 10, pp. 352–378, 2009.

[HUI 10] HUIDOBRO P.A., NESTEROV M.L., MARTIN-MORENO L., *et al.*, "Transformation optics for plasmonics", *Nano Letters*, vol. 10, pp. 1985–1990, 2010.

[JIK 94] JIKHOV V.V., KOZLOV S.M., OLEINIK O.A., *Homogenization of Differential Operators and Integral Functionals*, Springer Verlag, New York, 1994.

[KAD 10] KADIC M., GUENNEAU S., ENOCH S., "Transformational plasmonics: cloak, concentrator and rotator for SPPs", *Optics Express*, vol. 18, no. 11, pp. 12027–12032, 2010.

[KAD 11] KADIC M., DUPONT G., GUENNEAU S., *et al.*, "Controlling surface plasmon polaritons in transformed coordinates", *Journal of Modern Optics*, vol. 58, no. 12, pp. 994–1003, 2011.

[KAD 11] KADIC M., DUPONT G., GUENNEAU S., *et al.*, "Plasmonic wormholes: Defeating the early bird", available at http://arxiv.org/abs/1102.2372, 2011.

[KOZ 99] KOZLOV V., MAZYA V., MOVCHAN A.B., *Asymptotic analysis of fields in multistructures*, Oxford Science Publications, 1999.

[KOH 08] KOHN R.V., SHIPMAN S.P., "Magnetism and the homogenization of micro-resonators", *SIAM Journal of Multiscale Modeling and Simulation*, vol. 7, pp. 62–92, 2008.

[KRE 68] KRETSCHMANN E., RAETHER H. "Radiative decay of nonradiative surface plasmons excited by light", *Verlag der Zeitschrift für Naturforschung*, vol. 23, pp. 2135–2136, 1968.

[LEO 06] LEONHARDT A., "Optical conformal mapping", *Science*, vol. 312, pp. 1777–1780, 2006.

[LI 04] LI J., CHAN C.T., "Double negative acoustic metamaterial", *Physical Review E*, vol. 70, p. 055602, 2004.

[LI 08] LI J., PENDRY J.B., "Hiding under the carpet: a new strategy for cloaking", *Physical Review Letters*, vol. 101, p. 203901, 2008.

[LIU 00] LIU Z.Y., ZHANG X.X., MAO Y.W., *et al.*, "Locally resonant sonic materials", *Science*, vol. 289, p. 1734, 2000.

[LIU 08] LIU R., JI C., MOCK J.J., *et al.*, "Broadband ground-plane cloak", *Science*, vol. 323, p. 366, 2008.

[LIU 10] LIU Y., ZENTGRAF T., BARTAL G., *et al.*, "Transformational plasmon optics", *Nano Letters*, vol. 10, 1991–1997, 2010.

[MAI 07] MAIER S., *Plasmonics: Fundamentals and Applications,* Springer Verlag, New York, 2007.

[MCP 94] MCPHEDRAN R.C., NICOROVICI N.A., MILTON G.W., "Optical and dielectric properties of partially resonant composites", *Physical Review B*, vol. 49, pp. 8479–82, 1994.

[MIL 06] MILTON G.W., BRIANE M., WILLIS J.R., "On cloaking for elasticity and physical equations with a transformation invariant form", *New Journal of Physics*, vol. 8, p. 248, 2006.

[MIL 06a] MILTON G.W., NICOROVICI N.A., "On the cloaking effects associated with localized anomalous resonances", *Proceedings of the Royal Society of London A*, vol. 462, p. 3027, 2006.

[MOV 04] MOVCHAN A.B., GUENNEAU S., "Localised modes in split ring resonators", *Physical Review B*, vol. 70, p. 125116, 2004.

[NIC 94] NICOLET A., REMACLE J.F., MEYS B., *et al.*, "Transformation methods in computational electromagnetics", *Journal of Applied Physics*, vol. 75, pp. 6036-6038, 1994.

[NIC 07] NICOROVICI N.A.P., MILTON G.W., MCPHEDRAN R.C., *et al.*, "Quasistatic cloaking of two-dimensional polarizable discrete systems by anomalous resonance", *Optics Express*, vol. 15, pp. 6314–6323, 2007.

[OBR 02] O'BRIEN S., PENDRY J.B., "Photonic band-gap effects and magnetic activity in dielectric composites", *Journal of Physics-Condensed Matter*, vol. 14, pp. 4035–4044, 2002.

[PEN 00] PENDRY J.B., "Negative refraction makes a perfect lens", *Physical Review Letters*, vol. 85, p. 3966, 2000.

[PEN 04] PENDRY J.B., MARTIN-MORENO L., GARCIA-VIDAL F.J., "Mimicking surface plasmons with structured surfaces", *Science*, vol. 305, p. 847, 2004.

[PEN 06] PENDRY J.B., SCHURIG D., SMITH D.R., "Controlling electromagnetic fields", *Science*, vol. 312, pp. 1780–1782, 2006.

[PEN 96a] PENDRY J.B., HOLDEN A.J., ROBBINS D.J., *et al.*, "Extremely low frequency plasmons in metallic mesostructures", *Physical Review Letters*, vol. 76, p. 4763, 1996.

[PEN 96b] PENDRY J.B., HOLDEN A.J., STEWART W.J., *et al.*, "Magnetism from conductors and enhanced nonlinear phenomena", *IEEE Transactions on Microwave Theory and Techniques*, vol. 47, pp. 2075–2084, 1996.

[RAI 12] RAINWATER D., KERKHOFF A., MELIN K., *et al.*, *New Journal of Physics*, vol. 14, p. 013054, 2012.

[RAT 88] RATHER H., *Surface Plasmons*, Springer-Verlag, Berlin, 1988.

[REN 10] RENGER J., KADIC M., DUPONT G., *et al.*, "Hidden progress: broadband plasmonic invisibility", *Optics Express*, vol. 18, (15), 15757–15768, 2010.

[RIT 57] RITCHIE R.H., "Plasma losses by fast electrons in thin films", *Physical Review*, vol. 106, pp. 874-881, 1957.

[RUS 03] RUSSELL P.S., MARIN E., DIEZ A., *et al.*, "Sonic band gap PCF preforms: enhancing the interaction of sound and light", *Optics Express*, vol. 11, p. 2555, 2003.

[SCH 06] SCHURIG D., MOCK J.J., JUSTICE J.B., *et al.*, "Metamaterial electromagnetic cloak at microwave frequencies", *Science*, vol. 314, pp. 977–980, 2006.

[SMI 00] SMITH D.R., PADILLA W.J., VIER V.C., *et al.*, "Composite medium with simultaneously negative permeability and permittivity", *Physical Review Letters*, vol. 84, p. 4184, 2000.

[SMO 08] SMOLYANINOV I.I., HUNG Y.J., DAVIS C.C., "Two-dimensional metamaterial structure exhibiting reduced visibility at 500 nm", *Optics Letters*, vol. 33, pp. 1342–1344, 2008.

[VAL 09] VALENTINE J., LI J., ZENTGRAF T., *et al.*, "An optical cloak made of dielectrics", *Nature Materials*, vol. 8, pp. 569-571, 2009.

[VES 68] VESELAGO V.G., "The electrodynamics of substances with simultaneously negative values of ϵ and μ", *Sov. Phys. Usp.*, vol. 10, pp. 509–514, 1968.

[WAR 96] WARD A.J., PENDRY J.B., "Refraction and geometry in Maxwellås equations", *Journal of Modern Optics*, vol. 43, pp. 773-793, 1996.

[WOO 02a] WOOD R.W., "On a remarkable case of uneven distribution of light in a diffraction grating spectrum", *Phil. Mag.*, vol. 4, p. 396, 1902.

[ZOL 07] ZOLLA Z., GUENNEAU S., NICOLET A., *et al.*, "Electromagnetic analysis of cylindrical invisibility cloaks and the mirage effect", *Optics Letters*, vol. 32, p. 1069, 2007.

Chapter 8

Classical Analog of Electromagnetically Induced Transparency

Metamaterials provide an attractive way to achieve dispersion-engineered electromagnetic media. Of particular interest are metamaterials that exhibit the so-called classical analog of electromagnetically induced transparency (EIT) because they combine large group delay with low absorption at the same frequency, making them suitable for delay lines in microwave photonics and slow-light applications at optical frequencies. Classical EIT metamaterials are also interesting for sensing applications, due to the high sensitivity of the resonance to the environment. We discuss the design and modeling of EIT metamaterials and some work on its applications for sensing and for media with nonlinear response.

8.1. Introduction

EIT is originally a quantum-mechanical effect that renders an otherwise opaque medium transparent in a narrow transmission window with low absorption [HAR 90]. It occurs in certain three-level atomic systems, e.g., alkali metal vapors, doped solid-state materials or quantum-dot-based systems, where destructive interference between two radiative transitions creates a dark dressed superposition state with no electric dipole moment [HAR 97, MAN 01, FLE 05]. In the simplest case, these atomic systems have

---

Chapter written by Philippe TASSIN, Thomas KOSCHNY and Costas M. SOUKOULIS.

two ground states and one common excited state (as in Figure 8.1(a)), transitions between the two ground states are forbidden. A laser beam (the probe) couples one of the ground states to the excited state, resulting in a typical Lorentzian absorption spectrum. When a second beam couples the other ground state to the excited state, a peculiar phenomenon is observed: destructive interference between both excitation pathways results in vanishing probability for the atomic system to be found in the excited state. The material decouples from the external field of the probe beam and behaves at this frequency almost like vacuum. The result is an incision (the transmission window) in the Lorentzian absorption spectrum of the probe, as shown in Figure 8.1(b). At the same frequency, there is very strong normal dispersion (Figure 8.2(c)), which can lead to a remarkable increase in the group delay of the sample.

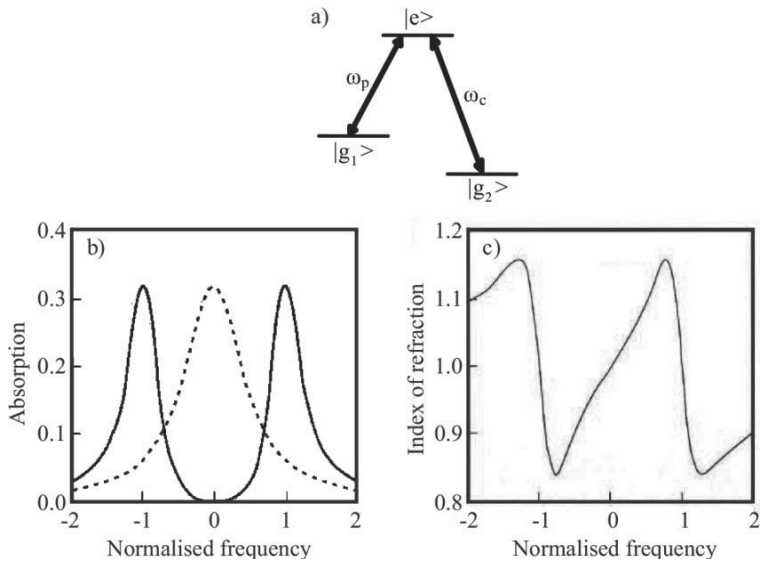

Figure 8.1. *a) Energy diagram of atomic EIT media; b) absorption spectrum of an EIT medium showing the transparency window inside the Lorentzian background; c) index of refraction of an EIT medium showing steep dispersion at the same frequency of the absorption minimum [HAR 97)*

Quantum-mechanical EIT has the potential for dramatic deceleration of light to a group velocity of about 17 m/s [HAU 99] and even for the storage of light [FLE 00, LIU 01]. However, the rather short coherence time of the dark superposition state necessitates complicated experimental handling,

often requiring cryogenic temperatures and/or strong magnetic fields. However, it was realized recently that the characteristic features of EIT – simultaneously low absorption and strong dispersion – can also be realized in purely classical systems such as coupled mechanical or electrical resonators [GAR 02], i.e. no quantum-mechanical superposition states are necessary. Although the physics of such classical EIT systems is very different from the quantum-mechanical EIT in atomic systems, the underlying idea is similar – there are two resonances that interfere destructively in a narrow transmission band causing decoupling from the external field. Many classical analogs have since been demonstrated in optical microresonators [XU 06] or coupled acoustic resonators [LIU 10a].

A few years ago, three groups of scientists independently proposed to create meta-atoms consisting of coupled electrical or plasmonic resonators to achieve effective metamaterials with an EIT response [ZHA 08, PAP 08, TAS 09a][1]. A very illustrative example is the meta-atom in Figure 8.2(a), which consists of two perpendicular split-ring resonators. An incident plane electromagnetic wave, propagating from bottom to top, can couple to the leftmost split-ring resonator, which has the magnetic dipole of its magnetic resonance parallel to the magnetic field. This resonator is commonly called the radiative or the bright resonator. However, the wave cannot couple directly with the other split ring, whose magnetic dipole is oriented perpendicularly – designated as the dark resonator. Of course, there is a capacitive (and inductive) interaction between the two split-ring elements, so when the magnetic dipole mode of the first ring is excited, energy will be exchanged between the two rings through the quasistatic interaction. The transmittance and absorbance of the resulting metamaterial is shown in Figure 8.2(b). We can observe the characteristic features of EIT: a transmission window with low absorption and strong dispersion. Note that the capacitive interaction can be straightforwardly altered by changing the distance between the two split rings. There is also no need for a pump beam to achieve the interaction between the two resonators as opposed to the quantum-mechanical version. In the past few years, classical EIT

1 Some authors have described this phenomenon as a classical analog of Fano resonances rather than EIT. The difference originates in whether the radiative resonator is considered a single resonance (it is indeed a single electromagnetic resonance) or a continuum of resonances (the electromagnetic resonance is broadened by dissipative loss or radiation loss). It is merely a matter of terminology.

metamaterials have been demonstrated experimentally by many scientists around the world[2].

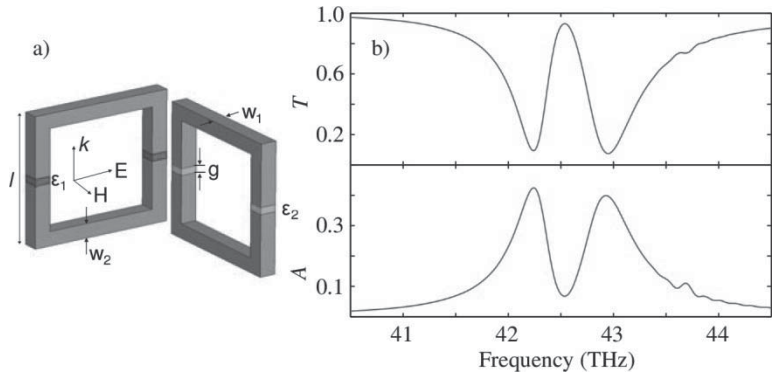

Figure 8.2. *a) Metamaterial implementing the classical analog of electromagnetically induced transparency using two coupled split-ring resonators; b) transmission and absorption spectra (source: adapted from Phys. Rev. Lett., vol. 102, 2009, p. 053901)*

8.2. Design of EIT metamaterials

The double split-ring meta-atom discussed above is very instructive in explaining the physics, but its three-dimensional geometry makes it impractical for fabrication. Planar metamaterials are indeed often preferred since they are much easier to fabricate than three-dimensional structures, e.g., with lithographic techniques. Figure 8.3(a) shows an example of a planar EIT metamaterial. The meta-atom contains a double-gap split-ring resonator and a cut wire. The incident wave propagates normal to the substrate and with the electric field polarized along the cut wire, so it can directly couple to the electric dipole resonance of the cut wire. The two-gap split-ring resonator is designed to have a magnetic resonance at the same frequency, but since it has a symmetry plane parallel with the electric field, the incident field cannot directly couple to it. The magnetic dipole resonance of the split ring is thus the dark resonance. Figure 8.3(b) plots the absorption spectrum. At $f = 9.75$ GHz, we observe the transmission window with minimal absorption. In Figure 8.3(c), we observe strong dispersion in the effective permittivity of the metamaterial (this metamaterial has a group delay that is 100 times larger

2 See, for example, [ZHA 08, PAP 08, TAS 09a, TAS 09b, LIU 09, LIU 10b, SIN 09, ZHA 10a, TSA 10, ZHA 10b, OOI 11, VER 11].

than in vacuum). It is instructive to look at the electric currents in the wire and the ring because they confirm the physics of destructive interference in the electric dipole moment. Figure 8.4(a) shows the electric current distribution at an absorption peak, i.e. away from the dark resonance frequency. We observe most of the electric current flows in the cut wire. At the EIT frequency, a large current is flowing in the split-ring resonator, i.e. the dark resonator is strongly excited, while there is almost no current in the wire. This is because the current directly induced by the external field in the wire cancels the current induced by the interaction with the split-ring resonator. As a result, the material decouples from the external field at this point and the effective permittivity is close to unity (like vacuum). The result is the excitation of a mode with a very small electric dipole moment – hence the large transmission.

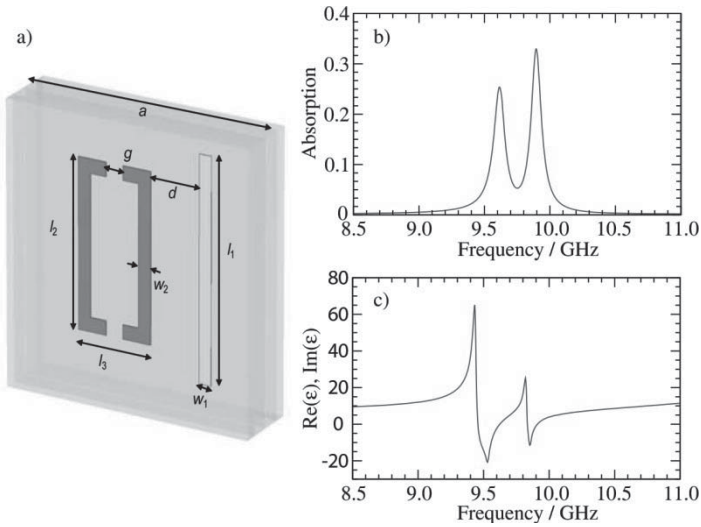

Figure 8.3. *a) A planar EIT metamaterial; b) absorption spectrum showing the transmission window with low absorption; c) effective permittivity of the EIT metamaterial showing the strong dispersion (source: from Opt. Express, vol. 17, 2009, pp. 5595–5605)*

An important aspect of classical EIT is the quality factor of the dark resonator. In section 8.5, we will see that EIT can only be achieved if the quality factor of the dark resonator is much larger than the quality factor of the radiative resonator. Special care must therefore be taken in the design of the dark resonator to reduce energy loss as much as possible. In general, there

are two mechanisms that contribute to the finite quality factor of the dark resonator:

– dissipative loss;

– radiation loss.

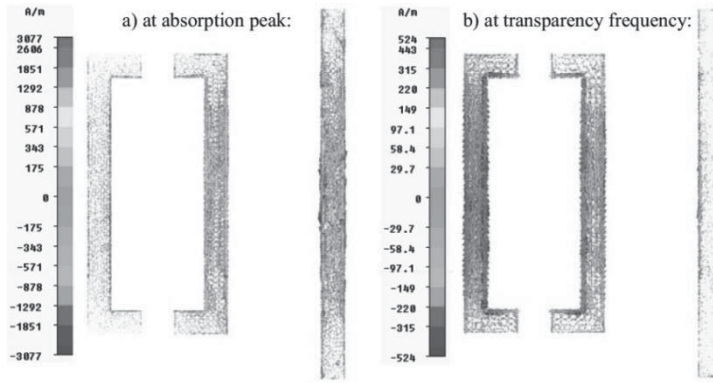

Figure 8.4. *Current distribution in the EIT metamaterial depicted in Figure 8.3(a): a) at the absorption peak; b) at the transparency frequency (source: from Opt. Express, vol. 17, 2009, pp. 5595–5605)*

Radiation loss occurs because the meta-atoms act as small antennas that reradiate electromagnetic waves. For the radiative resonator, this is desired since its radiated fields combine to form the transmitted and reflected waves of the metamaterial. We do not need radiation loss in the dark resonator, of course, but reradiation by the split-ring resonator of Figure 8.3(a) into a mode that is orthogonal to the incident wave can still happen. The quality factor of the dark resonator can be increased by reducing the radiation loss. This is achieved in the metamaterial shown in Figure 8.5(a). The unit cell contains a double planar split-ring resonator symmetrically located around a metal wire. Similar as above, the cut wire has an electrical dipole moment providing for the radiative resonator. The transmitted waves (Figure 8.5(b)) indicate that this metamaterial does not have just one, but three dark modes.

The current distributions at the maximum-transmission frequencies illustrate what is happening. In Figure 8.6(a), displaying the current distribution at $f = 10.62$ GHz (the feature labeled *a* in Figure 8.5(b)), there is a large current density in the wire only; this is the radiative electric dipole resonance of the wire. At the EIT feature at $f = 10.30$ GHz (*b* in Figure 8.5(b)), we see large currents in the split rings and only a small current

in the wire commensurate with a dark mode excitation (Figure 8.6(b)). The current distribution reveals that this dark mode is one of the hybridizations of the electric dipole resonances of the split-ring resonators. We see that the currents in the two different split rings flow in opposite directions. The EIT feature at f = 10.41 GHz (c in Figure 8.5(b)) has the main currents circling around the split rings – one in a clockwise direction and the other in a counterclockwise direction (Figure 8.6(c)); this is the symmetric hybridization of the magnetic dipole resonances of the split-ring resonators. At the frequencies of the EIT feature at f = 10.49 GHz (d in Figure 8.5(b)), the current density is again circling the split-ring resonators, but now in the same direction for both split rings (Figure 8.6(d)). This is the anti-symmetric hybridization of the magnetic dipole resonances of the split-ring resonators.

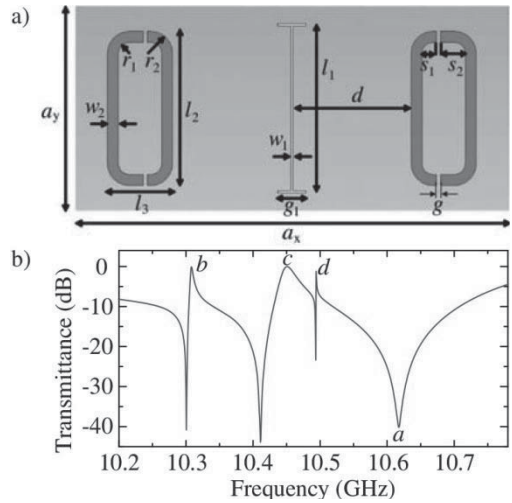

Figure 8.5. *a) Meta-atom with a dark element that has no dipole moment to reduce radiation loss; b) transmittance spectrum of this EIT metamaterial (source: from Phys. Rev. Lett., vol. 107, 2011, p. 043901)*

The resonances in Figure 8.6(b) and (c) are especially attractive because they eliminate the electric (magnetic) dipole moment, i.e. they are quadrupole modes. This eliminates any dipole radiation from the dark resonator, increasing its quality factor. In other words, a good geometrical design of the dark resonator can improve EIT metamaterials significantly. It is important to note that the dark "resonator" does not need to be a distinct physical structure, but can rather be just another electromagnetic eigenmode of the meta-atom. The electric quadrupole mode has another advantage here: when

the wire is placed exactly in the symmetry plane of the double ring structure, there is no interaction between the dark and bright resonators. This enables us to create a very small coupling strength by moving the wire slightly away from the symmetry plane.

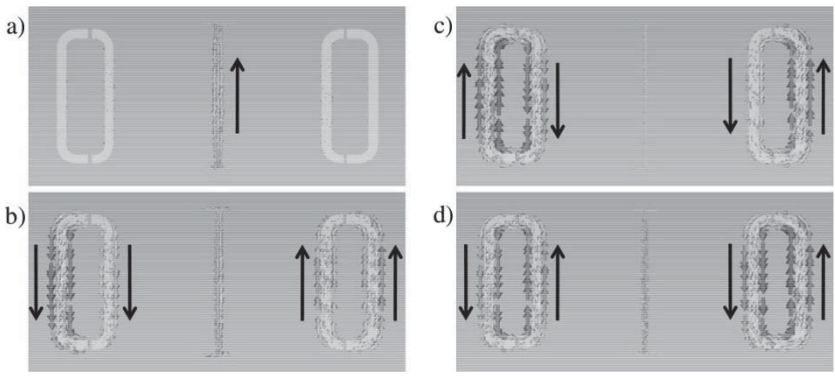

Figure 8.6. *Current distributions in an EIT metamaterial with a dark resonator with vanishing dipole radiation. The labels a)–d) correspond to the spectral features marked with the same label in Figure 8.5(b) (source: from Phys. Rev. Lett., vol. 107, 2011, p. 043901)*

To reduce the dissipative loss, we can use the techniques described in Chapter 5. At microwave frequencies, a very effective way to address dissipative loss in the dark resonator is to fabricate it out of a superconductor and using high-quality substrates. This strategy was actually used in the metamaterial depicted in Figure 8.5(a), where the split rings are made out of a superconducting niobium (Nb) film. When cooled down sufficiently below the critical temperature, Nb has a resistivity that is five orders of magnitude smaller than the resistivity of silver at room temperature (at 10 GHz). With the use of a superconductor, we have achieved group delays of 300 ns in the X band from a subwavelength-thin metamaterial (see group delay measurements in Figure 8.7). For this 250-μm-thick metamaterial, the measured delay corresponds to a group velocity of roughly 1000 m/s – or slowdown of light by a factor of 250,000 – and may find application as compact delay lines in microwave photonics. The delay-bandwidth product (DBP) of the metamaterial shown in Figure 8.5(a) is 0.3, which approaches the DBPs in resonant cavities (DBP ≈ 1), but is still smaller than media containing atomic vapors (DBP ≈ 10) and some photonic crystal waveguides (DBP ≈ 100), but we should keep in mind that the latter systems are much longer than a single wavelength.

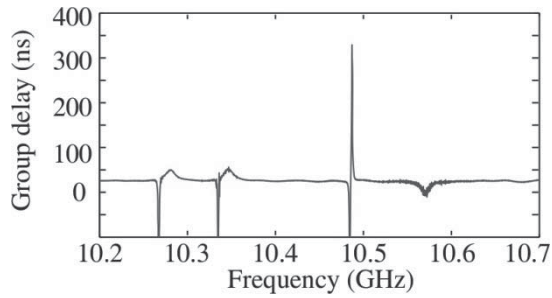

Figure 8.7. *Experimentally measured group delay of an EIT metamaterial with a dark resonator made from the superconductor niobium to minimize dissipative loss (source: from Phys. Rev. Lett., vol. 107, 2011, p. 043901)*

8.3. A simple model for EIT metamaterials – and electromagnetically induced absorption

To further our understanding of EIT metamaterials and to aid in their design, it is desirable to have a simple model describing their main properties.

8.3.1. *The two-oscillator model*

The simplest model to describe classical EIT systems is a set of two coupled mass-spring oscillators or two RLC circuits coupled by a shunt capacitor (see Figure 8.8), i.e. two coupled harmonic oscillators with a linear interaction term:

$$\begin{aligned} \omega_{\mathrm{r}}^{-2}\ddot{p}(t)+\gamma_{\mathrm{r}}\omega_{\mathrm{r}}^{-1}\dot{p}(t)+p(t)&=f(t)-\kappa q(t),\\ \omega_{\mathrm{d}}^{-2}\ddot{q}(t)+\gamma_{\mathrm{d}}\omega_{\mathrm{d}}^{-1}\dot{q}(t)+q(t)&=-\kappa p(t). \end{aligned} \qquad [8.1]$$

The radiative resonator with resonance frequency ω_{r} and damping factor γ_{r} is described by the excitation $p(t)$ and is driven by the external force $f(t)$. The dark resonator with resonance frequency ω_{d} and damping factor γ_{d} is described by the excitation $q(t)$. Both resonators are linearly coupled with coupling strength κ. The individual oscillators are electromagnetic resonators or electromagnetic resonances of the meta-atoms.

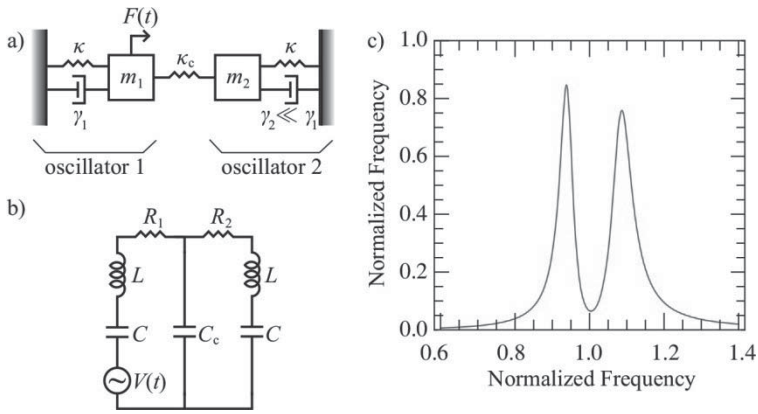

Figure 8.8. *Two-oscillator models: a) mechanical analog; b) electrical circuit analog; c) absorbed power spectrum in a system of two linearly coupled harmonic oscillators*

The equations of model [8.1] reflect the essential ingredients of EIT systems: they contain two coupled resonances that are asymmetrically driven by the external force. They can be solved in the frequency domain to obtain:

$$p(\omega) = \frac{D_{\mathrm{d}}(\omega) f(\omega)}{D_{\mathrm{d}}(\omega) D_{\mathrm{r}}(\omega) - \kappa^2},$$
$$q(\omega) = \frac{\kappa f(\omega)}{D_{\mathrm{d}}(\omega) D_{\mathrm{r}}(\omega) - \kappa^2}, \qquad [8.2]$$

where $D_{\mathrm{r}}(\omega) = 1 - (\omega/\omega_{\mathrm{r}})^2 - \mathrm{i}\gamma_{\mathrm{r}}(\omega/\omega_{\mathrm{r}})$ and $D_{\mathrm{d}} = 1 - (\omega/\omega_{\mathrm{d}})^2 - \mathrm{i}\gamma_{\mathrm{d}}(\omega/\omega_{\mathrm{d}})$.

The dissipated power per unit cell, shown in Figure 8.8(c) and obtained from:

$$Q = \frac{1}{2}\mathrm{Re}\left[f \times \dot{p}\right] = \frac{\omega^2}{2}\left(\gamma_{\mathrm{r}} |p(\omega)|^2 + \gamma_{\mathrm{d}} |q(\omega)|^2\right), \qquad [8.3]$$

has a Lorentzian shape with a sharp incision at the resonance frequency if $\omega_{\mathrm{r}} \approx \omega_{\mathrm{d}}$, $\gamma_{\mathrm{d}} \ll \gamma_{\mathrm{r}}$ (i.e. the quality factor of the dark resonator must be larger than the quality factor of the radiative resonator), and $\gamma_{\mathrm{d}}\,\gamma_{\mathrm{r}} \ll \kappa^2 \ll 1$. Based on the two-resonator model, we can derive a few rules of thumb by expanding equation [8.3] in the vicinity of the EIT resonance frequency. These rules of thumb are depicted in Figure 8.9. It is important to note that the bandwidth of

the EIT resonance is related to the coupling strength κ, and not to the quality factor as would be the case for a simple Lorentzian resonance.

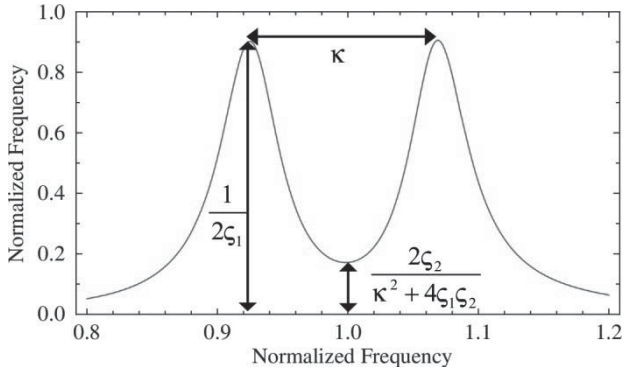

Figure 8.9. *Rules of thumb for the bandwidth of the transmission window and the absorption minimum of the EIT spectrum*

Even though the two-resonator model can qualitatively describe the absorption of classical EIT analog, it fails to model the scattering parameters of metamaterials exhibiting a classical EIT response, i.e. there is no information about the transmission and reflection spectra. This is especially troublesome since it makes it impossible to determine the group delay, quite an essential parameter for slow-light media.

8.3.2. *The radiating two-oscillator model*

To obtain a model that rigorously describes both the microscopic and the macroscopic responses in terms of the radiated field (i.e. the incident, reflected and transmitted waves), we have to include the actual coupling of the bright resonator to the external world. Most of the EIT metamaterials fabricated to date are essentially single-layer structures rather than bulk media. Hence, their effective response can be described by an electric current sheet with surface conductivity σ_{se}. The scattering parameters of an electric current sheet are:

$$R = -\frac{\zeta\sigma_{se}}{2+\zeta\sigma_{se}},$$
$$T = \frac{2}{2+\zeta\sigma_{se}}, \qquad [8.4]$$

where ζ is the wave impedance of the external waves. Equations [8.4] serve as the *world model*, i.e. they describe the interaction of the medium with the external electromagnetic field. The local microscopic behavior of the EIT medium can still be described by the two-resonator model as given by equations [8.1].

In order to complete the radiating two-oscillator model, we have to find a connection between the external behavior of the system (the surface field $E_s = R\,E_{in} = (1 + T)\,E_{in}$) and the surface conductivity σ_s) and the microscopic behavior (the excitations p and q and the driving force f). First, we observe that each of the constituent meta-atoms contributes a dipole moment p to the metamaterial, and if there are n_s atoms per unit of surface area, the average polarization current thus equals:

$$\left\langle j_s(t)\right\rangle = n_s \dot{p}(t) \leftrightarrow \left\langle j_s(\omega)\right\rangle = -\mathrm{i}\omega n_s\, p(\omega). \qquad [8.5]$$

The dark resonator does not contribute to the surface current since it has no dipole moment commensurate with the external field. Second, we need to find a connection between the surface field E_s, which drives the dipole oscillation in the world model, and the driving force f in the microscopic model, i.e. we seek the proportionality constant C in $f(t) = C\,E_s$. (Note that the surface field E_s is different from the incident field because of the scattering from the meta-atoms.) This can be done by recalling that for our linear meta-atom the average dipole moment must be proportional to the electric field at the surface:

$$n_s p(\omega) = \varepsilon_0 \chi_{se}(\omega) E_s(\omega), \qquad [8.6]$$

where χ_{se} is the surface susceptibility. In the static limit, this yields:

$$\epsilon_0 \chi_{se}^{(static)} E_s(0) = n_s p(0) = n_s \left(1-\kappa^2\right)^{-1} f(0) \approx n_s f(0), \qquad [8.7]$$

where we used the fact that κ^2 « 1 under EIT conditions. Using equations [8.5], [8.6] and [8.7], we can now determine the surface conductivity:

$$\sigma_{se} \approx \varepsilon_0 \chi_{se}^{(static)} \frac{-\mathrm{i}\omega p(\omega)}{f(\omega)} = \frac{-\mathrm{i}\omega\beta D_d(\omega)}{D_d(\omega) D_r(\omega) - \kappa^2}, \qquad [8.8]$$

where $\beta \equiv \varepsilon_0 \chi_{se}^{(static)}$. Once we have determined the surface conductivity, we can calculate the scattering parameters from equations [8.4] and other derived quantities, in particular the absorbance and the group delay:

$$A = 1 - |T|^2 - |R|^2 = |T|^2 \,\mathrm{Re}(\zeta \sigma_{se}),$$
$$\tau_g = \mathrm{Im}\left(\frac{\mathrm{d}\ln T}{\mathrm{d}\omega}\right) = -\frac{1}{2}\mathrm{Im}\left(T\frac{\mathrm{d}\zeta\sigma_{se}}{\mathrm{d}\omega}\right). \qquad [8.9]$$

In Figure 8.10, we compare results of the radiating two-oscillator model with experimental data for a copper-on-alumina EIT metamaterial that takes advantage of the quadrupole dark mode described in section 8.2. The model describes the experimental results very well. It is a very useful tool when deciding what parameters need to be changed in order to achieve a certain dispersion and absorption spectrum. For example, in Figure 8.9, we see that larger coupling strength results in an EIT resonance with larger bandwidth, in agreement with the rule of thumb derived in section 8.3.1.

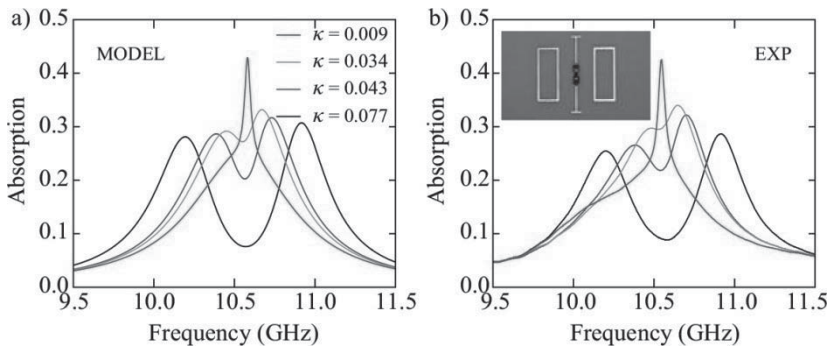

Figure 8.10. *Comparison between absorption spectra obtained from a) the radiating two-oscillator model and b) from experimental results of an EIT metamaterial for several values of the coupling strength (source: from Phys. Rev. Lett., vol. 109, 2012, p. 187401)*

8.4. Electromagnetically induced absorption

One of the spectra in Figure 8.10 ($\kappa = 0.009$) has a curious feature – it has an absorption peak instead of an absorption dip at the EIT resonance frequency. It can therefore be considered as the classical analog of electromagnetically induced *absorption* (EIA) first studied by Akulshin *et al*. [AKU 98] in atomic systems. This classical analog was recently predicted

and observed by several groups. Let us use the radiating two-oscillator model to study this phenomenon in more detail.

In Figure 8.11(a), we show how the absorption, transmission and group delay spectra evolve if we decrease the dissipative loss factor γ_r of the radiative resonator. There is still a frequency window with high transmission, but the incision in the absorption spectrum becomes smaller and finally disappears. This does not mean, however, that the dark resonance has disappeared, as we can clearly see from the enhanced group delay. Rather, the background absorption of the radiative resonance is decreased, but the radiative resonance is still sufficiently broadened by radiation damping, while the excitation of the dark resonance is barely changed. At a certain point, the absorption reduction in the radiative resonator due to the destructive interference mechanism is exactly cancelled by the absorption in the dark resonator. When we further decrease the dissipative loss of the radiative resonator, the absorption spectrum turns into a very shallow and weak background with a narrow peak at the resonance frequency ω_d. The transition between EIT and EIA can also be observed when we increase the dissipative loss of the dark resonator (see Figure 8.11(b)). When γ_d is increased, the radiative resonance remains unaltered, but the absorption in the center of the transparency window goes up. Eventually, the loss in the dark resonator overcomes the loss reduction due to the destructive interference in the radiative resonator. Finally, EIA can also be achieved by decreasing the coupling strength κ. Weaker coupling creates a narrower transparency window with larger excitation in the dark resonator. This in turn increases the absorption at the resonance frequency, resulting in EIA when the dissipation in the dark resonance overcomes the loss reduction in the radiative resonance.

We believe the classical analog of EIA may be interesting for applications in spectroscopy and sensing, since it produces a spectral feature with a narrow bandwidth. The width of the peak is reduced by the lack of radiation damping in the dark resonator and the additional narrowing due to the coupling mechanism. Note that the EIA effect could only be described by the radiating two-oscillator model, since the bare two-resonator model lacks the radiative broadening of the radiative resonator. Alternatively, EIA can be achieved by introducing a retardation-induced phase shift in the interaction between the dark and bright resonators [TAU 12] or by coupling both the dark and bright resonator to the external wave but with different phase advance [VER 12].

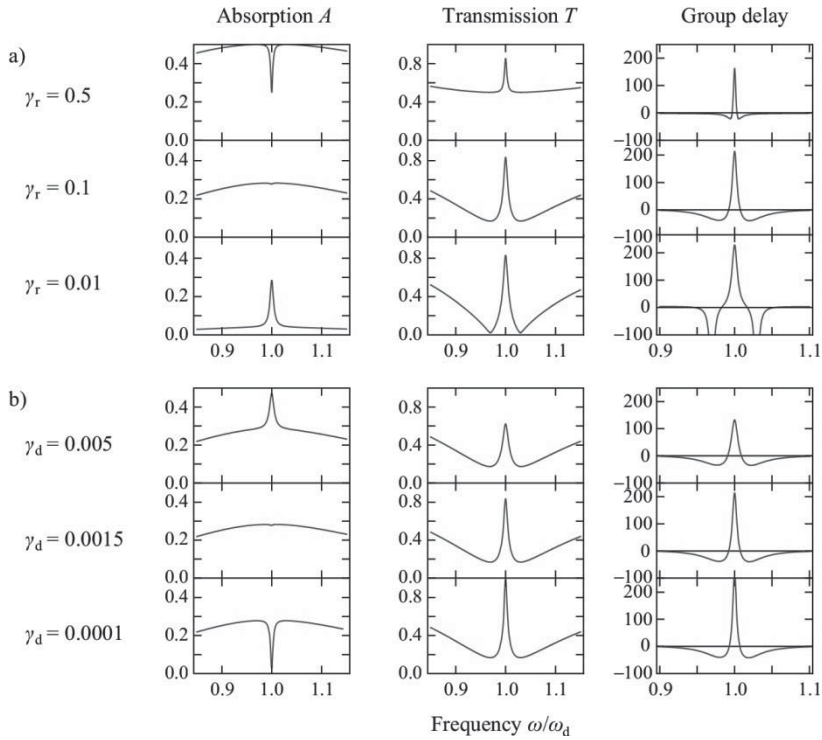

Figure 8.11. *Study of the radiating two-oscillator model and appearance of electromagnetically induced absorption when a) the dissipative loss of the bright resonance is decreased and b) the dissipative loss of the dark resonance is increased (source: from Phys. Rev. Lett., vol. 109, 2012, p. 187401)*

8.5. EIT metamaterials for sensors

The spectral feature of EIT metamaterials can be very narrow – only limited by dissipative loss, not by radiation loss – and the large fields in the dark resonator make it very sensitive to changes in the (dielectric) environment. These two characteristics make EIT metamaterials suitable for sensing applications. In an early work by researchers at the University of Stuttgart [LIU 10b], an EIT metamaterial was constructed by creating cut-outs in a gold film on a glass substrate (see Figure 8.12(a)). The cut-outs are designed to have a quadrupole resonance and a dipole resonance at the same frequency. Note that this is a complementary structure, so the radiative resonance creates a (broad) reflection dip and at the EIT frequency the radiative resonance is silenced to create a narrow peak in reflectance.

Figure 8.12(b) plots the reflectance spectra of the sensing metamaterial when either water (n = 1.332) or a 25% aqueous glucose solution (n = 1.372) is put on the sample's surface. The result is a wavelength shift of 23.5 nm of the EIT feature. This corresponds to a sensitivity of 588 nm/RIU.[3]

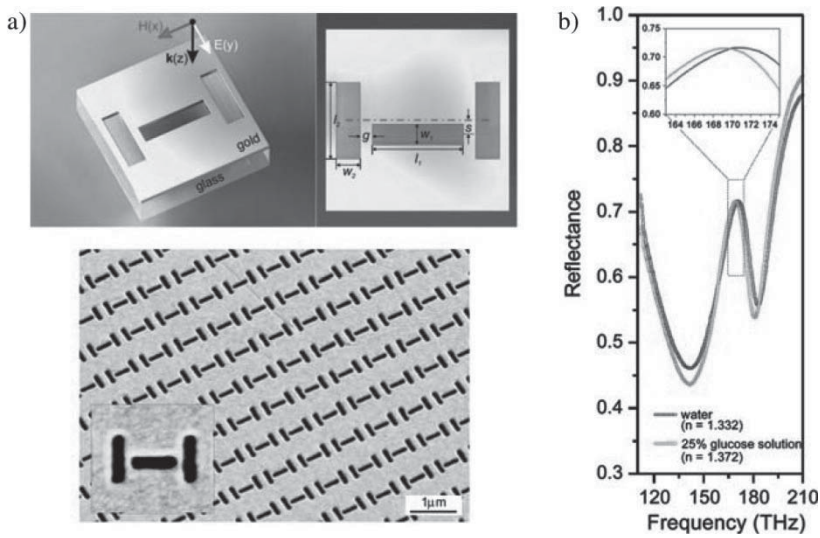

Figure 8.12. *a) EIT metamaterial optimized for refractive index sensing in the infrared; b) reflectance spectra of the metamaterial, one with water and one with a glucose solution on the sample's surface; the inset zooms in on the frequency shift of the reflectance peak at the resonance frequency (source: from Nano Lett., vol. 10, 2010, pp. 1103–1107)*

Optical refractive index sensors based on EIT metamaterials were further developed by several authors. Improved sensitivity was obtained from the metamaterial structure shown in Figure 8.13 – the cross, which has a quadrupole resonance, is the dark resonator and the wire is the radiative resonator as before [VER 11]. This structure allows for sensitivities up to 1,000 nm/RIU for a spectral feature of only 60 nm wide. Further enhancement of the sensitivity has been predicted by integrating gain media into the EIT metamaterial [DON 11], but this has not yet been experimentally demonstrated at the time of printing.

3 Definition: RIU = refractive index unit.

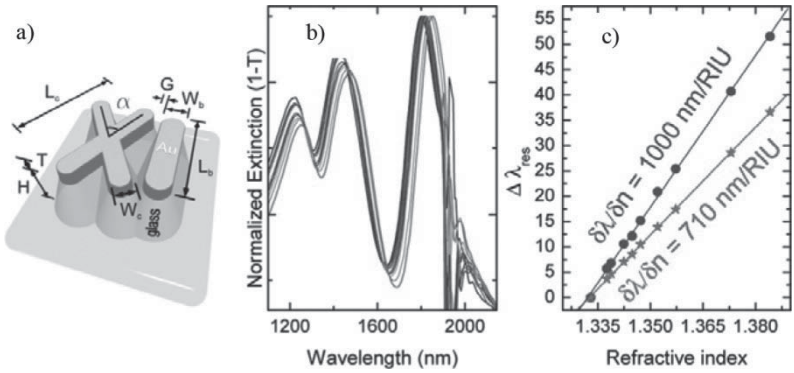

Figure 8.13. *a) Unit cell of another EIT metamaterial for refractive index sensing; b) extinction spectra; c) sensitivity (source: from Nano Lett., vol. 11, 2011, pp. 391–397)*

8.6. EIT metamaterials for nonlinear and tunable operation

A second application of EIT metamaterials is the construction of metamaterials with nonlinear response. The idea is to introduce a nonlinear medium in the vicinity of the dark resonator where the near field is very strong. One possibility is fabricating the dark resonator out of a superconducting material. The meta-atom shown in Figure 8.14(a) is the same as the one discussed in section 8.2, but now we have deliberately introduced very sharp corners in the split-ring resonators [KUR 12]. At low input power (P < 10 dBm), the EIT metamaterial works as usual and we observe the resonance with high transmittance and large group delay (see Figure 8.14(b)). However, if we increase the power of the incident beam, we observe that the EIT transmission window disappears, i.e. we can switch the transmission window through the input beam without need for an external signal. The disappearance of the EIT window is related to local field hotspots at the corners of the split rings, which we observe in numerical simulations and local field measurements (Figure 8.14(c)). The localized spots of highly enhanced current density can reach the critical current density of the superconductor. In that state, there is magnetic flux generated by the microwave currents that enters the Nb film and causes dissipation. As the critical state extends further into the material (see measured current distributions in Figure 8.14(d)), the dissipation leads to thermal runaway and eventually to quenching of the superconductivity at 22 dBm. This in turn leads to a decrease in the resonator's quality factor and to a switching off of the EIT features.

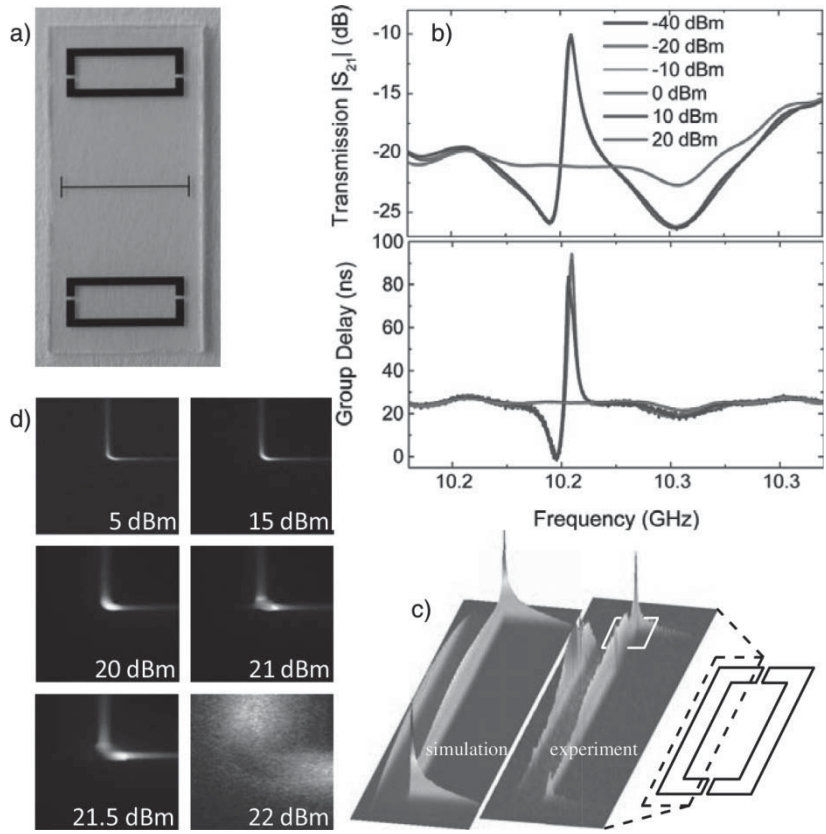

Figure 8.14. *a) EIT metamaterial with nonlinear response; b) transmittance and group delay spectra as a function of input power; c) field hotspots at the corners of the split-ring resonators; d) thermal runaway and quenching of the superconducting state (source: from Appl. Phys. Lett., vol. 100, 2012, p. 121906)*

Similarly, the strong near fields allow for the creation of tunable slow-light metamaterials, e.g., by using a semiconductor substrate and changing the carrier density by thermal control [BAI 10], or by photo-exciting carriers in a silicon substrate using an optical pump [GU 12]. All these examples essentially amount to changing the quality factor of the dark resonance to take advantage of the sensitive nature of the response of EIT metamaterial to this parameter.

8.7. Bibliography

[AKU 98] AKULSHIN A.M., BARREIRO S., LEZAMA A., "Electromagnetically induced absorption and transparency due to resonant two-field excitation of quasidegenerate levels in Rb vapor", *Physical Review A*, vol. 57, pp. 2996–3002, 1998.

[BAI 10] BAI Q., LIU C., CHEN J., *et al.*, "Tunable slow light in semiconductor metamaterial in a broad terahertz regime", *Journal of Applied Physics*, vol. 107, p. 093104, 2010.

[DON 10] DONG Z.-G., LIU H., CAO J.-X., *et al.*, "Enhanced sensing performance by the plasmonic analog of electromagnetically induced transparency in active metamaterials", *Applied Physics Letters*, vol. 97, p. 114101, 2010.

[FLE 00] FLEISCHHAUER M., LUKIN M.D., "Dark-state polaritons in electromagnetically induced transparency", *Physical Review Letters*, vol. 84, pp. 5094–5097, 2000.

[FLE 05] FLEISCHHAUER M., IMAMOGLU A., MARANGOS J.P., "Electro-magnetically induced transparency: optics in coherent media", *Reviews of Modern Physics*, vol. 77, pp. 633–673, 2005.

[GAR 02] GARRIDO-ALZAR C.L., MARTINEZ M.A.G., NUSSENSVEIG P., "Classical analog of electromagnetically induced transparency", *American Journal of Physics*, vol. 70, pp. 37–41, 2002.

[GU 12] GU J., SINGH R., LIU X., *et al.*, "Active control of electromagnetically induced transparency analogue in terahertz metamaterials", *Nature Communications*, vol. 3, p. 1151, 2012.

[HAR 90] HARRIS S.E., FIELD J.E., IMAMOGLU A., "Nonlinear optical processes using electromagnetically induced transparency", *Physical Review Letters*, vol. 64, pp. 1107–1110, 1990.

[HAR 97] HARRIS S.E., "Electromagnetically induced transparency", *Physics Today*, vol. 50, pp. 36–42, 1997.

[HAU 99] HAU L.V., HARRIS S.E., DUTTON Z., *et al.*, "Light speed reduction to 17 metres per second in an ultracold atomic gas", *Nature*, vol. 397, pp. 594–598, 1999.

[KUR 11] KURTER C., TASSIN P., ZHANG L., *et al.*, "Classical analogue of electromagnetically induced transparency with a metal-superconductor hybrid metamaterial", *Physical Review Letters*, vol. 107, p. 043901, 2011.

[KUR 12] KURTER C., TASSIN P., ZHURAVEL A.P., *et al.*, "Switching nonlinearity in a superconductor-enhanced metamaterial", *Applied Physics Letters*, vol. 100, p. 121906, 2012.

[LIU 01] LIU C., DUTTON Z., BEHROOZI C.H., *et al.*, "Observation of coherent optical information storage in an atomic medium using halted light pulses", *Nature*, vol. 409, pp. 490–493, 2001.

[LIU 09] LIU N., LANGGUTH L., WEISS T., *et al.*, "Plasmonic analogue of electromagnetically induced transparency at the Drude damping limit", *Nature Materials*, vol. 8, pp. 758–762, 2009.

[LIU 10a] LIU F., KE M., ZHANG A., *et al.*, "Acoustic analog of electromagnetically induced transparency in periodic arrays of square rods", *Physical Review E*, vol. 82, p. 026601, 2010.

[LIU 10b] LIU N., WEISS T., MESCH M., *et al.*, "Planar metamaterial analogue of electromagnetically induced transparency for plasmonic sensing", *Nano Letters*, vol. 10, pp. 1103–1107, 2010.

[MAN 01] MANDEL P., "Electromagnetically induced transparency", *Hyperfine Interactions*, vol. 135, pp. 223–231, 2001.

[OOI 11] OOI K., OKADA T., TANAKA K., "Mimicking electromagnetically induced transparency by spoof surface plasmons", *Physical Review B*, vol. 84, p. 115405, 2011.

[PAP 08] PAPASIMAKIS N., FEDOTOV V.A., ZHELUDEV N.I., *et al.*, "Metamaterial analog of electromagnetically induced transparency", *Physical Review Letters*, vol. 101, p. 253903, 2008.

[PAP 09] PAPASIMAKIS N., FU Y.H., FEDOTOV V.A., *et al.*, "Metamaterial with polarization and direction insensitive resonant transmission response mimicking electromagnetically induced transparency", *Applied Physics Letters*, vol. 94, p. 211902, 2009.

[SIN 09] SINGH R., ROCKSTUHL C., LEDERER F., *et al.*, "Coupling between a dark and a bright eigenmode in a terahertz metamaterial", *Physical Review B*, vol. 79, p. 085111, 2009.

[TAS 09a] TASSIN P., ZHANG L., KOSCHNY T., *et al.*, "Low-loss metamaterials based on classical electromagnetically induced transparency", *Physical Review Letters*, vol. 102, p. 053901, 2009.

[TAS 09b] TASSIN P., ZHANG L., KOSCHNY T., *et al.*, "Planar designs for electromagnetically induced transparency in metamaterials", *Optics Express*, vol. 17, pp. 5595–5606, 2009.

[TAU 12] TAUBERT R., HENTSCHEL M., KASTEL J., *et al.*, "Classical analog of electromagnetically induced absorption in plasmonics", *Nano Letters*, vol. 12, pp. 1367–1371, 2012.

[TSA 10] TSAKMAKIDIS K.L., WARTAK M.S., COOK J.J.H., *et al.*, "Negative-permeability electromagnetically induced transparent and magnetically active metamaterials", *Physical Review B*, vol. 81, p. 195128, 2010.

[VER 11] VERELLEN N., VAN DORPE P., HUANG C., *et al.*, "Plasmon line shaping using nanocrosses for high sensitivity localized surface plasmon resonance sensing", *Nano Letters*, vol. 11, pp. 391–397, 2011.

[VER 12] VERSLEGERS L., YU Z., RUAN Z., *et al.*, "From electromagnetically induced transparency to superscattering with a single structure: a coupled-mode theory for doubly resonant structures", *Physical Review Letters*, vol. 108, p. 083902, 2012.

[XU 06] XU Q., SANDHU S., POVINELLI M.L., *et al.*, *Physical Review Letters*, vol. 96, p. 123901, 2006.

[ZHA 08] ZHANG S., GENOV D.A., WANG Y., *et al.*, "Plasmon-induced transparency in metamaterials", *Physical Review Letters*, vol. 101, p. 047401, 2008.

[ZHA 10a] ZHANG L., TASSIN P., KOSCHNY T., *et al.*, "Large group delay in a microwave metamaterial analog of electromagnetically induced transparency", *Applied Physics Letters*, vol. 97, p. 241904, 2010.

[ZHA 10b] ZHANG J., XIAO S., JEPPESEN C., *et al.*, "Electromagnetically induced transparency in metamaterials at near-infrared frequency", *Optics Express*, vol. 18, pp. 17187–17192, 2010.

List of Authors

Shah Nawaz BUROKUR
Institut d'Électronique
Fondamentale (IEF)
University of Paris Sud
Orsay
France

Stefan ENOCH
Institut Fresnel
University Aix Marseille
France

Mohamed FARHAT
Institut Fresnel
University Aix Marseille
France

Sébastien GUENNEAU
Institut Fresnel
University Aix Marseille
France

Muamer KADIC
Institute of Applied Physics
Karlsruhe Institute of Technology
Germany

Thomas KOSCHNY
Ames Lab
Iowa State University
Ames
USA

Éric LHEURETTE
Institut d'Électronique de
Microélectronique et de
Nanotechnologie (IEMN)
University of Lille 1
Villeneuve d'Ascq
France

Didier LIPPENS
Institut d'Électronique de
Microélectronique et de
Nanotechnologie (IEMN)
University of Lille 1
Villeneuve d'Ascq
France

André DE LUSTRAC
Institut d'Électronique
Fondamentale (IEF)
University of Paris Sud
Orsay
France

Romain QUIDANT
Institute of Photonic Sciences
(ICFO)
Barcelona
Spain

Bruno SAUVIAC
Laboratoire Claude Chappe
(LT2C)
Télécom Saint-Étienne
University Jean Monnet
Saint-Étienne
France

Divitha SEETHARAMDOO
Institut Français des Sciences et
Technologies du transport, de
l'aménagement et des réseaux
(IFSTTAR-Lille)
Villeneuve d'Ascq
France

Costas M. SOUKOULIS
Ames Lab
Iowa State University
Ames
USA

Philippe TASSIN
Department of Applied Physics
Chalmers University
Gothenburg
Sweden

Paul-Henri TICHIT
Institut d'Électronique
Fondamentale (IEF)
University of Paris Sud
Orsay
France

Index